

University of Nottingham
UK | CHINA | MALAYSIA

Experimental and Computational Investigation into Oil Shedding from an Aeroengine Ball Bearing

Jee Loong Hee
MEng

Submitted to the University of Nottingham for the degree of *Doctor of Philosophy*, October 2018.

Abstract

Aero-engines contains ball bearings that support the shafts and react to the loads. During the investigation of improvements and the pursuit for higher bypass ratio, propulsion and thermal efficiency, regimes are explored where an aero-engine's core is subjected to higher mechanical and thermal loadings as it is required to operate at a higher temperature, pressure and speed. There is thus a need for continual development in aero-engine oil systems in order to meet the demands for optimised cooling and lubrication ie good cooling performance without increasing engine weight. Using computational fluid dynamics (CFD) to model aeroengine transmissions elements and systems is an attractive research approach but a pre-requisite for an accurate simulation lies within the 'exactness' of the boundary conditions. The research presented in this thesis is dedicated to understanding the oil shedding process of an aero-engine ball bearing operating at moderate speeds and to acquire the boundary conditions for CFD simulations. This thesis further presents a computational investigation that develops bearing chamber modelling techniques.

In the past, studies on rotating elements in aero-engines have largely been based on empiricism. Roller bearings have been experimentally investigated but this is not directly applicable to ball bearings because of key differences including: lubrication method, geometry, dynamic effects and axial loading. Prior data is limited for aero-engine ball bearings particularly with regard to how the oil sheds and its interaction with the air in the surrounding bearing chamber.

A test rig was built at the Gas Turbine Transmission Research Centre (G2TRC) to understand the bearing oil shedding process. It consists of an aero-engine ball bearing fitted onto a direct-drive electric motor and contained within two chambers. Oil is fed through under-race lubrication and the churning of oil from the mechanically rotating ball bearings results in shedding at the orbiting cage in the forms of droplets, ligaments and oil sheets. The oil impinges onto the outer periphery of the chamber wall, merging with the axially exiting oil from bearing gap and forms a layer of thin continuous film driven around by interfacial shear stress and gravity (at low speed). High speed imaging was used during the experimental investigation.

A new optical image processing technique was developed as part of this research and used to determine the oil film thickness at various angular positions of the bearing containment. Application was to the co-current and counter-current sides of the chamber wall where gravity acts with and opposing the interfacial shear stress respectively. The technique employed the use of the temporal-averaging scheme known as 'median-stacking' along with gradient detection and spatial calibration to determine the film thickness. High-speed imaging was also used in the

assessment of modes of droplet disintegration from the orbiting cage and characterisations of the structure of the wave on the surfaces close to the bearing. An inversely proportional relation between oil film thickness and shaft rotational speed was established, with no significant effect of change of oil flow rate observed. Axial load was found to be axial-plane specific in affecting the oil film thickness. In particular at a plane very close to the ball bearing the film thickness was found to be proportional to the load. The effect is attributed to changes in dynamic behaviour of the ball bearing. A correlation for ligament number was also developed for aero-engine operating conditions and geometry for the first time. The ligament number was comparable with those from classical studies involving rotary disks and cups.

Image analysis revealed the existence of multiscale wave structures on the surface of the film. At low shaft speed, the waves exhibit gravity-capillary like structures with distinctive in-phase wave-fronts, long wavelength and low frequency. In contrast at higher rotational speed, small scale wave structures were observed known as capillary waves which contain steeper wave-fronts, shorter wavelength and higher frequency. These structures are of primary importance in the momentum transfer between air and oil, and are reported as difficult to model during published prior numerical studies. Further modelling challenges were highlighted by observed droplet impact outcomes which included splashing and jetting.

A computational modelling strategy was developed and validated against a published study. This strategy centres on the application of coupled Volume-of-Fluid, Discrete Phase Model and Eulerian Thin Film Model (VOF-DPM-ETFM) where different parts of the flow are modelled based on the cost and accuracy suitable for the regime. In particular, the uniform thickness shear-driven film at high rotational speed is a suitable candidate of ETFM with droplets tracked using DPM. An efficient computational guideline was established in the assessment of the fidelity and numerical stability of coupled DPM-ETFM to ensure that the model works as intended. This is based on the simulation of jet-breakup and thin film formation in cross-flow that is transferable to bearing chamber modelling. The studies indicated that the developed approach is capable of modelling the discrete-phase and thin film to a certain level of accuracy but instability remains when specialised terms for gas-film momentum, edge separation and surface tension are activated. It was found that the thin film model with inclusion of stripping criteria, yields the best result compared with the published experimental study at 28.9% difference.

The experimental research presented in this thesis represents a significant step forward in understanding how oil sheds from a bearing and what the influencing operational factors are. The computational study has made an important contribution to the development of an industrially relevant bearing chamber modelling framework.

List of Publications

1. J. L. Hee, R. Santhosh, K. Simmons, G. Johnson, D. Hann, and M. Walsh, *"Oil Film Thickness Measurements on Surfaces Close to an Aero-engine Ball Bearing using Optical Techniques"*, Conference Proceedings ASME GT2017-63813, 2017.

2. R. Santhosh, J. L. Hee, K. Simmons, G. Johnson, D. Hann, and M. Walsh, "*Oil Shedding from an Aero-engine Ball Bearing at Moderate Speeds"*, Conference Proceedings ASME GT2017-63815, 2017.

3. J. L. Hee, K. Simmons, B. Kakimpa, and D. Hann, *"Computationally Efficient Modelling of Oil Jet Breakup and Thin Film Formation for Bearing Chamber Applications"*, Conference Proceedings ASME GT2018-76172, 2018.

4. J. L. Hee, K. Simmons, D. Hann, and M. Walsh *"Characterisations of Waves and Ligaments in Films Close to an Aero-engine Ball Bearing"*, Conference Proceedings ASME GT2019-91698, 2019.

Acknowledgement

I would like to express my sincere gratitude to my supervisor Dr Kathy Johnson for her dedication and patience in guiding me through the PhD. Having been able to undertake the research has meant a lot for me and I am delighted to be given the opportunity. I would like to thank Dr David Hann for his advice, guidance and input in the research and academic teaching. Thirdly but not least, my co-supervisor Dr Bruce Kakimpa who helped me through computational fluid dynamics (CFD). The research completion must also be credited Dr R Santhosh who aided me in experimental research and provided great insights in the work. I am pleased to learn from them.

Apart from academics, Dr Graham Johnson who provided the direction in the research and advice on instrumentation. The financial support of Rolls Royce Plc and Technology Strategy Board (TSB) is also gratefully acknowledged. I am also very pleased to have the University of Nottingham for sponsoring my PhD and also thanks to Dr Carol Eastwick for detailed reviews of my work as an internal examiner. Support from the technical team and APM are acknowledged as well.

In my period in Gas Turbine and Transmissions Research Centre (G2TRC), I was very fortunate to have met many great individuals. Special thanks to my mentors in CFD – Dr Adeniyi Akinola and Dr Thiago Piazera de Carvalho who stepped forward to guide me whenever needed or not. Additionally, I also thank my colleagues in G2TRC for making this memorable; Dr Stephen Ambrose, Dr Kiran PVS, Dr Evgenia Korsukova, Dr Keith Evans, Dr Andrea Bristot, Dr Omar Iracheta, Dr Gerry Salerno, Piotr Zacharzewski, Andrew Nicoli, Dafne Gaviria Arcila, Martin Berthold among others, a very important individual who is selfless in helping me in life, academic and coding – Ossama Muhammad. Special thanks to Dr Ali Aliyu for feedback relevant to my work and many interesting scientific discussions. Last but not least, thanks to my family for giving me great encouragement and support.

Contents

Abstract I

List of Publications III

Acknowledgement IV

Contents V

List of Figures XI

List of Tables XX

Nomenclature XXII

Chapter 1 Introduction 1

1.1 Background 1

1.2 Future Concepts and the Importance of Oil Systems 2

1.3 Aero-Engine Ball Bearing 3

1.4 Full Flow Oil Systems 4

1.4.1 Aero-Engine Bearing Chamber Flow Phenomena 5

1.5 Industrial Driver & Research Gaps 9

1.6 Aim and Objectives 12

1.7 Proposed Methodology 12

1.8 Thesis Structure 13

Chapter 2 Literature Reviews 15

2.1 Experimental Studies 15

2.1.1 Early Investigations on Bearing Chamber 15

2.1.2 Measurement of Airflow in Bearing Chamber 16

2.1.3 Measurement of Film Thickness in Chamber Wall 17

2.1.4 Modes of Droplet Disintegration from Rotating Devices 18

2.1.4.1 Critical Correlation for the Transition of Direct-Drop, Ligament and Sheet 22
2.1.4.2 Droplets Generation from Roller Bearing 27
2.1.4.3 Power Losses in Bearing Chamber 28
2.1.5 Turbulent Jets in Bearing Chamber 28
2.1.6 Taylor-Couette Flow in Coaxial Cylinders 29
2.1.7 Flow Regimes in Bearing Chamber 31
2.1.8 Shear-Driven Liquid Film 33
2.1.8.1 Droplet Impingement on Shear-Driven Liquid Film 33
2.2 Numerical Studies 34
2.2.1 Airflow in Chambers and Cavities 35
2.2.2 Direct Numerical Simulation of Turbulent Taylor-Couette Flow 36
2.2.3 Multiphase Flow Simulation in Bearing Chamber 37
2.2.3.1 Volume-of-Fluid Approach in Bearing Chamber Modelling 38
2.2.3.2 Coupled VOF-DPM 39
2.2.3.3 Evaluation of VOF in Bearing Chamber 39
2.2.3.4 Turbulence Damping, ***B*** 40
2.2.3.5 Progression in Eulerian Thin Film Model 40
2.2.3.6 Coupled VOF-ETFM 41
2.2.4 Comparison of Unsteady Reynolds Averaged Navier Stokes (URANS) versus Large Eddy Simulation (LES) 43
2.2.5 Meshing and Verification 45
2.3 Bridging Knowledge Gaps in Bearing Chamber Research 47
2.4 Summary of Literature Reviews 50
Chapter 3 Test Rig for Trent 1000 Aero-Engine Ball Bearing 52
3.1 Introduction 52
3.2 Rig Design & Description 53
3.2.1 Oil Systems 55
3.2.1.1 Bearing Oil Feeds 57

3.2.1.2 Bearing Oil Flow Rates 58
3.2.2 Axial Loading by Electromagnetic Actuator 59
3.2.3 Control System of the Rig 60
3.2.4 Rig Instrumentations 63
3.2.5 Proposed Measurements 63
3.3 Summary of Test Rig for Trent 1000 Aero-Engine Ball Bearing 65
Chapter 4 High Speed Imaging 66
4.1 Introduction 66
4.1.1 Principle of Imaging I – Resolution & Frequency 67
4.1.2 Principle of Imaging II – Field of View & Focal Length 69
4.1.3 Principle of Imaging III – Exposure Time & Aperture 70
4.1.4 Principle of Imaging IV – Illumination 72
4.1.5 Long Distance Microscope 73
4.1.5.1 Setup for Coupled LDM-HS 73
4.1.6 Comparison of Optical Resolution for HS & LDM-HS 77
4.1.7 Acquisition Position of High Speed Imaging 79
4.1.7.1 Angular Positioning – **θ** / PX 79
4.1.7.2 Axial Positioning 80
4.1.8 Accuracy of Test Instruments 84
4.1.9 Repeatability of Flow Structure 85
4.2 Oil Film Thickness Measurement by Optical Technique 88
4.2.1 Experimental Test Cases for Film Thickness Measurement 88
4.2.2 Image Processing I – Temporal Averaging & Median Stacking 89
4.2.3 Image Processing II – Edge Detection of Oil Film 92
4.2.4 Image Processing III – Edge Detection of Solid Surface 96
4.2.5 Image Processing IV – Spatial Calibration Factor 97
4.2.6 Accuracy of Film Thickness Measurement using Optical Technique 100
4.2.7 Qualitative Analysis of Oil Film Thickness 104
4.2.8 Quantitative Analysis of Oil Film Thickness 107

4.2.8.1 Effect of Speed, Gravity and Flow Rate 109
4.2.8.2 Effect of Axial Bearing Load 110
4.2.9 Curve Fitting for Oil Film Thickness with Respect to Varying Operating Condition 111
4.2.10 Error Propagation 115
4.3 Mechanisms of Oil Breakup at Aero-engine Ball Bearing 117
4.3.1 Experimental Test Cases for Characterisation of Oil-Breakup 119
4.3.2 Qualitative Observations of Oil Shedding from Cage Edge 120
4.3.3 Summary of Oil Shedding & Preliminary Comparison 135
4.3.4 Ligament Number – $\boldsymbol{K}$ 140
4.3.4.1 Operating Speeds where Ligaments Are Observed 140
4.3.4.2 Methodology of Ligament Detection 142
4.3.4.3 Nonlinear Regression & Comparison of $\boldsymbol{K}$ with Published Data 144
4.4 Dynamics of Waves on Surfaces Close to an Aero-engine Ball Bearing 148
4.4.1 Surface Waves – Period & Frequency 149
4.4.2 Surface Waves – Instabilities 150
4.4.3 Critical Wavelength for Surface Waves 152
4.4.4 Methods of Calculating – Wavelength & Frequency 153
4.4.5 Wavelength of Surface Waves – $\boldsymbol{\lambda}$ 158
4.4.6 Frequency of Surface Waves – $\boldsymbol{fwave}$ 161
4.5 Summary of High Speed Imaging 162
Chapter 5 Computational Fluid Dynamics 165
5.1 Introduction 165
5.2 Motivations of Computational Modelling 166
5.3 The Developments of 2D Thin Film Model 169
5.4 Governing Equations 170
5.4.1 Continuity Equation 170
5.4.2 Navier-Stokes Equation (N-S) 171
5.5 Turbulence Modelling 172

5.5.1 Unsteady Reynolds-Averaged Navier-Stokes Equations (URANS) 172
5.5.2 Choice of Turbulence Model – Menter $\boldsymbol{k-\omega}$ SST Turbulence Model 173
5.5.3 Near Wall Treatment 174
5.6 Discretisation Scheme 175
5.6.1 Spatial Discretisation 175
5.6.2 Temporal Discretisation for Time-Marching 176
5.6.3 Pressure-Velocity Coupling (P-V) 178
5.7 Discrete-Phase Model 178
5.7.1 Particle Force Balance Equation 179
5.7.1.1 Dynamic Drag Model 179
5.7.1.2 Interphase Momentum Exchange 180
5.7.2 Primary Atomisation of Plain Orifice Model 181
5.7.2.1 Nozzle State 181
5.7.2.2 Exit Velocity 182
5.7.2.3 Spray Angle, $\boldsymbol{\theta}$ 182
5.7.2.4 Droplet Diameter Distribution 183
5.7.3 Secondary Atomisation of Droplets 186
5.7.4 Turbulent Dispersion of Particles 187
5.8 Eulerian Thin Film Model 188
5.8.1 Continuity Equation for ETFM 188
5.8.2 Momentum Equation for ETFM 188
5.8.3 DPM Collection 189
5.8.4 Splashing 189
5.8.5 Edge Separation 190
5.8.6 Shear Stripping 191
5.9 Mesh and Grid Generation 195
5.10 Numerical Settings 197
5.10.1 Physics of Jet Breakup and Thin Film Formation in Crossflow 199
5.10.2 Flow Development 200

5.10.3 Sensitivity Study for Particle Time-Step Size 201
5.10.4 Mass Convergence 203
5.11 Field Variables 204
5.11.1 Particle Field 204
5.11.2 Particle Diameter and Pressure Field 205
5.11.3 Velocity Field 206
5.12 Solution Variables 207
5.12.1 Number of Injection Stream 210
5.12.2 Airflow Time-Step 211
5.12.3 Mesh Dependency Test 212
5.12.4 Turbulent Dispersion 212
5.12.5 Pressure Gradient and Spreading 214
5.12.6 Instabilities of Surface Tension 215
5.12.7 Stripping Criteria 216
5.12.8 Error Calculation 217
5.13 Summary of CFD 217
Chapter 6 Conclusion **220**
6.1 Summary of Main Findings 220
6.2 Contribution to Knowledge 223
6.3 Recommendations for Future Work 224
6.3.1 Experimental Investigations 224
6.3.2 Computational Investigations 225
References **227**
Appendix **239**
Images for calculation of Ligament number 240

List of Figures

Figure 1.1: A schematic of three-spool jet-engine showing location of bearings (Adapted from [3]) 3

Figure 1.2: A schematic of a simplified full flow oil system (Recreated based on concept from [3]) 4

Figure 1.3: Schematic illustration of the aero-engine bearing chambers used in the research 6

Figure 1.4: The physics of flow at various angular positions of the front chamber 7

Figure 1.5: Droplet impingement at an oblique angle as observed in bearing chamber from 6 o'clock position at operating conditions of 5000 rpm, 10 kN and 5.2 litre/min 8

Figure 1.6: Updated trend toward increased DN values for mainshaft bearings (baseline points extracted from [10]) 11

Figure 2.1: Disintegration by (a) Direct drop formation (b) Ligament formation (c) Sheet formation [20] 19

Figure 2.2: Mechanisms of liquid disintegration by Frost [21] at unspecified conditions; (a) Direct-Drop formation (b) Ligament formation (c) Sheet formation.....19

Figure 2.3: Mechanisms of liquid disintegrations by Matsumoto *et al.* [26];.....20

Figure 2.4: Mechanisms of liquid disintegrations by Liu *et al.* [27]; 20

Figure 2.5: Variability in local liquid flow rate over a disc surface due to eccentricity of feeding tube. (Adapted from Frost [21]) 21

Figure 2.6: Droplet disintegration map [28] 24

Figure 2.7: Design of bearing support: **90°** edge (left) and curved edge (right) between the outer ring and the support [34] 27

Figure 2.8: Demarcation lines for flow regions in annulus with inner cylinder rotating [35] 31

Figure 2.9: Determination of the change in flow regime in an aero-engine bearing chamber; (a) front view of the location of capacitive sensors (b) film thickness at $\phi = 315°$ versus speed, dashed line indicates regime change [45] 32

Figure 2.10: Outcomes of droplet impact onto liquid surface (Adapted from [47]).....34

Figure 2.11: Number of wind tunnel testing in the past five decades and the timeline of the development of general turbulence models [51] 35

Figure 2.12: Herringbone-like streaks demonstrated based on plot of azimuthal velocity along z-direction for (a) $Re = 1000$, (b) $Re = 3000$, (c) $Re = 5000$, (d) $Re = 8000$ [53].....37

Figure 2.13: Three-dimensional oil structure separated at the edge of a chamber wall.....43

Figure 2.14: A hierachy of CFD methods based on computational cost and the level of resolution [89].....45

Figure 2.15: Image showing (a) Structured hexahedral mesh and (b) Unstructured tetrahedral mesh with prism layers. [90] 46

Figure 3.1: General arrangement of bearing oil shedding rig (adapted from [97]).....54

Figure 3.2: Cross-sectional view of mid-plane across bearing oil shedding rig showing various sub-components (adapted from [97]).....55

Figure 3.3: Schematic of oil system for the test rig 56

Figure 3.4: Independent oil feed system featured on the rig.....58

Figure 3.5: Dynamics of ball bearing under axial loading (recreated based on [93]).....60

Figure 3.6: Graphical User Interface (GUI) for rig operation.....61

Figure 3.7: Full digital listing window.....62

Figure 3.8: Location and type of instruments embedded into the rig (Adapted from [97]) ● Temperature, ● Force, ● Torque, ● Flow, ● Speed, ● Acceleration.....63

Figure 3.9: Proposed measurement options (Adapted from [97]).....64

Figure 4.1 Image resolution showing reducing size in horizontal pixel yielding smaller image but higher frame rate 68

Figure 4.2: Concept of field of view, focal length and magnification. (Recreated based on *Nikon*^{TM} information [99]) 70

Figure 4.3: Effect of shutter speed on Ferris wheel at night [102] 71

Figure 4.4: Sample images corresponding to different f-number/aperture at night time [103] 71

Figure 4.5: LEDs illumination for experimental campaign on bearing oil shedding rig 72

Figure 4.6: Long distance microscope *QM-1* being setup for imaging 73

Figure 4.7: Schematic of experimental setup for LDM-HS 74

Figure 4.8: Focus calibration for LDM-HS 75

Figure 4.9: Comparison of image resolution (in mm) taken by HS and LDM-HS 77

Figure 4.10: Schematic of front view of bearing oil shedding rig depicting 4 angular positions based on clockwise rotation (P1 - $\mathbf{0}°$, P2 - $\mathbf{90}°$, P3 - $\mathbf{180}°$, P4 - $\mathbf{270}°$) 79

Figure 4.11: Cross-sectional view of the ball bearing showing axial planes of focus for image acquisition from A to G 80

Figure 4.12: Sample HS images (without oil flow) at visualisation plane A, D, F and G taken from viewing position P2 81

Figure 4.13: Sample HS images (with oil flow) at visualisation plane A, D, F and G taken from viewing position P2 81

Figure 4.14: Sample LDM-HS images (with flow) at visualisation plane B, D and G from viewing position P2 82

Figure 4.15: Data logging from sensors within the test rig taken at operating condition - speed 3000 rpm, flow rate 5.2 lpm and axial load 10 kN. The instantaneous value for flow-rate, speed and load are plotted in subplot (A), (B) and (D). The corresponding mean and standard deviation are plotted in (D), (E) and (F). 85

Figure 4.16: 'Median' images of oil film thickness obtained at different day at the same operating condition (speed 3000 rpm, flow rate 5.2 lpm and load 10 kN) on (a) 03/03/2016 (b) 12/04/2016 and (c) 19/02/2016.....86

Figure 4.17: Oil film profiles for test case S3000-F5.2-L10-P2 taken at (a) $\tau = 0$ (b) $\tau = 0.25$ (c) $\tau = 0.5$ (d) $\tau = 0.75$.....89

Figure 4.18: Time-averaging and 'median-stacking' process which yield steady-state flow feature.....91

Figure 4.19: Vector search for image intensity of the radial distribution of oil flow case and the application of smoothing function to suppress background noise.....93

Figure 4.20: Comparison of smoothing function based on averaging of different discrete point.....94

Figure 4.21: Determination of oil film thickness ($\boldsymbol{\delta}$).....94

Figure 4.22: Detection of solid surface using peak at axial location: (a) Plane of focus B (3 mm (b) Plane of focus D (10 mm) and (c) Plane of focus G (36.8 mm) with 2.5x digital zoom on the right.....96

Figure 4.23: The process of 'Spatial Calibration' to correlating the subject with object of known dimension.....99

Figure 4.24: Median-stacked images used in the uncertainty study 101

Figure 4.25: Detection of air-oil interface based on manual selection of 10 volunteers at different test point to determine the accuracy 103

Figure 4.26: Sample HS images (top row) and LDM-HS (bottom row) at different shaft speeds at co-current side (P2), plane of focus D 105

Figure 4.27: Sample HS images (top row) and LDM-HS (bottom row) at different shaft speeds at counter-current (P4), plane of focus D.....105

Figure 4.28: Variation of oil film thickness (δ) comparing co-current and counter-current regions (P2 and P4). Based on effect of shaft rotational speed, bearing axial load and oil flow rate. Planes B, D and G. 108

Figure 4.29: Free body diagram depicting key forces and angles characterising ball-bearing statics [93].....110

Figure 4.30: Curve fitted for oil film thickness versus changing shaft speed, oil flow rate and bearing axial load. Subplot (a), (b) and (c) corresponded to curve fitted at co-current regime (P2). Subplot (d), (e) and (f) corresponded to curve fitted at counter-current side (P4) 114

Figure 4.31: Cross-sectional view of *Trent* 1000 HP location bearing showing edges of bearing cage (marked as location '1' and '2') and static surfaces (marked as '3') 117

Figure 4.32: Direction of liquid flow for (a) Rotary disk and (b) Rotary cup 118

Figure 4.33: Oil-breakup mechanism (direct-drop) as seen from Plane F for S1000-F5.2-L10-P2 (a) $t = 0\ s$ (b) $t = 0.062\ s$ (c) $t = 0.124\ s$ (d) $t = 0.186$ s (e) $t = 0.2484$ s.....123

Figure 4.34: Oil-breakup mechanisms (ligament & sheet) as seen from Plane F for S1700-F5.2-L10-P2 (a) $t = 0.017$ s (b) $t = 0.049$ s (c) 0.1006 s (d) $t = 0.120$ s (e) $t = 0.164$ s 124

Figure 4.35: Oil-breakup mechanisms (sheet & ligament) as seen from Plane F for S2000-F5.2-L10-P2 (a) $t = 0.0301$ s (b) $t = 0.0892$ s (c) $t = 0.1295$ s (d) $t = 0.1564\ s$ (e) $t = 0.1763$ s.....125

Figure 4.36: Oil-breakup mechanisms (fine ligament & sheet) as seen from Plane F for S2400-F5.2-L10-P2 (a) $t = 0.0139$ s (b) $t = 0.0324$ s (c) $t = 0.0748$ s (d) $t = 0.1005\ s$ (e) $t = 0.1844$ s.....126

Figure 4.37: Oil breakup mechanisms (finer ligaments & sheet) as seen from Plane F for S3200-F5.2-L10-P2 (a) $t = 0.0164$ s (b) $t = 0.0609$ s (c) $t = 0.0961$ s (d) $t = 0.1283$ s (e) $t = 0.1857$ s 127

Figure 4.38: Oil-breakup mechanisms (sheet & extra-fine ligament) as seen from Plane F for S3800-F5.2-L10-P2 (a) $t = 0.0078$ s (b) $t = 0.0497$ s (c) $t = 0.0854$ s (d) $t = 0.1102$ s (e) $t = 0.1474$ s 128

Figure 4.39: Oil-breakup mechanisms (ruffled sheet & finest ligament) as seen from Plane F for S4300-F5.2-L10-P2 (a) $t = 0.0078$ s (b) $t = 0.0189$ s (c) $t = 0.0528$ s (d) $t = 0.1319$ s (e) $t = 0.1863$ s 129

Figure 4.40: Oil-breakup mechanisms (ruffled sheet) as seen from Plane F for S5000-F5.2-L10-P2 (a) $t = 0.0205$ s (b) $t = 0.0450$ s (c) $t = 0.0894$ s (d) $t = 0.1366$ s (e) $t = 0.1863$ s 130

Figure 4.41: Oil breakup mechanisms (secondary ligaments & ruffled sheets) as seen from Plane F for S5500-F5.2-L10-P2 (a) $t = 0.0047$ s (b) $t = 0.0466$ s (c) $t = 0.0912$ s (d) $t = 0.1340$ s (e) $t = 0.1780$ s 131

Figure 4.42: Oil breakup mechanisms (ruffled sheet & secondary ligaments) as seen from Plane F for S6000-F5.2-L10-P2 (a) $t = 0.0317$ s (b) $t = 0.0733$ s (c) $t = 0.1152$ s (d) $t = 0.1308$ s (e) $t = 0.1730$ s 132

Figure 4.43: Oil breakup mechanisms (ruffled sheet & secondary ligaments) as seen from Plane F for S6500-F5.2-L10-P2 (a) $t = 0.0314$ s (b) $t = 0.0727$ s (c) $t = 0.1096$ s (d) $t = 0.1281$ s (e) $t = 0.1790$ s 133

Figure 4.44: Oil breakup mechanisms (ruffled sheet & secondary ligaments) as seen from Plane F for S7000-F5.2-L10-P2 (a) $t = 0.0127$ s (b) $t = 0.0652$ s (c) $t = 0.0961$ s (d) $t = 0.1149$ s (e) $t = 0.1662$ s 134

Figure 4.45: Oil shedding process beginning from direct-drop to ligament & sheet to ruffled sheet & secondary ligament operating based on changing shaft speed.....136

Figure 4.46: Validation of critical correlations based on observations.....137

Figure 4.47: Observation of ligaments at different speeds ($\omega shaft$) and their corresponding spacing λ shown in inset images.....141

Figure 4.48: Instantaneous HS image and Canny's edge detection [113] showing ligaments locations from 1 to 27 pointing towards the central axis.....142

Figure 4.49: Plot of K versus We for comparison with published data.....145

Figure 4.50: Classification of waves based on frequency spectrum [116] 149

Figure 4.51: Instantaneous surface height measured using Synthetic Sclieren showing 'wrinkle' regime at (a) $Ua = 3.2$ m/s and (b) $Ua = 5.9$ m/s. Images at (c) and (d) are corresponding to 2D waves [117] 151

Figure 4.52: Regimes of horizontal stratified-wavy flow [118] 151

Figure 4.53: Wave patterns observed in gas-liquid flow. Regime map by Hanratty [119] and images from Lucie [120].....152

Figure 4.54: Determination of wavelength from (a) HS and (b) LDM-HS 153

Figure 4.55: Reference location used for determination of surface wave frequency for HS and LDM-HS 156

Figure 4.56: Instantaneous images depicting the transitioning of surface waves from gravity-capillary wave to capillary wave by increasing shaft rotational speed at co-current regime (P2) 158

Figure 4.57: Instantaneous images depicting the transitioning of surface waves from gravity-capillary wave to capillary wave by increasing shaft rotational speed at counter-current regime (P4) 159

Figure 4.58: $\boldsymbol{\lambda/\lambda crit}$ for con-current and counter-current regime for (a) flow rate 5.2 lpm (b) flow rate 7.3 lpm 160

Figure 4.59: Wave frequency versus rotational speed for co-current and counter-current side at flow rate (a) 5.2 lpm (b) 7.3 lpm 161

Figure 5.1: Illustration of film and interface resolution requirements for VOF (left) and ETFM (right) [81] 167

Figure 5.2: Proposed modelling approach for respective flow structures [126] 168

Figure 5.3: Cross-sectional view of aero-engine ball bearing corresponding to view A-A [126] 168

Figure 5.4: Mean velocity profile and subdivision of boundary layer. Flow condition at $2530 < Re < 27300$. Dash-dotted line ($U+ = (1/0.38)\ln y + +4.1$) [136]. .175

Figure 5.5: Discretisation of a 2D-triangular cell [135] 176

Figure 5.6: Particle size distribution based on different injection streams 185

Figure 5.7: Cumulative mass fraction for Rosin-Rammler distributions 185

Figure 5.8: Taylor Analogy Breakup based on spring-mass system [135] 187

Figure 5.9: Wef vs Ref at gas velocity of 82 m/s using power curve fitting [144] 191

Figure 5.10: critical Weber number for onset of shear stripping 195

Figure 5.11: Hexahedral grid generation based on structured mesh 196

Figure 5.12: (a) 2D Schematic of the domain for jet-breakup in cross-flow and phenomena governing the flow (b) 3D Schematic of jet-breakup in cross-flow 199

Figure 5.13: Flow development for turbulence quantities at the inlet 200

Figure 5.14: Computed trajectories at flow time $t = 9 \times 10 - 4$ s.....201

Figure 5.15: Mass convergence at bottom surface (legend shows turbulence model, timestep, number of injections, mesh size and activity of discrete random walk) 203

Figure 5.16: Particle trajectories in high shearing crossflow.....204

Figure 5.17: (a) Particle diameter and corresponding (b) Pressure field 205

Figure 5.18: Normalised velocity and velocity contours taken at mid-plane of the expansion 206

Figure 5.19: Line of measurement for relevant variables and film thickness.....207

Figure 5.20: Film thickness measurement along mid-line based on effect of (a) Number of particle injection streams (b) Airflow time-step, $\Delta tair$ (c) Mesh densities.....208

Figure 5.21: Film thickness measurement along mid-line based on effect of (d) Turbulent dispersion (b) Pressure gradient with spreading term (d) Stripping criteria.....209

Figure 5.22: Particle distribution (a) before and (b) after breakup for 1000 injection streams where (a) is taken at $t = 5 \times 10 - 5$ s and (b) is taken at $t = 2.5 \times 10 - 3$ s.210

Figure 5.23: The component of wall shear stress with its corresponding velocity magnitude 211

Figure 5.24: DPM mass source on bottom surface due to turbulent dispersion 213

Figure 5.25: Velocity field on mid-plane due to turbulent dispersion 213

Figure 5.26: Pressure gradient effect on (a) Time-averaged spanwise film thickness and (b) Time-averaged spanwise z-velocity 214

Figure 5.27: Contour of film thickness for non-pressure gradient term (static pressure and hydrostatic pressure) and with pressure-gradient term.....215

Figure 5.28: Contour of film thickness for full pressure gradient term (including surface tension) 216

Figure 6.1: Proposed dye tracking for film velocity measurement and BBLIF for details waves and film thickness analysis 225

Figure A 1: Images of ligament at (a) S1700-F5.2-L10-P2 (b) (c) S2000-F5.2-L10-P2 (d) (e) (f) S2400-F5.2-L10-P2.....240

Figure A 2: Images of ligament at (g) (h) S3200-F5.2-L10-P2 (i) (j) S3800-F5.2-L10-P2 (k) (l) S4300-F5.2-L10-P2.....241

List of Tables

Table 2.1: Correlations for direct-drop to ligament and for ligament to sheet from previously published literatures.....25

Table 3.1: Shaft speeds and oil flow rates employed in experimental investigations.....59

Table 4.1: Comparison between high-speed camera and conventional camera.....67

Table 4.2: Details of image settings employed for high speed imaging.....68

Table 4.3: Comparison between resolution of images taken by HS and LDM-HS.....78

Table 4.4: Test cases and their respective naming convention.....88

Table 4.5: Spatial calibration factor used for different locations.....98

Table 4.6: Uncertainty band in film thickness measurement using optical technique.....102

Table 4.7: List of coefficients derived for the empirical model using nonlinear regression model.....113

Table 4.8: Experimental test cases considered for the investigations of oil breakup mechanisms based on changing: rotational speed, at constant flow rate and axial load.....119

Table 4.9: Visualisation test cases proposed for future study.....139

Table 4.10: Operating conditions and their corresponding angular spacing angle and ligament number.....143

Table 4.11: Previously published correlations for ligament number.....144

Table 4.12: Measurement of Mean Absolute Percentage Error (MAPE) measured relative to Hee *et al*'s [114] ligament number.....147

Table 4.13: Experimental test cases considered for co-current regime.....148

Table 4.14: Experimental test cases considered for counter-current regime.....148

Table 4.15: Classification of waves' spectrum [116].....150

Table 4.16: Experimental test cases for co-current regime (P2) 155

Table 4.17: Experimental test cases for counter-current regime (P4) 155

Table 4.18: Wave frequency for co-current side 157

Table 4.19: Wave frequency for counter-current side 157

Table 5.1: Rosin-Rammler parameters for size distributions per injection time-step ($\Delta t = 5 \times 10 - 5$ s) 184

Table 5.2: Hexahedral grid density and corresponding geometry 196

Table 5.3: Airflow time-step, injection number, particle time-step, cell count and sub-models 198

Table 5.4: Parameters of sensitivity studies for particle time-step size 201

Nomenclature

Acronyms

2D	Two dimensional
3D	Three dimensional
AMB	Active magnetic bearing
AMR	Adaptive Mesh Refinement
APM	Administrative Professional and Managerial
CFD	Computational Fluid Dynamics
CFL	Courant-Friedrich-Lewy
CMOS	Complementary metal-oxide semiconductor
CPUh	Central processing unit hour
DL	Direct Drop to Ligament
DPM	Discrete Phase Model
DRW	Discrete Random Walk
ETFM	Eulerian Thin Film Model
EVM	Eddy Viscosity Model
FOV	Field of view
FPS	Frame per second
G2TRC	Gas Turbine Transmission Research Centre
HP	High pressure
HS	High speed
IGPH	Imperial gallons per hour
IP	Intermediate pressure
ITS	Institute fur Thermische Stromungsmaschinen
ISO	International Organisation for Standardization
K-H	Kelvin Helmholtz instability
KIT	Karlsruhe Institutes of Technology
LDM	Long distance microscope
LDV	Laser Doppler Velocimetry
LES	Large Eddy Simulation

LF	Ligament to Film
LP	Low pressure
lpm	Litre per minute
M	Million
MUSL	Monotonic Upwind Scheme for Conservation Laws
N.B.	Nota Bene / Note well
NRMSE	Normalised root mean square error
N-S	Navier-Stokes
PIV	Particle Image Velocimetry
P-R	Plateau Rayleigh instability
P-V	Pressure-Velocity Coupling
RAM	Random access memory
RMSE	Root mean square error
ROI	Region of interest
RPM	Revolution per minute
RSM	Reynolds Stress Model
R-T	Rayleigh Taylor instability
SA	Spalart-Allmaras
SMD	Sauter Mean Diameter
SOR	Statement of requirement
SST	Shear Stress Transportation
STP	Stripping
TUI	Text User Interface
URANS	Unsteady Reynolds Average Navier-Stokes
VOF	Volume-of-Fluid

Characteristic Numbers

C_f	Courant number
F_g	Geometric Factor
V^+	Non-dimensional flow rate
y^+	Non-dimensional wall distance / First cell centroid distance from the wall

Ma	Mach number
On	Ohnesorge number
Re_h	Reynolds number based on hydraulic head
Re_f	Reynolds number of film
Re	Reynolds number
St	Stability number
We^*	Modified Weber number
We_G	Weber number of gas
We_f	Weber number of film
We_{rel}	Relative Weber number
We	Weber number

Greek Letters

Δ	Increment / Size
∇	Gradient
$\sum$	Algebraic sum
ε	Turbulent dissipation energy [$m^2 s^{-3}$] / Entrainment coefficient
L	Largest length scale [m]
k	Turbulent kinetic energy [$m^2 s^{-3}$]
Γ	Diffusion coefficient
α	Ball bearing contact angle [°] / Droplet impingement angle [°]
β	Ball bearing rolling angle [°] / Sheltering parameter
γ	Mass percentage
δ	Film thickness [m] / Non-dimensional film thickness
ζ	Gaussian probability distribution
η	Kolmogorov length scale [m]
θ	Angle [°] / Ligament spacing angle [°]
λ	Wavelength [mm] / Integral length [m]
μ	Dynamic viscosity [Ns/m^2]
μ_t	Turbulent viscosity [Ns/m^2]

ν	Kinematic viscosity $[m^2s^{-1}]$ / Velocity $[ms^{-1}]$
ρ	Density $[kgm^{-3}]$
σ	Surface tension $[Nm^{-1}]$
τ	Shear stress $[Nm^{-2}]$ / Non-dimensional time
ω	Specific dissipation rate $[s^{-1}]$ / Angular velocity $[radsm^{-1}]$ /Rotational speed [rpm]
∂	Partial
ϕ	Scalar / Diameter $[m]$

Subscripts / Superscripts (Number)

0	Initial
1	Upstream / First
2	Downstream / Second
32	Sauter mean

Subscripts / Superscripts (Upper Case)

D	Drag
F	Force constant
L	Liquid
M	Mass
RR	Rosin-Rammler
V	Volume

Subscripts / Superscripts (Lower Case)

a	Coefficient of We based on non-linear regression
air	Air
$axial$	Axially
b	Coefficient of St based on non-linear regression
bl	Boundary layer
c	Critical / Centre
$cage$	Cage

cfd	Computational fluid dynamics
$crit$	Critical
d	Damping constant / Drag
du	Ultimate discharge
eff	Effective
$even$	Even number
exp	Experimental
f	Film
$faces$	Faces
g	Gas
i	First variable / Inner
ii	Second variable
iii	Third variable
$incep$	Inception
j	Jet
k	Spring constant
l	Liquid
lf	Liquid film
lfc	Liquid film critical
m	Momentum / Mean
$mean$	Average
$n+1$	Next time advancement
$n-1$	Previous time
o	Initial / outer
odd	Odd number
p	Particle / Pressure
r	Relative / Relaxation time
rim	Rim of a disk
s	Shear
s	Source
$shaft$	Shaft
$sphere$	Sphere

t	Turbulent
v	Vapour
vc	Vapour critical
w	Wall
$wave$	Wave
xx	Normal to the surface and parallel to x-direction
xy, yx	Parallel to x and y-direction
xz, zx	Parallel to x and z-direction
yy	Normal to the surface and parallel in y-direction
yz, zy	Parallel to y and z-direction
zz	Normal to the surface and parallel in z-direction

Latin Symbol (Upper Case)

A	Oil feed in the front
A	Plane of focus at 0 mm based on reference from front face
B	Oil feed in the middle
B	Plane of focus at 3 mm based on reference from front face
C	Oil feed in the rear
C	Plane of focus at 6 mm based on reference from front face
D	Plane of focus at 10 mm based on reference from front face
E	Plane of focus at 15 mm based on reference from front face
F	Plane of focus at 30 mm based on reference from front face
G	Plane of focus at 36.8 mm based on reference from front face
P1	Angular position at 0° based on reference point at 12 O'clock
P2	Angular position at 90° based on reference point at 12 O'clock
P3	Angular position at 180° based on reference point at 12 O'clock
P4	Angular position at 270° based on reference point at 12 O'clock

Latin Symbol (Italic)

A	Area $[m^2]$
C	Coefficient of Ligament number K

D	Disk Diameter $[m]$
E	Impingement energy
F	Additional forces [N] / Force [N]
J	Momentum flux ratio
K	Cavitation number (e.g., K_{incep}, K_{crit}) / Ligament number
L	Length $[m]$ / Characteristics length $[m]$
N	Rotational speed $[rpm]$
NP	Number of parcel
Q	Flow rate $[kg/s]$
R	Radius $[m]$ / Ratio of Film Thickness to Geometric Distance
S	Source term in the continuity equation and momentum equation
T	Temperature $[K]$
U	Velocity $[ms^{-1}]$
X	Distance along x-direction $[m]$

Latin Symbol (Accents)

$\vec{F}$	External forces
$\widetilde{U}$	Mean velocity $[ms^{-1}]$

Latin Symbol (Lower Case)

a	Radius of the cylinder $[m]$
b	Width of annulus $[m]$
c	Chord $[m]$
d	Nozzle diameter $[m]$ / Diameter $[m]$ / Gap Width $[m]$
f	Focal length
g	Gravitational acceleration [9.81 ms^{-2}]
h	Centre coordinate 1 / Height $[m]$
k	Centre coordinate 2
m	Mass $[kg]$

n	Shape factor / Total number / Shaft speed $[rpm]$ / Total number of frame
q	Volumetric flow rate $[m^3 s^{-1}]$
r	Radius $[m]$
t	time $[s]$
u	Velocity in x-direction $[ms^{-1}]$
u'	Velocity fluctuation in x-direction $[ms^{-1}]$
v	Velocity in y-direction $[ms^{-1}]$
v'	Fluctuating velocity in y-direction $[ms^{-1}]$
w	Velocity in z-direction $[ms^{-1}]$ / Width $[m]$
w'	Velocity fluctuation in z-direction $[ms^{-1}]$
x	Displacement $[m]$
y	Distortion of droplet $[m]$ / Radial distance $[m]$

Derivatives

Δt	Time-step size $[s]$
Δx	Characteristics length of the computational cell $[m]$
∇I	Gradient of image intensity
$\Delta \rho$	Relative densities
div	Divergence
$\partial h/\partial \theta$	Rate of change of film height in polar coordinate system $[m]$
$\partial \rho/\partial t$	Time-dependent term for pressure $[kgm^{-3}s^{-1}]$
$\partial \phi/\partial t$	Time-evolution of variable ϕ $[unit/s]$
$\partial I/\partial x$	Derivative of image intensity in x-direction

MATLAB operations

$abs(y)$	Returns absolute value of an array
$mean(y)$	Returns the average value of an array
$median(y)$	Returns the middle value of an array (Parallel Code in Appendix)
$impoint$	Returns the coordinate of the point selected by user

$imadjust$	Increase contrast of the image
$imsharpen$	Increase sharpeness of the image
$solve$	Algebraic solver for simultaneous equations
$fitnlm$	Solve the model function

Conventions

Sxxxx-Fy.y-Lzz-Pn	The condition in which the rotational speed is xxxx rpm, flow rate is y.y lpm, load of zz kN and at angular position Pn

Chapter 1 Introduction

1.1 Background

Passenger traffic in civil air transportation is expected to grow at a rate of 4.7% per annum from 2009 to 2028 according to a global market forecast [1]. This emphasises the importance of continual development in civil aerospace in terms of efficiency and reliability. Air transportation of any kind contributes to approximately 2% of the global CO_2 emissions and is expected to grow to 5% by 2040. The 2020 targets set in January 2001 by the Advisory Council for Aeronautics Research in Europe (ACARE) aimed at a more efficient, reliable and environmentally friendly air transportation [2]. The targets require aviation consortiums (e.g. airframe and engine manufacturers) to reduce emissions and noise pollution while improving fuel economy. These targets include CO_2 reduction of 50% per passenger km, NO_x reduction by 80% and perceived noise level by 50%. The directives placed tremendous challenge on aero-engine manufacturers as the reduction in emissions are highly linked to the engine performance. As such a more efficient engine with high reliability, low operating and maintenance cost are the ultimate goal.

Many approaches were implemented in improving the efficiency of an aero-engine. These include higher overall pressure-ratio, higher turbine inlet temperature and the use of advanced lightweight materials. During these improvements and the pursuit for higher bypass ratio, propulsion and thermal efficiency, the engine core is subjected to higher thermal stresses and mechanical loading as the shafts are required to spin faster. There is physical limit to many of the improvements, for example, the tip of a fan blade can only spin so fast as losses begin to increase during supersonic tip flow. Also, the nacelle can only become bigger to a point where pressure drag offsets the bypass ratio benefits.

With potential increase in churning and increased load transmission rotating elements such as shaft, bearings, gears and splines need to be cooled effectively and adequately. To avoid unnecessary weight penalty, an engine's oil system should operate at its optimum condition. The focus of this research is on a subsystem of an aero-engine, notably, the fluid dynamics associated with an aero-engine's ball bearing.

1.2 Future Concepts and the Importance of Oil Systems

In aero-engines the mechanical components are usually reliable and robust. In particular ball bearings have been used for over a century and can be found in almost all rotating devices ranging from industrial appliances to automotive to aerospace applications. A future concept for replacing the conventional oil-cooled bearing in aerospace applications is the active magnetic bearing (AMB). AMB is classed as a revolutionary step as they replace the conventional oil system with the use of oil-less, magnetic levitating rotating elements powered by electric current [3]. This allows the rotating elements to have no physical contacts and therefore zero friction except for drag induced by viscous forces of the air molecules. Up till today, the search for a material that has a high magnetic force to weight ratio suitable for aerospace application is still on-going.

A second more feasible concept known as the E-fan X hybrid electric aircraft demonstrator was proposed by *Airbus*, *Rolls-Royce* and *Siemens* [4]. In this concept, the conventional jet engines mounted on the wings were to be replaced with quieter electric motors for thrust and propulsion. The energy needed to power the electronic motors is derived from a gas turbine located at rear of the aircraft. All these devices, however, still require ball bearings for structural support, friction reduction and load balancing.

It is clear that oil-cooled/lubricated bearings will continue to be part of modern aero-engines for some time to come. Consequently research of this kind presented in this thesis is both relevant and timely.

1.3 Aero-Engine Ball Bearing

Aero-engines contain bearings that support the shafts and react to the loads. It is also very important that torques and loads are transmitted effectively by the bearings to achieve the lowest frictional losses. In a typical three-spool aero-engine, a blend of roller-bearings, ball bearings and journal bearings is found. The most prevalent ones are ball bearings and roller bearings. For a typical 3-shaft engine the locations of key ball bearings and roller bearings are shown in a schematic in Figure 1.1.

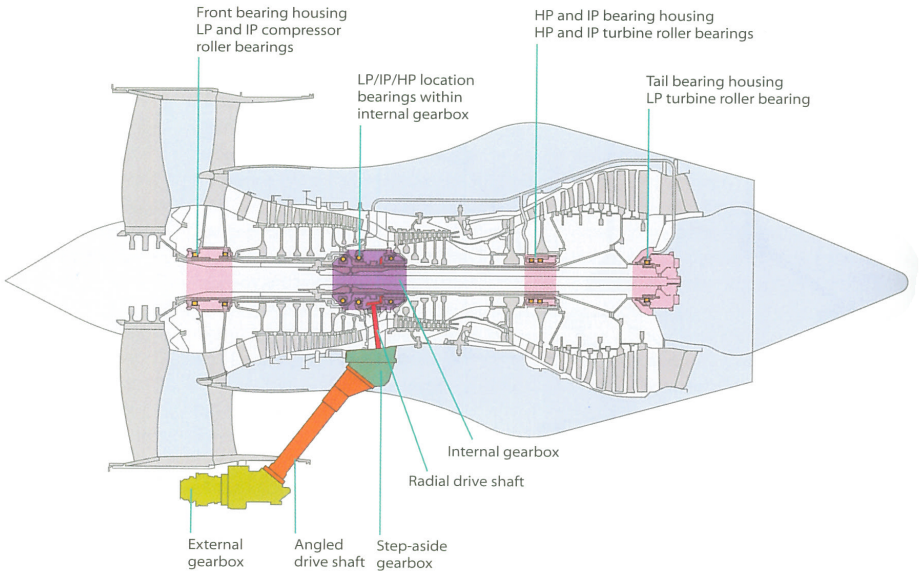


Figure 1.1: A schematic of three-spool jet-engine showing location of bearings (Adapted from [3])

Here, it is shown that the location bearings of interest to this current research are located within the internal gearbox (IGB). Due to continuous operations at high-speed (e.g. 11000 rpm), the bearings need to be cooled and lubricated. Synthetic oil is used as the working fluid to provide lubrication, cooling and corrosion protection. The next section explains the fundamental operation of the oil system in a typical aero-engine.

1.4 Full Flow Oil Systems

In a modern jet-engine, a full flow oil system is commonly employed as the mechanisms to supply the oil to the location bearings. This system allows smaller oil pumps to be used compared to another type of system known as pressure relief valve system (more details are given in [3]). A diagram of a simplified oil system is given in Figure 1.2.

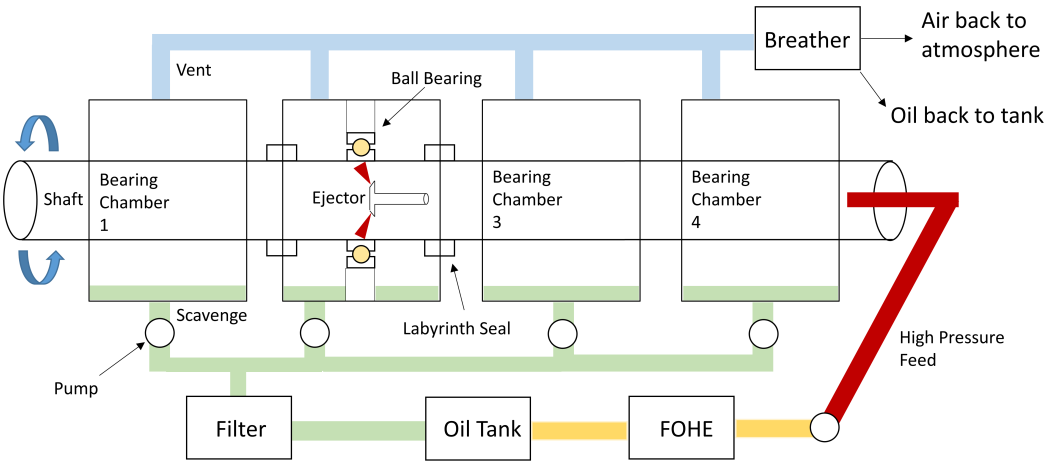


Figure 1.2: A schematic of a simplified full flow oil system
(Recreated based on concept from [3])

In some locations and systems, lubrication oil is fed via a jet injector onto machined surfaces in the inner-race location, known as ‘scallops’. Centrifugal action leads to the feeding of oil into the bearings. The oil, which is significantly cooler than the bearings absorbs the heat and is ejected out of the bearings in the form of droplets, ligaments and sheet (images are given in Section 1.4.1). A containment housing that holds the bearings and the heated oil creates a ‘bearing chamber’. To prevent the oil from leaving the chambers, non-contacting seals often labyrinth seals are used. Bleed air from the compressor stages is fed to the seals to provide positive pressure, hence preventing the oil from going into other parts of the engine. The mixing of the air and oil in the chamber creates a highly complex two-phase flow.

At bearing chamber outlet a positive displacement pump is used for oil scavenging. Typically the oil is first gravitationally collected and then pumped. The hot oil must be removed to ensure residence time is low such that it does not undergo chemical decomposition due to rise in temperature. Oil deposition onto surfaces can also lead to coking, which reduces flow areas. A vent pipe connected to a centrifugal breather is used to extract particles (e.g. mist) that circulating in the core. In the breather, the oil and air are separated through a combination of cyclonic action

and the effect of porous metallic foams [5]. The air is ejected overboard, along with any of the oil mist that was not captured. The captured oil is returned to the tank.

The hot oil from scavenge is subsequently passed through magnetic chip detector and filters in order to remove debris that could damage the bearings causing reduced lifespan. After returning to the oil tank, heat is rejected onto the cold aircraft's fuel stored in the wings through a heat exchanger known as the fuel oil heat exchanger (FOHE). In return, the heated fuel reduces the chance of ice precipitation forming which could be problematic for combustion. The oil is reintroduced into the bearings through high-pressure feed delivered by screw pumps. The processes are repeated in cycle for the whole operation of the aircraft.

1.4.1 Aero-Engine Bearing Chamber Flow Phenomena

The physics of flows in bearing chambers are complex. This section aims to provide a general description of the type of flow to be expected within the bearing chambers and how the oil system is linked to the location bearing. An illustration of the bearing chamber rig module used in this research along with actual images taken to assess the flow physics are given in Figure 1.3 and Figure 1.4 respectively. In Figure 1.3, a cross-sectional schematic view of the ball bearing splitting the front and rear chambers is given along with the sub-components. Optically accessible windows are located in the front face of the chamber providing the images shown in Figure 1.4. More information about the test rig is given in Chapter 3.

In this bearing chamber, pressure is set as ambient. There is no pressure differential across the chambers ($\Delta P = 0$). The inner-race is rotated in a clockwise direction, whereas, the oil feeds are kept static and are non-contacting with the rotor as there is a small gap. An air vent is located at the circumferential top-section of each chamber. The oil is supplied through the inner-race and is centrifuged onto the bearings through channels. A numerical study of oil flow through ball bearing of the same dimensions as in this rig can be found in the work of Adeniyi *et al.* [6]. Oil exits the bearings and forms films on the outer-race and chamber housing indicated by the blue-coloured liquid in Figure 1.3. The physics of oil flow in bearing chamber can be better observed in Figure 1.4.

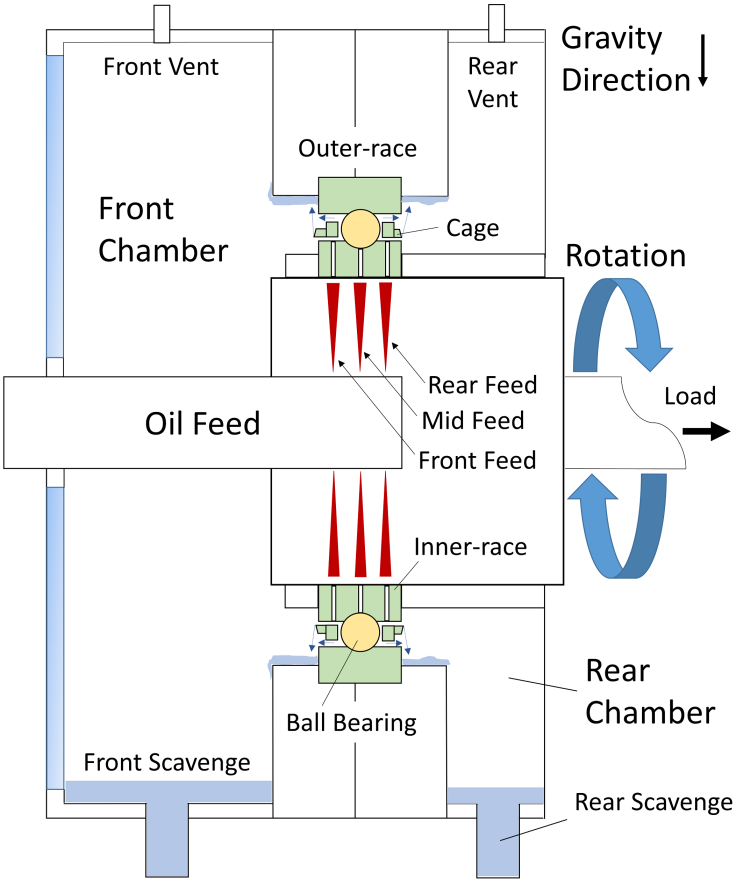


Figure 1.3: Schematic illustration of the aero-engine bearing chambers used in the research

Four optically accessible windows are located at 3, 6, 9 and 12 o'clock. For further images, please see Chapter 3 and Chapter 4. For physics at the 3 o'clock position, combined images are given in Figure 1.4b. At the top part of image in Figure 1.4b, a no oil flow case is shown where the bearing outer-race/housing is clear of oil. And below the demarcation line of Figure 1.4b, oil film can be seen on the surfaces of the bearing housing at speed of 3000 rpm taken at plane of focus 0 mm (and is labelled 'Focus: 0 mm' in Figure 1.4b). Here, the plane of focus can be defined as the axial plane in which the object is in focus.

Detailed information about plane of focus and choices of operating conditions are given in Chapter 4. The oil is flowing in the direction of the shaft rotation and accelerated towards 6 o'clock position. The oil is azimuthally driven by the core gas-velocity (shown in green arrow of Figure 1.4). Note that azimuthal velocity component of core airflow is illustrated as linearly decreasing with the increase in radial distance from inner-race to the wall film. The axial velocity component is not depicted here.

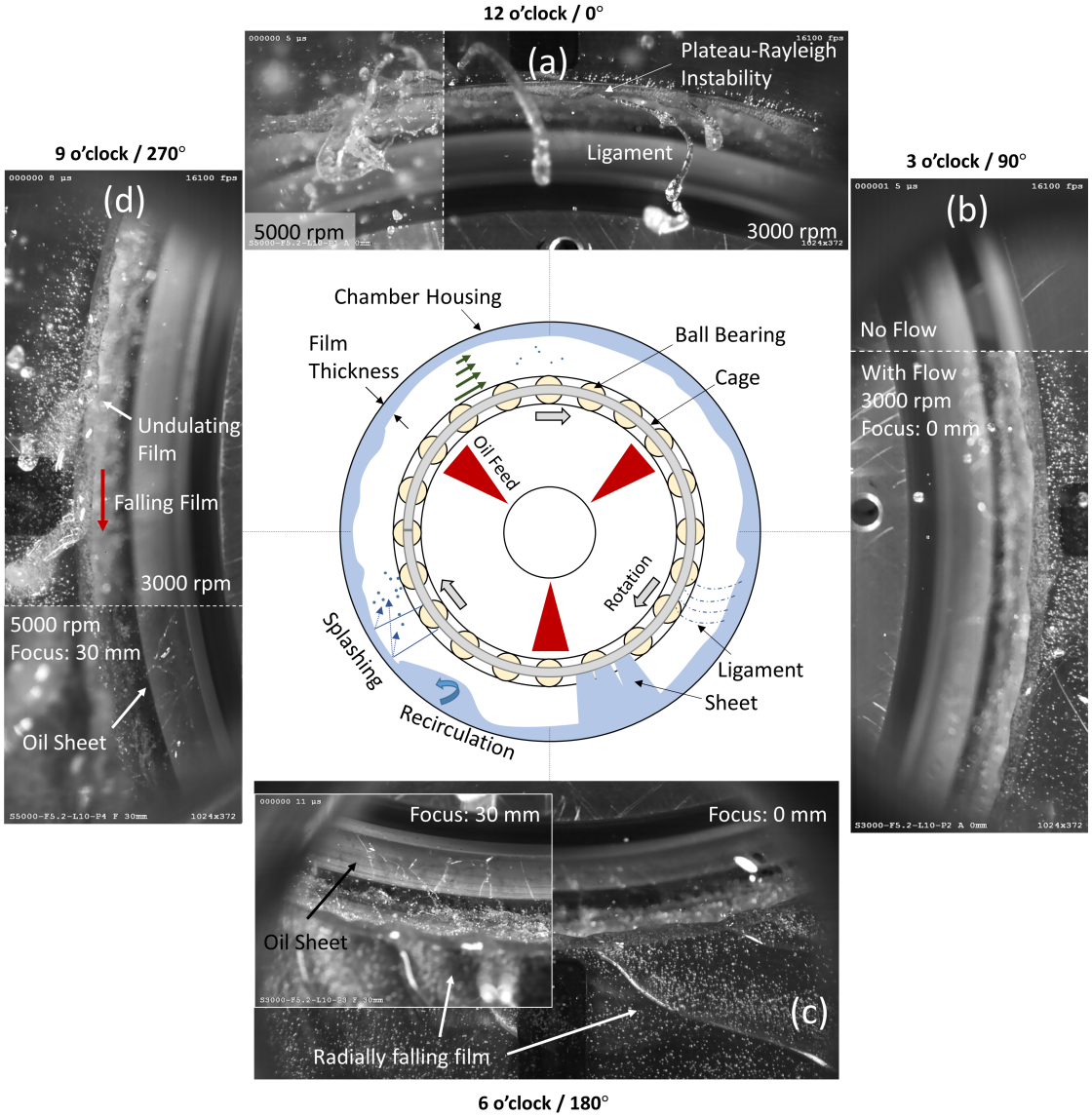


Figure 1.4: The physics of flow at various angular positions of the front chamber

For the physics at the 6 o'clock position, oil can be seen travelling from right to left, again in the direction of the shaft. The wave-fronts and wave crests show the moving film falling off the edge radially towards the scavenge area. Gravity is greater than the inertia of the moving film, hence no strong separation is seen at the bottom location. By changing the plane of focus from 0 mm to 30 mm as shown in Figure 1.4c (specifically, focusing at the bearing cage), an oil sheet can be seen to be ejected radially from the cage inner-landing towards the outer-race. And the radially falling film is out-of-focus.

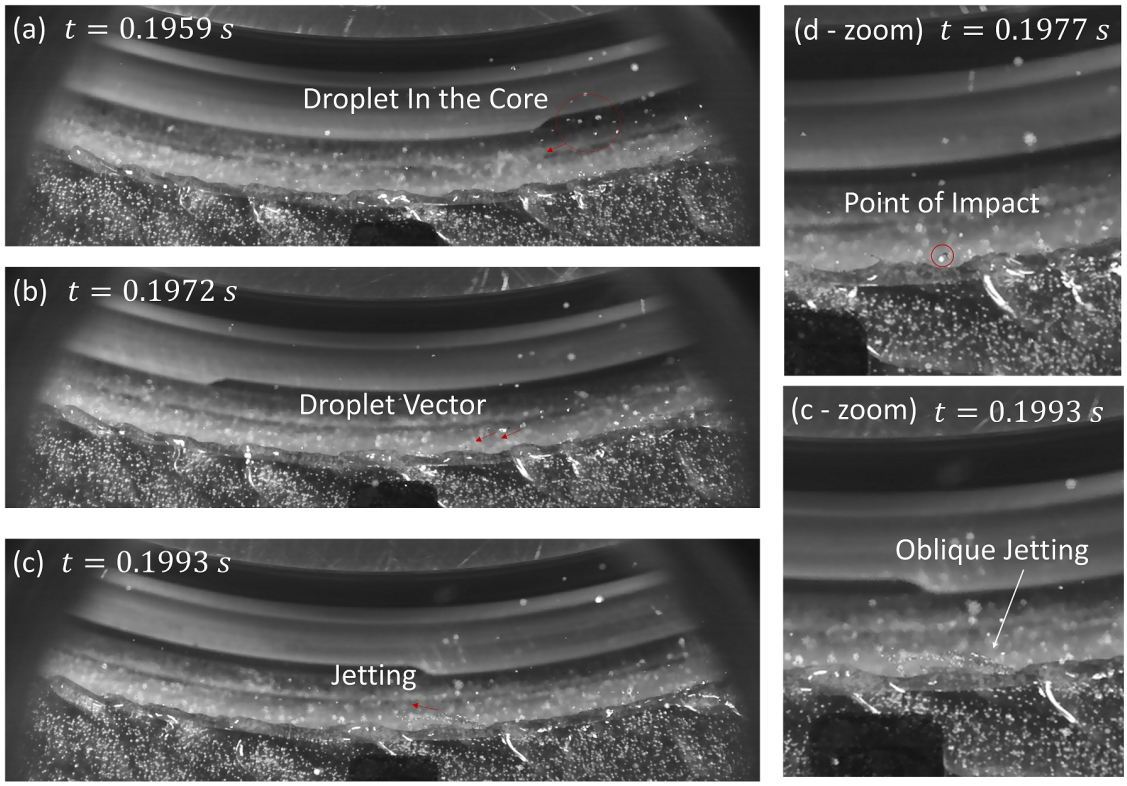


Figure 1.5: Droplet impingement at an oblique angle as observed in bearing chamber from 6 o'clock position at operating conditions of 5000 rpm, 10 kN and 5.2 litre/min

Additional phenomena in the bearing chamber include droplet impingement which can be easily seen at the 6 o'clock position from time (see Figure 1.5), t of $0.1959\ s$ to $0.1993\ s$ at operating conditions of 5000 rpm, 10 kN and 5.2 litre/min. The droplets from the core travel at an oblique angle and impinge onto the film causing jetting of liquid similar to that mentioned by Mitchell *et al.* [7] and Okawa *et al.* [8]. These events are one of the sources of droplet re-entrainment into the core. In this thesis, the analysis of the 6 o'clock and 12 o'clock positions were not conducted. Note that, the droplet vector shown in Figure 1.5 is for pure illustration purposes and was not produced based on regional cross-correlation as detailed in conventional technique like Particle Image Velocimetry (PIV) [9].

The physics of flow at the 9 o'clock position is different to that at 3 o'clock. At 3000 rpm, the film is seen to be falling off with considerable undulation on the surfaces. This is due to the net downward resultant force through combination of gravity force and the opposing shear force. At the same location but different plane focus (see Figure 1.4d, Focus: 30 mm), an oil sheet is also seen to be ejected onto the bearing housing at 5000 rpm. Note that ligaments were observed at lower speeds from the cage and the information here is intended only to provide preliminary insight into the flows within the bearing chamber before moving to the core chapters.

At the 12 o'clock position, a different oil flow is seen. At a speed of 3000 rpm, oil film is being obstructed by a long and thick ligament that is at least the size of the oil film or even thicker (see Figure 1.4a, Focus: 0 mm). As oil is continuously supplied from inside and exiting axially, the ligament grows through surface tension. The surface tension force is no longer able to hold the liquid indefinitely and Plateau-Rayleigh instability occurs causing necking of ligament. Eventually it splits into large satellite droplets. By looking at the 5000 rpm case (see Figure 1.4a with label '5000 rpm'), the stronger shearing airflow is causing the ligaments to 'shear-breakup' and creating a significant number of satellite droplets that saturate the front chamber. This angular position shall be analysed in the future for both experimental and computational purposes.

This section has provided a general description of the complexity of the oil flow in vicinity of a high bypass aero-engine ball bearing and showed how the oil system is linked to the location bearing. It is clear that these phenomena relevant to a high-bypass ratio aero-engine ball bearing were not yet available in the scientific literature and represent something new. Many of the early studies of liquid film in a shear-driven environment were largely based on empirical data of rimming flow, assumption and lack the complexity of the bearing chamber described here where multiple flow features co-exist concurrently (i.e. shedding, impingement, shearing and heat transfer). This means that many scientific explorations are available, for instance the physics of oil shedding and the shear-driven thin film in a highly turbulent environment. The understanding of flow within the bearing chamber and close-up observations were scant and their effect on the heat and oil management system were still lacking. As today computational modelling tool is more commonly being adopted, the accuracy of these models are still in question. This motivates the work of this thesis – to bridge the gap between developing scientific understanding of two-phase flow in an aero-engine ball bearing and translate them into pratical engineering application; developing advance modelling and design tool for aero-engine. Further strengthing the proposition of conducting this scientific research, the industrial driver that leads to this research and the research gaps are given in next section.

1.5 Industrial Driver & Research Gaps

Aerospace ball bearing is an integral part of the jet-engine, it serves as a rotor support structure [10] and is used in load transmission. Today, the demand for highly *reliable* and long life aerospace ball bearing is becoming ever more important [11]. Time between overhauls (TBO) has been stretched even further with more airlines eyeing for engines that are low maintenance and fuel efficient. A long history of the development of aerospace ball bearing and its lubrication system can be traced back to 1970 when Brown reported the importance of achieving high DN

levels for lower fuel consumption and high thrust-to-weigh ratios [10]. DN levels refer to the product of the bearing bore (D) in mm and speed (N) in rpm [12].

In order to achieve high level of performance, the mechanical speed is increased [10] linking to either high bypass ratio or shaft speed. As a consequent of that the increase in mainshaft diameter increases the DN levels. The first generation turbofan engines were reported to be able to achieve a DN levels of not greater than 1.5×10^6 depending on the type of lubrication system employed [10].

One could refer to an updated chart of the trend towards increased DN values for mainshaft bearings as depicted in Figure 1.6. Brown [10] complied various Pratt and Whitney (PW) commerical engines from 1940 and 1970 in terms of the highest DN levels. The author highlighted that with conventional jet lubrication (or jet oiling method) the cooling performance for the ball bearing was not sufficient when the jet-engine needs to achieve higher speed. Oil jetting method has saturated where further increase in oil flow-rate will not cool the bearing, instead leading to higher churning loss. Furthermore at such speed, the oil is thrown centrifugally outward rendering oil jet lubrication less effective [12]. The increase in flow-rate also demands a larger scavenge pump, adding unnecessary weight to the system [10].

To overcome the aforementioned issue, under-race lubrication was developed and allow identifical-type ball bearing to run cooler [10]. This method allows direct cooling of the contact point between the ball and inner-race resulting in lower inner-race temperature. Despite having warmer outer-race, outer-race cooling was also developed in such configuration [12]. Such development has led to engine with a higher DN value.

Referring to Figure 1.6, the *Trent* 1000 aero-engine ball bearing used in G2TRC's test rig has a calculated DN value of 3.1×10^6 (based on Pitch Circular Diameter of 260 mm and speed of 12,000 rpm). This is a new record for jet-engine and has exceeded what was predicted back in 1970 (see the label *ADVANCED ENGINE prediction by Brown (1970)*). In 2006, Flouros tested the RB211 ball bearing that has a DN values of less than 2.1×10^6 DN, structually, their lubrication system only supply oil to the cage front and rear landing. In contrast, the G2TRC's bearing shedding rig oil system supplies oil to three different location: front, mid and rear with the independent feed rate control. This is unique from a research perspective and relevant to industry application in many ways. In addition to that, many of the early bearing chamber studies were largely based on empiricsm and experiment. Advancement in numerical modelling has allowed the design of aeroengine bearing chamber to be quickler with less iterations, hence reducing development cost. This leads to the industrial driver question of enchancing the oil system by means of experimentation and numerical modelling in order to achieve *reliable*,

optimised and *lightweight* system. The following research questions for this thesis were developed in conjunction to industrial driver as following:

1. Have the physics of flow within a bearing chamber of this scale and configuration been adequately quantified and studied?
2. In such complex two-phase flow environments, how does the oil leave the ball bearing and into the bearing chamber? Is the oil in the form of droplets, ligaments, sheets or a combination of all?
3. Is there secondary droplet production and re-entrainment of droplets back into the core? Does it contribute to the momentum, mass and heat transfer into the film?
4. What is the oil film thickness and the behaviour of oil after it cools and lubricates the bearings at various operating conditions? Are they similar to the first and second generation jet engines? Does empirical or analytical modelling of any kind be applicable to chamber of this scale and range of conditions? How will this information enhance aero-engine modelling tools?
5. Can the oil system be further optimised in terms of weight and reliablity?
6. Can today's computational modelling tools help design the bearing chamber by adequately reproducing the exact physics of air and oil within the chamber?

Based on the above research questions, the aim and objectives of this research were developed and are given in subsequent section.

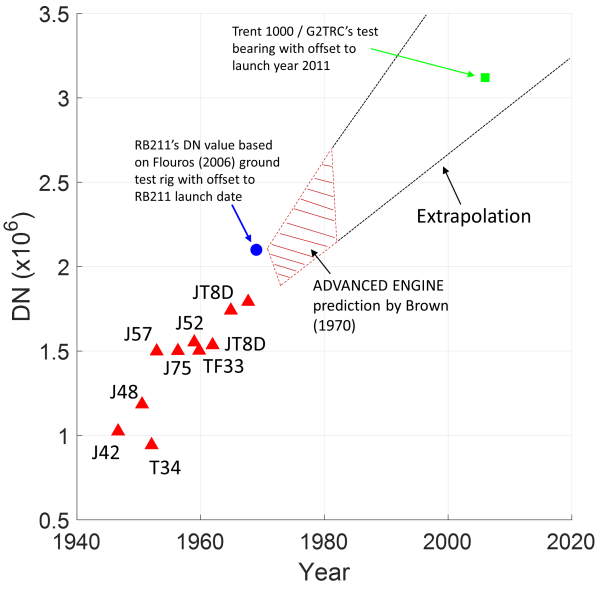


Figure 1.6: Updated trend toward increased DN values for mainshaft bearings (baseline points extracted from [10])

1.6 Aim and Objectives

The aim of the research is to enable improved heat and oil management through comprehensive understanding of the oil shedding process in a *Trent* 1000 aero-engine ball bearing and through improved modelling capability. The objectives of the research are outlined as following:

- To investigate the mechanism of oil disintegration from an aero-engine ball bearing in terms of changing operating conditions
- To analyse factors that influence oil shedding in terms of changing operating conditions
- To measure the oil film thickness on surfaces close to the aero-engine ball bearing
- To analyse the dynamics of oil film on surfaces close to the aero-engine ball bearing
- To establish modelling guidelines and a modelling strategy for coupling the Discrete Phase Model (DPM) and Eulerian Thin Film Model (ETFM) for application to aero-engine ball bearing

1.7 Proposed Methodology

For the experimental work it was proposed that in the visualisation of the behaviours of oil at aero-engine ball bearing, a high-speed camera should be used as a conventional camera was not capable of capturing the flow due to the high velocity involved. Hence, an available high-speed camera of resolution of 1 megapixel at a frame-rate of $6000 \sim 16100$ fps with minimum exposure of $1\mu s$ was used to temporally-resolve the flow features. Equally important, a high-magnification lens known as long distance microscope is also needed to spatially-resolve the oil film. *IDT* Motion-studio was used as a pre-processing tool for the captured images. *MATLAB* numerical computing software was used as a tool to process the images. A new concept proposed includes the use of temporal-averaging or 'median-stacking' and gradient-detection to determine the oil film thickness in terms of quantifiable units. This differs with many techniques applied by other researchers such as ultrasonic and capacitive film thickness measurement techniques.

For the development of a two-dimensional thin film model and numerical simulation, the commercial CFD software *ANSYS* Fluent is selected. In the numerical studies, a systematic approach is proposed where the fidelity and numerical stability of the coupled Discrete Phase Model and Eulerian Thin Film Model (DPM-ETFM) are explored based on simulating the jet-breakup and thin film formation in a crossflow taken from a published work. This is to ensure that the models work as intended before moving into an actual bearing chamber application. The

dispersed phase in the domain of interest is to be tracked using Euler-Lagrangian framework, notably, Discrete Phase Model and the turbulent crossflow is to be modelled in the Eulerian framework using the two-equation $k\omega - SST$ turbulence model. For the film deposition and transportation, the depth-averaged Eulerian Thin Film Model (ETFM) is proposed.

1.8 Thesis Structure

This chapter described the background for the research relevant to aero-engine oil systems. Information regarding the importance of designing a reliable, robust and efficient oil system for a gas turbine transmission are highlighted along with some future concepts. The fundamental principles of oil systems employed in modern aero-engines is presented along with the physics of flows within a bearing chamber. Industrial driver and research questions are defined by looking at the history of the development of aero-engine ball bearings. The aim and objectives of the research are given with the stated goals of understanding the complex flow structures and improving aero-engine design capability using the knowledge derived from the experiments. The proposed methodology using the latest equipment and modelling software are highlighted.

Chapter 2 contains a review of published prior work relevant but not limited to aero-engine bearing chambers both experimentally and computationally. Various techniques and physics in the chambers were reviewed. Measurements of film and airflow using laser diagnostics were reported along with different flow regimes in the chamber. Papers relating to droplet generation from simple rotary devices as well as actual bearings were also reviewed. The numerical simulation of air-oil flow in bearing chambers along with recent developments were systematically described in terms of their capabilities and the research gaps.

Chapter 3 describes the experimental test facility at the Gas Turbine and Transmissions Research Centre (G2TRC) known as bearing oil shedding rig in terms of its functionality and operations. Detailed information regarding the selection of operating conditions for speed, flow rate and axial load are given. The instruments available and software interface needed to gather data and monitor for rig performance before data acquisition are also provided. A list of the experimental techniques applied to achieve the test objectives are described.

In Chapter 4, the experimental investigations of oil shedding from an aero-engine ball bearing subjected to various operation conditions are highlighted. First, the principles of high-speed imaging required for capturing high-quality images are given. Comparison of the two types of utilised imaging lenses is made in terms of their ability to spatially resolve different flow features within the bearing chamber. The research made use of the lens mounted directly on the high speed

camera (HS lens) and a combination of the camera lens with a long distance microscope (HS-LDM). Reasoning behind the need to measure film thickness at different axial planes and angular positions of the chamber wall is explained. The Section 4.2 on image-processing gives details of temporal-averaging of the unsteady oil film and the detection of the air-oil interface using a gradient detection method. Quantified film thickness data is provided in the first part of Chapter 4 noting that this is useful for boundary conditions of a computational model. The second part of the experimental study focuses on characterisation of oil disintegration modes at the rotating cage. Dimensional analysis was performed to see if scaling and similarity exist between aero-engine ball bearing and simple rotary devices. The third and final part of the experimental chapter will focuses on the study of wave structures on the thin film when subjected to two driving force; gravity and shear.

Chapter 5 describes the computational modelling of jet-breakup and thin film formation in crossflow with the aim of establishing a modelling guideline for coupled DPM-ETFM and to also assess the stability of the model prior to full implementation of coupled VOF-DPM-ETFM in an actual bearing chamber. First, the motivation for computational modelling along with the developments of the 2D thin film model are given. The theories underpinning computational fluid dynamics (CFD) and the numerical settings are given. A systematic approach is taken to assess the parameters that affect the solution of the thin film model when coupled with the continuous phase. Among the parameters investigated are injection streams, airflow time step, mesh densities, particle dispersion and sub-models of the film. These numerical results are compared against the data of Arienti *et al.* [13].

In Chapter 6, the findings and contribution to knowledge from the research were highlighted along with the difficulties experienced during the process. A list of recommendations for future work is presented which includes the use of dye techniques for obtaining mean film velocity measurements as well as laser diagnostic techniques.

Chapter 2 Literature Reviews

In this chapter, a literature survey for studies relevant but not limited to bearing chamber was conducted. It aimed at providing understanding of the flow physics, development and techniques available in bearing chamber research. The survey was subdivided into experimental and computational. In the former, the investigations involving multiphase air-oil flow, single-phase airflow, dispersed phase and flow regimes using sensor and laser diagnostic were reviewed. The studies of droplet generations from rotary atomiser and actual bearings were reviewed to assess if correlations could be adopted in bearing chamber analysis. Experimental studies of regimes in bearing chambers are complicated, shear-driven liquid in straight duct and also dimensional analysis of droplet impingement on moving film were also summarised. In the latter, the modelling of pure airflow in bearing chambers and cavities were reviewed in terms of the strategies and choice of turbulence models. Subsequently, the numerical modelling of flow in bearing chambers was systematically reviewed from the inception of 2D thin film model to Eulerian approach, Euler-Lagrangian approach as well as towards more advanced techniques like hybrid coupled VOF-DPM and VOF-ETFM. Finally, justification on the suitability of the turbulence model was also made by comparing it with LES. Reviews on the meshing technique and CFD verification methods were also provided as part of the CFD guideline.

2.1 Experimental Studies

2.1.1 Early Investigations on Bearing Chamber

Early experimental investigations into the aero-engine bearing chamber were conducted by Wittig *et al.* [14] looking at the influence of speeds on oil film thickness and heat transfer coefficients. An ultrasonic sensor was employed to measure the film thickness on chamber walls and it was demonstrated that the film thickness is a function of speed. The increase in circumferential velocity caused by higher shaft speed resulted in a uniform film distribution on the chamber wall. The heat transfer coefficients were found to be strongly dependent on the oil flow rate. A high heat transfer coefficient was related to the increase in oil concentration.

The work was further extended by Glahn and Wittig [15] to characterise the behaviour of oil film in terms of velocity profile utilising fibre-optic Laser Doppler Velocimetry (LDV). The

experiments were conducted under the engine operating speed of 3000 to 16000 rpm, lubrication flow rate of 2.5 lpm and sealing air flow of 10 g/s. It was shown that the film velocity is proportional to the rotational speed of the shaft. The interfacial shear stress on surface of gas and liquid increases as a function of gas velocity in the core. Analysis was made by comparing the experimentally derived film profile with theoretical approach of Wurtz and Deissler. The non-dimensional velocity profiles (u_F^+) were found to be turbulent in nature and compares well with Deissler's analytical turbulent film model, and in contrary, less with laminar or Wurtz's proposed turbulent model.

Further experimental and numerical approach for bearing chamber study were made by Glahn *et al.* [16] using Phase Doppler Particle Analyser (PDPA) to measure the droplet size and velocity. The numerical approach has successfully shown for the first time the feasibility of simulating continuous phase and Lagrangian tracking in a simplified bearing chamber geometry. The simulation qualitatively assessed the capability of CFD code in predicting the trajectories of discrete particles (of size: 50 μm, 100 μm and 200 μm) that interacted with air flow. At that point of time, quantitative validations are not recommended.

2.1.2 Measurement of Airflow in Bearing Chamber

The understanding of the flow field of single-phase in bearing chamber environment is as important as the understanding of oil phase. Gas-phase along with the gravity are the main driving force for the oil film and is also influencing the trajectories of particles. To support the numerical studies (i.e. CFD), Gorse *et al.* [17] performed experimental investigations of pure air flow in bearing chamber using 3D-Laser Doppler Anemometry (LDA). The air was seeded with tracer particles and the oil flow was suppressed using bearing generator to avoid containment of the optical assessment region. In the assessment, different sealing flow rates were tested from 4.2 to 17.0 g/s and the rotational speed was varied from 3000 to 13000 rpm. It was revealed that different flow fields could occur depending on the ratio of velocity, R_v (i.e. ratio of shaft speed to axial inlet velocity). At sealing flow rate of less than 8.5 g/s, two vortices dominated the chamber and was termed as rotational speed drive mode (RSDM). For higher sealing flow rate of greater than 8.5 g/s, one vortex disappears. Hence, this feature was known as sealing air driven mode (SADM). The finding indicated that the mixing between these flow fields with oil could resulted in a complex two-phase flow environment.

The measurement of single-phase airflow for bearing chamber was also performed by Lee *et al.* [9] using Particle Image Velocimetry (PIV), it was indicated that the tangential flow velocity

can be measured to a good accuracy as it is a dominant component that gives better signal in cross-correlation. The uncertainties in measurement of normalised tangential velocity is only 2% on average. In contrast, radial velocity normalised with shaft speed was found to be a weaker component in the flow causing larger deviations. The vector plot shows that the geometry of the chamber has strong impact on the flow field.

2.1.3 Measurement of Film Thickness in Chamber Wall

Knowing the film quantities on chamber wall are essential as the cooling and scavenge efficiency are highly dependent on them. Gorse *et al*. [18] experimentally investigated the effect of changing bearing chamber geometries and operating conditions on film thickness. The film thickness and velocity were measured using capacitive probes and LDV respectively. Characterisation of liquid wall film at fixed oil flow rate shows that interfacial shear stress increases with respect to the shaft rotational speed. A low interfacial shear stress or speed resulted in majority of oil settling at the bottom of the cavity due to stronger influence of gravity. And accordingly at high speeds, the oil was distributed homogenously along the circumference (In this thesis, homogenous oil film shall be referred as uniform). This suggests that the film thickness decreases as a function of high gas velocities. The experimentally measured film thickness and velocity were used as input conditions alongside with the predicted airflow velocity from 1-D gas-model of Glahn and Wittig in the numerical simulation of film distribution [15]. In their model, assumptions were made such as constant interfacial shear stress along the circumference, neglecting momentum transfer of oil to film and from the film to the core. Their validation indicates that the assumption of constant shear stress along all circumferential positions is not true and failed to capture many real features of the film such as constant film thickness at speed greater than 12000 rpm and film reversal at speed less than 12000 rpm. In the speed measured 6000 to 16000 rpm, the film thickness was measured as $h_f =$ 0.5 to 1.5 mm.

The influence of film thickness as a function of different offtake designs were also characterised by Kurz *et al.* [19] using the same rig but of different modules. From the assessments, 3 scavenge offtakes were tested – Baseline, shallow ramp without cover and deep ramp with a 21° cover. First, the scavange efficiency was found to be poor at high speed for baseline model and recirculation was found near the scavenge area. The scavenge efficiency (n_{sc}) was increased from 39% to 88% by using ramp and cover. The film thickness was found to be corresponding to different offtake designs. A much better efficiency relates to thinner film and

in contrast, a poor efficiency relates to thick film on circumferential locations. As gravity dominates at $\varphi = 180°$ (bottom location), the film was seen to increase towards the bottom. On average, the film was found to be thin at close to the vent location due to strong momentum needed. The 21° ramp cover effectively recovers the momentum of the film also allows better collection of the oil at the bottom hence resulted in lowest h_f for all speed (e.g. 5000, 10000 and 15000 rpm). From the reviews, it is possible to conclude that the G2TRC test rig is different with that of KITs. In particular the sump is not presented directly on the circumferential wall of the bearing containment where the oil is expected to recirculate and losses momentum for travelling up the rising side.

2.1.4 Modes of Droplet Disintegration from Rotating Devices

The mechanisms of oil disintegration from cage-edge of a ball bearing rotating at high speeds could resemble the flow patterns observed in rotating disks and cups. These simplified rotary device were used extensively during the past in chemical processing, agricultural, food and metallugrical industries [20-22]. In the agricultural field, droplets sizes produced by such devices are narrow in range to minimise wastage and therefore is used for pesticides sprays. A study by Frost [21] showed that application rates were reduced from 200 litre/hectar to 35 litre/hectar by using rotary atomiser.

The earliest published study of the mechanisms of liquid breakup in rotary devices was made by Hinze and Milborn [20], three different types of spray formation were identified at the edge of a spinning disk, namely, direct-drop formation, ligament formation and sheet formation. At relatively low flow-rate or speed, direct-drop formation was observed where droplets of large uniform sizes were centrifuged off the rim at random locations.

Through the investigations of increasing flow rate and rotational speed, direct-drop formation is transitioned to ligament formation [20]. In this mode, fine liquid threads known as ligaments were formed around the rim of the disk and droplet of approximately the same characteristics diameter as the ligament separated when centrifugal force exceeded the surface tension and viscous forces. The formation of these ligaments with distinctive spacing was proposed to come from a combination of instabilities, namely, Kelvin-Helmholtz (K-H) and Rayleigh-Taylor (R-T). Studies by Kamiya [23], Wang *et al.* [24] and Wang *et al.* [25] pointed that waves were first formed on the surfaces of the rotating devices by large velocity differences between air and liquid known as K-H instability. R-T instability further increases the disturbance by pushing lighter fluid on the heavier fluid at the interface. As centrifugal force exceeded surface tension

and viscous forces, the waves were amplified forming ligaments with uniform spacing. Subsequently drag force gives rise to the deflected shape seen on ligament. As the thread continues to extend towards a critical length, Plateau-Rayleigh instability caused the ligament to disintegrate into droplet of same diameter as the thread.

The third form of oil disintegration is atomisation by sheet formation. The transition of ligament to oil sheet occurs when oil flow rate or shaft speed is increased. As the ligament no longer able to accommodate the disintegration frequency, it merges to form a layer of sheet which extends several distance away from the rim or edge before disintegrate. The droplets produced by this mode has a larger diameter distribution compared to ligament or direct-drop formation. It is common to term it as bimodal particle distribution. To aid the explanation of direct-drop, ligament and sheet formation. Experimental observations made by Hinze and Milborn [20], Frost [21], Matsumoto *et al.* [26] and Liu *et al.* [27] on the described mechansims are given in a chronological order in Figure 2.1, Figure 2.2, Figure 2.3 and Figure 2.4 respectively.

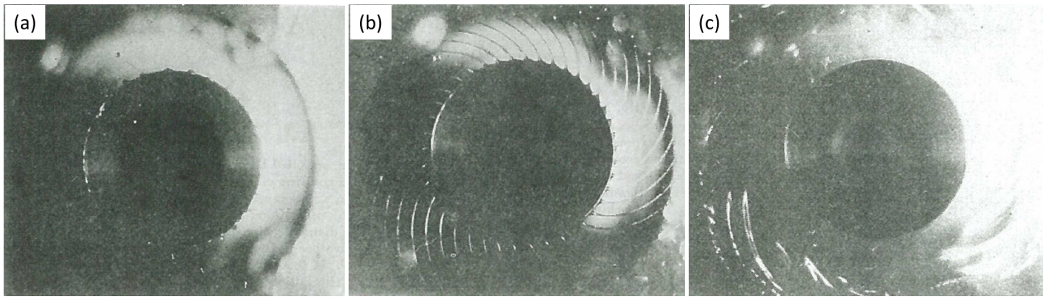


Figure 2.1: Disintegration by (a) Direct drop formation (b) Ligament formation (c) Sheet formation [20]

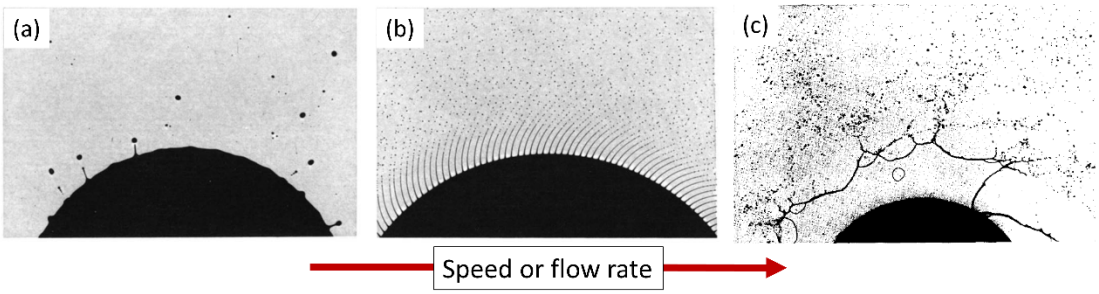


Figure 2.2: Mechanisms of liquid disintegration by Frost [21] at unspecified conditions; (a) Direct-Drop formation (b) Ligament formation (c) Sheet formation

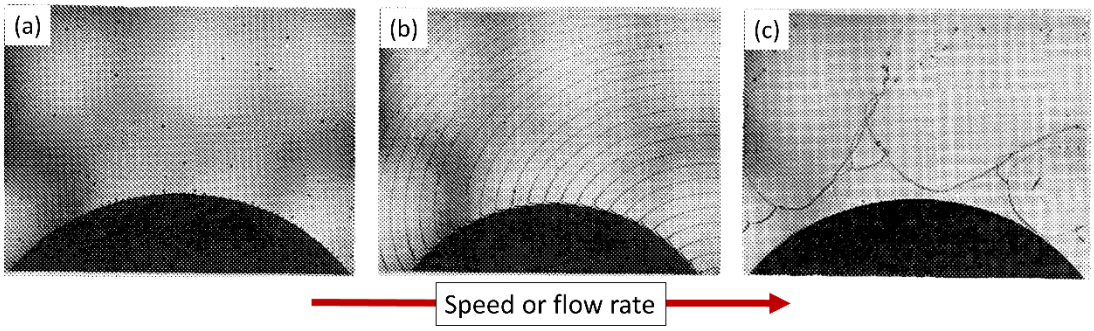


Figure 2.3: Mechanisms of liquid disintegrations by Matsumoto *et al.* [26];

(a) Direct–Drop Formation	(b) Ligament Formation	(c) Film Formation
$R = 6\ cm$	$R = 5\ cm$	$R = 6\ cm$
$N = 1000\ rpm$	$N = 1000\ rpm$	$N = 1000\ rpm$
$\mu = 0.598\ poise$	$\mu = 1.70\ poise$	$\mu = 0.598\ poise$
$\rho = 1.21\ g/cm^3$	$\rho = 1.23\ g/cm^3$	$\rho = 1.21\ g/cm^3$
$\sigma = 63.0\ dyne/cm^3$	$\sigma = 62.0\ dyne/cm^3$	$\sigma = 63.0\ dyne/cm^3$
$Q = 2.0\ cm^3/sec$	$Q = 8.0\ cm^3/sec$	$Q = 16.8\ cm^3/sec$

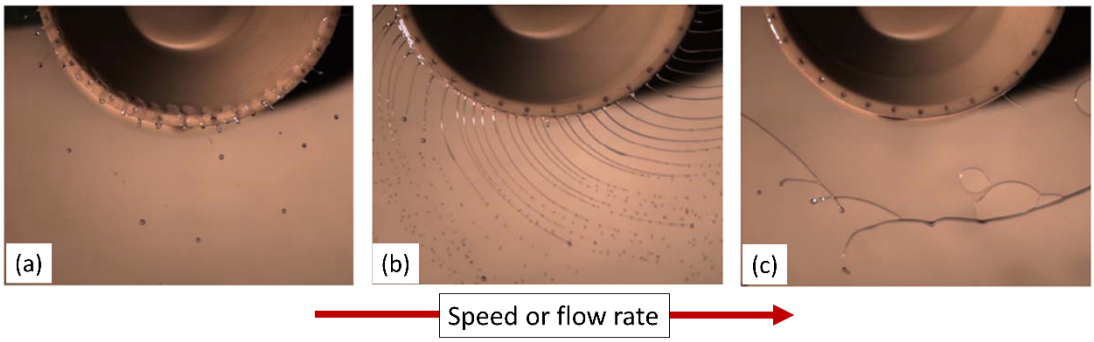


Figure 2.4: Mechanisms of liquid disintegrations by Liu *et al.* [27];

(a) Direct–Drop Formation	(b) Ligament Formation	(c) Film Formation
$R = 6.4\ cm$	$R = 6.4\ cm$	$R = 6.4\ cm$
$N = 287.0\ rpm$	$N = 287.0\ rpm$	$N = 640.3\ rpm$
$\mu = 0.072\ Pa\ s$	$\mu = 0.072\ Pa\ s$	$\mu = 0.072\ pa\ s$
$\rho = 1.21\ g/cm^3$	$\rho = 1.21\ g/cm^3$	$\rho \sim 1.165\ g/cm^3$
$\sigma = 63.0\ dyne/cm^3$	$\sigma = 63.0\ dyne/cm^3$	$\sigma = 63.0\ dyne/cm^3$
$Q = 2.49\ cm^3/sec$	$Q = 23.5\ cm^3/sec$	$Q = 23.5\ cm^3/sec$

Apart from the above mechanisms, Frost [21] reported that the local variability of liquid flow rate over the surface of the disk caused by the eccentricity in the position of the feed tube resulted in the formation of both ligament and sheet on rim of the disk rim simultaneously. The lower range of oil flow rate resulted in ligament formation, whilst a higher end produced sheet. This feature is shown in Figure 2.5.

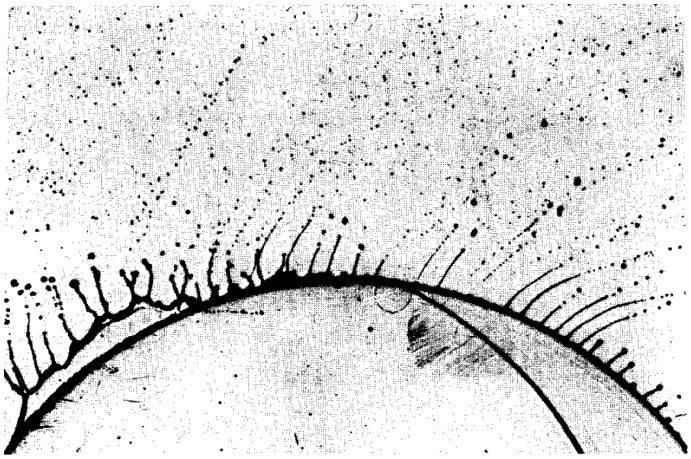


Figure 2.5: Variability in local liquid flow rate over a disc surface due to eccentricity of feeding tube. (Adapted from Frost [21])

For application that is relevant to an aero-engine bearing chamber, Glahn *et al.* [28-30] investigated the mechanisms of oil disintegration from rotating disk, radial holes cylinder and axial passage cylinder based on operating conditions and geometry that were scaled towards that of aero-engine (i.e. rotational speed, $N = 16000\,rpm$). Three similar regimes existed, namely, direct-drop, ligament and sheet.

Modifications to the transitional correlations of Matsumoto *et al.* [31] and also to that of Hinze and Milborn [20] were made to ensure that they fit to aero-engine operating conditions. It was concluded that by increasing the flow rate or rotational speed, oil was seen to be transitioned from direct-drop to ligament and finally to sheet. The general empirical Sauter mean diameter for atomisation was found to be suitable to the one given by Lefebvre (log-normal) distribution based on rotary devices as [32]:

$$SMD = \frac{15.6}{n}\left(\frac{\sigma}{D^2\rho_L}\right)^{0.4} q^{0.5} \tag{2.1}$$

Where, n is the shaft speed, D is disk diameter, ρ_L is liquid density, σ is surface tension, q is volumetric flow rate. Glahn *et al.* [28] dismissed the relation that $SMD \propto q^{0.5}$ as they obtained a constant particle size distribution relative to flow rate. However, they agreed that $SMD \propto \omega^{-1}$ or $\propto V_{rim}^{-1}$ as the increase in aerodynamic force led to finer sprays. To further acquire information to support the development of numerical models for phase interaction in bearing chambers, Glahn *et al.* [30] further analysed rotating cylinder with radial holes indicated the same regime of disintegrations. PDPA was used to measure a total of 224 data points for droplet sizing and velocimetry. It was also indicated that droplet size distribution follows the log-normal size distribution. The variations of droplet size and velocity with respect to flow rate

were not reported. The relation for velocity of droplet with operating conditions were derived and was proposed to be applicable for all flow rates in aero-engine as [29, 30]:

$$\frac{\bar{V}_d}{V_{rim}} = 1.5 - 0.1327 \ln(We^{*^{0.5}}) \tag{2.2}$$

2.1.4.1 Critical Correlation for the Transition of Direct-Drop, Ligament and Sheet

Various criteria and correlations were developed in the past to describe flow conditions in which one mode is transitioned to another. These semi-empirical correlations describe the transition in regimes based on changing flow rate, disk diameter or rotational speed. Hinze and Milborn [20] proposed the criterion for ligament to sheet in Equation (2.3) as:

$$V^+ = 0.5083\, On^{-0.333}\, We^{*-0.60} \tag{2.3}$$

Correspondingly, Matsumoto *et al.* [28] proposed the correlation for direct drop to ligament in Equation (2.4) as:

$$V^+ = 0.0333\, On^{-0.333}\, We^{*-0.85} \tag{2.4}$$

Note that the above equations were excerpted and modified by Glahn *et al.* [28] such that they fit onto the same disintegration map. The non-dimensional groups stated above are given as follows:

For modified Weber number:

$$We^* = \frac{1}{8}\frac{\rho_L \omega^2 D^3}{\sigma} \tag{2.5}$$

And for Ohnesorge number:

$$On = \frac{\mu_L}{\sqrt{\rho_L D \sigma}} \tag{2.6}$$

The asterisked Weber number is known as the ratio of destabilising aerodynamic forces to stabilising surface tension forces. Ohnesorge number is ratio of viscous forces to inertial and surface tension forces. For non-dimensional flow rate, V^+ it was defined as:

$$V^+ = \frac{\rho_L q^2}{\sigma D^3} \tag{2.7}$$

The individual meaning for the symbols could be referred in Nomenclature. Fundamental study was also performed by Glahn *et al.* [28] based on engine-realistic conditions to examine oil film disintegration at the rim of a rotating disk at high rotational speeds. And modifications were made to the coefficients of the empirical correlation to better fit for their application. Glahn *et al.* [28] proposed the correlation for direct drop to ligament as:

$$V^+ = 0.0854\, On^{-0.9}\, We^{*-0.85} \tag{2.8}$$

And ligament formation to film as:

$$V^+ = 0.1378\, On^{-0.33}\, We^{*-0.435} \tag{2.9}$$

The above correlations: Equation (2.3), (2.4), (2.8) and (2.9) were being validated by Glahn *et al.* [28] based on 62 different operating conditions. It was mentioned that these operating points were tested for fixed fluid properties of T_{oil} = 295 K and T_{oil} = 364 K. The disintegration map developed by Glahn *et al.* [28] is shown in Figure 2.6.

In this droplet disintegration map, Glahn *et al.* [28] compared the critical correlations in which the transition occurs. The label Eqn (1) in Figure 2.6 refers to the correlation of Hinze and Milborn [20] which is the correlation stated in the Equation (2.3) of this thesis. Subsequently, the label Eqn (2) in the Figure 2.6 refers to the correlation of Matsumoto *et al.* [31] which is the correlation stated in Equation (2.4). Referring to Figure 2.6, as the volumetric flow rate increases, the oil disintegration mode is transitioned from one mode to another depending on the respective operating speed or We number. Glahn *et al.* [28] proposed new correlations that redefined the boundaries of transition as previous correlations failed to accurately predict the transition.

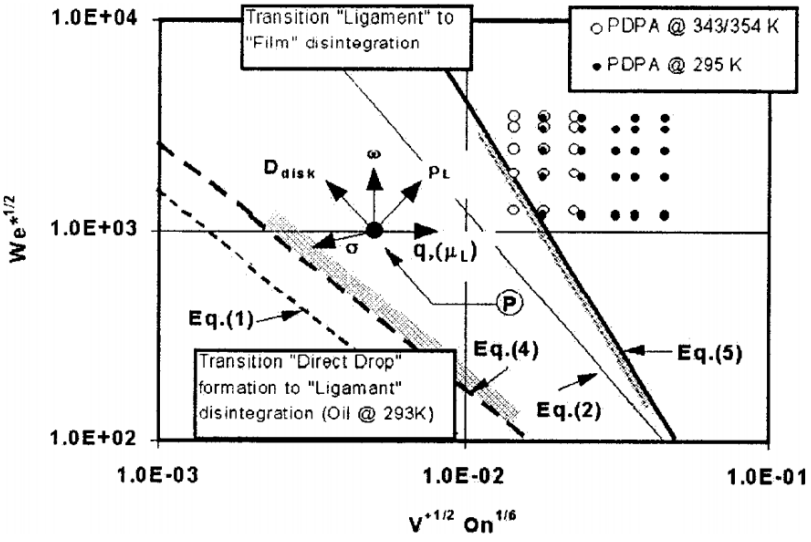


Figure 2.6: Droplet disintegration map [28]

The droplet disintegration map developed by Glahn *et al.* [28] will be used as a foundation for validating the critical correlation for *Trent* 1000 aero-engine ball bearing. Subsequently, correlations for direct-drop to ligament and ligament to sheet from other published literatures such as work of Liu *et al.* [27] and Peng *et al*. [33] are summerized and tabulated in Table 2.1. These correlations will be used extensively for comparative study and analysis in Chapter 4.

Table 2.1: Correlations for direct-drop to ligament and for ligament to sheet from previously published literatures

Authors	Atomiser	Correlation	Regime
Hinze and Milborn [20]	Rotary Cup	$\frac{\rho_L q^2}{\sigma D^3} = 0.5083\left(\frac{\mu_L}{\sqrt{\rho_L D\sigma}}\right)^{-0.333}\left(\frac{1}{8}\frac{\rho_L\omega^2 D^3}{\sigma}\right)^{-0.60}$	Ligament – Sheet
Frost [21]	Rotary Disk	$Q < 1.52\left(\frac{\rho\sigma D}{\mu^2}\right)\left(\frac{\mu D}{\rho}\right)\left(\frac{\omega\rho D^2}{\mu}\right)^{-0.95}$	Direct Drop – Ligament
		$Q < 19.8\left(\frac{\rho\sigma D}{\mu^2}\right)^{0.9}\left(\frac{\mu D}{\rho}\right)\left(\frac{\omega\rho D^2}{\mu}\right)^{0.84}$	Ligament – Sheet
Matsumoto *et al.* (from [28])	Rotary Disk	$\frac{\rho Q^2}{\sigma D^3} = 0.0333\left(\frac{\mu}{\sqrt{\rho D\sigma}}\right)^{-0.9}\left(\frac{1}{8}\frac{\rho\omega^2 D^3}{\sigma}\right)^{-0.85}$	Direct Drop – Ligament
Glahn *et al.* [28]	Rotary Disk	$\frac{\rho_L q^2}{\sigma D^3} = 0.0854\left(\frac{\mu_L}{\sqrt{\rho_L D\sigma}}\right)^{-0.9}\left(\frac{1}{8}\frac{\rho_L\omega^2 D^3}{\sigma}\right)^{-0.85}$	Direct Drop – Ligament
		$\frac{\rho_L q^2}{\sigma D^3} = 0.1378\left(\frac{\mu_L}{\sqrt{\rho_L D\sigma}}\right)^{-0.33}\left(\frac{1}{8}\frac{\rho_L\omega^2 D^3}{\sigma}\right)^{-0.435}$	Ligament – Sheet

Authors	Atomiser	Correlation	Regime
Liu *et al.* [27]	Rotary Cup	$\frac{Q}{\omega R^3} = 6.5 \left(\frac{\rho\omega^2 R^3}{\sigma}\right)^{-1.161} \left(\frac{\mu^2}{\rho R\sigma}\right)^{-0.0705}$	Direct Drop – Ligament
		$\frac{Q}{\omega R^3} = 5.13 \left(\frac{\rho\omega^2 R^3}{\sigma}\right)^{-0.789} \left(\frac{\mu^2}{\rho R\sigma}\right)^{-0.036}$	Ligament – Sheet
Peng *et al.* [33]	Rotary Disk	$\left(\frac{Q}{\omega D^3}\right) = 0.308 \left(\frac{1}{8}\frac{\rho\omega^2 D^3}{\sigma}\right)^{-0.994} \left(\frac{\rho Q}{\mu D}\right)^{0.201}$	Direct Drop – Ligament
		$\left(\frac{Q}{\omega D^3}\right) = 0.257 \left(\frac{1}{8}\frac{\rho\omega^2 D^3}{\sigma}\right)^{-0.75} \left(\frac{\rho Q}{\mu D}\right)^{0.133}$	Ligament – Sheet

Reviews of the above correlations will be made in Section 4.3.3

2.1.4.2 Droplets Generation from Roller Bearing

Previous studies were largely based on idealised and controlled environment for oil disintegrations from rotary devices. A study of droplet generation from an actual cylinder roller bearing subjected to realistic conditions was conducted by Gorse *et al.* [34] looking at the effect of pressure differential across two chambers and the design of the bearing support structure on droplet generations. The test cases focused on changing the sealing pressure of chamber I and II, therefore allowing the crossflow ($\dot{m}_{g,I-II}$) to be varied from 0 to 8 g/s. Subsequently, two types of bearing support structures: 90 degree edge and smooth curved were tested to assess if the structure was causing instability on the oil film. The designs of the bearing support are provided in Figure 2.7.

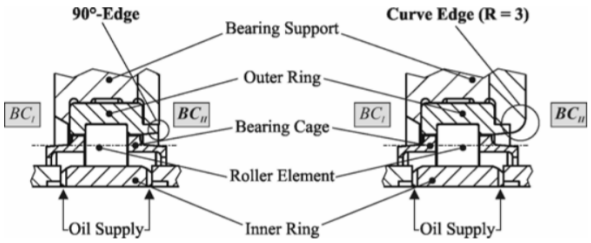


Figure 2.7: Design of bearing support: **90°** edge (left) and curved edge (right) between the outer ring and the support [34]

The observations of droplet behaviour were made using endoscope coupled high-speed camera. It reveals that at low speed of 4000 rpm, a smooth layer of oil film leaves the bearing between the outer-race and cage. As the crossflow was systematically increased to 3 g/s while maintaining the speed and flow rate, instability was seen on the oil film exiting the gap. Further increase in crossflow to 6 g/s induces minor droplet generation and strong droplet generation was seen at 7.5 g/s. The investigations indicated that curved edge bearing support has delayed the droplet generation. Only minor droplet generations were seen at 7.5 g/s. Further quantification of droplet generation shows that at high crossflow, the vorticity structure similar to that measured by pure airflow of Gorse *et al.* [17] disappeared and droplets followed the established flow field from roller bearing towards the front plate due to weakened tangential velocity component of airflow.

2.1.4.3 Power Losses in Bearing Chamber

Power losses were found to be linked to droplets in bearing chamber. Flouros [35] investigated the reduction of power losses in bearing chamber by enclosing a ball bearing with porous screen. Endoscopic imaging showed that significant amount of droplets from the bearings were impeded by the porous screen (of $\phi = 3$ mm). They were collected in the form of liquid by gravitational scavenging. To confirm that the porous screen is promoting more 'efficient' scavenging, two vents were used. The first is flush vent (where extraction surface is at the same datum as the chamber wall) and the second is 15 mm protrusion vent from chamber wall. The results were consistent with scavenge indicated that with porous screen less oil is vented out. Less droplets were loaded in the air compared to unscreened ball bearing. It was believed that the reduction of power losses were due to lower residence time of the mixture in the chamber where Flouros refers them as 'dwelling' time. It should be highlighted here that, during the commission of rig the vent pipe of the test rig extracted a higher amount of oil when a flush type vent is used. This is indeed similar to cases of Flouros where the vent quantities were measured to be higher for flush type. Oil film with sufficient tangential momentum is driven towards the upper chamber wall and enters the vent pipe causing it to be extracted. With protrusion, liquid are guided around the pipe and hence only film deposited by droplets or mist can be extracted. The measurement of the amount of vented oil was not part of the experimental assessments.

2.1.5 Turbulent Jets in Bearing Chamber

Within the bearing chamber the air is regarded as highly turbulent, qualitative analysis by Krug *et al.* [36] using high-speed shadowgraphy reveals significant interaction between airflow and oil jet depending on their respective momentum. Supply of oil jet was targeted onto shaft with machined feed holes, the interaction meant that not all oil was caught by the device and subsequently only part of them being fed to the bearings. The oil was loss in the form of droplets, ligaments and films deposition on chamber wall. Momentum flux ratio, $q = \rho_l u_{l,jet}^2 / \rho_g u_g^2$ was used as the relation to access the driving force of breakup and deflected oil jet. It was found that at low momentum flux, jet failed to reach the delivery slot and instead, deflected as the momentum of air was too large. The oil capture efficiency, η was measured to be poor for low momentum flux. At q beyond 500, the efficiency was found to be greater than 70%. It was reported that efficiency of 90% is not possible. In additional to the momentum flux ratio, the impingement angle (α) was also found to affect the capture efficiency. A shallow angle was found to be the best and resulted in less splashing. In the last assessment, different nozzle size was tested and a

small nozzle was found to have the least droplet generation as instabilities at the jet surface was smaller. The findings underpinned the effect of airflow and jet in a chamber-like environment, and is shown to be turbulent.

2.1.6 Taylor-Couette Flow in Coaxial Cylinders

Bearing chamber could be idealised as an annular area of two concentric cylinders at its simplest form with inner or outer surface rotating. The efficiency within turbomachinery, journal bearings and even electric machinery are driven by such flows to a certain extend. For example, the moment of coefficients are affected by the flow structures in rotating spindles and shafts [37]. The existence of laminar flow in the rotating surfaces was first investigated by Couette to determine the viscosity of a fluid. Taylor [38] then discovered the existence of rotating cellular cells in rotating coaxial cylinders. It was discovered that when a critical condition is achieved, the laminar viscous flow will turn into axially-periodic counter-rotating vortices known as Taylor vortices. And the study of such flow is name after Taylor and Couette as Taylor-Couette flow.

For laminar Couette flow in an annulus gap, an exact solution to Navier-Stokes equations exist [37]. The laminar, isothermal and incompressible circumferential velocity profile can be expressed as:

$$u_t(r) = \frac{1}{r_o^2 - r_i^2}\left[r\left(r_o^2\omega_o - r_i^2\omega_i\right) + \frac{r_o^2 r_i^2(\omega_i - \omega_o)}{r}\right] \tag{2.10}$$

The notations can be referred in the Nomenclature. In Lee's work, by having the outer cylinder stationary, the analytical solution for laminar flow was found to match that of CFD calculation at 5 rad/s. However, for higher shaft speed ($n = 3000$ rpm or 314.2 rad/s) the solution no longer valid. It was indicated that turbulent flow exists at higher shaft speed and turbulence model should be incorporated in the CFD [9].

The classical experimental study of Taylor vortices were extended by Coles [39], it was shown that the Taylor vortices is transitioned into wavy vortices in azimuthal direction when speed is increased. This is known as double periodic flow. Subsequently, Cole investigated Taylor-vortex instability in relation to the axial length of cylinders [40]. It was found that the onset of wavy instabilities were much earlier compared to 'infinitely' long cylinder (i.e. gap length $\ll$ axial length). Experimental study by Koschmieder further reveals that beyond certain Taylor number,

the wavy instabilities of Taylor vortices disappear and fully turbulent Taylor vortex flow begins [41].

Kaye and Elgar [42] also reported the existance of 4 types of flow regime in rotating inner cylinder with axial throughflow as: (1) Laminar flow (2) Laminar flow plus Taylor vortices (3) Turbulent flow and (4) Turbulent flow plus Taylor vortices. The authors' findings were based on flow visualisation and hotwire anemometry. The demarcation lines that differentiate the transitional regime were further refined by work of Becker and Kaye [43] based on the study of the effect of heat tranfer in an air gap of a rotating electrical machine. The transition from laminar flow to turbulent flow was found to be at Reynolds number of 1800 when axial throughflow is imposed. Here, the regime map of Becker and Kaye [43] is used as the basis for verifying the regime of flow that might be expected in G2TRC's bearing chamber. The regime map is provided in Figure 2.8 with x-axis representing modified Taylor number and y-axis representing axial Reynolds number. The equations are given as below:

Modified Taylor number is defined by Becker and Kaye [43] as:

$$Ta_{modified} = \frac{\omega^2 r_m b^3}{\nu^2} \frac{1}{F_g} \tag{2.11}$$

Where, ω is rotational speed of inner cylinder, r_m is arithmetic mean radius of the annulus, b is width of annulus ($r_o - r_i$). ν is air kinematic viscosity. F_g is geometric factor (for full description refer to the publication [43])

Axial Reynolds number is defined by Becker and Kaye [43] as:

$$Re_{axial} = \frac{2V_{axial} b}{\nu} \tag{2.12}$$

Where, V_{axial} is imposed axial velocity, b is width of annulus ($r_o - r_i$) and ν is kinematic viscosity of air. For axial velocity, there is no experimental data available, prediction for G2TRC's Reynolds number was calculated based on the axial velocity of CFD at 3000 rpm as 2.307 m/s. This was achieved by linearly interpolate the available preliminary CFD result at 13000 rpm. Air kinematic viscosity used in the calculation is 1.516×10^{-5} which is based on the mean ambient temperature of thermocouple at 20.37℃.

The generalised Taylor number by Childs [37] is also used since an unphysically large Modified Taylor number was obtained based on definition of Becker and Kaye [43]. The generalised Taylor number is given as following:

$$Ta = \frac{\omega r_m^{0.5}(b-a)^{1.5}}{\nu} \tag{2.13}$$

Where, ω is shaft rotational speed, $r_m = (a+b)/2$, a is inner radius, b is outer radius and ν is kinematic viscosity of air.

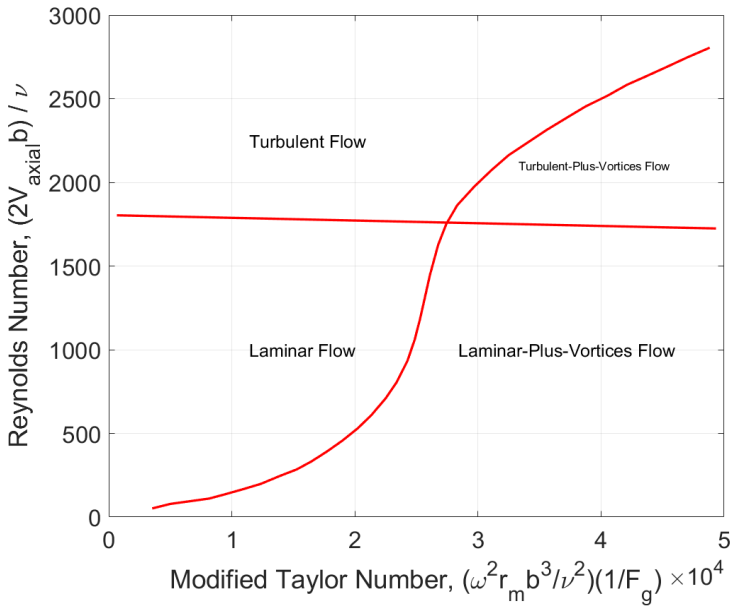


Figure 2.8: Demarcation lines for flow regions in annulus with inner cylinder rotating [35]

Based on the above equations, the regime predicted for G2TRC's ball bearing is turbulent as the axial Reynolds number is 6.39×10^3. Referring to the plot in Figure 2.8, there is possibility of 'turbulent'-type Taylor vortex cells as the generalised Taylor number obtained is 9.82×10^4 and the modified Taylor number is 7.353×10^9. Based on the above argument, it is clear that the flow regime in an aeroengine ball bearing is turbulent and hence the viscous model for CFD should be turbulence model.

2.1.7 Flow Regimes in Bearing Chamber

Early investigations of bearing chamber emphasised on film thickness and heat transfer, little was made to understand the film dynamics. In order to understand the film dynamics relative to the driving forces: shear and gravity. Hashmi *et al.* [44] attempted to recreate the flow conditions of a bearing chamber using ITS stratified test rig. The experimental module aimed at providing factors that influencing the film dynamic corresponding to co-current and counter-

current side. The increase in gas velocity on film loading of 5.07 lpm and 8.34 lpm indicated a transition of waveforms from smooth and flat waves to three dimensional waves. It was reported that the amplitude and frequency increases with velocity of gas. To include the effect of gravity, the rig was inclined from 5° to 25°. The increasing inclination reduces the wave amplitude and frequency. And to simulate counter-current regime, the film loading is applied opposite to the gas velocity. The waves were seen to be highly turbulent and have the form of solitary waves.

Identifying the regimes of oil flow for the actual KIT high speed bearing chamber test rig are crucial. For example, a partially wetting surface could affect heat transfer compared to fully wetting surface. Kurz and Bauer [45] identified two regimes in KIT test rig. The first regime is when oil is only partially driven by the air resulting in a very thin layer of oil film at the upper part of the chamber. Regime two is when oil has been driven by the air around the circumference and transported over the vent towards the co-current side. The critical point in which the regime change occurs was based on measuring the thickness distribution at capacitive sensor of angular position $\phi = 315°$ (see Figure 2.9 (a)). When the speed is increased incrementally, a sudden film thickening indicates that the critical speed is obtained. This can be referred in Figure 2.9 (b) where the regime of change was measured at 11600 rpm.

Kurz and Bauer [45] proposed that critical momentum flux for regime change decreases with increasing in oil flow rate. It also shown that larger chamber is more likely to result in regime one. Conclusively, the authors indicated that it was still not possible to fully derive a correlation that is valid for all conditions and geometries.

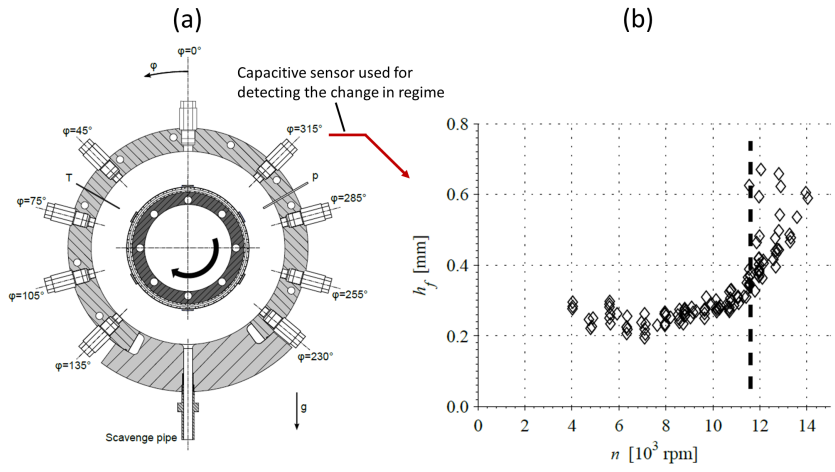


Figure 2.9: Determination of the change in flow regime in an aero-engine bearing chamber; (a) front view of the location of capacitive sensors (b) film thickness at $\phi = 315°$ versus speed, dashed line indicates regime change [45]

2.1.8 Shear-Driven Liquid Film

Besides the investigation of Hashmi *et al.* [44], application of shear-driven liquid film is also important in pre-filming airblast atomiser. Wittig *et al.* [46] investigated the film profile of a shear-driven liquid in a test rig that was designed to mimic the flow conditions of a pre-filming airblast atomiser. Light absorption technique was used to measure the film thickness and for velocity measurement, a liquid dye was injected at a known pulsation from the bottom of the channel. Cross-correlation was obtained from the scattering signals hence allowing determination of film velocity. Wittig *et al.* [46] applied the same theoretical model from Wurtz and compared with experimentally measured values. The film profile was found to be laminar in pre-film airblast atomiser. This in contrast differs with Glahn *et al*'s [15] finding that the film is somehow turbulent in bearing chamber. The increase in gas velocity also shown to reduce the film thickness. It was concluded that turbulent air and waviness of film surfaces are not causing the film to be turbulent.

2.1.8.1 Droplet Impingement on Shear-Driven Liquid Film

As shown in Chapter 1, the chamber began to be saturated with mist and droplets at higher shaft speed of 5000 rpm due to greater activity of droplet impingement and re-entrainment (from splashing). The understanding of droplet impingement and its outcomes in bearing chamber were still limited. However, a large body of investigations during last decades focuses on droplet impingement on static film surface. To close the gap, Mitchell *et al.* [7] investigated the impingement of a single droplet falling under influenced of gravity onto a supercritical film (e.g. Froude Number > 1). Four possible outcomes of droplet impingement with static film were summarised based on work of others as: floating, bouncing, coalescence and splashing. Note that splashing can be derived from crown or jet depending on the energy of impact.

Floating is termed as regime when kinetic energy of droplet is insufficient to break the layer of liquid interface. Hence it remains above the film and slowly being absorbed by the interface due to gravity. If the kinetic energy is further increased, droplet could bounce on the liquid layer. Two most important physics are coalescence and splashing. If the kinetic energy of droplet further exceed that of bouncing, the droplet could penetrate and mixes with the liquid through coalescence. At highest kinetic energy, droplet that impacts the surface could form crater or at times, jetting creating smaller droplets. These outcomes are also influenced by the angles of impingement and the depth of the film usually denoted by the normalised height δ (dividing film height and droplet diameter). Examples of different outcomes from droplet impact onto liquid film are shown in Figure 2.10.

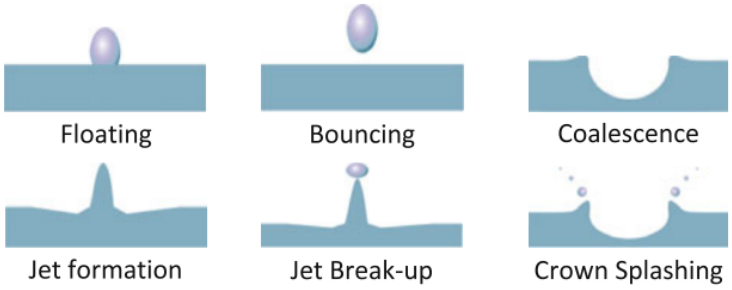


Figure 2.10: Outcomes of droplet impact onto liquid surface (Adapted from [47])

Mitchell *et al*'s [7] studies showed that in order for the correlations of droplet impingement onto a static film to be valid and applicable to a moving film, the resultant component of velocity based on definition of Okawa *et al.* [8] should be used. However for analysis of crater evolution, the authors found that normal velocity component of droplet should be applied instead and matches well with Bisighini *et al*'s [48] cavity model. The depth of the crater in supercritical moving film is overestimated by the model. Asymmetric crater cavity was observed due to film transportation. In conjunction to studies of Mitchell *et al.* [7], Okawa *et al.* [8] indicated that no secondary droplets are produced if the impingement angle exceeds 70° even subjected to high splashing parameter, K. Generally, the summary of splashing parameter K indicated that splashing is likely to occur at $K > 2100$. In comparison to a dry wall, the K value for splashing was found to be 57.7 by Mundo *et al.* [49].

2.2 Numerical Studies

Numerical modelling tool - Computational Fluid Dynamics (CFD) enables the prediction of the fluid flow within a system of interest. This is achievable by supplying a set of initial condition, boundary condition onto the mathematical and physics models that govern the flow. In the field of fluid mechanics, notably aerodynamics where CFD was first popularized, a case study published by the Boeing Company indicated that the number of wind tunnel tests have greatly reduced with the usage and development of CFD [50].

Historically, aerodynamicists relied on empirical, analytical and experimental wind tunnel test for the design of aircraft in order to predict the performance of the aerodynamic flight characteristics. Studies have shown that over the period of several decades, the number of wing test has reduced by 87%. The statistics along with the timeline of the development of turbulence model can be referred to in the Figure 2.11 [50]. CFD has great added value, the Boeing Company cited that

less wings were physically tested across different aircraft programms, notably, the 777, 757 and 767 programms due to the adoption of CFD numerical tool [50]. Although CFD is a great prediction tool but it is still no able to fully replace the physical experiment for both product certification and durability test. Nonetheless, CFD is able to complement experimental data in many ways. Such benefits were also applicable to the design and development of a new bearing chamber where CFD enables fluid flow prediction and understanding. This section presents the literature review of CFD in bearing chamber modelling.

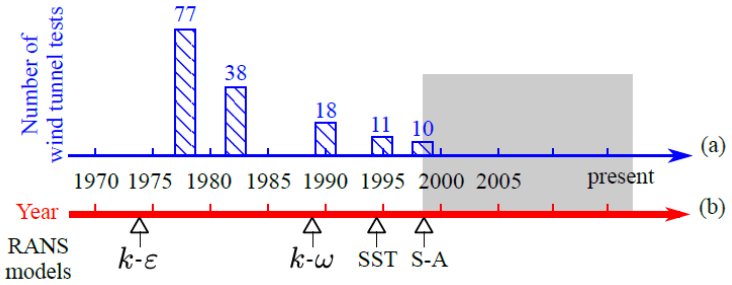


Figure 2.11: Number of wind tunnel testing in the past five decades and the timeline of the development of general turbulence models [51]

2.2.1 Airflow in Chambers and Cavities

Single-phase air flow is the driving force for liquid film on the chamber wall through shear stress transportation. It also impacts the trajectories of light particles (typically one with low Stokes number) in the chamber. Early numerical modelling of bearing chamber was performed by Glahn *et al.* [16] looking at droplet trajectories influenced by gaseous-phase. Droplet of different class sizes were initiated based on experimental data from PDPA. Result showed that smaller droplets experience larger effect from the airflow compared to larger droplets. The curvature of trajectories increases with respect to decrease in droplet diameters.

Lee *et al.* [9] performed comprehensive studies of rotating airflow in a HP-IP bearing chamber that is representative of a Trent-series aero-engine. The numerical results were validated with data obtained from particle image velocimetry (PIV). In the studies, the flow was regarded as highly turbulent and evidence of Taylor vortex cells were not present. Two turbulence modelling approaches were tested, namely, standard $k-\varepsilon$ (SKE) and Reynolds Stress Model (RSM). The SKE relies on modelling the turbulent viscosity through Boussinesq approximation while the RSM solves full transport equations of the Reynolds stresses. The single-phase investigations indicated that RSM is superior compared to SKE in predicting the turbulence intensity and

velocity profile. The agreement for tangential velocity between experiment and RSM accounts for 8% error and 35% with SKE.

Numerical study of turbulence models was also performed by Vinod *et al*. [52] for flow in a rotating cylinder cavities with radial inflow (of an aero-engine internal air systems). Although for different application, it was reported that RSM gave the best result against experimental data for measurements of pressure, velocity and temperature. The eddy viscosity models (e.g. $k-\varepsilon$ and Spalart Allmaras) overpredicted the turbulent diffusion in the core flow. And solutions were sensitive to wall functions.

2.2.2 Direct Numerical Simulation of Turbulent Taylor-Couette Flow

In Section 2.1.6, the regime of flow (laminar or turbulent) was predicted based on reviewing several experimental works of simplified rotating systems. Here, secondary verification of the flow regime was made based on the numerical work of Dong [53]. Direct Numerical Simulation (DNS) of turbulent Taylor-Couette flow for rotating cylinder of radius ratio 0.5 at Reynolds number ranging from 1000 to 8000 was performed [53]. In Dong's numerical configuration, only inner cylinder is rotating.

The author discovered that the flow remains laminar at Reynolds number of 1000, somehow much lower than what described by Becker and Kaye [43]. This was justified based on the observation of Herringbone-like streaks structure due to so-called '$Görtler$' votices in the turbulent regime of Reynolds number from 3000 to 7000. An azimuthal velocity plot of the herringbone-like streaks was given in Figure 2.12.

Based on Figure 2.12, at $Re = 1000$, the flow possesses the characteristics of laminar flow where the pathline remains highly continous and uniform along the z-axis. In contrast at $Re = 3000$, 5000 and 7000 respectively, the azimuthal velocity across the axial length z is changing rapidly, possessing the chracteristics of turbulent flow. Using the equations provided by Dong [53], the regime of flow for the current experiments can be further verified in order to decide on the type of viscous model to be used in CFD. Here, Reynolds number based on Dong's definition [53] is:

$$Re = \frac{U_o d}{\nu} \tag{2.14}$$

Where, U_o is the rotational velocity of the inner cylinder, d is the gap width ($R_2 - R_1$) and ν is

the kinematic viscosity of air. For G2TRC's ball bearing, the gap width d is calculated based on the outer radius of 142.5 mm and the inner radius of 122.0 mm. A shaft speed of 3000 rpm is used. Using Equation (2.7), the Re obtained is 5.183×10^4 indicating highly turbulent flow. Based on the above arguments, a turbulence model will be used as the viscous model for modelling the flow in the numerical work of this thesis.

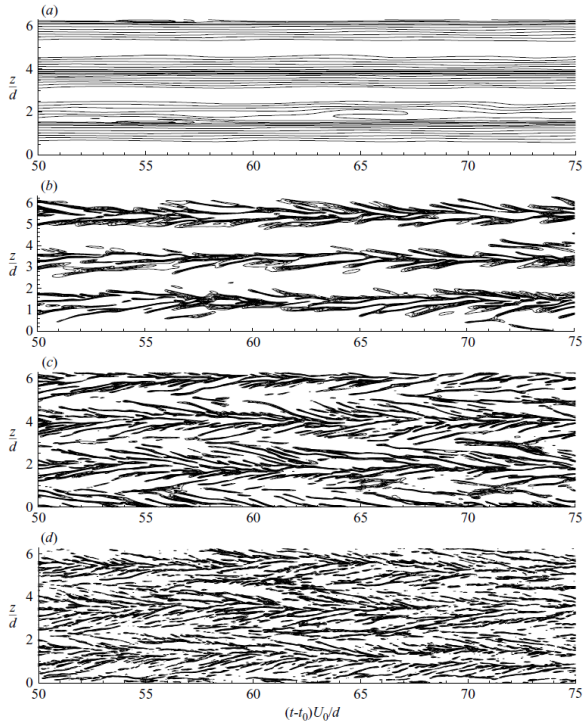


Figure 2.12: Herringbone-like streaks demonstrated based on plot of azimuthal velocity along z-direction for (a) $Re = 1000$, (b) $Re = 3000$, (c) $Re = 5000$, (d) $Re = 8000$ [53]

2.2.3 Multiphase Flow Simulation in Bearing Chamber

The use of computational fluid dynamics (CFD) in the modelling of multiphase flow within bearing chambers is highly desirable as it enhances predictive capabilities in bearing chamber design as well as providing insight into the flow structures during various engine operating envelopes [9, 54]. These also include the ability to study heat-transfer across chamber housing. Analytical and theoretical models were successfully implemented for simple cases as reported by Glahn *et al.* and Wittig *et al.* [14, 15]. Analysis of oil film was performed by Chew [55] using integral method with assumption of zero axial flow variation. This represented the first step in using 2D thin film approach in solving problem of wall film in bearing chamber.

The numerical studies of wall film and droplet trajectories in chamber similar to KIT were extended by Farrall *et al.* [56]. Euler-Lagrangian approach was used to track droplets through rotating airflow and a 2D integral model was used for solving the dynamics of wall film. Droplets based on Rosin-Rammler size distribution were released from the cage and assuming to have azimuthal component of velocity equal to that of bearing cage. The interaction between droplet and wall is based on work derived from direct-injection diesel engines, notably work of Senda *et al.*, Bai *et al.*, and Stanton *et al.* [57-59]. It was reported that the film thickness and velocities are highly sensitive to boundary conditions, in particular at scavenge port.

2.2.3.1 Volume-of-Fluid Approach in Bearing Chamber Modelling

The thin film approach has limitations as well as cost benefits. Some of the limitations include inability to simulate region of oil recirculation and ligaments. Notably in areas where gravity is dominant, region of sump could be problematic for thin film approach. The Volume-of-Fluid (VOF) method devised by Hirt and Nicholas [60] in 1981 was found to be useful in the context of aero-engine air and oil systems by Young and Chew [61]. Various test cases involving liquid in vertical rotating drum, horizontal rotating drum and hydraulic seals were tested.

The approach of free-surface simulation was performed by Hashmi *et al.* [62] in a shear-driven flow. Enchanced VOF was proposed by Peduto *et al.* [63] to address the short coming of Hashmi *et al*'s VOF model in interface capturing, in particular problem associated with 'false momentum transfer'. A model of Karlsruhe Institute of Technology (KIT)'s bearing chamber with only lower half of the domain was simulated by Peduto *et al.* [63] in order to save cost. The usage of VOF in the vicinity of scavenge was justified as oil is thick at around 4 mm compared to other areas. Additional simplification includes neglecting droplets in bearing chamber. It was shown that the absence of interface physics of gas and liquid in VOF is the main factor for the discrepancy. The turbulent viscosity was found to be unphysically high and interface treatment was implemented using User-Defined-Function (UDF) to correct the turbulent viscosity at the interface giving velocity profiles closer to experiment.

Building upon work of Peduto *et al.* [63], the fixed mesh approach employed has resulted in a significant number of cells being wasted, in particular, grid locations where oil is not transiting. These cells have reached the threshold of grid density needed to capture the solution gradient of airflow. An adaptive mesh refinement was performed by Pillot and Morvan [64] to assess the performance benefits. Refinement based on gradient of interface was made and resulted in better

capturing of oil morphology released from the cage at fraction of the computational cost of fixed mesh.

2.2.3.2 Coupled VOF-DPM

Moving away from Eulerian approach, Adeniyi *et al.* [65] implemented a hybrid model for solving the two-phase flow in a bearing chamber by means of coupling Volume-of-Fluid with Discrete Phase Model (VOF-DPM). Droplets that shed from rotating elements were tracked using DPM and upon interaction with interface of VOF, mass and momentum source were exchanged. The outcomes of droplet impingement onto liquid surface are based on work of Cossali *et al.* [66] and Yarin *et al.* [67]. In terms of number of secondary droplets produced from the impingement, correlations based on work of Peduto *et al.* [68] is used. The hybrid approach reduces the need for explicitly model the interface of droplets, where in some cases, could be a fraction of the thickness of the film. This allows the droplet to be tracked using DPM.

2.2.3.3 Evaluation of VOF in Bearing Chamber

Krug *et al.* [69] investigated the VOF approach in simulation of multiphase flow in KIT bearing chamber. Numerical studies of two different scavenge offtakes were performed, namely, baseline case and covered ramp case. In the studies, no specification on convergence of the models being mentioned. The numerical studies implied that VOF is suitable for capturing the oil patterns coming out of the annular gap of bearing and interacted with core flow. The film thicknesses is in agreement with the experimental data but discrepancies were observed. The discrepancies are associated with grid solutions and short coming of VOF in capturing the momentum transfer between air and oil which was also highlighted earlier. Three main meshes: 0.6M, 1.7M and the adaptive mesh refinement (AMR) case of 7M were found to be giving different oil patterns. Mesh with AMR gave the best qualitative oil structure with experiment with ligaments and droplets well-resolved. The AMR case required order of magnitude time-step of 5 time-step/CPUh compared to 16 time-step/CPUh and 48 time-step/CPUh respectively.

Based upon the work of previous authors, Bristot *et al.* [70] developed a method of evaluating the convergence of VOF in bearing chamber by incorporating the Robinson sump model devised in the University of Nottingham and also assessed the cost benefits of using implicit formulation for VOF interface capture. Due to the unsteady nature of the oil film and complex two-phase flow

interaction, sampling of flow is performed to obtain time-averaged value. The numerical studies indicated that implicit VOF formulation with Compressive Interface Reconstruction Scheme is cheaper compared to Geometric Reconstruction (e.g. 13440 CPUh/s vs 88320 CPUh/s). CPUh/s is the amount of computing resources needed to compute one second of physical flow time and is obtained by multiplying the number of cores used with hours of simulation needed for one second of flow time. $k-\omega$ SST Turbulence model was deemed a good choice as it uses standard wall function close to the shaft (e.g. $y^+ = 70$) and close to the chamber wall near-wall treatment is automatically used (e.g. $y^+ = 3$). However, the usage of such turbulence model introduced the concept of turbulence damping that aims at correcting the high velocity gradient at the interface. The recommendation of Egorov [71] and Tkaczyk [72] for B = 100 has smeared out the waves' structure at the liquid interface. It was said to be a factor for the under-prediction of film thicknesses at 15000 rpm.

2.2.3.4 Turbulence Damping, *B*

The effect of turbulence damping in VOF was subsequently being assessed by Bristot *et al.* [54]. Two turbulence damping factors, B were tested: 10 and 100. The distribution of film thickness around the circumferential position is closer to experiment for lower damping factor of 10. Two types of liquid flow were observed. At low turbulence damping, the flow was said to be gravity-driven. Whereas, at higher damping factor, the flow was regarded as shear-driven. The difficulty with finding an appropriate damping factor makes the simulation as being imposed rather than predicted. The oil residence volumes were also reported to be higher for lower damping factor. More work needs to be done to find an appropriate damping factor or to improve the model. The studies of dynamics of waves in experimental chapter will serves as a good study for understanding the transfer of momentum in gas-liquid interface.

2.2.3.5 Progression in Eulerian Thin Film Model

In Chew's [55] thin film model, two test cases were run: a stationary drum with swirling source flow and partially filled rotating drum without swirling source flow. The discrepancy between the first numerical test case with the rotating drum of White and Higgins [73] (experimental) was said to be originated from the negligence of air-liquid interaction by using a fixed drag coefficient in computing the momentum of film. Inaccuracy was said to be further increased if waves are present on the surface. For second test case, Chew [55] showed that the

thin film model is able to model that of Wittig *et al*'s experimental cases for both laminar and turbulent film. The model was inconclusive due to uncertainties with input conditions like cage speed, outlets condition and three-dimensional effects as well as underlying assumptions.

To overcome the shortcoming of previous thin film models, Williams [74] developed a thin film with inclusion of droplet-film interaction term. Wang *et al.* [75] further extended the model by evaluating the momentum equation term-by-term to assess its stability and the implementation shows close results with that of commercial solver Fluent [76]. Wang *et al.* also expressed that the adoption of thin film in terms of Lagrangian formulation (where the continuity of the film is represented by tracking the volume of impinging droplets [77]) is not suitable for bearing chamber application as the droplets are significantly fewer compared to spray physics in internal combustion engine. Wang's [76] thin film model has difficulty of simulating problem with shear stress of less than 1.75 Pa which corresponded to shaft speed of 8000 rpm. Kay *et al.* [78] showed that film inertia term can provide a significant leading-order mechanisms in momentum equation and must not be neglected due to droplet impingement and shearing effect. Of all these models, the depth-averaging formulation is used, example for velocity is given in Equation (2.15):

$$\bar{u}(s,t) = \frac{1}{h}\int_0^h u(s,y,t)\,dt \tag{2.15}$$

Where, y is radial distance, s is azimuthal distance, h is film height, t is time and u represents velocity component. Further details on thin film model will be made clearer in Chapter 5.

2.2.3.6 Coupled VOF-ETFM

Significant cost will incur if relatively laminar and two-dimensional thin films were to be resolved using VOF for bearing chamber modelling in particular at high rotational speed. There are still regions where VOF is needed some of them include the location at the edge where film separates (refer Figure 2.13). Prior to coupling of both models, Kakimpa *et al.* [79] tested the fidelity of VOF and ETFM on simulation of isothermal thin film flow over a rotating plate. The ETFM was able to provide comparable accuracy relative to experimental data of Rice *et al.* [80].

Following the feasibility studies, a coupled VOF-ETFM framework was presented by Kakimpa *et al.* [81] using a rimming flow test case. A transition criteria was specified in order for the mass and momentum source term to be converted at the interface of VOF and ETFM. To switch to ETFM, the volume of fraction measured within the cell should be lower than a critical cut-off value and for the opposite to occur, the volume fraction should exceed the critical cut-off value.

The authors specified 0.5 as the critical value in their studies. The numerical studies showed that VOF-ETFM predicted the film without dry-patches and full VOF simulation contains many spots without oil. The cost benefit was measured to be approximately 3 times lower for VOF-ETFM.

Further progress was made regarding solution stability and accuracy of thin film model by Kakimpa *et al.* [82]. In the studies, three common types of rimming flow were simulated (e.g. smooth, shock and pool). In smooth flow, interfacial shear overcomes gravity resulting in liquid uniformly coating around the cylinder. For shock, the interfacial shear and gravity is in same order of magnitude hence, recirculation accompanied by a steep wave-front could be seen at the rising side. For pool flow, the gravity is order of magnitude stronger than shear hence causing majority of oil lumping at the bottom with only a very thin layer of oil coating on the upper half of the cylinder.

The simplified inertia term proposed by Wang *et al.* [76] was found to be less accurate compared to full inertia term where the quadratic velocity profile is used instead of the usual uniform velocity profile. The full inertia term managed to numerically resolve the oscillatory capillary ripples similar to one seen on experimental falling wavy film of Liu and Gollub [83]. The authors also expressed that the use of high surface tension in previous thin film models were unphysical as they are order of magnitude higher than is usually present in engineering applications. A proposed stable numerical solution (without relying on high surface tension value) is to use a time-step constraint and sufficient grid resolution [82].

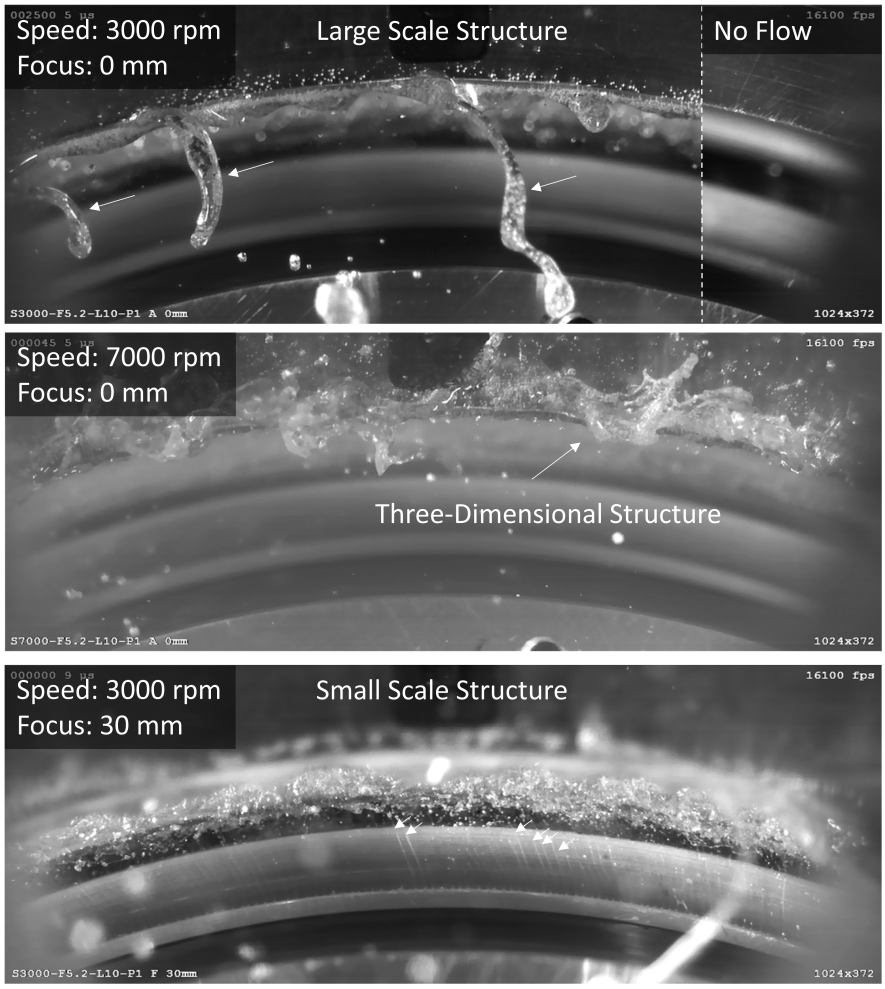


Figure 2.13: Three-dimensional oil structure separated at the edge of a chamber wall

2.2.4 Comparison of Unsteady Reynolds Averaged Navier Stokes (URANS) versus Large Eddy Simulation (LES)

Referring to early subsections, it is conceivable that most of the computational fluid dynamicists have favoured Reynolds Averaged Navier Stokes (RANS) Model or Reynolds Stress Model (RSM) for the modelling of fluid flow. In this section, a review was carried out to investigate if Large Eddy Simulation (LES) is suitable for multiphase flow simulation due to its known accuracy in comparison to RANS.

Two-equation model can involve either steady-state calculation or transient calculation depending on the problem. Steady-state calculation refers to the usual Reynolds Averaged Navier Stokes (RANS) equations where the final solution consists of the mean and fluctuating component. It is meant for problem with very low Reynolds number or low turbulence level. For transient calculation, two-equation model uses time-marching formulation that involves time-derivative

term in the calculation, at each time-step the solution is also expressed in terms of mean and fluctuating. This type of calculation is known as Unsteady Reynolds Averaged Naiver Stokes (URANS) equations and is good at capture time-dependent flow phenomena [84]. RANS and URANS have been proven to be robust in most engineering application such as wall bounded flow and unconfined external aerodynamic problem [84].

The most widely used two-equation models in the industry are the $k-\varepsilon$ and $k-\omega$ model [84]. The $k-\varepsilon$ model was first proposed by Brian and Launder [85] whereas $k-\omega$ was proposed by Wilcox [86]. The two-equation models are computationally efficient as they compute the turbulent viscosity from two transport equations. In such approach, the scalar property is ensembled averaged where the inherently time-dependent eddies of various length scale are smoothed. This method could be problematic for combustion and acoustic modelling since there are high level of unsteadiness and fluctuations within the mean flow. Subsequently, combustion modelling also relies on turbulence for mixing of chemical species [87].

A way to alleviate the problem with smoothening or averaging is by resolving the anistropic mean-flow that contain large eddies. This approach is known as subgrid-scale modelling (SGS) or more commonly Large Eddy Simulation (LES). LES resolves the energy-containing large eddies by solving the Navier Stokes equations rather than modelling it. LES was first proposed by Smagrinsky [88] back in 1963. It is only in recent decades, that LES was put into practice due to the advancement in computing power. In LES, a sub-grid filter is placed as a cutoff point for which eddies to be resolved and which to be modelled. Generally, the smallest eddies are modelled, if not the solution will tends towards Direct Numerical Simulation (DNS) [84]. To capture large eddies, the grid and time-step requirements are generally in an order of magnitude larger than that of RANS/URANS. A chart that summarises the computational cost of resolving and modelling the flow using different models is presented in Figure 2.14.

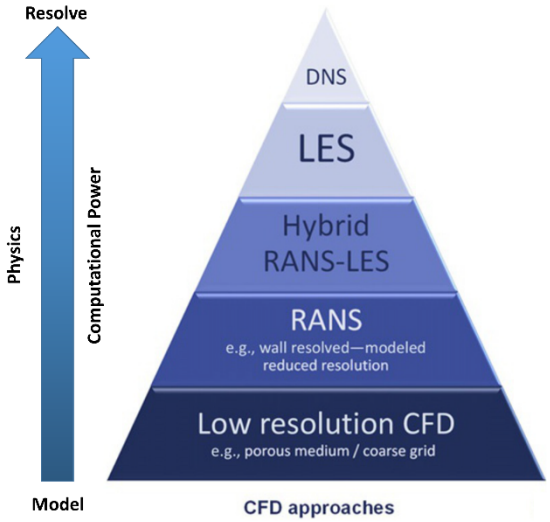


Figure 2.14: A hierachy of CFD methods based on computational cost and the level of resolution [89]

Comparison of the computing cost for LES with 7-equation model RSM by Ferziger (based on the text book [84]) was found to be twice as much. In the modelling of multiphase flow, the equation for solving the secondary phase using interface tracking method like VOF will make the simulation prohibitively more expensive making it impratical for LES to be used in bearing chamber modelling. Although RANS model is less accurate compared to LES, Roelofs [89] expressed that a highly resolve URANS simulation can be as good as a wall-modelled LES in capture similar scale structures in modelling of two-phase flow in nuclear applications. Based on the above argument, two-equation turbulence model is the preferred choice in solve the continuum phase and will be adopted in this thesis.

2.2.5 Meshing and Verification

Grid generation is an early stage of the CFD process, the accuracy and stability of the numerical solution are linked to type of mesh generated. There are two types of mesh available for general purpose CFD: (1) Structured and (2) Unstructured.

Structured mesh is a grid with regular nodes connectivity between two adjacent cell faces [90]. An example of structured mesh is given in the Figure 2.15(a). In this mesh, the hexahedral 2D face can be seen to have 4 nodes, these nodes extended with a certain depth forming a rectangular cell depending on the aspect ratio. The advantage of structured mesh is low skewness and it is

easy to be programmed for the solver [91]. This translates to good convergence criteria and low cell count. The user also gains better control of the growth rate of the mesh in multiple directions as it is known that a sudden change in mesh size between two neighbouring cells will result in poor flux exchange leading to residual imbalance or worse, divergence. The disadvantages of structured mesh is the inability to conform to complex geometry that contains many curves and features [91]. As blocking technique will make it difficult to associate with such surfaces. This issue, however, could be mitigated by using a much more 'automated' meshing approach known as unstructured meshing which uses tetrahedral elements.

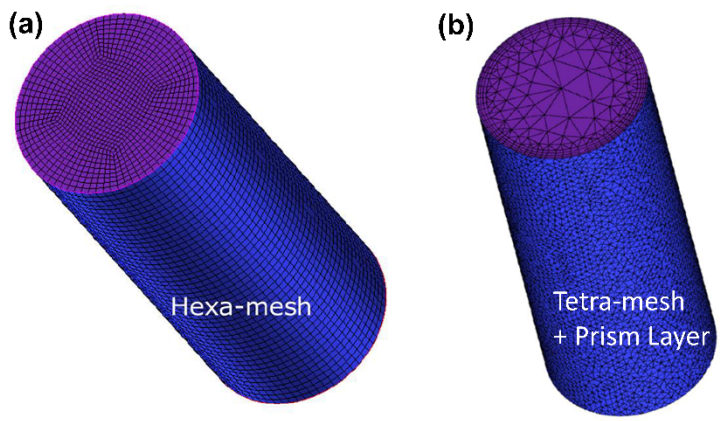


Figure 2.15: Image showing (a) Structured hexahedral mesh and (b) Unstructured tetrahedral mesh with prism layers. [90]

An example of tetrahedral mesh with prism layer is shown in Figure 2.15(b). Tetrahedral contains large amount of tetrahedron cell which can be see in the core of the cylinder. Tetra elements have known deficiency of ineffective in resolving the boundary layer present on wall-bounded flow. Most CFD algorithms today incorporate prism layer or hexahedral cells along with tetrahedral elements to mitigate the issue [91]. Apart from that, unstructured tetra elements also generate large amount of cell count compared to equivalent 'accuracy' structured mesh. The above criteria were used as a basis for deciding the type of mesh for our simulation.

Apart from grid generation, verification process is needed to ensure that the CFD models implementation reflects an accurate description of the developer's concept description of the model and the solution to the model [92]. Four sources of error could exist in CFD and can be defined as following based on definitions of Versteeg and Malalasekera [84] and American Institute of Aeronautics and Astronautics's guideline [92]: (1) Roundoff error, (2) Spatial discretisation error, (3) temporal discretisation error and (4) iterative convergence error.

Roundoff error can be mitigated easily by setting the precision of calculation from 'single' to 'double' [84], this increases the data size slightly but usually recommended. Of all, the most important aspect of reducing the discretisation error is systematical refinement of grid and time-step size [92]. Generally, time-step size can be determined much more easily by knowing the Courant-Friedrichs-Lewy (CFL) of the convective flow field. By systematically reducing the CFL number, the solution accuracy will increase. However, excessively small CFL slows down the simulation at the expense of accuracy. CFL can be expressed as:

$$CFL = \frac{|\vec{u}|}{\left(\frac{\Delta x}{\Delta t}\right)} \tag{2.16}$$

Where, $|\vec{u}|$ is the velocity of fluid in the cell, Δx is the grid spacing and Δt is the time-step size. By setting different Δt, the CFL obtained will result in different flow solution. By using the right CFL, temporal discretisation error can be minimised.

In terms of reducing spatial discretisation error, mesh independence study is performed where the geometry is discretized with mesh of various density, three grid densities are generally recommended, (1) coarse, (2) medium and (3) fine. The flow solution for different test cases is benchmarked with the finest mesh to ensure that the solution variable no longer changes with respect to the grid density. The basis of CFD verification was adopted and implemented as reported in Section 5.12.

To solve error no. (4) in the verification process, the residuals level is reduced to a reasonable value to ensure that the conservativeness of mass and momentum are achieved. Subequently the iteration number per time-step size should also be acceptable such that the solution variable no longer varies with further iteration. They are achieved by checking the mass imbalance at inlet and outlet as well as checking the solution accuracy when number of iteration per unit time-step is reduced. The above guidelines were used in CFD studies of this thesis.

2.3 Bridging Knowledge Gaps in Bearing Chamber Research

Referring to the work of previous authors, it is clear that the experimental studies of droplet generation by simple rotary devices scaled to aero-engine operating conditions by Glahn and co-workers were inadequate as it lacks the complexity of an actual aero-engine ball bearing [28-30]. In all cases, roller bearings were employed where they lack many dynamic features of a ball bearing [14, 15, 18, 19, 45], among them being contact angle, rolling angle and axial load

[93]. Flouros [94] who performed experimental investigations of a RB211 aero-engine ball bearing found that the oil split into the front and rear chamber was affected by the bearing axial load [94]. This indicates that roller-bearings lack certain feature as they only take radial load. There is no mention of the effect of oil split ratio for all research that involve roller bearings [14, 15, 18, 19, 45]. Subsequently, Flouros's research was largely based on studying the power loss [35], thermal profile of bearing structure [95], outer-race cooling [96] and have yet to report on the oil shedding process as well as the resulting film formation and film dynamics. Although Gorse *et al.* [34] did report on the droplet generation of a roller bearing based on the effect of pressure difference and geometry in the chamber, the findings mainly cover droplet generation with no mention of ligament and sheet formation. Furthermore, none of the above mentioned authors highlighted the aftermath of droplet production, film formation on bearing outer-surfaces and its behaviour. Argubly, Gorse *et al.* [18, 34] briefly mentioned about observations of oil film on the bearing chamber wall but only descriptively depicting the flow features using very general snapshots significantly lacking many information such as close up observations and analysis of multiscale wave structures (see the images in publications [18, 34]). Therefore, the experimental part of this thesis will close the gap by providing information regarding the flow features around an aero-engine ball bearing by using high-speed imaging. Additionally, the experimental data is useful for verification of CFD by providing an 'exact' boundary condition and can also be used for CFD validation.

Computational approaches for bearing chamber modelling were undertaken about 3 decades ago to assess the feasibility of simulating complex two-phase flow environments to inform the design process of aero-engine oil systems. Throughout the decades many methods have evolved. Early CFD models were inadequate. For example, Chew [55] looked at the modelling of thin liquid films in a circular drum with the assumption of a constant momentum source term. Glahn *et al.* [16] modelled the trajectories of dispersed droplets using Euler-Lagrangian approach in a simplified geometry without considering film formation. Furthermore, an assumption was made on particle initial condition since it was lacking from experimental data. The results were said to be purely qualitative [16].

The development of a conventional multiphase flow method – Volume-of-Fluid (VOF) by Hirt and Nichols [60] was proposed for implementation in an aero-engine bearing chamber by Chew and Young [61]. The model was practical but computationally costly for bearing chamber modelling where in some cases further simplifications were needed to cut down the cost. For instance, Peduto *et al.* [63] modelled only half of the chamber geometry with uniform oil input being imposed. Adaptive mesh-refinement was also used to track the region of high solution gradient signifying the high cost of VOF model [64]. In all cases, the oil generation source in bearing chamber modelling was simulated separately [6]. This severly limits the fidelity of the

simulation. Among the numerical issue faced by bearing chamber researchers was 'false momentum diffusion' at the air-liquid interface resulting in unphysical velocity profile [63].

The next step in bearing chamber modelling is coupling all physical models together, droplet tracking using Euler-Lagrangian approach, modelling thick liquid pools with VOF and resolve regions of thin film using Eulerian thin film model. This coupled approach saves tremendous computational cost. However, the stability and numerical fidelity of such an approach were still unknown. Kakimpa *et al.* [79, 81] did successfully performed coupling of VOF and Eulerian thin film model for a flat disk rotating with liquid on it. The model enables efficient use of computational resources at regions where it is most suited for. Adeniyi *et al.* [65] on the other hand successfully implemented VOF-DPM transition in a geometry representative of an aero-engine bearing chamber. However, none of the previous authors have looked at the numerical stability and fidelity of coupling DPM with Eulerian thin film model (ETFM). As such, the work that involves coupling all three models, VOF-DPM-ETFM is viewed as the next progressive step in bearing chamber research. Prior to full implementation of VOF-DPM-ETFM, the DPM-ETFM model is expected to work as intended.

In the computational work of thesis, the work by Arienti *et al.* [13] will be used as the validating test case for assessing the model's stability and numerical accuracy. Various submodels within the DPM and ETFM will also be explored. For instance, effect of turbulence dispersion on particle trajectories and impingement location, the momentum transporation of thin film and mass removal due to shear stripping.

2.4 Summary of Literature Reviews

The literatures on flow relevant but not limited to bearing chamber were reviewed. Studies indicated that two major forces that drove the phenomena within the chambers. The first being surface force – interfacial shear stress and second being body force – gravitational acceleration. The investigations showed that single-phase airflow has strong effect on the liquid-phase. In particular the oil film on the wall and the trajectories of particles within the core are highly influenced by gas-phase. The rotating airflow derived its momentum from the rotating shaft. At low shaft speed, gravity was seen as primary force in driving the film towards the bottom of the chamber wall. For higher shaft speed, surface force such as shear force is seen to cause the film to be transported around the circumference of chamber wall with uniform thicknesses. Experimental observations denoted that the dispersed-phase within the gas was originated from atomisation of liquid, droplet impingement as well as generation from rolling elements.

Study of single-phase airflow indicated that the air is highly turbulent and flow field is driven by shaft speed, sealing airflow rate and geometry of the system. Flow regimes were identified and can be termed to be similar to that of rimming flow such as smooth, pool and shock flow. Droplet impingement on moving film contains dimensional similarity to that of static film where correlations could be applied depending on the component of velocity used. The splashing parameter (K), impingement angle (α) and non-dimensional film height (δ) are factors affecting the secondary droplet production.

Numerical studies of airflow in the chambers and cavities were performed by various authors. The flow was said highly turbulent and evidence of Couette flow and Taylor-Couette vortex cells were not present in the intricate cylinders-like rotating geometry. Turbulence modelling were needed to model the flow structures and RSM model was found to be superior to two-equation models but this model were mainly tested on 2D axisymmetric mesh.

Further assessment was made to investigate as to whether the airflow is turbulent or laminar for G2TRC's bearing shedding test rig by reviewing the experimental work of concentric rotating cylinders in electrical machinery and DNS of Taylor-Couette flow. The flow was found to be turbulent for G2TRC's bearing shedding test rig as the Reynolds number calculated was higher than the prescribed value of the different authors [43, 53].

The approaches of multiphase flow in bearing chamber studies showed success of modelling the liquid film and dispersed-phase driven by gas-phase. However, discrepancies need to be addressed in particular problem with momentum transfer form gas to liquid as mentioned by

Chew, Peduto *et al*, and Bristot *et al.* [54, 55, 63]. Coupling of VOF-DPM and VOF-ETFM represent the latest advancements in bearing chamber modelling.

Chapter 3 Test Rig for Trent 1000 Aero-Engine Ball Bearing

In this chapter, the experimental test facility that was used for the investigation of oil shedding from a *Trent* 1000 aero-engine ball bearing is described in terms of the functionality and operations. Detailed subsystem of the test rig along with the software interface required for setting and maintaining the test conditions for the experiments are given. The test matrices for the experiments consisting rotational speed, flow rate and axial load are given. Information as to how the oil flow rates are derived from interpolation of *Rolls Royce plc* data and the load requirement needed to produce the representative in-flight bearing contact angles are also discussed. In the final section, the proposed measurements needed to achieve the test objectives are outlined.

3.1 Introduction

The Bearing Oil Shedding Rig is specifically built to investigate the nature of oil shedding from a *Trent* 1000 aero-engine ball bearing. The on-going capability acquisition aimed at improved oil management system and reduced heat-to-oil in aero-engine transmission system. This state-of-the-art facility located at *Gas Turbine and Transmission Research Centre* (G2TRC) is designed to provide maximum optical access to facilitate observation and characterisation of oil shedding behaviour under various engine-realistic operating conditions. In this context, the experimentation of oil shedding is not limited only to how oil imparted from fast rotating rolling elements but also assessing various phenomena, some of them include thin film formation and dynamics of thin film.

The Bearing Oil Shedding Rig is essentially a *Trent* 1000 High Pressure - Intermediate Pressure (HP – IP) location bearing fitted onto a direct-drive unit which is driven by an electric motor. In a conventional three-spool aero-engine, rolling elements such as ball bearings or roller bearings are used to support the shafts and react to loads. They are located in various locations of the engine which could include the following [3]:

- Front bearing housing (i.e. between compressor and fan)
- LP/IP/HP bearing chamber of the internal gearbox (IGB)
- HP-IP bearing housing (i.e. located close to turbines)
- Tail bearing housing (i.e. at end of LP turbine)

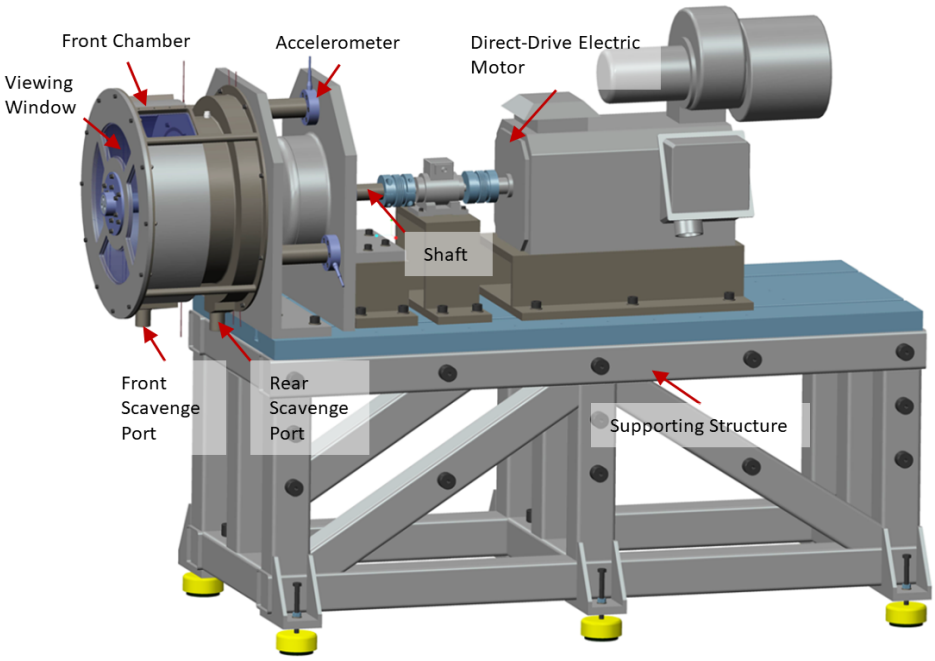
The understanding of oil shedding process is important as the location bearing is not only used in load transmission and friction reduction but also for clearance control, structural support and vibrational attenuation [3].

3.2 Rig Design & Description

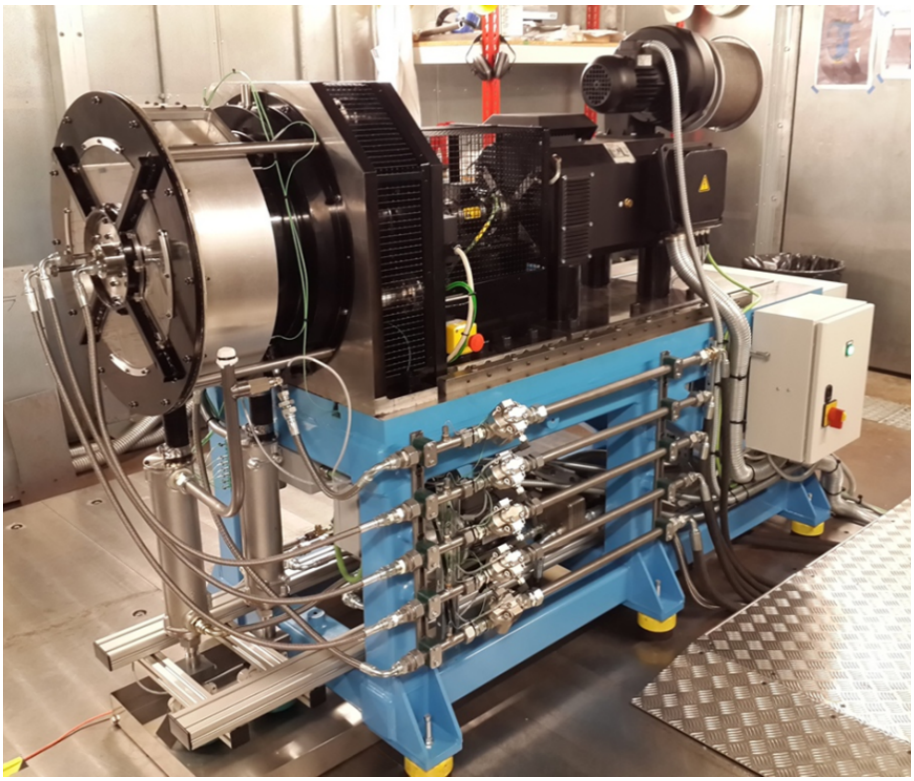
The general layout of Bearing Oil Shedding Rig is shown in Figure 3.1 and a mid-plane cross-sectional view showing detailed sub-components of the rig is shown in Figure 3.2. In this layout, the rig could be divided into two sections: driven section and working section. The working section corresponds to the region on the left, whereas, the driven section corresponds to the region on the right. The *Trent* 1000 HP-IP location bearing which is also known as test bearing is located in between both of these sections; splitting the front and rear chambers. The location bearing and main shaft are driven by a 49 kW direct-drive *OSWALD* electric motor which has a maximum attainable speed of 20,000 rpm through flexible coupling. A torque-meter is installed along the shaft to measure the torque transmitted and speed of the shaft. A brush seal is included to prevent oil leaking through the rear chamber.

In order to exert the right amount of axial load onto the test bearing to replicate a representative aero-engine conditions (i.e. achieving the right ball bearing contact angle and rolling angle), an electromagnetic actuator is employed. The actuator is capable of exerting a uni-directional axial load of 0 to 35 kN. Accelerometers were installed on the tie-bars to measure the displacement and axial force generated by the electromagnetic actuator. Additionally, accelerations were monitored consistently by the rig software *RIO* to indicate the health of the rig (mainly to avoid resonance and vibration). Minor vibrational issues due to mass imbalance were systematically rectified during the early-stages of the rig commissioning test by the engineers.

Referring to the working section, 4 optical accessible windows are located at the front face of the front chamber. They are located angularly 90 degrees from one another, 2 additional optical accessible windows are also located at the circumferential position for lighting purposes. As shown in Figure 3.2, the test bearing assembly consists of an under-race fed ball bearing with inner-race fitted onto the stub-shaft and outer-race fitted to the support housing. The cage is located in between the inner-race and outer-race designed to hold the balls together.



(a) CAD model



(b) Actual test rig

Figure 3.1: General arrangement of bearing oil shedding rig (adapted from [97])

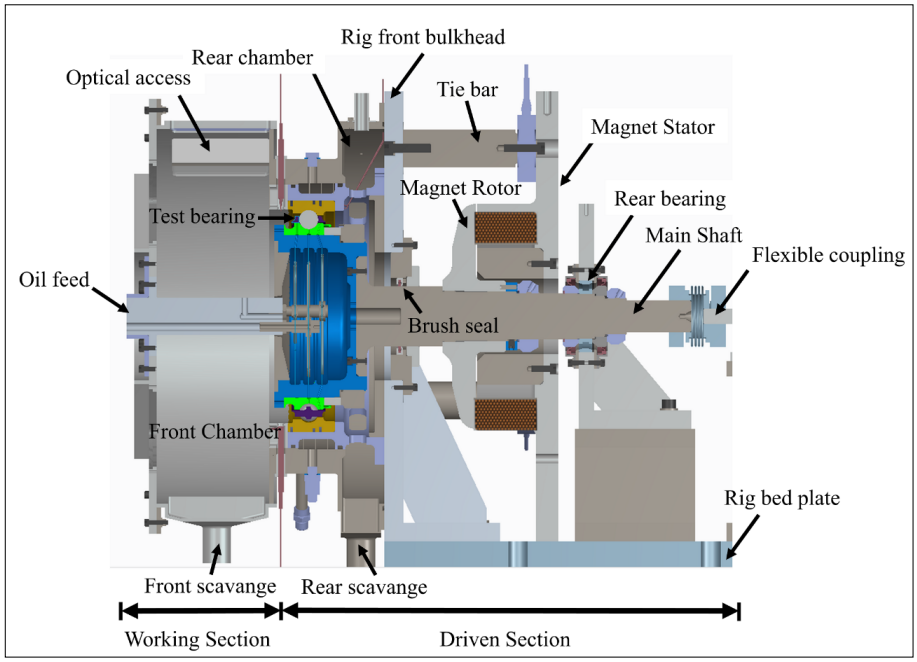


Figure 3.2: Cross-sectional view of mid-plane across bearing oil shedding rig showing various sub-components (adapted from [97])

Oil is fed to the bearing at 3 axial locations (N.B. the axial location is depth along the shaft) through a series of holes linked from an annular region. On the rig, a series of delivery tubes (also known as sprinkle) feed the lubricating oil into separate compartments (see Figure 3.4). This rig enables shaft speed, axial load and oil flow rate to be parametrically altered for different experimental conditions.

3.2.1 Oil Systems

Oil is primarily used for cooling, lubrication and corrosion protection of the bearing [3]. In an aero-engine, cooling process is needed to prevent oil degradation, thermal expansion of material and accident like oil fire could occur if they contact with hot part of the engine. The lubrication oil is also needed to reduce friction between rotating components as well as removing any debris that could damage the transmission system contributing to reduce lifespan. To supply a continuous feed of oil into the bearing, an oil system fairly similar to that of aero-engine is adopted; closed loop oil system. Oil is injected onto the grooves of the inner-race via sprinkles (known as scallops in aero-engine), it is then removed via scavenge pumps after absorbing heat from rotating elements, filtered, cooled through heat exchangers and subsequently reintroduced. The whole process is illustrated schematically in Figure 3.3 (N.B. the diagram is a simplified version of an actual complex oil system in statement of requirement report [98]).

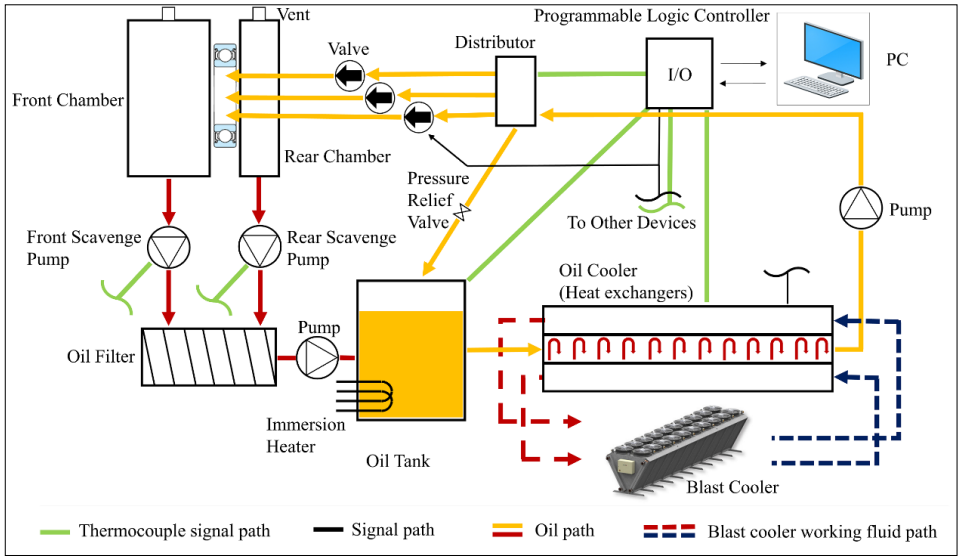


Figure 3.3: Schematic of oil system for the test rig

A 3 centistoke *Aeroshell Turbine Oil 390* (viscosity measured at 100°C) made by *Shell*^{TM} was selected for the test purposes. To achieve a controlled experiment, a feedback system was designed to control the feed pressure and temperature ensuring the right amount of oil quantity at the right temperature is fed into the bearing.

Aeroshell 390 is kept in a large reservoir tank that has an indicative level of the oil volume. The level was maintained to ensure the immersion heater is well submerged. Although it is a closed-loop system, oil could still escape via air-vent located above the front and rear bearing chambers in the form of vapours [98]. This process prevents vapours from saturating the chamber impeding optical imaging. The immersion heater is used to maintain a reasonable oil temperature in the tank to avoid solidification of oil or being highly viscous during a cold-day.

To ensure that oil is fed into the bearing at constant temperature of 35 °C, a temperature feedback system is employed. This reduces the effect of viscosity and surface tension variations that could arise from changing oil temperature which may affect the results. To regulate the temperature, temperature data were collected from scavenge pumps, tanks, heat exchangers and distributor through a series of thermocouples. At high rotational speed, a higher heat sink is needed to compensate for the dramatic rise in oil temperature in the returning tank (see Figure 3.3, oil path). This is accomplished by increasing the blast cooler and heat exchanger heat removal rate. The temperature change by oil could significantly varies between 60 to 95°C for corresponding shaft speed operating at 3000 rpm and 7000 rpm according to tests ran.

Air valves, pumps and pressure relief valves were employed to regulate the oil flow rate into the test bearing (see Section 3.2.1.2 for further details on bearing oil flow rate). The scavenge pumps

are used to extract oil from the sumps located at the front and rear of bearing chambers. They are consistently held at 50% volumetric capacity (volumetric capacity refers to the volume of oil within the measuring device), overshooting occurs during initial start-up indicating a gush of oil is ejected by the test bearing due to transient effect. The level meter also acts as an indication of the transient phenomenon such as transition in rotational speed from 3000 to 5000 rpm. As it reaches a constant value, data acquisition is performed. Another indicator of time-independent condition in the experiment is when the temperature readings on thermocouples of bearing chambers cease changing. This is usually a few minutes after changing speed, load or oil flow rate. The speed by far has the most effect on the temperature due to massive increase in heat-to-oil as churning process is enhanced. The oil filter is placed upstream of the tank to remove debris such as metallic impurities. If any anomaly in the readings of scavenge pumps is spotted, the oil filter is checked and cleaned.

3.2.1.1 Bearing Oil Feeds

One unique feature of the bearing oil shedding rig is the ability to independently feed different oil flow rate into the bearing under-race sections. This feature is not common in actual aero-engine configuration where the relative distribution of oil between different feeds is fixed with little control. The oil feed cross-sectional view is shown in Figure 3.4. In this illustration, the bearing under-race lubrication channel could be subdivided into A, B and C which corresponds to front, mid and rear section. The gutters are channel with dividers between each section to prevent axial cross-talk. Cross-talk in this context referred to oil from one designated gutter entering adjacent gutter. It was agreed in the statement of requirement (SOR) of the rig construction that oil must be delivered from static feed (i.e. sprinkle) uniformly around the circumference of the inner-race distributor. This is accomplished by having 6 feeds (sprinkles) located at each section. It was also designed that no oil migration should occurs from distributor cavity into the main chamber and therefore corrupting measurements [97].

The circumference of inner-race for front section contains 9 holes each 40° apart that linking oil from the stub-shaft gutter into the bearing. Meanwhile, the midsection contains 6 slots of each 60° apart and the rear section contains 6 slots of each 60° apart as well. These slots are built-in features made by bearing manufacturer. The inner stub-shaft or oil distributor (see blue colour geometric feature in Figure 3.4) are designed with slots to match that of bearing inner-race. In the configuration of Figure 3.4, each individual oil feed could be summarized with the following function:

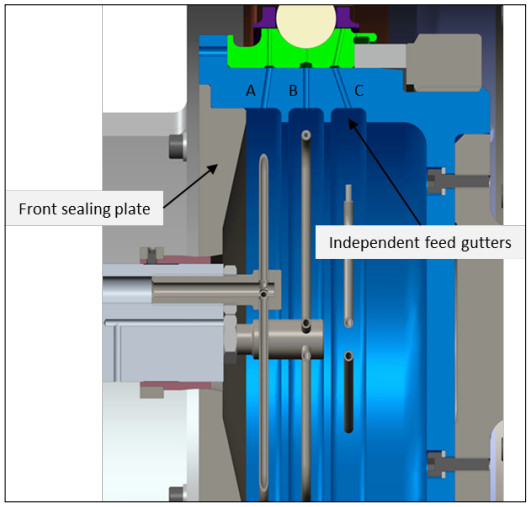


Figure 3.4: Independent oil feed system featured on the rig

- Front feed supplies oil to the front bearing cage (see Figure 3.4 label A)
- Mid feed supplies oil to the ball bearing (see Figure 3.4 label B)
- Rear feed supplies oil to the rear bearing cage (see Figure 3.4 label C)

The oil delivery system is enclosed within the cavity by 'front sealing plate' with a very minimal gap between rotating part and oil feed pipes to avoid direct contact. The performance of oil distributor was validated during rig commissioning test where it was observed that oil cross-talk occurred at below 1000 rpm. Meanwhile at 3000 rpm, minor oil splash occurs which does not adversely affecting the overall performance (negligible oil loss). Consensus was made to conduct experiment for test with speed beyond 1000 rpm [97].

3.2.1.2 Bearing Oil Flow Rates

Choosing an appropriate bearing oil flow rate is not a trivial exercise as HP location bearing does not operates below 7000 rpm in real aero-engine operating conditions. Due to current limitation of operating bearing oil shedding rig of up to 7000 rpm due to vibrational concern, further agreement on appropriate flow rates would need to be rectified for bearing operating below typical aero-engine condition (i.e. at speed of 3000, 5000 and 7000 rpm). During the rig design stage, the flowrates were chosen with the reference to values provided in Table 3.1 to fulfill the design of experiment of varying the operating condition.

Table 3.1: Shaft speeds and oil flow rates employed in experimental investigations

HP shaft speed selected for tests (rpm)	Flow rate to be used in experiments (litre/min)
3000	5.2
5000	5.2
7000	7.3

3.2.2 Axial Loading by Electromagnetic Actuator

Axial bearing load of aero-engine is important in many aspects. First, they react to compressor forward and turbine rearward load. In actual aero-engine, bearing loads are balanced by altering air in sealing elements [3]. In an unloaded situation, ball bearing could skid (i.e. ball is sliding along the surfaces instead of rolling) along the inner-race causing damages. Likewise, an overloaded ball bearing could cause significant damages as the ball deformed under high contact point load. Therefore, it is crucial to appropriately apply the axial load to match that of aero-engine operating conditions. Another important feature of axial loading is the dynamics of ball bearing which changes significantly based on the loading. In bearing oil shedding rig's SOR, it was specified that a minimum of 5 kN to a maximum 30 kN is to be applied to the bearing at all time.

There is no radial load requirement apart from the weight of the shaft itself and the centrifugal loading generated by spinning action. In the rig, an electromagnetic actuator was designed to impart the uni-directional load required with uncertainty of 6%. In this rig configuration, the load is applied such that shaft is pulled towards the rear end (i.e. direction facing the electric drive) and away from front bearing chamber. This produces the representative bearing contact and rolling angles such as one shown in Figure 3.5.

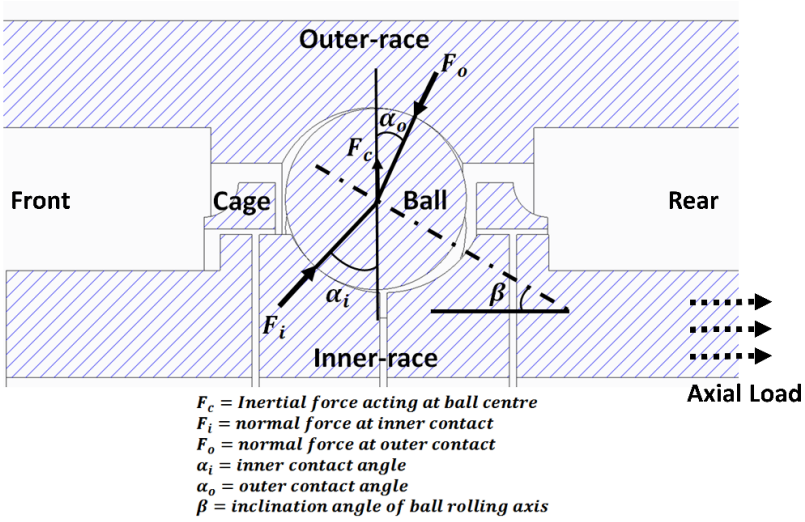


Figure 3.5: Dynamics of ball bearing under axial loading (recreated based on [93])

In this experiment, two axial loads were selected; 10 kN and 30 kN to assess the effect of changing axial load on oil film thickness. 30 kN was not being used when the bearing inner-race operates at 3000 rpm due to discrete screeching noise generated during rig commissioning test.

3.2.3 Control System of the Rig

This section describes the interface used to control the bearing oil shedding rig allowing various parametric changes to be made for different test cases. The rig control system has been coded on a stand-alone real time operating system. This system monitors and ensures the safe operation of the rig independent of operator intervention. Additional to the real time system, a number of physical emergency stop buttons (also known as E-stops) are located strategically in the rig cell and control room. Separately an executable that runs on a window PC provides user with the interface to operate the rig. The main operator interface is shown in Figure 3.6.

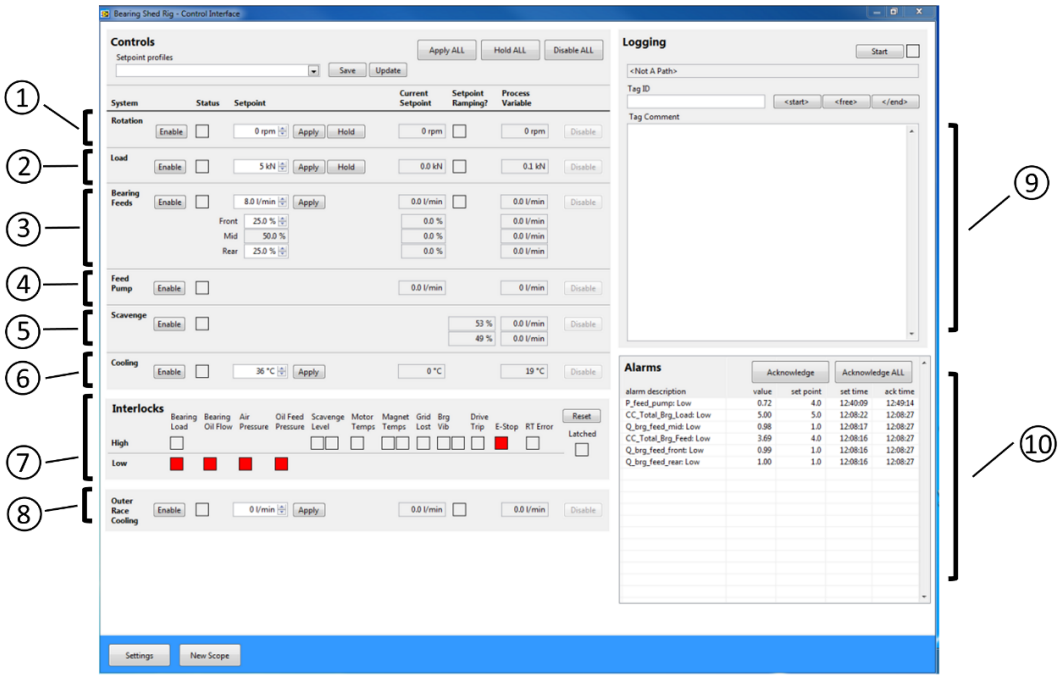


Figure 3.6: Graphical User Interface (GUI) for rig operation

In conjunction to the oil system explained in Section 3.2.1 (see Figure 3.3), the GUI provides the user with the capability of controlling the rotational speed, bearing axial load, flow rates or activate bearing outer-race cooling which is not needed at the point of the research. In the GUI, most subsections have a status indicator which when activated will flag green. The following instructions summarised the procedures for safe operation:

I. Establish stable overall oil flow across the system by enabling ④, *Feed Pump*. This is a fully automated with no control on the amount of flow rate. When activated, the oil from tank travels across the system except into the bearings.

II. Establish a bearing load by enabling ②, *Load*. A minimum of 5 kN is hard-coded into the system. And a maximum of 35 kN is limited by the software.

III. Activate the scavenge pumps by enable ⑤, *Scavenge*. The variables in the process variable column represents the level of oil volume occupying the scavenge reservoir. The oil flow rate is provided in l/min.

IV. Prior to initialising the rotation, a sufficient amount of oil must be fed into the bearings. It is hard coded as a safety feature to prevent bearings from operating in the absence of lubrication. The lubrication systems are activated by enabling ③, *Bearing feeds*. In this control section the flow rates for mid, front and rear are expressed in percentage of a total flow rate into the distributor. In most circumstances, the mid feed is fixed at 50% of the total flow rate (e.g. 50% of 5.2 l/min)

V. Activate the heat exchanger to maintain constant oil feed temperature of 35 ℃ by enabling ⑥, *Cooling*. Intervention is needed when the temperature deviates too far from the desired setpoint. A lower cooling value increases the blast cooler rate of heat removal.

VI. Upon activating all main features in *I, II, III, IV and V*. The physical interlock or E-stops must be reset in all locations to enable the rotation. The rotation could only be activated once all indicators in GUI diminished (see Figure 3.6 – Interlocks ■), this is accomplished by entering a desired setpoint (i.e., 3000 rpm) in speed column as well as enabling ①, *Rotation*.

VII. In most cases, outer-race cooling is not needed ⑧. During operation, alarms could flag in ⑩, *Alarms* which need to be resolved to avoid rig from shutting down.

Apart from the above description of rig operation procedures on the main GUI, a secondary data interface provides readings of sensors on scavenge flow rate, oil feed, test bearing temperature. It also provides real-time conditions of the rig health in temperature as well as vibrational values. These are illustrated in Figure 3.7.

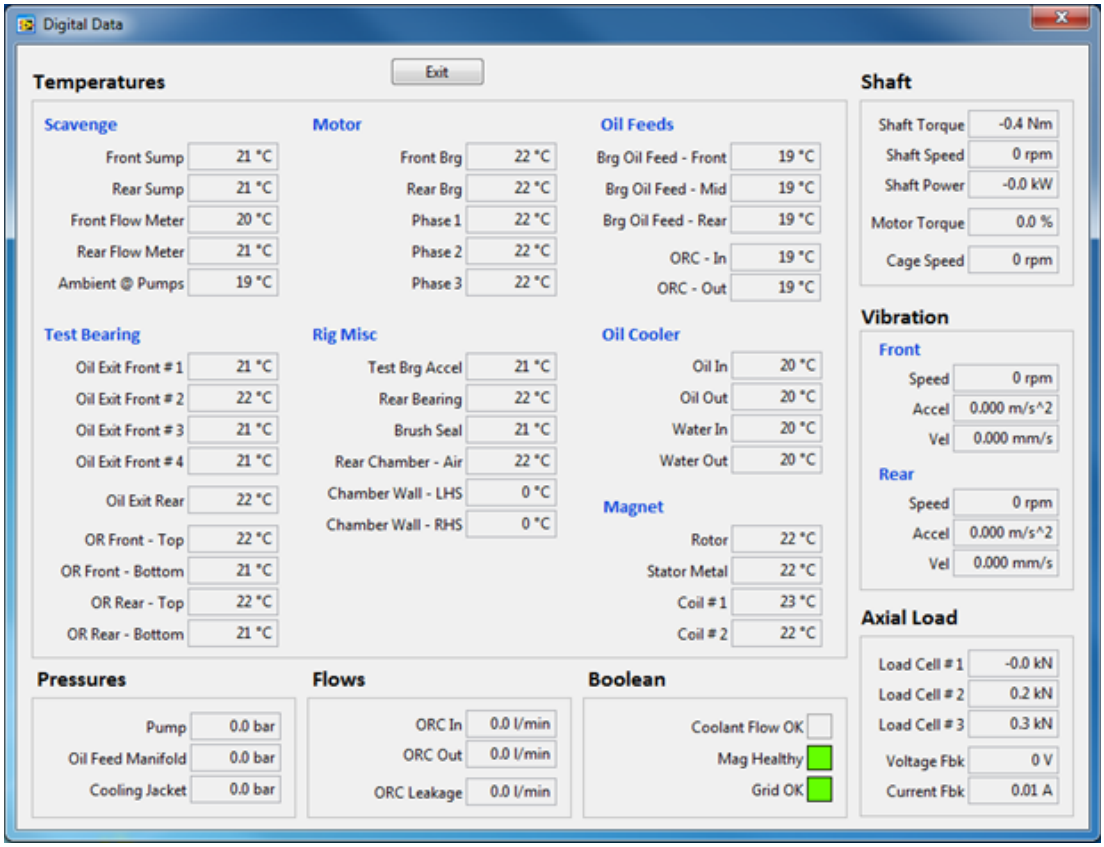


Figure 3.7: Full digital listing window

3.2.4 Rig Instrumentations

To support the safe operation of the rig, an amount of instrumentations are permanently embedded into the rig. The values from all sensors are logged for potential post-processing in the future. The corresponding sensors' log values are similar to the one described in Figure 3.6 and Figure 3.7. A diagram showing the location and type of instrumentation embedded into the rig is shown in Figure 3.8.

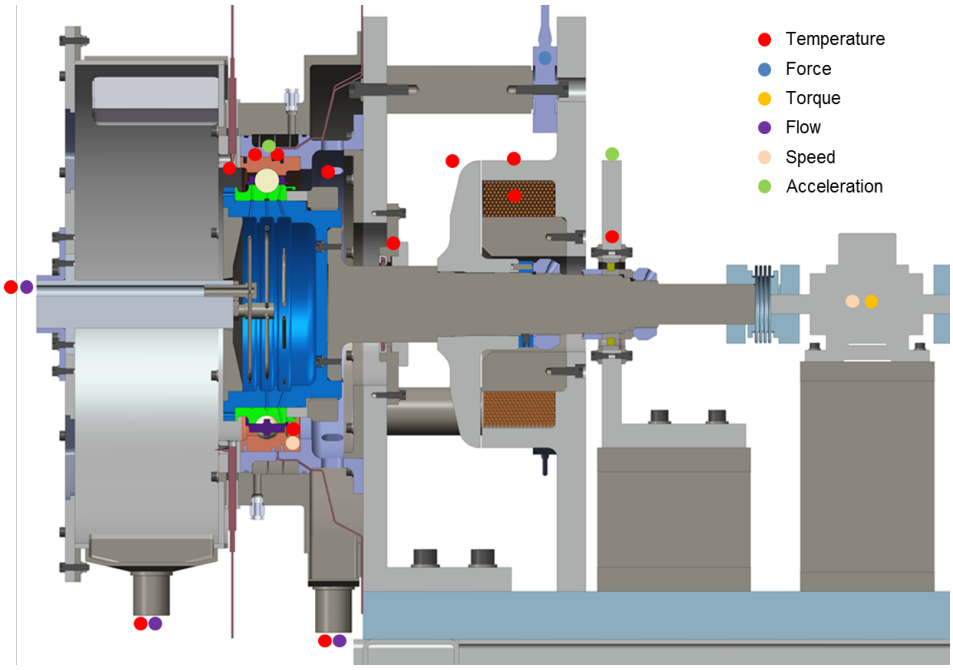


Figure 3.8: Location and type of instruments embedded into the rig (Adapted from [97])
● Temperature, ● Force, ● Torque, ● Flow, ● Speed, ● Acceleration

3.2.5 Proposed Measurements

Measurements are crucial to meet the test objectives. There are three main test objectives laid to meet the research objectives. These include the following derived from SOR:

- Task 5.4.1.2: Video Imaging (low speed & high speed) of oil exiting the test bearing over a range of operating conditions
- Task 5.4.1.3: Quantitative data to characterise the oil shedding process over a range of operating conditions
- Task 5.4.1.4: Video Imaging (low speed & high speed) of oil films formed by bearing oil shed on the walls of a typical bearing chamber containment over a range of operating conditions

The intent was to make these observations and measurements as close to the bearing exit as possible, as indicated by Figure 3.9. The following measurement techniques would be applied:

✓ Conducted

1. Visualisation
    - High speed & low speed video imaging ✓
    - Frozen still images ✓
2. Film thickness
    - Optical technique ✓

In this thesis optical technique will be used to obtain film thickness data, other techiques (e.g. capacitive sensor, ultrasonic sensor and laser confocal displacement sensor) are possible but require significant changes to the rig to implement the methods. Detailed explanations of the optical film measurement technique are presented in Chapter 4.

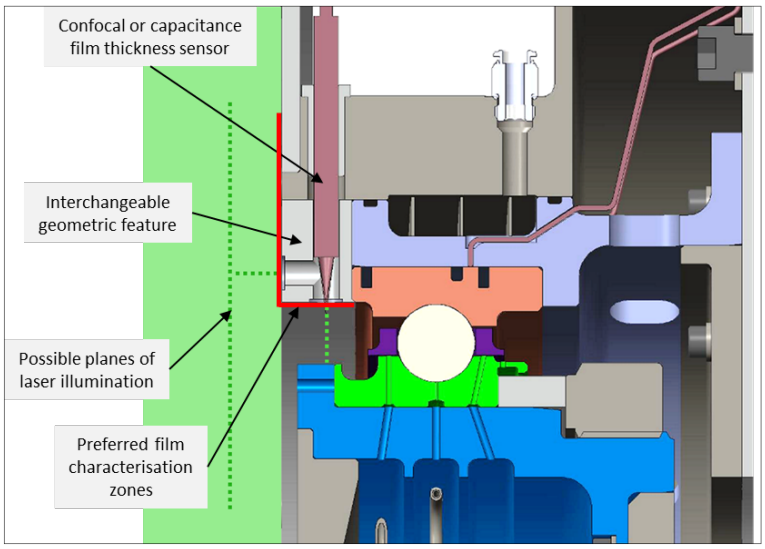


Figure 3.9: Proposed measurement options (Adapted from [97])

Referring to Figure 3.9, the probe insertion region is not used. The preferred film characterisation zones are highlighted as shown and it is the location in which the film thickness is measured and where wave structures are analysed.

3.3 Summary of Test Rig for Trent 1000 Aero-Engine Ball Bearing

The experimental test facility for the investigations of oil shedding from a *Trent* 1000 aero-engine ball bearing is presented. The operating speeds are needed to assess the effect of shaft speed on oil breakup and the shearing effect that drives the oil film. The speeds are quantified as 1000 to 7000 rpm reflecting existing capability due to issue with vibrations. Recommissioning is proposed to rectify the issue and to bring the speed to beyond 7000 rpm for future studies.

For oil flow rates, 5.2 lpm and 7.3 lpm are chosen for assessing the effect of oil flow rates on the oil shedding process and the dynamics of thin film on the containment wall. Subsequently, the axial bearing loadings necessary for producing the representative aero-engine ball bearing contact angle (α) and rolling angle (β) are given as 10 kN and 30 kN respectively. It allows the assessment of the effect of loads on the oil shedding and thin film. From preliminary commissioning test, 30 kN was not recommended for 3000 rpm due to discrete screeching noise generated from the bearing.

From the rig instrumentation available, consensus was made that data acquisitions are to be taken when steady-state feature is achieved. This should be corresponded to the time when volumetric reading of the sump and thermocouples stop changing. A list of test objectives was given which includes high-speed imaging over a range of operating conditions and film thickness measurement. The optical technique for film thickness measurement introduced is new and differs with that of capacitive and ultrasonic methods in the literature. The techniques and results of the experiments will be discussed in details in Chapter 4.

Chapter 4 High Speed Imaging

In this chapter, high speed imaging is used in the visualisation of oil disintegration mechanisms at the orbiting cage of an aero-engine ball bearing. The formation of thin film on the surfaces of the bearing containment is also visualised. Comparison between two types of optical imaging lenses were made in terms of their ability to spatially-resolve the flow features which include direct-drops, ligaments, oil sheet and oil films. Subsequently, the need for different plane of imaging and angular position are explained. A new optical-based image-processing method was developed to measure the film thickness at co-current and counter-current sides in order to assess the effect of gravity on the film profile. Assessments were also made by changing the operating conditions, namely, shaft speed, oil flow rate and axial load. The existence of different regimes of oil breakup were investigated and compared with that of rotary atomiser based on only changing the operating speed. Based on the notion that the mechanisms of oil breakup at aero-engine ball bearing is fairly similar to that of rotary atomiser, preliminary dimensional analysis is made to assess if dynamic similarity exists. Dimensional analysis of ligament number was also made and is compared with classical studies available in the literature. This is presented along with the studies of wave structures of the film on surfaces close to the ball bearing. The determination of wavelength and wave frequency were made to confirm the existence of different wave spectra, namely, gravity-capillary and capillary waves.

4.1 Introduction

High speed imaging is an image acquisition technique that allows a subject moving at high speed to be captured at a high frame rate and therefore allowing more details to be analysed. These flow features are usually moving at a velocity scale too fast to be perceived by the naked eye viewing from inertial frame of reference. The main differences between the high speed camera and conventional camera are frame rate, shutter speed and light sensitivity (e.g. due to discrete pixel size). Another terminology commonly used interchangeably throughout this thesis for frame rate and shutter speed is frequency and exposure time. (N.B. exposure and exposure time have different meaning, exposure is the amount of light per unit area, whereas exposure time is the time in which the sensor is exposed to light). A comparison of high speed camera and conventional (i.e. *IDT Vision* Os4v3 versus *Canon* EOS-1D X Mark II) are given in Table 4.1:

Table 4.1: Comparison between high-speed camera and conventional camera

	***IDT Vision* Os4v3-S3**	***Canon* EOS-1D X Mark II (Not used)**
Camera body		
Frequency	6000 fps	14 fps / 120 fps (at full HD)
Maximum resolution	1024×1024 (~1.0 megapixels)	5472×3648 (~20.2 megapixels)
ISO sensitivity	6000 ISO mono	Auto 100 – 51200
Sensor size	14.0×14.0 mm	36.0×24.0 mm
Discrete pixel size	$13.68 \times 13.68\ \mu m$	$6.58 \times 6.58\ \mu m$
Exposure time	$1\ \mu s$ (min)	$125\ \mu$s or $(1/8000$ s)

IDT camera is selected due to the following reasoning:

- *IDT's* frequency $\gg$ *Canon's* frequency (6000 FPS vs 120 FPS)
- *IDT's* exposure time $\ll$ *Canon's* exposure time ($1\ \mu s$ vs $125\ \mu s$)
- *IDT's* pixel size $\gg$ *Canon's* pixel size ($13.68\ \mu m$ vs $6.58\ \mu s$)

The list of acronym can be referred in Nomenclature

Remarks: The maximum resolution *IDT* camera of 1 megapixels is sufficient to cover the region of interest for the test purposes. *IDT's* ISO sensitivity of 6000 is reasonable due to larger discrete pixel size. Higher ISO sensitivity is not needed which could increase noise level.

Next sections explain the principles of high speed imaging, theory of optics and the type of lens used in different situations.

4.1.1 Principle of Imaging I – Resolution & Frequency

Os4v3 is a compact camera manufactured by *IDT Vision*, it uses a complementary metal oxide semiconductor (CMOS) image sensor to convert light into electrical signal. This monochromatic camera has a maximum image resolution of 1024×1024 pixels. Resolution in broad term can be expressed as the total number of pixel in a sensor, subsequently in later Section

4.1.6, another 'class' of resolution known as "optical resolution" will be explained in detail to avoid ambiguity. The "optical resolution" term is known as the smallest detail in which the sensor could spatially-resolves (i.e. detecting the size of an atomic structure of 10 nanometres in width as compared to detecting the size of droplet at 10 microns in diameter).

In this section, image resolution could be decomposed into two directions; vertical resolution and horizontal resolution which corresponds to dimensionless unit of pixel. The ratio of the image resolution is also known as aspect ratio (i.e. width to height of an image). At full resolution of 1 megapixel or 1024×1024 pixels, the sensor is capable of operating at frequency of 6000 fps. This setting is useful for capturing images of the oil film moving on the outer-race of the ball bearing due to relatively low film velocity. However, to capture ligaments and oil sheets that possess a much greater velocity due to centrifugal action, a higher frame rate setting is needed. A higher frame rate could be obtained by compensating the image resolution size in pixel (either horizontally, vertically or both). This reduces the computing demand on the processor allowing a magnitude increase in frame rate. The image resolution settings employed for high speed imaging are tabulated in Table 4.2 and an example of the reduced region of interest (ROI) to increase the frame rate is shown in Figure 4.1.

Table 4.2: Details of image settings employed for high speed imaging

Settings	Units	Value
Image resolution	Pixel	1024×1024
		1024×372
Frame rate	fps	6000 (corresponding to 1024×1024 pixels)
		16200 (corresponding to 1024×372 pixels)
Exposure time	μs	$6 - 10$

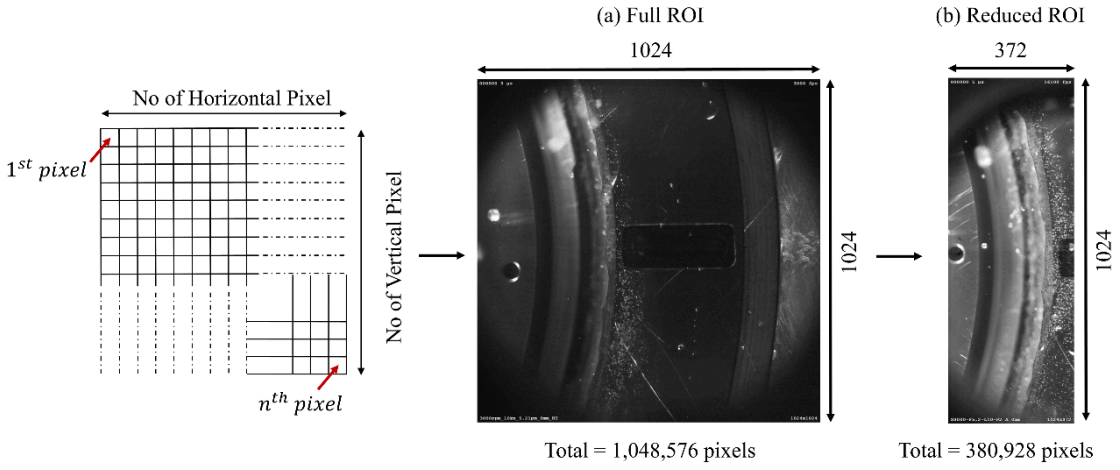


Figure 4.1 Image resolution showing reducing size in horizontal pixel yielding smaller image but higher frame rate

In the Figure 4.1, the first image showing a grid of horizontal pixel times vertical pixel. As it is impossible to show the grid size of 1 million pixels, a simplified version is shown. The first sub-grid region labelled '1st pixel' is the index of first pixel and subsequently the last in the global grid represents the final 'nth pixel' which in this case is pixel number 1,048,576. The subsequent two images showing full resolution and reduced ROI for increase in frame rate.

4.1.2 Principle of Imaging II – Field of View & Focal Length

In bearing oil shedding experiments, two type of lenses were employed. The first is a standard 60 mm f/2.8D *Nikon™ Nikkor* lens and the second is *Questar* long distance microscope. In this research context, images acquired by the former lens will be identified as "HS". Whereas, images acquired by the latter will be denoted as "LDM-HS". The functionality of both lenses will be discussed based on the basic theory of optics. In optics, lenses are used to focus and deflect beams of light. The most common type of lenses available are concave and convex lens. To focus an image onto a sensor of a high speed camera, the camera body is mounted with a lens between the sensor plane of focus and the object at a distance away. These lenses usually contain a multiple array of discrete lens arranged internally (i.e. concave, convex or both) such that light is directed in the best possible manner.

For simplification, we will refer all these lenses as a single system or camera lens in upcoming part of the thesis. For a standard zoom lens (*Nikon™*) such as the one mentioned earlier, the rated focal length, f of 60 mm implies that lens mechanisms has a maximum focal length of 60 mm. In most circumstances, these lenses will also have a minimum working distance associated for which the object remaines in focus. For this given lens, the minimum working distance is quoted as 220 mm by the manufacturer. An illustration of the concept of field of view, focal length and magnification factor in the research context is given in Figure 4.2.

Based on the illustration of minimum working distance, if the real object (i.e. the word ABC) is placed at 100 mm object distance away from the lens (which is less than the rated working distance of 220 mm or u_o), the sensor will cast a blurry image (or word) as if it fell out of the plane of focus. Another important principle of optics is the relation between viewing angle or field of view (FOV) with respect to focal length (f).

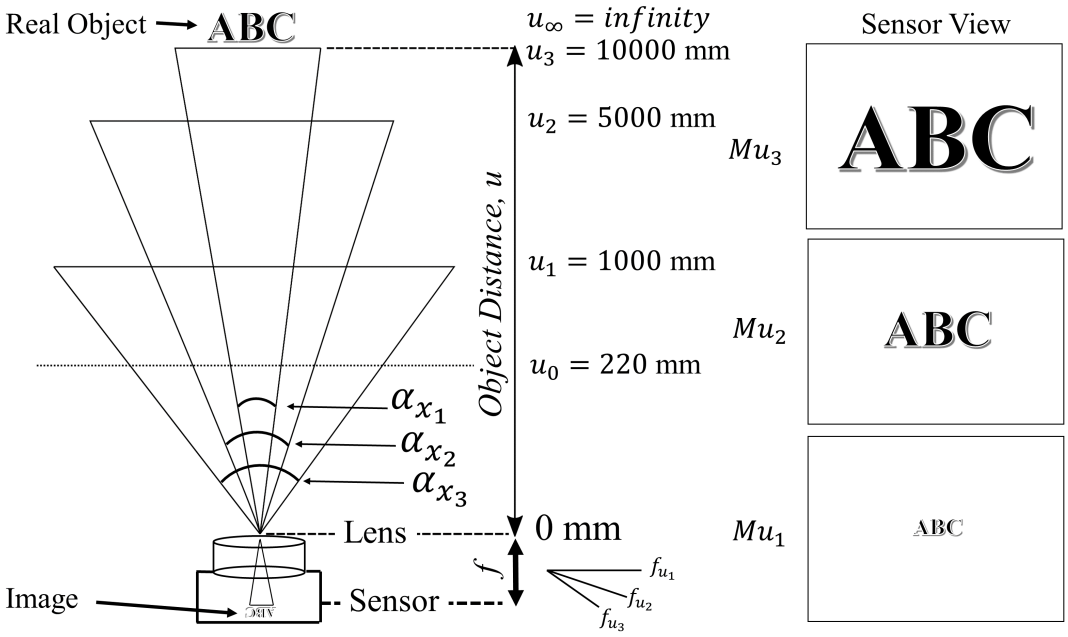


Figure 4.2: Concept of field of view, focal length and magnification. (Recreated based on *Nikon*^{TM} information [99])

As the focal length for lens is ranged from a minimum of 15 mm (quoted by manufacturer) to a maximum of 60 mm (as limited by the lens mechanism), the focal length in this example could be specified as arbitrary constants of f_{u_1}, f_{u_2} and f_{u_3} which corresponded to object distance of u_1, u_2 and u_3. In the example shown in Figure 4.2, the real object remains at its static position of 10000 mm object distance away from the lens. As the focal length is increased from f_{u_1} to f_{u_3}, the FOV captured reduces greatly which gives a magnified image (see sensor view M_{u_3} in Figure 4.2). Vice versa, when a larger viewing angle is used (i.e. FOV); a less magnified image is cast onto the sensor as shown in M_{u_1} of Figure 4.2. The optical magnification offered by both lenses will be further justified in which circumstances one lens is preferred over the other in Section 4.1.6.

4.1.3 Principle of Imaging III – Exposure Time & Aperture

Obtaining the correct combination of exposure time, aperture and frequency is not a trivial task when it comes to bearing chamber imaging. First, the environment lacks light due to confined space and intricate geometry. Secondly, the object in focus is moving very fast which forces the exposure time to be as short as possible. Setting a low exposure time limits the light receiving capacity producing dimmer image. Hence, setting the exposure time, aperture and

frequency is crucial in order to obtain a good image quality with low digital noise. Exposure time which is commonly known as shutter speed is the time in which the CMOS sensor is exposed to light. The shorter the shutter speed the darker the image [100]. However, it is important that a short shutter speed is used to freeze the fast moving object such as droplets and ligaments that were emitted from the bearing. The low light condition is compensated by maximising the aperture size or reducing the f-number (another term interchangeably) [101]. Sample images showing the effect of changing shutter speed and f-number are given in Figure 4.3 and Figure 4.4 respectively.

In the setting of Figure 4.3, a low exposure time 1/120 of a second freezes the light of individual ferries wheel's spokes. And with a higher exposure time such as 4 seconds, a bright image was captured with spokes occupying the whole ferries wheel not representing the real feature of the rotating object. Based on Figure 4.4, a larger aperture enables more light to enter the sensor and hence producing brighter image with a shallow depth of field. Whereas, a small aperture results in so-called 'underexposed image' with a wide depth of field [101].

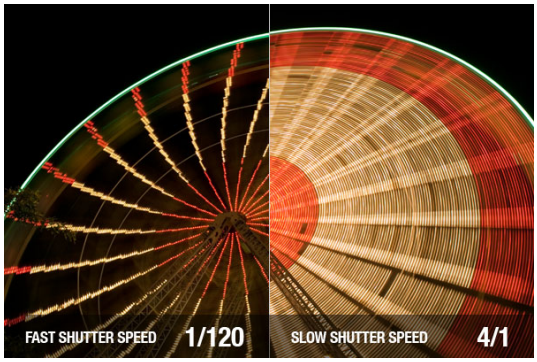


Figure 4.3: Effect of shutter speed on Ferris wheel at night [102]



Figure 4.4: Sample images corresponding to different f-number/aperture at night time [103]

4.1.4 Principle of Imaging IV – Illumination

One of the important principles of imaging is illumination. The bearing oil shedding rig operates in an enclosed chamber limiting the amount of light reaching the subject. To obtain a good quality image, a sufficient amount of light intensity is needed. This is accomplished by supplying artificial light into the region of interest. In this experiment, the light is provided by coherent light emitting diodes (LEDs) attached around different viewing windows via a multi-degree of freedom articulated arm. The LEDs brand is *Veritas Consetallation 120E* which 12700 lumens of continuous light and with strobe setting, 22000 lumens of light intensity is achievable for short pulse of 2 μs. In this example, continuous light setting is used as it provides a sufficient amount of light needed to characterise oil breakup as well as producing decent quality image for measuring film thickness. The details description of how images are used for film thickness measurement is given in Section 4.2.

An example of light setup is shown in Figure 4.5. The LEDs are synchronised with the high speed camera using sync-in port that accepts an incoming pulse from the camera. A daisy-chain was established across multiple luminaries via sync-out ports. These allowed lights to reach from different angles. The advantages of LEDs are prolonged operational time and low heat generation compared to conventional halogen-power lamps.

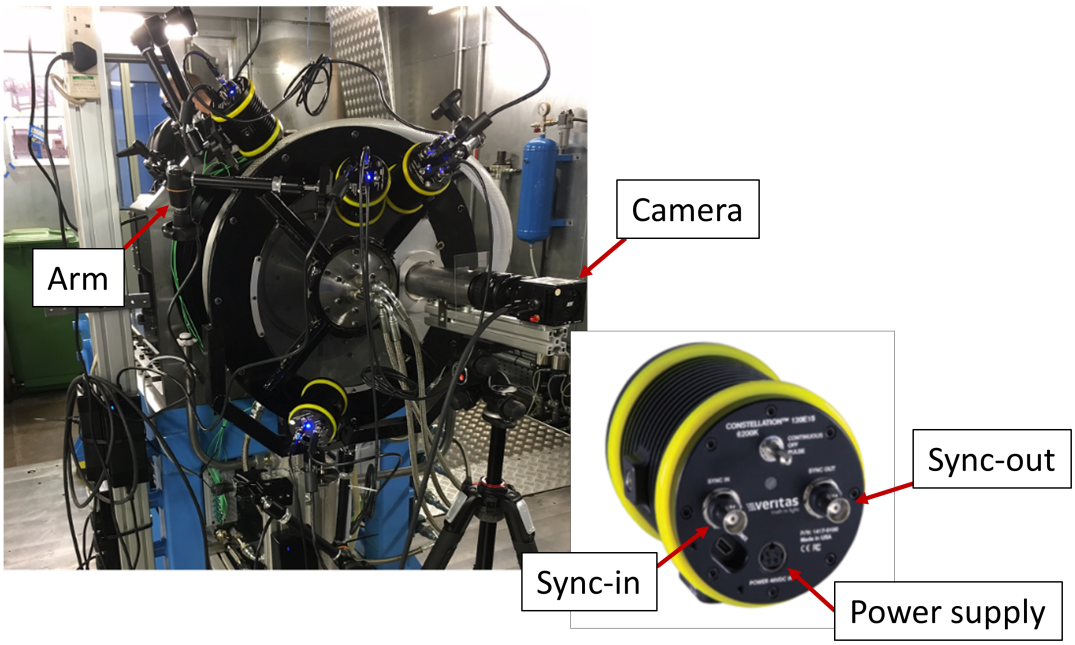


Figure 4.5: LEDs illumination for experimental campaign on bearing oil shedding rig

4.1.5 Long Distance Microscope

As portraits by its name, long distance microscope (LDM) is a type of "astronomical" lens that has a similar mechanical property as optical microscope which allows a very high magnification. However, this class of 'microscope' is capable of working at a very long distance of greater than 56 cm unlike conventional microscope which normally operates at less than 10 cm away from the specimen. This application is extremely useful for looking at object that is hazardous, an example is characterising the dynamics of oil film in bearing chamber at far away (see Figure 4.6). In addition to the incredibly high magnification and further working distance, the depth of field is also remarkably shallow allowing object close to the subject plane of focus to be omitted.

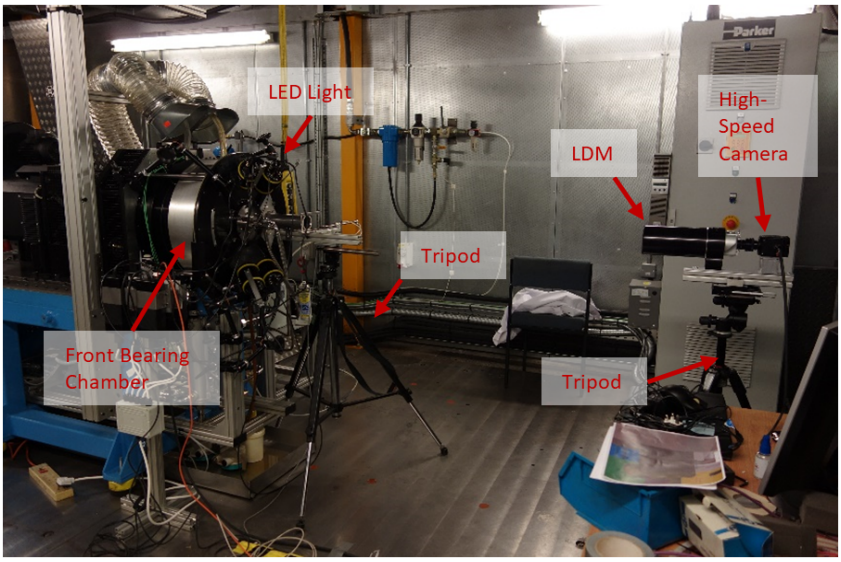
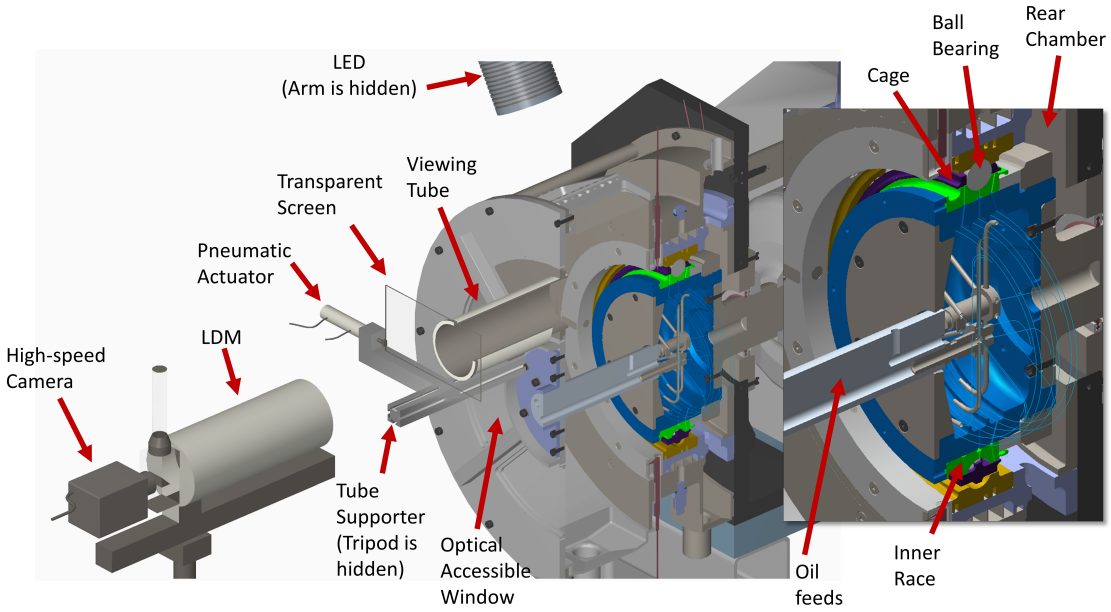


Figure 4.6: Long distance microscope *QM-1* being setup for imaging

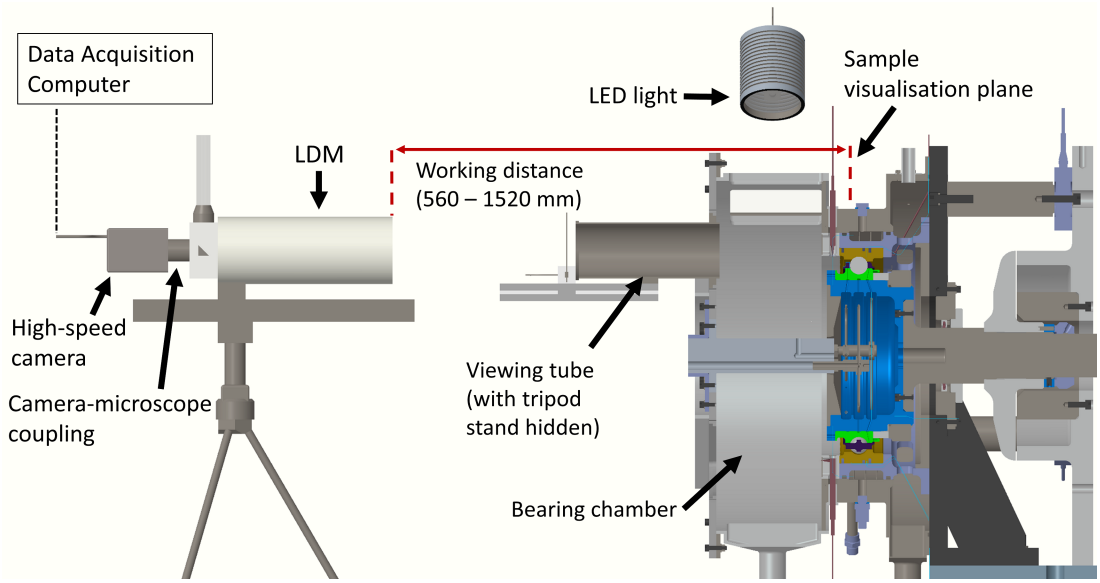
4.1.5.1 Setup for Coupled LDM-HS

This section describes the setup of LDM-HS for capturing the images of oil shedding from an aero-engine ball bearing. A schematic of LDM-HS is shown in Figure 4.7, the high speed camera is coupled with LDM via a mounting adapter and is positioned at a working distance away from the plane of visualisation. As specified by *Questar* (the manufacturer of LDM), the working distance is ranged from 560 mm to 1520 mm capable of producing optical resolution of 3 μm to 12 μm. The optical resolution as coined in Section 4.1.1 is known as the smallest scale detectable. For the minimum working distance of 560 mm, the smallest size detectable is 3 μm. The LDM-

HS is attached on a longitudinal traversing platform adjustable via a micrometre screw knob, this platform has a range of 0 to 50 mm with incremental adjustable step of 0.5 mm. For moving the LDM-HS in larger increment, the tripod could be moved in horizontal position. To ease longitudinal adjustment and helps minimises parallax error a guiding rail should be constructed in the future. The tripod also enables height to be adjusted accordingly. A meniscus spirit level is used to check the tilt level of LDM. The high speed camera is connected to a 19-Pin signal hub for lighting synchronisation and subsequently connected to the PC via Ethernet cable.



(a) Isometric view of the setup



(b) Side view of the setup

Figure 4.7: Schematic of experimental setup for LDM-HS

In Figure 4.7a, it can be seen that LDM-HS is positioned coaxially with axis-centre of the ball bearing at 12 O'clock position as the cross-sectional view passes through the mid-plane of the CAD model test rig (for illustration purposes). To ensure perfect alignment, the viewing tube is positioned based on the desired angular position that images are taken (see the arrow ➞ with label Viewing Tube in Figure 4.7a).

The inserted viewing tube is flush mounted to the surface of the optically accessible port with a rubber seal in between the gap, the sealing prevents air from leaking into the chamber which could adversely affecting the pressure and velocity field. Additionally, there are vent ports located at the top of the front and rear chamber which are exhausted to the atmosphere, hence, ensuring pressure balance. Since the tube is far away from the immediate oil exit of the bearing, the impact is expected to be minimal and insufficient to affect the flow close to the ball bearing. The support for the viewing tube and traversing platform was provided by a tripod rested onto the ground. The viewing tube was custom made with a diameter of approximately 65 mm to ensure that the region of interest is well-captured by the camera. Subsequently, an illustration of how focus calibration is completed is depicted in Figure 4.8.

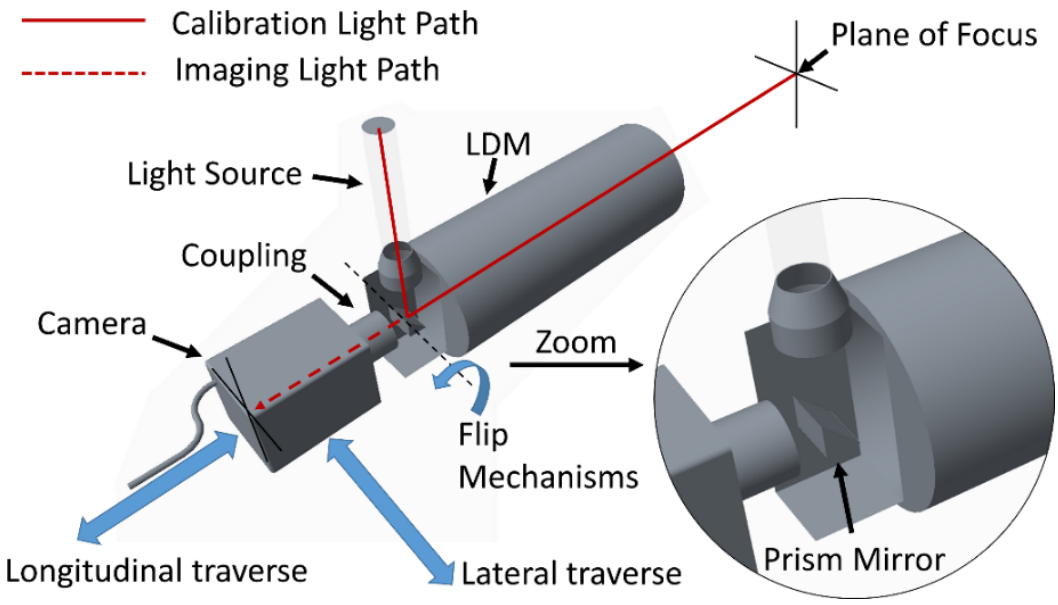


Figure 4.8: Focus calibration for LDM-HS

To ensure the visualisation plane is in focus, a light source (i.e. torch) is coupled at the port perpendicular to the LDM body. The prism actuation knob is switched such that light is reflected 90 degrees by the prism and focuses onto the plane of focus (see label ▬ Calibration Light Path on Figure 4.8). When light with sharp 'o' shape is seen at the plane of focus, the prism mirror

actuation knob is flipped such that light is redirected towards the sensor as denoted by dash-line (see label ---- Imaging Light Path on Figure 4.8). Prior to carrying out any experiments, the calibrated position is examined qualitatively by connecting the camera directly to a portable laptop to check the quality of image. Once satisfied, the connection is re-established to the image acquisition PC situated in the control room.

4.1.6 Comparison of Optical Resolution for HS & LDM-HS

As mentioned in Section 4.1.5, employing LDM enables a higher magnification within a very small area ($\sim 1\ cm^2$). A comparison of the image resolution in millimetre for HS against LDM-HS is given in Figure 4.9. In this comparison the image taken by a standard zoom lens (60 mm f/2.8D *Nikon*^{TM} *Nikkor*) is measured as 111.7 mm × 40.5 mm. Any attempt at higher magnification is not possible due to maximum focal length of 60 mm. To increase the magnification, LDM is used which enhanced the optical resolution as shown in Figure 4.9. The optical resolution can be calculated based on the following expression (4.1):

$$\text{Optical Resolution} = \frac{\text{Field of View (mm)}}{\text{Number of Pixel } (-)} \tag{4.1}$$

Details as to how the above image resolution (or field of view) in millimetre is obtained from dimensionless pixel value are shown in Section 4.2.5, spatial calibration.

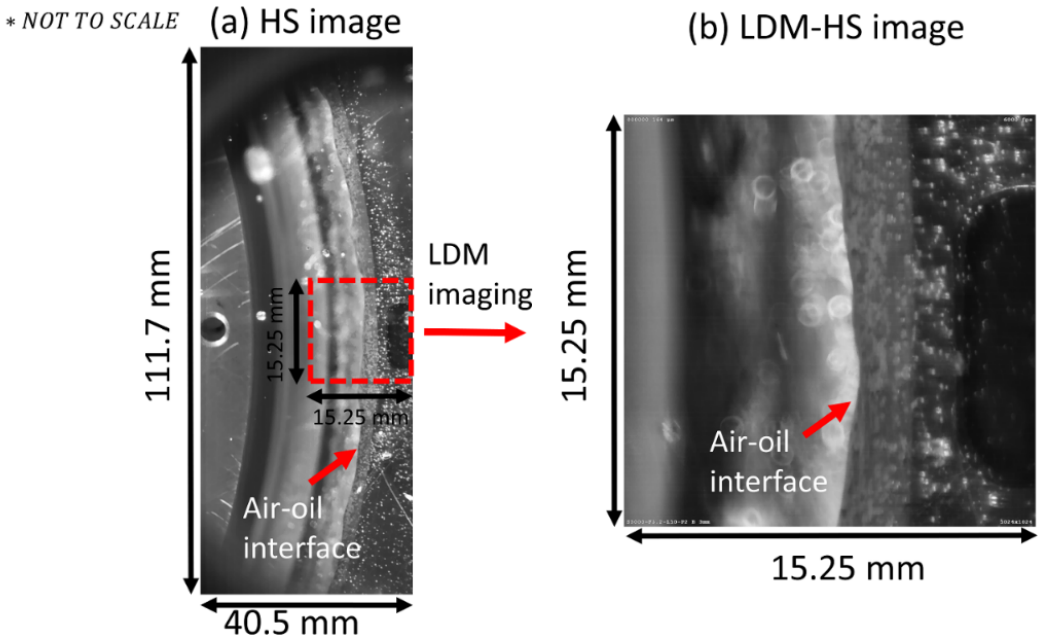
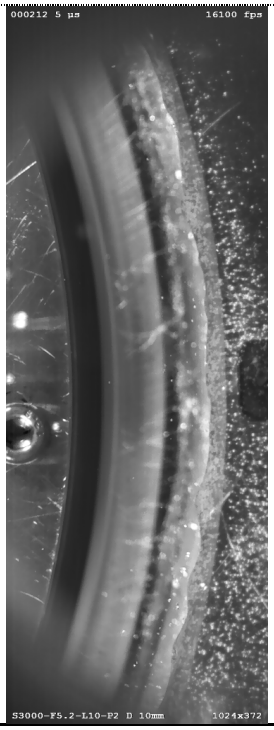
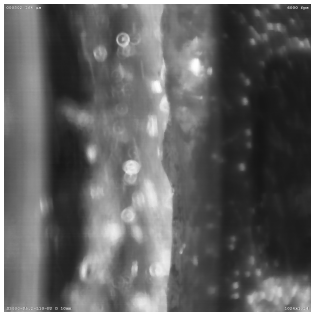


Figure 4.9: Comparison of image resolution (in mm) taken by HS and LDM-HS

The following Table 4.3 summarises the optical resolution obtained based on pixel density and FOV:

Table 4.3: Comparison between resolution of images taken by HS and LDM-HS

Description	**HS**	**LDM-HS**
Horizontal pixel	372	1024
Horizontal length	40.5 mm	15.25 mm
Optical resolution	108 μm/pixel	14.9 μm/pixel
Type*		

*Not to scale

Based on Table 4.3, it is possible to conclude that LDM-HS has a much higher optical magnification with optical resolution of 14.9 μm/pixel. Hence, making LDM-HS 7.2 times more sensitive to detecting smaller objects. This effectively reduces the error of film thickness measurement as missing one pixel is equivalent to an error of 0.0149 mm. Whereas, missing a single pixel in HS imaging could led to overestimation or underestimation of film thickness by 0.108 mm.

4.1.7 Acquisition Position of High Speed Imaging

There are two important positioning needed to capture the flow features in oil shedding process, the first is angular position of the front face and the second is axial position along the depth of the ball bearing. Details explanations are described as follow in Section 4.1.7.1 and Section 4.1.7.2.

4.1.7.1 Angular Positioning – θ / PX

The classification of different angular positions are necessary to examine different flow features occurring in the oil shedding process. These flow features include the effect of gravity on oil film in co-current and counter-current side justified the need of having images taken at different angular positions. Therefore, high speed images were acquired at four different angular positions, namely, 0°, 90°, 180°, and 270°. Notations were given for angular positions that corresponded to 0°, 90°, 180°, and 270° as P1, P2, P3 and P4 respectively. The reference datum for angular position in the experiment is set at 0° or P1. An illustration of the proposed angular positions is given in Figure 4.10.

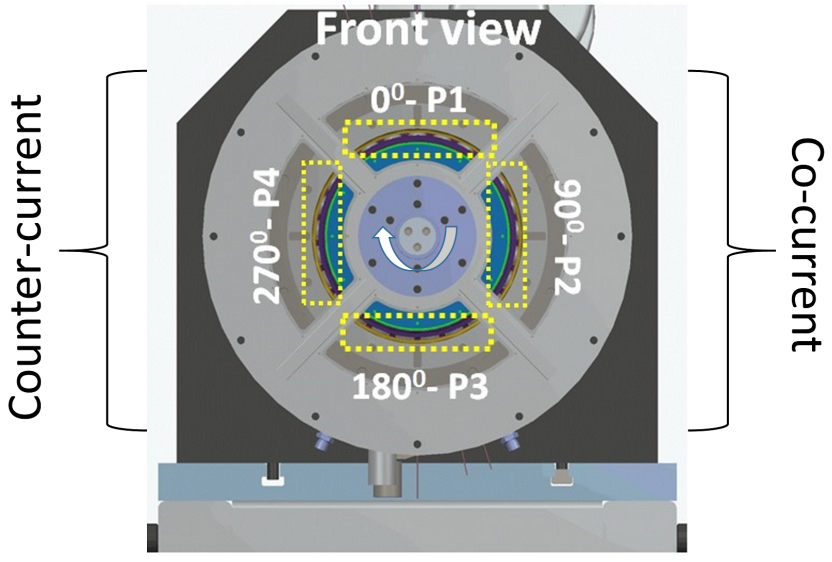


Figure 4.10: Schematic of front view of bearing oil shedding rig depicting 4 angular positions based on clockwise rotation (P1 - **0**°, P2 - **90**°, P3 - **180**°, P4 - **270**°)

4.1.7.2 Axial Positioning

Apart from understanding the flow features in two-dimensional view of the angular position, image acquisition and measurements were also made at different axial plane of focus to examine oil flow at different depth relative to the front face of the rig. These include looking at oil flow very close to the ball bearing, cage or far away from rotating elements (i.e. closer to front chamber). An illustration of the discussed axial plane of measurements is shown by the cross-sectional view of the bearing in Figure 4.11.

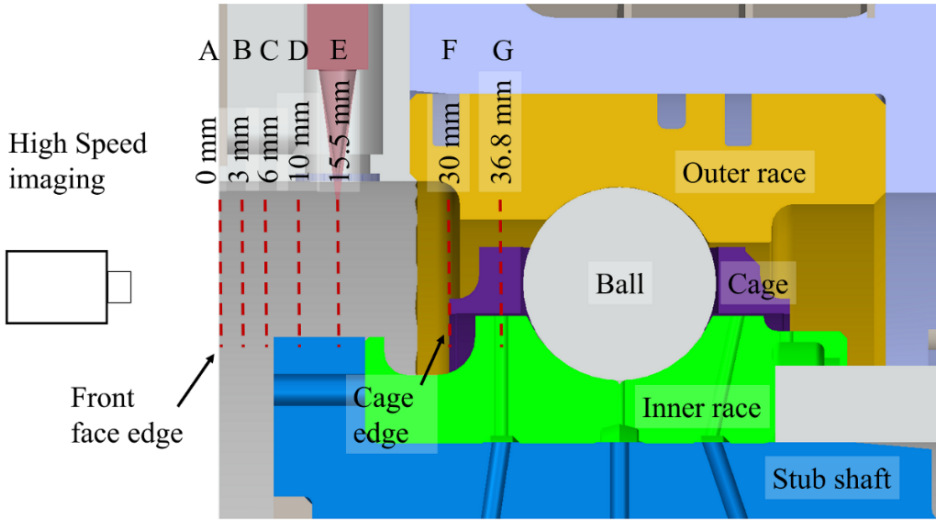


Figure 4.11: Cross-sectional view of the ball bearing showing axial planes of focus for image acquisition from A to G

In the cross-sectional view of Figure 4.11. A total of 7 axial planes of focus are classified from A to G which corresponded to 0 mm to 36.8 mm respectively. The plane of focus in which image acquisition is taken is firstly referenced to datum plane (A --- 0 mm). This plane represents the outermost location of the rotating parts of the bearing assembly which coincide with the first entry point into the front bearing chamber. Another terminology of 'A --- 0 mm' is '→ Front face edge' (see Figure 4.11). By moving 15.5 mm inwards, plane of measurement 'E --- 15.5 mm' is reached which coincide with the probe insertion. Whereas at 'F --- 30 mm', the cage edge is in focus which will enable images of ligament and sheet breakup to be captured. In 'G --- 36.8 mm', the oil flow through the ball could be observed.

The best illustration for the proposed plane of focuses mentioned earlier and the need for these axial plane of measurements (to understand the flow inside the ball bearing) is by providing real images acquired at the respective locations. The images that were captured from the proposed

locations are shown in Figure 4.12 and Figure 4.13. In Figure 4.12, the instantaneous HS image at angular position P2 ($\theta = 90°$) at axial plane A, D, F and G without oil flow and rotation are shown.

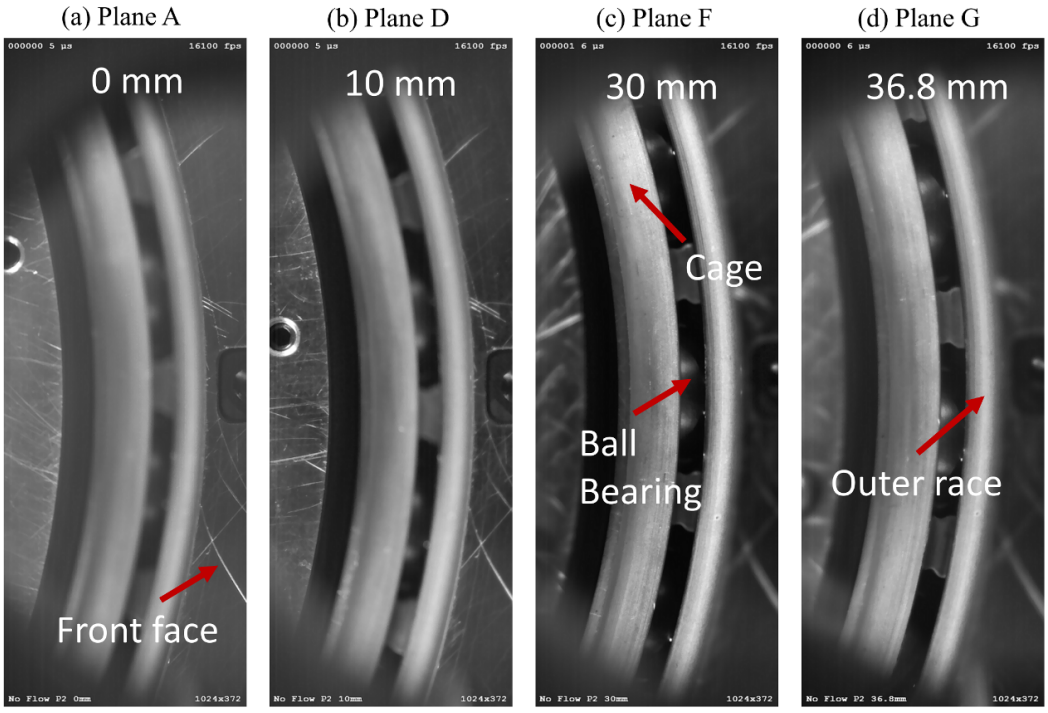


Figure 4.12: Sample HS images (without oil flow) at visualisation plane A, D, F and G taken from viewing position P2

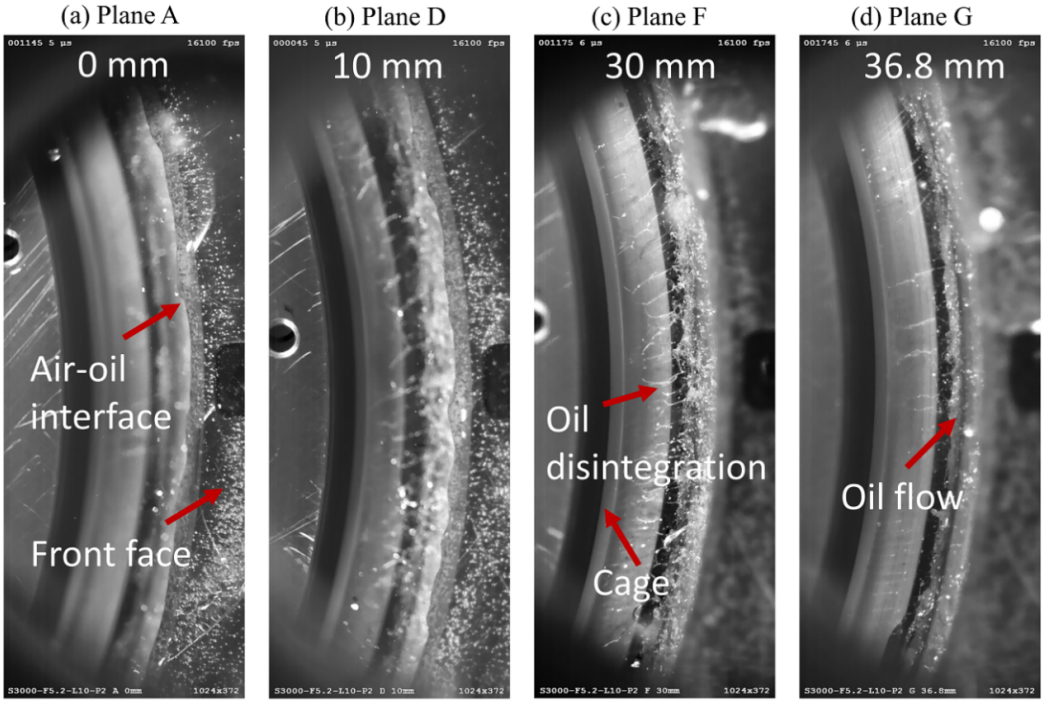


Figure 4.13: Sample HS images (with oil flow) at visualisation plane A, D, F and G taken from viewing position P2

At the axial plane of focus A (0 mm), the front face is in focus and the surface details such as machining mark, edges and geometric feature of probe insertion are well in focused (see Figure 4.12a). Meanwhile, at plane of focus D (10 mm), the stubshaft is in focused and front edge is marginally defocused but still visible due to relatively large depth of field of the HS lens (see Figure 4.12b). In contrast, for plane F and G or axial location of 30 mm and 36.8 mm, the cage and ball bearings are well in focused while the features described at 'front face' are not.

Samples instantaneous HS images acquired at same plane as that of Figure 4.12 but with oil flow is shown in Figure 4.13. In oil flow condition, a high resolution air-oil interface is visualised at plane A of 0 mm (see Figure 4.13a). However, the same flow features (air-oil interface) are not in focus in plane F (36.8 mm). At plane F, a distinctively different oil flow features could be visualised. It is possible to see that oil disintegration occurred at the cage of plane F. Therefore, it is concluded that different plane of visualisation has to be performed at multiple axial planes along the depth of the ball bearing in order to understand the journey of oil flow from inner ball bearing to the outer chamber. Similarly for LDM-HS, 3 instantaneous high speed images taken at plane B, D and G are shown in Figure 4.14.

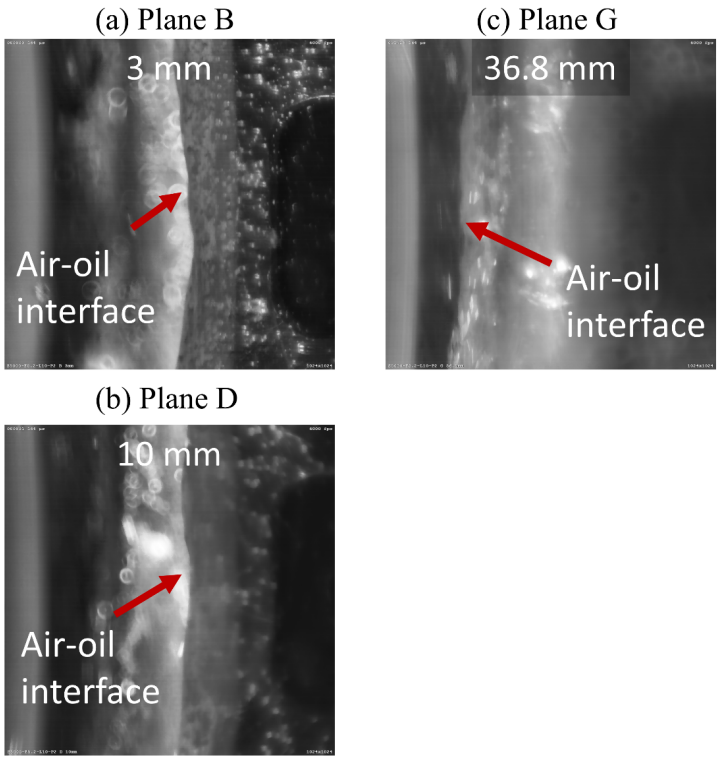


Figure 4.14: Sample LDM-HS images (with flow) at visualisation plane B, D and G from viewing position P2

The purpose of taking only B and D instead of A, C and E is due to the fact that no appreciable differences are seen along these depths where oil film are visualised at the same flow condition. By taking images at Plane B and D, it is possible to double verify if there is significant difference on oil film along the axial plane when parametric changes are made. Meanwhile at plane G (36.8 mm), the air-oil interface in the gap between cage and outer-race is visualised. As the oil droplets and ligaments are moving at a velocity scale too fast to be captured by LDM, the exposure of 164 μs is not sufficient to freeze the droplets in each frame. Therefore, plane F (at cage edge) is not considered for image acquisition of LDM-HS.

In summary, the scientific reasoning behind taking the measurements or images at different plane of focus whether using HS or LDM-HS are summarised as following:

Visualisation of the plane of focus A (0 mm) enables the examination of oil separation at the edge as it begins to leave the bearing outer-surface and entering the chamber. Visualisation will confirm whether the film will separate as droplets or remain attach as a film. For the visualisation of plane of focus B (3 mm), the film is still driven by the shear imposed by the rotating stub shaft and has yet to be separated from the edge, this makes analysis of the film easy and possible as the film is less affect by the sharp edge downstream of the flow. Plane of measurement C (6 mm) is not needed in this thesis since the data needed is also covered by plane of focus D, hence reducing data overload. At the plane of focus D (10 mm), the effect of the shear is most prominent since the stub shaft is positioned radially with the film surface, fully facilitates momentum transfer.

Subsequently, the plane of focus E (15.5 mm) is the plane in which the probe insertion is strategically located, it will be used in future experiments when brightness based laser induced fluorescence (BBLIF) or other localised probe is employed. It is safe to assume that the data at this plane can be represented with data at the adjacent plane of focus D (10 mm). The plane of focus F (30 mm) is used in the visualisation of oil breakup at the bearing cage and also for ligament number calculation. The oil shedding process at this plane is different to that of other planes since the rotating element resembles both disk and cup. Here, it is important to note that the speed of the surface of the rotating bearing cage is approximately half that of stub shaft (refer to [93]). Finally for plane of focus G (36.8 mm), it is the plane in which the oil exits the bearing gap, the shearing effect is largely driven by the rotating cage and prior to that oil could split by exiting the rear or front resulting in different oil split ratio, hence making the measurement and visualisation at this plane important.

4.1.8 Accuracy of Test Instruments

According to the technical report for bearing shedding rig construction [98], the test instruments were reported to have a measurement uncertainty of less than 2% of full scale (FS). The individual specifications were not provided, however, several instruments can be identified as they were commercially available. These were reported as follows:

The flow meter used in the test rig is an oval gear positive displacement flow meter [104]. This flow meter measures the rate in which an amount of liquid is filling the cavities of the gears. The rotational rate of the gear is sent back via a pulsating signal to the receiver enabling the flow rate to be correlated. This flow meter has a measurement range of 0.05 lpm to 10 lpm on a 30 cSt oil. If the liquid medium is water, the measurement range is expected to change. The accuracy of flow meter was reported to be $\pm 0.5\%$ of full scale and has a repeatability of $\pm 0.1\%$. For example, at the measurement test point of 5.2 l/min, the accuracy of the measurement would be 5.2 ± 0.05 lpm. Between each successive measurements, the reading is repeatable to 5.2 ± 0.01 lpm – much smaller than what could be measured by the signal.

Thermocouple was used in the experiment to measure temperature of oil inside the delivery conduit and the scavenging pipes. Typically, a K-type thermocouple is widely used in the industry. K-type thermocouple produces voltage reading based on changing electrical signal of the resistive materials. A standard thermocouple (e.g. Fluke 80PK-27) has a measurement range of $-40℃$ to $816℃$ [105]. The accuracy is reported to be $\pm 2.2℃$ (as % of the reading) for the range of temperature from $-40℃$ to $293℃$. For the temperature of $55℃$, the accuracy would be $55 \pm 2.2℃$. Beyond $293℃$, the accuracy is $\pm$ 0.75% of the measured value. The repeatability of of the device was not provided in the specification data sheet.

Shaft speed is one of the parameters used in the experimental study. Shaft speed for bearing shedding rig was measured using the built-in motor driver feedback (or specifically an encoder attached to the servo motor). According to the statement of requirement report [98], the motor has an adjustment accuracy of $\pm$ 15 rpm at all set points. The encoder (model: ERO1420) has a measurement accurcy of 1 ± 0.271 revolution from 0 rpm to maximum permissable speed of 30000 rpm. For true speed of 3000 rpm, the encoder is able to accurately measure the angular rotational to 3000 ± 1.2071 rpm.

For bearing axial load, a load cell is used to measure the amount of force exterted onto the test bearing based on a strain gauge principle [106]. A generic load cell (e.g. Siemens load cell) has a measurement range of 0 to 13 tonnes [106]. The accuracy is quoted in terms of minimum load cell verification intervals of 13000. For a 35 kN load, it is translated to ± 2.69 N. The uncertainty

in measurement or so-called ‘combined error’ is 0.023%. Combined error is a collective term in load cell measurement technique which takes into account creep error and other form of errors (e.g. nonlinearity in calibration curve when load is removed and reapplied).

4.1.9 Repeatability of Flow Structure

It is important to examine the repeatability of the flow structure in a given set of experiments, this is to ensure that the data recorded are reliable, reproducible and thus, subjected to an acceptable range of error. The data log file presented below was obtained from various instruments embedded in the test rig (such as ones described in Section 3.2.4). The data log file in the form of National Instrument file format was post-processed using MATLAB. The subplot (A), (B) and (C) in Figure 4.15 show the instantaneous value for the total oil input flow-rate, shaft speed and bearing axial load. Subsequent time-averaged and standard deviation are plotted adjacent to the instantaneous value, as shown in subplot (D), (E) and (F) respectively.

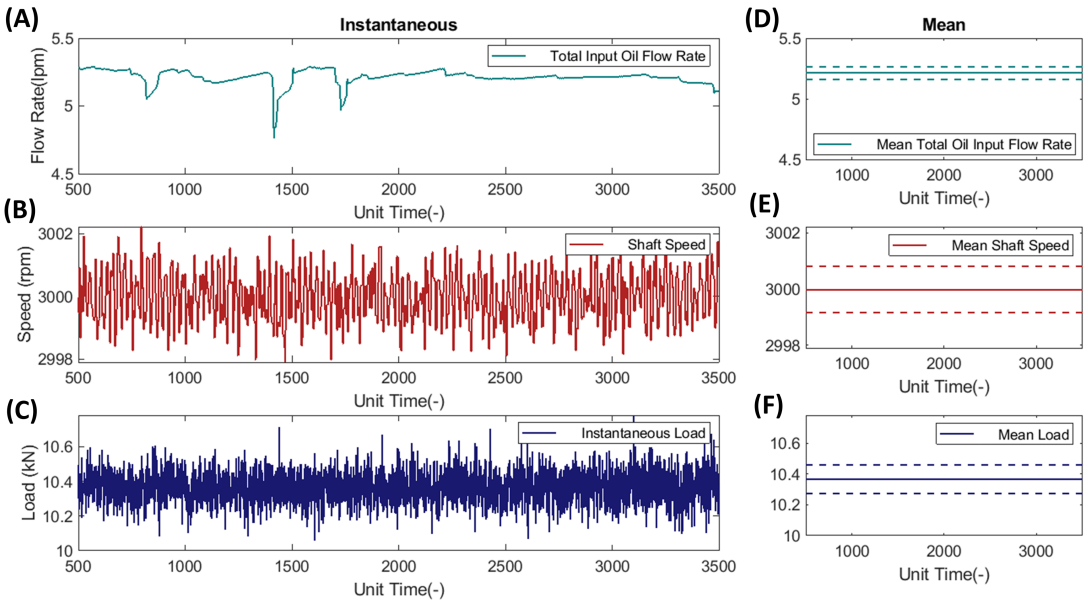


Figure 4.15: Data logging from sensors within the test rig taken at operating condition - speed 3000 rpm, flow rate 5.2 lpm and axial load 10 kN. The instantaneous value for flow-rate, speed and load are plotted in subplot (A), (B) and (D). The corresponding mean and standard deviation are plotted in (D), (E) and (F).

In this study, the test case for operating condition of speed 3000 rpm, oil flow rate 5.2 lpm and bearing axial load 10 kN was systematically reviewed. Based on Figure 4.15 (E) the time averaged

quantities show that the speed produced by the shaft was highly stable with a mean value of 3000 rpm. The standard deviation for shaft speed accounts for only 0.03% or 0.9 rpm.

In terms of bearing axial load, it can be seen that the electromagnetic actuator consistently over-apply forces exceeding the desired set-point by 0.37 kN yielding a mean value of 10.37 kN. The standard deviation of the bearing load was calculated to be 0.89% or 0.09 kN. These can be referred in Figure 4.15 (F).

For the total oil input flow rate, the mean value was obtained as 5.21 lpm. This was only 0.192% higher than the desired set-point. The standard deviation obtained from unit time 500 to 3500 was 0.05 lpm, corresponding to 0.959%. The data processing was performed from unit time 500 to 3500 with aim of avoiding transient effect from changing speed, oil or load that could affect the reliability of the measurements.

The following subsection further discuss the study of the repeatability of the flow structure. A series of 'median-stack' images of oil film thicknesses are presented in Figure 4.16 (for detail description of 'median-stack' images, reader is advised to refer to Section 4.2.2, for the time-being, it could be defined as the mean film solution).

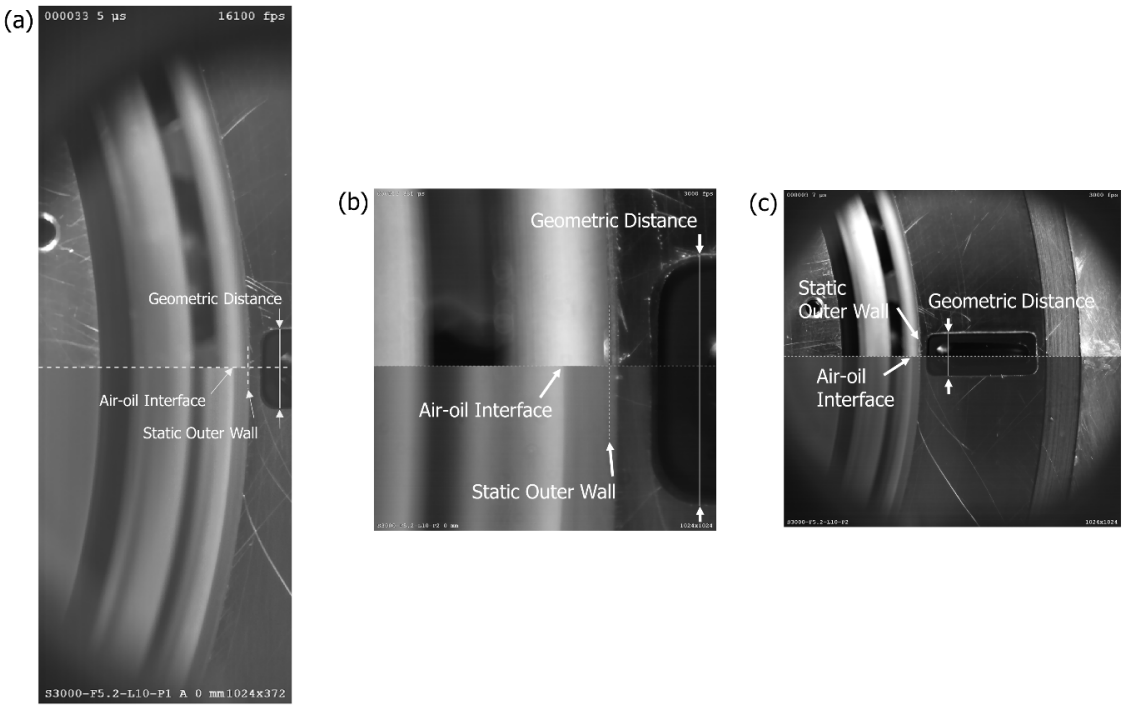


Figure 4.16: 'Median' images of oil film thickness obtained at different day at the same operating condition (speed 3000 rpm, flow rate 5.2 lpm and load 10 kN) on (a) 03/03/2016 (b) 12/04/2016 and (c) 19/02/2016

The images in Figure 4.16 represents the 'time-averaged' film solution taken on 03/03/2016, 12/04/2016 and 19/02/2016 respectively at the same flow condition (e.g. shaft speed 3000 rpm, flow rate 5.2 lpm and load 10 kN). The film thickness was measured along a radial line (as indicated by the dash line) by taking the pixel value of air-oil interface minus the static outer wall. The film thickness was determined by correlating it to a geometric feature (as shown in the label 'Geometric Distance' in Figure 4.16), this yields the ratio of film thickness. The comparison of the ratio of film thickness between different test cases will determine the degree of flow repeatability. The formula for the ratio of film thickness, R is defined as following:

$$R = \frac{Film\ Thickness\ [Pixel]}{Geometric\ Distance\ [Pixel]}$$

A similar value for R for different day is the most desirable as it indicates flow repeatability. R for the day 03/03/2016 was obtained as 0.1983 and R for 12/04/2016 and 19/02/2016 were 0.18 and 0.1797 respectively. Since R for 12/04/2016 has the highest optical resolution due to the type of lens used (e.g. LDM), it was chosen as the benchmark test case. The flow was measured to be repeatable to within 0.166 and 10%. Due to the amount of data available, the results above are preliminary indication of the repeatability of flow structure, future test cases will involve a greater number of data point.

4.2 Oil Film Thickness Measurement by Optical Technique

Droplet, ligament and oil sheet disintegrated from the cage and impinged onto the outer periphery of the bearing containment. The flow is combined with the axially exiting oil from the gap between cage and outer-race and thus forming a thin layer of substrate referred as thin film. This thin film has profound impact on momentum, heat and mass transfer in the chamber. A pre-requisite for an accurate numerical simulation is the accuracy of the boundary condition. This section informs details of film thickness measurement using new optical technique.

4.2.1 Experimental Test Cases for Film Thickness Measurement

To parametrically investigate the effect of rotational speed (ω), axial load and flow rate on the thickness of the film (δ), three shaft speeds were considered, namely; 3000 rpm, 5000 rpm and 7000 rpm. Speed of greater than 7000 rpm was not selected due to vibrational issue that opt to be rectified in future recommissioning. For bearing axial load, 10 kN and 30 kN were selected to determine the effect of increasing axial load on film thickness. The flow rates used are 5.2 lpm and 7.3 lpm. Justification on the flow rates were given in Section 3.2.1.2. The parametric test cases have been named with the following convention: '*Sxxx-Fyy-Lzz-Pn*' where '*xxxx*' denotes the shaft speed (unit: rpm), and '*yy*', '*zz*' and '*Pn*' represent the oil flow rate (unit: lpm), bearing axial load (unit: kN), and angular position (unit: -) respectively. For example for test case with shaft speed of 3000 rpm, oil flow rate of 5.2 lpm, bearing axial load of 10 kN and visualisation position 'P2' is represented as '*S3000-F5.2-L10-P2'*. A combination of all these factors yield the following test matrix shown in Table 4.4.

Table 4.4: Test cases and their respective naming convention

No	Rotational speed (rpm)	Flow rate (l/min)	Axial load (kN)	Test case name
1	3000*	5.2	10	S3000-F5.2-L10-PX
2	3000*	7.3	10	S3000-F7.3-L10-PX
3	5000	5.2	10	S5000-F5.2-L10-PX
4	5000	7.3	10	S5000-F7.3-L10-PX
5	5000	5.2	30	S5000-F5.2-L30-PX
6	5000	7.3	30	S5000-F7.3-L30-PX
7	7000	5.2	10	S7000-F5.2-L10-PX

8	7000	7.3	10	S7000-F7.3-L10-PX
9	7000	5.2	30	S7000-F5.2-L30-PX
10	7000	7.3	30	S7000-F7.3-L30-PX

*Case 1 and 2 were not run with load of 30 kN due to screeching noise generated

4.2.2 Image Processing I – Temporal Averaging & Median Stacking

The oil film thickness profile is time-dependent, wavy and is formed by quasi-periodic phenomena (definition of quasi-periodic: recurring in an irregular periodicity that is unpredictable as opposed to periodic interval). In this section, two descriptions of time are given as follows: (1) the instantaneous time is the physical time in which an event occurs. In this event, the flow exhibits a certain quantity of velocity, temperature, fluid property (e.g. density, viscosity) and turbulence quantities. (2) temporal averaging or 'median-stacked' time is the time that was derived from performing a mean calculation of a sampling flow. These quantities are the mean or median value of the flow based on the duration and sampling frequency. An example of the dynamic of oil film for test case S3000-F5.2-L10-P2 at normalized time (τ) and flow time (t) of 0 to 0.75 and 0 to 0.25s are shown in Figure 4.17. The normalised flow time is calculated by dividing the frame number at a specific instant over the total number of frames of the whole acquisition duration.

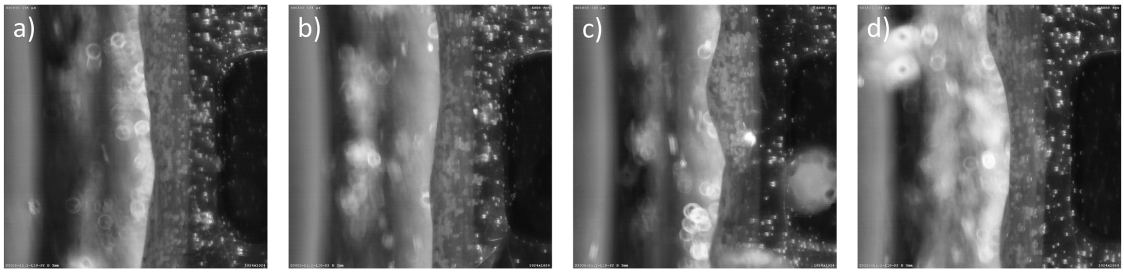


Figure 4.17: Oil film profiles for test case S3000-F5.2-L10-P2 taken at (a) $\tau = 0$ (b) $\tau = 0.25$ (c) $\tau = 0.5$ (d) $\tau = 0.75$

By referring to Figure 4.17, it is conceivable that the film thickness does not have a regular film profile or thickness at any instance in time due to turbulence airflow and time-dependent phenomena. Therefore, temporal averaging or 'median-stacking' is selected to obtain a steady-state feature prior to measuring the film thickness.

Temporal-averaging or time-averaging is a mathematical operation that determines the mean value of a variable within a sample. To perform time-averaging for the test cases. A common mathematical approach of arithmetic mean of an image intensity was performed by evaluating a series of image intensity values within a time-series (i.e. summing up the image intensity value in the direction of time and divide it by total frequency). The formula for time-averaging of image intensity is given in Equation (4.2):

$$I_{mean} = \frac{1}{n}\sum_{\tau=0}^{1} I_i \tag{4.2}$$

Where, I_{mean} is the mean image intensity, n is the total number of frames (total frequency), I_i is image intensity at instantaneous time.

For 'median-stacking', the middle number of a re-order image intensity series in ascending order is extracted. To perform 'median-stacking' of an image intensity within a sample the mathematical formula commonly established for median calculation is used. For median calculation with odd number of total number of frames, Equation (4.3) is used. Whereas, for total number of frames with even number, Equation (4.4) is used.

$$I_{median,odd} = \left(\frac{n+1}{2}\right)^{th} term \tag{4.3}$$

$$I_{median,even} = \frac{\left(\frac{n}{2}\right)^{th} term + \left(\frac{n}{2}+1\right)^{th} term}{2} \tag{4.4}$$

To illustrate the process for time-averaging and median-stacking, Figure 4.18 is provided. In this example, *MATLAB* 2016b numerical computing software is used. In Figure 4.18, the images of test case S3000-F5.2-L10-P2 are stacked such that they form a 3D-array (definition of 3D-array: a multi-dimensional array that contains information in all 3 directions; row, column and depth). The depth of k-vector of the 3D-array is the time-series where each individual unit represents frame number. The stacking is completed when all the images are stacked from $\tau = 0$ to $\tau = 1$ which represent the total flow time from 0 to 0.332s. Time-averaging process is performed by using *MATLAB* built-in syntax *mean(A,3),* where *A* denotes the 3D-array and number *3* in parenthesis denotes the direction for calculation which in this case, k-vector. For 'median-stacking', *MATLAB* built-in syntax *median(A,3)* is used. By referring to the first image in Figure 4.18, the time-averaged intensity value of the sub-region I_1 at the first position is obtained by summing up all the discrete I_1 values along the time-series and dividing them by the total

frequency. Subsequent process is performed for all sub-region cells (i.e. I_2, I_3 and… I_i). Hence, yielding a single time-averaged high speed image.

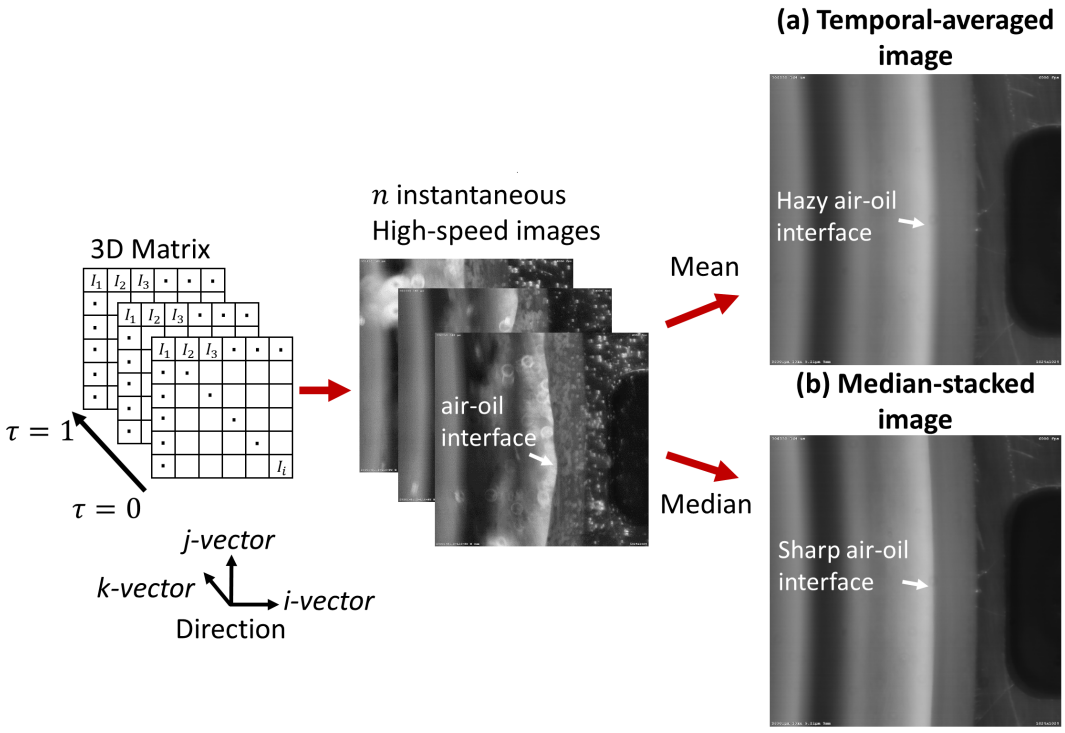


Figure 4.18: Time-averaging and 'median-stacking' process which yield steady-state flow feature

For 'median-stacking', a seemingly similar process is conducted except where the image intensity in the sub-region I_1 is obtained by first reorder the image intensity values of the time series in ascending order and subsequently extracting the middle number. Median-stacking operation requires enormous computer's random access memory (RAM) since 'median-stacking' requires all variables to be kept in the workspace at all time. An alternative way of overcoming memory shortage is by processing median in various chunks from top to bottom. This reduces RAM requirement and speed up calculation.

By observing the time-averaged and 'median-stacking' images, the differences could be seen by the clarity of the air-oil interface. The former has a diffusive air-oil interface which is hard to be differentiated as the intensity change at the air-oil boundary is not abrupt but occurring over a finite distance [107]. Whereas, the latter has a sharply defined air-oil interface due to sudden change in image intensity at the boundary adjacent pixels. The technique 'median-stacking is commonly found in astronomical science application, as for example used by White *et al.* [108]. As outlined by White *et al.* [108], median-stacked images have two advantages over the more-usual temporal-averaged images. Firstly, it significantly increases the signal-to-noise ratio which

produces clear edges as shown in Figure 4.18b. Secondly, objects that move across the subject (plane of focus) between the time intervals in the stack are eliminated. This is important to exclude the many oil droplets that broke-off from the edge and moved across the area of focus during image acquisition period. As such, median images are used for subsequent film thickness measurement.

4.2.3 Image Processing II – Edge Detection of Oil Film

The process of oil film thickness (δ) determination from the median-stacked images involved accurate identification of air-oil interface. This is accomplished by inspecting the occurrence of 'peaks' in the gradient plot and subsequently cross-validating the detected location with the actual image itself to avoid anomaly as identifying the location of interface using gradient plot itself is not sufficient and make little sense. To better explain the process, a reference Figure 4.19 is given.

First, a vector search is performed on the 2D-matrix of the median-stacked image to obtain the radial distribution of image intensity across the horizontal cut-section passing through the centre-line for oil flow case (N.B. the median-stacked image presented in Figure 4.19 is a composite image of oil flow case (top half) and with no-flow case (bottom half) taken at the same viewing position). In this example the vector-search is performed at vertical location of pixel number 512 for purpose of illustration. In most cases, the vector search is performed at midline between the geometric features of the probe insertion. Minor discrepancy in the selection of measurement location for radial distribution is tolerable due to the fact that film thickness is too small compared to radius curvature of the bearing.

The image intensity extracted along the horizontal line is plotted for the oil flow case. These intensities represent the brightness in which light is registered on the discrete location (also known as grey level for monochrome sensor). A 8-bit format is selected as there is no gain in quality from a higher bit rate. The image intensity of a pixel in 8-bit format could varies from 0 to 255. An image intensity of 0 represents black, whereas, value of 255 represents white. The plot of image intensity shows the maximum brightness achieved in this image is 191.

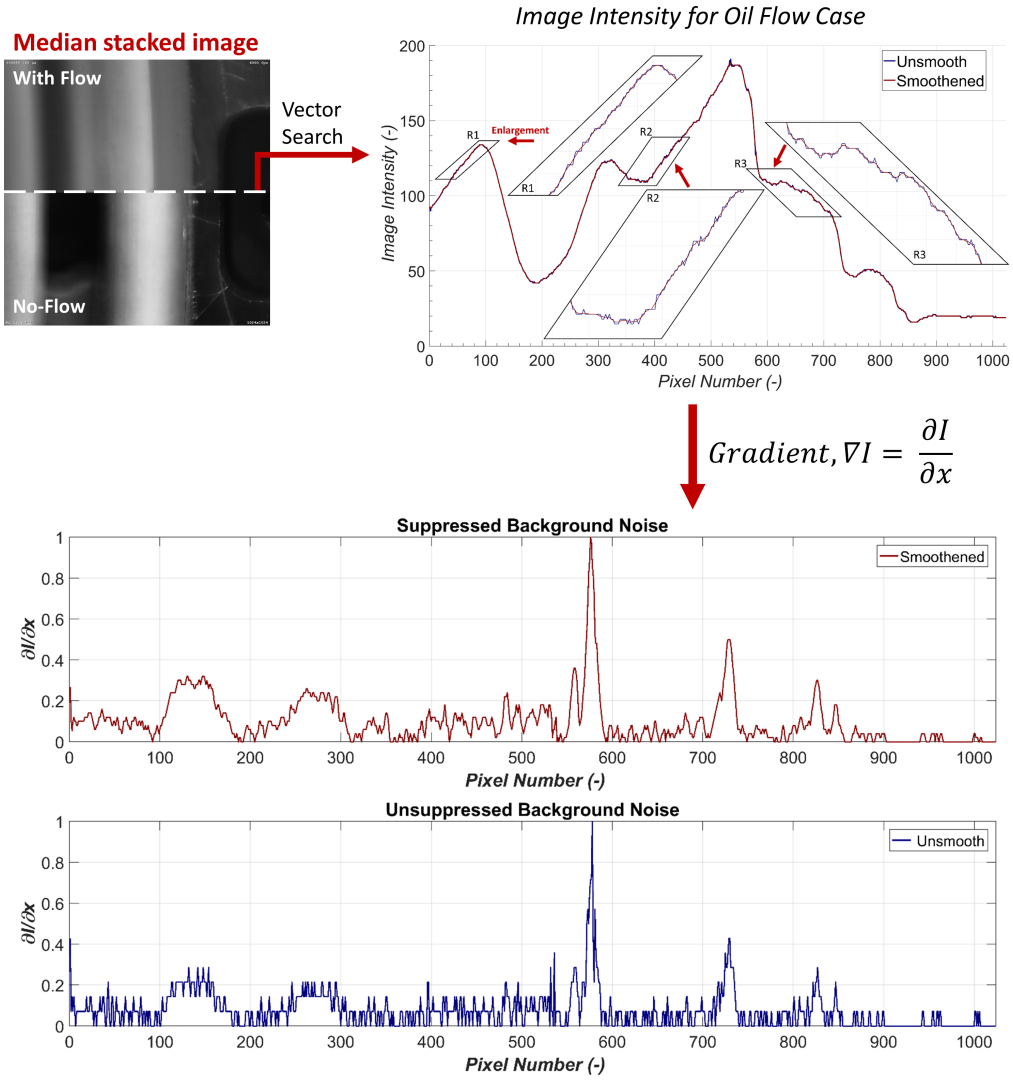


Figure 4.19: Vector search for image intensity of the radial distribution of oil flow case and the application of smoothing function to suppress background noise

In the plot of Figure 4.19, two curves were shown. The first is an unsmooth curve derived from the original image intensity in which the sensor perceived. It was shown by the enlarged inset images (Figure 4.19 R1, R2 and R3) that this curve is step-wise in nature reflecting a digital-like signal. The step-wise signal contains background noise which could be amplified during differentiation as detailed by Petrou [107]. To eliminate the tendency of background noise interfering with detection of peaks in gradient plot, *MATLAB* built-in function *smooth* is used. *Smooth* averages out the respective image intensity based on five of its discrete neighbouring values. The effect of smoothing could be seen by the red curve of the image intensity plot as well as within the enlarged inset images (R1, R2 and R3). Smoothing function of three, four or five discrete points were shown to make no difference to the image gradient (see Figure 4.20). Therefore, a minimum of three discrete points smoothing was proposed for all the test cases in

order to minimise background noise. It should be noted that the location of a peak in gradient plot could also shift by two pixels between a smoothed plot and an unsmooth plot.

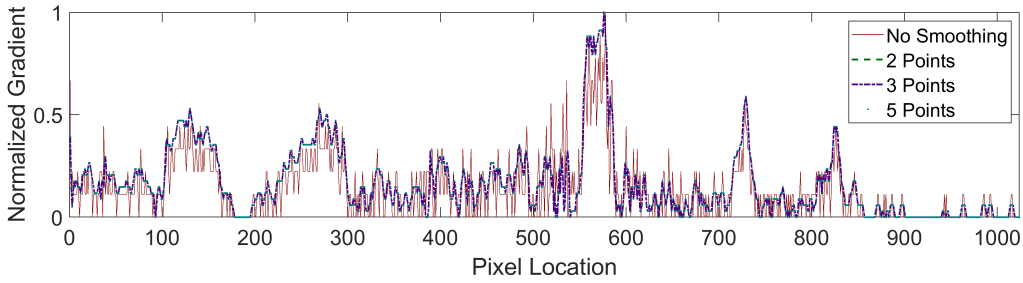


Figure 4.20: Comparison of smoothing function based on averaging of different discrete point

The subsequent process after smoothening is the calculation of derivative of image intensity which yields gradient. Here, the occurrence of peaks are observed. The peaks in gradient plot correspond to regions where pixel intensity changes significantly in a given direction. An abrupt change in image intensity between two adjacent pixels or a high value of gradient signify boundary/edge/interface. As only magnitude of gradient is needed regardless of its direction of change, absolute function *abs(y)* is used to obtain the positive gradient. In Figure 4.19, the derivatives of image intensity for suppressed background noise and unsuppressed background noise were given. The peaks generated clearly shown that noise suppression is needed.

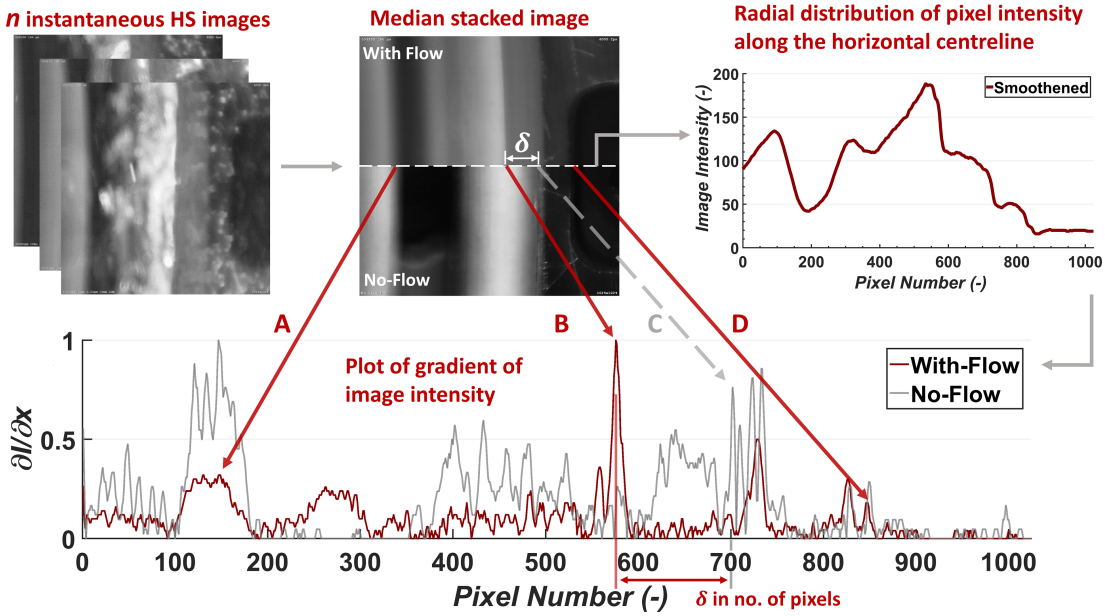


Figure 4.21: Determination of oil film thickness (***δ***)

Lastly for measuring film thickness in pixel value, a similar process to Figure 4.19 is performed with the exception that an extra curve in gradient plot of a no-flow case is plotted as shown in Figure 4.21. In the plot, two consecutive peaks in the approximate pixel range where the oil film is intended to be determined are observed. The film thickness pixel range is obtained by taking the oil film interface pixel (see Figure 4.21, arrow **B** ➞) minus solid-liquid interface pixel (see Figure 4.21, arrow **C** ➞). In Figure 4.21, the location of air-oil interface is at pixel number 576 (denoted by $\partial I/\partial x$ of 1, legend — With-Flow) and air-solid interface is at pixel number 702 (denoted by $\partial I/\partial x$ of 0.75, — No-Flow). As the stub-shaft at arrow A is out-of-focus, the peak or gradient value is low which resulted in difficulty of detection. For arrow D, the location of geometry feature is also poorly captured based on low peak due to oil film covering the feature. By multiplying the film thickness pixel range (see Figure 4.21, **δ in no. of pixels**) by the spatial calibration factor (unit: mm/pixel), the actual film thickness in SI unit could be obtained. The process of obtaining the spatial calibration factor is well described in Section 4.2.5.

4.2.4 Image Processing III – Edge Detection of Solid Surface

The process of determine air-oil interface was well-described in Section 4.2.3. Correspondingly the process of determine solid-surface in no flow state is not dissimilar. This section further elaborate measures taken to decide the boundary of solid-surface when the surface is out-of-focus (such as for plane of focus 10 mm or D). In this section, images at plane B, D and G or 3, 10 and 36.8 mm in no flow state is shown in Figure 4.22.

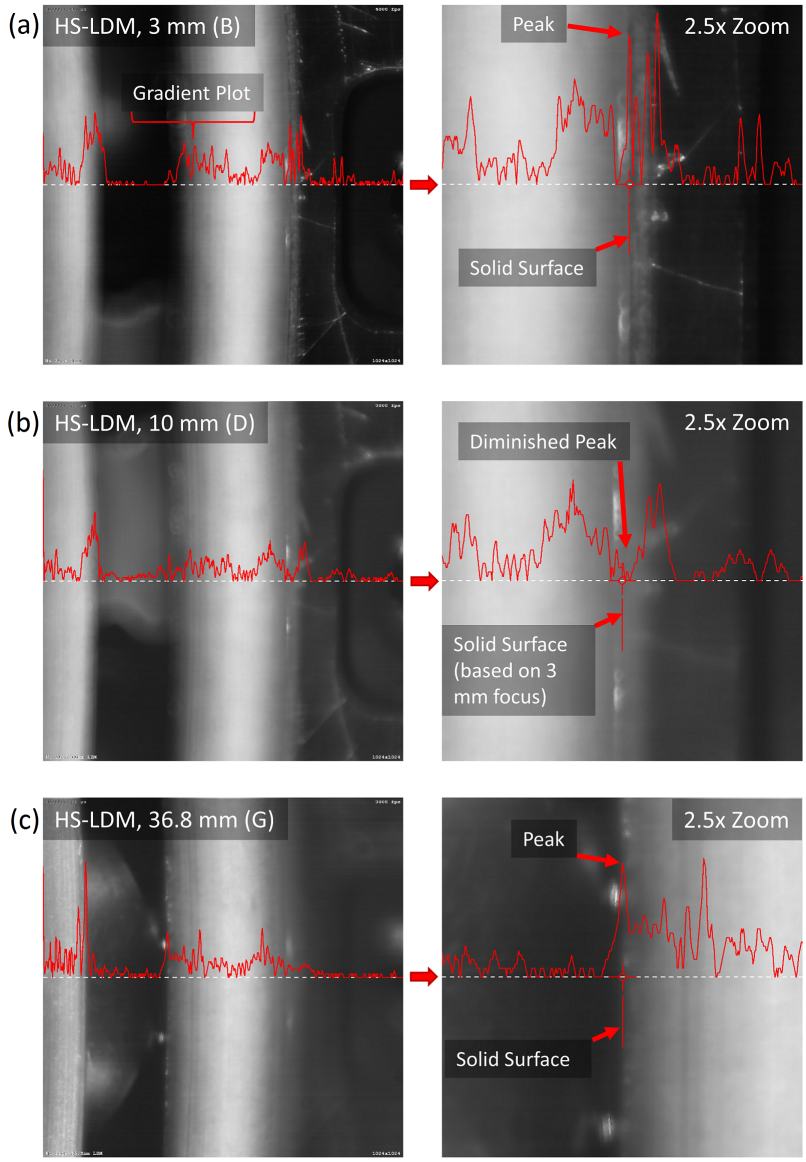


Figure 4.22: Detection of solid surface using peak at axial location:
(a) Plane of focus B (3 mm (b) Plane of focus D (10 mm) and (c) Plane of focus G (36.8 mm) with 2.5x digital zoom on the right

The images on second column of Figure 4.22 are 2.5x enlargement adjacent of the main images at expected solid surface. To simplify the detection of solid boundaries, gradient plot of the radial distribution at the midpoint was superimposed onto the image of no oil flow. These images are taken at the same viewing position of each test cases prior to running the test rig with oil and rotation.

In plane of focus B, the solid-edge is detectable based on the apparent peak and known surface that is in focused in the image (see Figure 4.22a Peak ➞). It is recognisable that the red colour gradient plot on Figure 4.22a is similar to that of grey colour gradient plot on Figure 4.21. As the plane of focus is moved to D (10 mm), the peak diminishes (see Figure 4.22b Diminished Peak ➞). The solid-edge at D is taken to be similar to that of plane B (3 mm). Similarly for the solid-edge in plane G, the outer-race of ball bearing is easily identified based on featured sharp peak in the gradient plot and known surface (see Figure 4.22c Peak ➞). These techniques applied eliminated the possibility of 'false' peak/edge detection due to refraction of light when solid-edge is covered by liquid film.

4.2.5 Image Processing IV – Spatial Calibration Factor

To obtain the oil film thickness in SI unit instead of dimensionless pixel. The pixel range for film thickness must be correlated to an object of known dimension. This process is known as spatial calibration. To achieve this, the actual size of the image must first be obtained (i.e. in mm). In reference to Figure 4.23, the process of spatial calibration are highlighted in 2 steps. First, an object of known dimension (i.e. ruler) is placed adjacent to the region of interest (ROI). This item must be placed strictly on the same plane of focus to avoid error in calibration (i.e. parallax error). Subsequently, the mm per pixel for respective image (of SONY in Figure 4.23B) is obtained by working out the number of pixels covering unit distance 1 mm on the ruler scaling. The calibration factor only valid for analysis on the respective image, to work out the true spatial calibration factor for LDM-HS of the IDT camera in Figure 4.23C. The geometric feature true dimension close to the probe insertion of 2.13 mm is used which is derived from previous image Figure 4.23B (i.e. 0.0333 mm/pixel).

Moving towards the image of LDM-HS (which is one used for film thickness calculation), a reverse process of obtaining the spatial calibration factor is held. The calculated dimension of the geometric feature of 2.13 mm spanning over 147 pixels in the LDM-HS yields a spatial calibration factor of 0.014489 mm/pixel. By using the derived spatial calibration factor, the film thickness value could be obtained by simply multiplying this factor with film thickness range in pixels

obtained in Section 4.2.3. Due to time-constraint, the spatial calibration was performed after data collection. Arguably, only one step is needed if the known scale is placed on the same image where no oil flow is taken. Hence, a recommendation was proposed for future experiments that the spatial calibration should be performed on the same imaging image to avoid discrepancy when reversing the process using separate images. Conclusively for this section, a similar process was applied to HS images. Hence, giving the dimension of image mentioned in Figure 4.9 of Section 4.1.6. Table 4.5 is tabulated to summarise the spatial calibrations factor used across all 60 test cases.

Table 4.5: Spatial calibration factor used for different locations

Test Condition	Plane of Focus	Angular Position	Spatial Calibration Factor (mm/pixel)
1. S3000-F5.2-L10 2. S3000-F7.3-L10 3. S5000-F5.2-L10 4. S5000-F7.3-L10	B, D, G	P2	0.0149
5. S5000-F5.2-L30 6. S5000-F7.3-L30 7. S7000-F5.2-L10 8. S7000-F7.3-L10 9. S7000-F5.2-L30 10. S7000-F7.3-L30	B, D, G	P4	0.0141

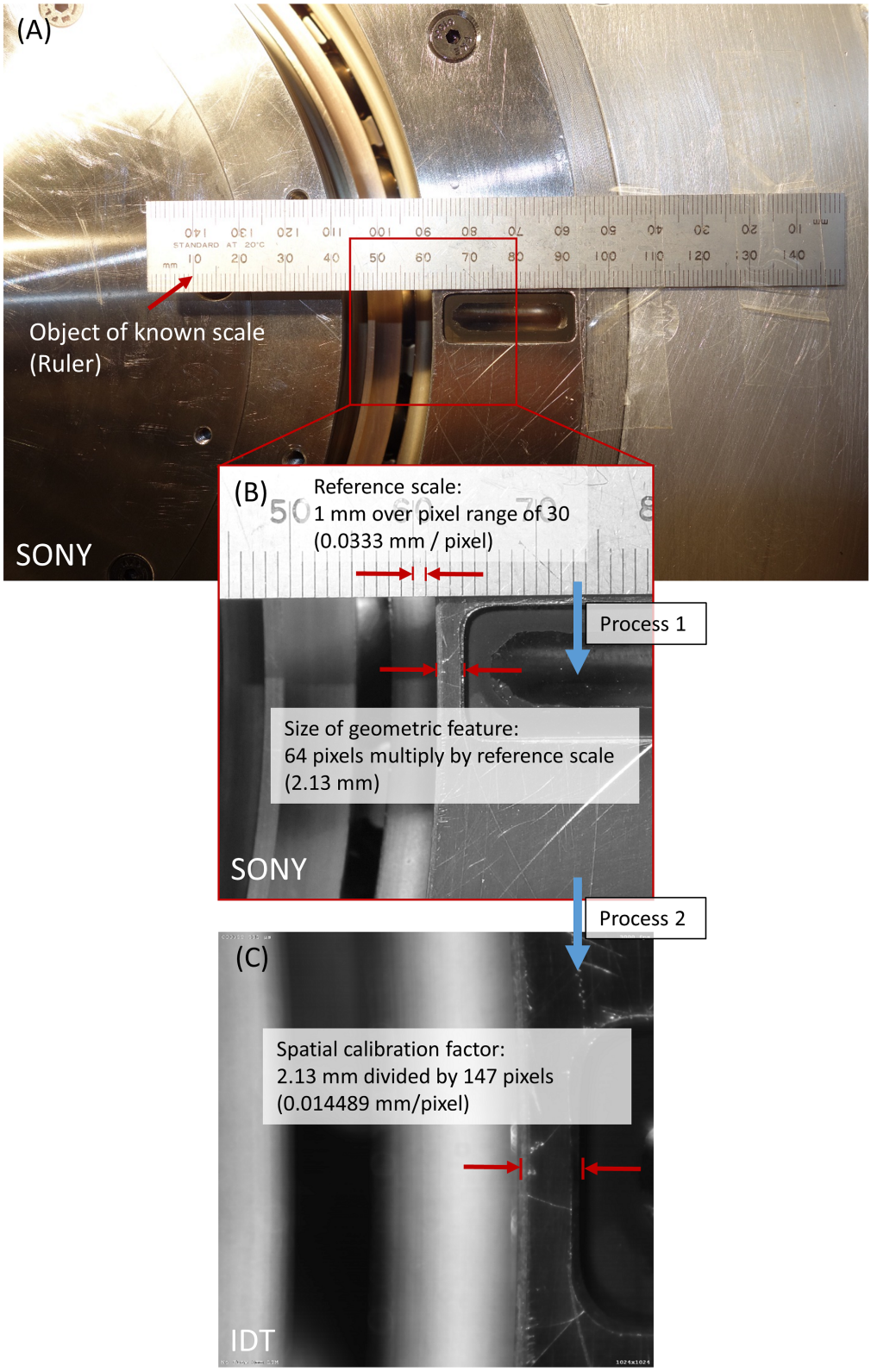


Figure 4.23: The process of 'Spatial Calibration' to correlating the subject with object of known dimension

4.2.6 Accuracy of Film Thickness Measurement using Optical Technique

This section reports the uncertainty in the detection of air-oil interface using optical technique as detailed in Section 4.2.3. The uncertainty study was performed by having 10 individuals selecting the air-oil interface of a series of median-stack images using MATLAB function *ginput* which returns the coordinate of the interface (see Figure 4.24). The process was aided by having a consistent line of measurement on each of the images prior to the selection so user could pick the interface at the right radial location. The outcomes of the studies were tabulated in Table 4.6 and plotted in Figure 4.25.

In this context, the uncertainty band is defined as the standard deviation relative to the mean film thickness. The higher uncertainty band the lower the accuracy. Referring to Figure 4.25a, the plot shows that the uncertainties are relatively small as most volunteers selected the same location. The uncertainty band for S3000-F5.2-L10-P2 is 1.14%, in comparison, the uncertainty band at counter-current side P4 is 19.56% (see Figure 4.25d). It is clear that the film is highly fluctuating about the mean value and resulted in a diffusive image when 'median-stacking' process was applied. The major qualitative difference between 'median-stacked' images at both sides is clear and could be referred to the Figure 4.24a and Figure 4.24j. The interface is sharp for co-current side, whereas relatively blurry for counter-current side.

Moving towards the plane of focus D (10 mm). The uncertainty band for co-current side still well-maintained below 3% for all rotational shaft speed from 3000 to 7000 rpm. Whereas for counter-current side, the uncertainty band is as high as 19.56% (see Table 4.6). Majority of the film thickness measurement at counter-current side was shown to have a high uncertainty band of between 6 ~ 19.56% at 3000 and 5000 rpm respectively. The trend has shown that the uncertainty band reduces as shaft speed increases, for example at plane of focus B, the uncertainty reduces from 19.56% to 14.29% and subsequently to 3.68% for 3000, 5000 and 7000 rpm respectively (see Figure 4.25d). Similar trend was observed for plane D and G. Such decrease was however, not observed at co-current side where for some instances the uncertainty band increases from 1.23% to 2.96% at plane D (see Table 4.6 and Figure 4.25b)

Apart from the film waviness, the secondary droplet production due to droplet impingement onto the film surfaces resulted in dense mist at moderate and high speed is also a factor that contributed to high uncertainty in the measurement as the image sharpness reduces. Future experiments will explore at using laser confocal displacement sensor and Brightness Based Laser Induced Fluorescene (BBLIF) to obtain local film thickness and the uncertainty band. These help verify

the accuracy of different methods in measuring film thickness. The uncertainty band from this Section will be incorporated in the film thickness plot in Section 4.2.8.

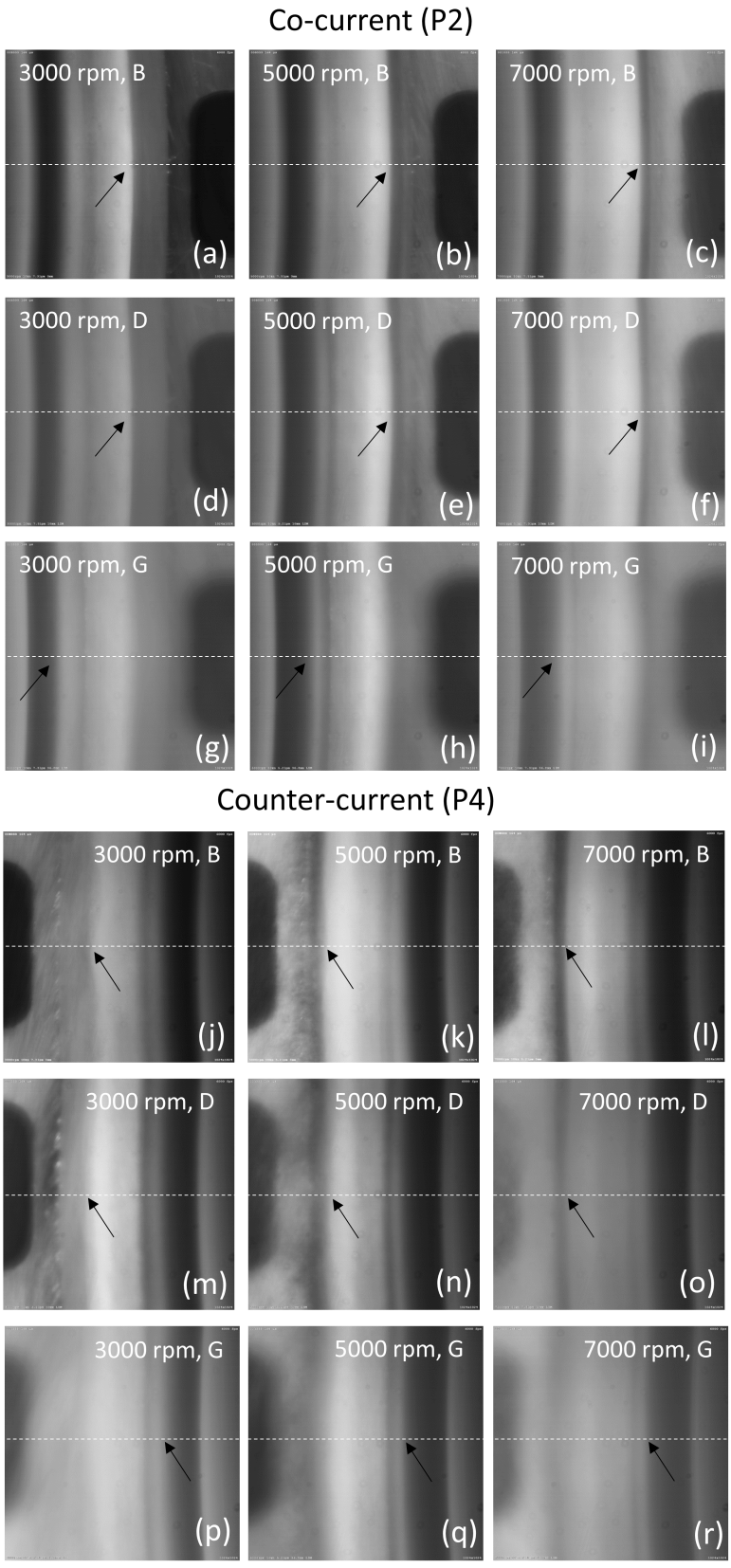


Figure 4.24: Median-stacked images used in the uncertainty study

Table 4.6: Uncertainty band in film thickness measurement using optical technique

Operating Condition	Angular Position	Plane of Focus	Mean Film Thickness (mm)	Standard Deviation (mm)	Uncertainty Band (%)
S3000-F7.3-L10	P2	B	1.935	± 0.022	1.14
S5000-F7.3-L30			1.026	± 0.027	2.63
S7000-F7.3-L30			0.774	± 0.024	3.1
S3000-F7.3-L10		D	2.1175	± 0.026	1.23
S5000-F5.2-L30			1.0575	± 0.0275	2.6
S7000-F7.3-L30			0.845	± 0.025	2.96
S3000-F7.3-L10		G	1.8125	± 0.0625	3.45
S5000-F5.2-L30			1.0625	± 0.125	11.76
S7000-F7.3-L10			1.0	± 0.125	12.5
S3000-F7.3-L10	P4	B	1.643	± 0.3214	19.56
S5000-F5.2-L30			1.0	± 0.1429	14.29
S7000-F5.2-L10			0.76	± 0.028	3.68
S3000-F5.2-L10		D	1.45	± 0.25	17.24
S5000-F5.2-L10			1.3	± 0.15	11.54
S7000-F7.3-L30			0.705	± 0.0429	6.09
S3000-F7.3-L10		G	1.242	± 0.1666	13.41
S5000-F7.3-L10			0.921	± 0.0571	6.20
S7000-F7.3-L10			0.825	± 0.0429	5.2

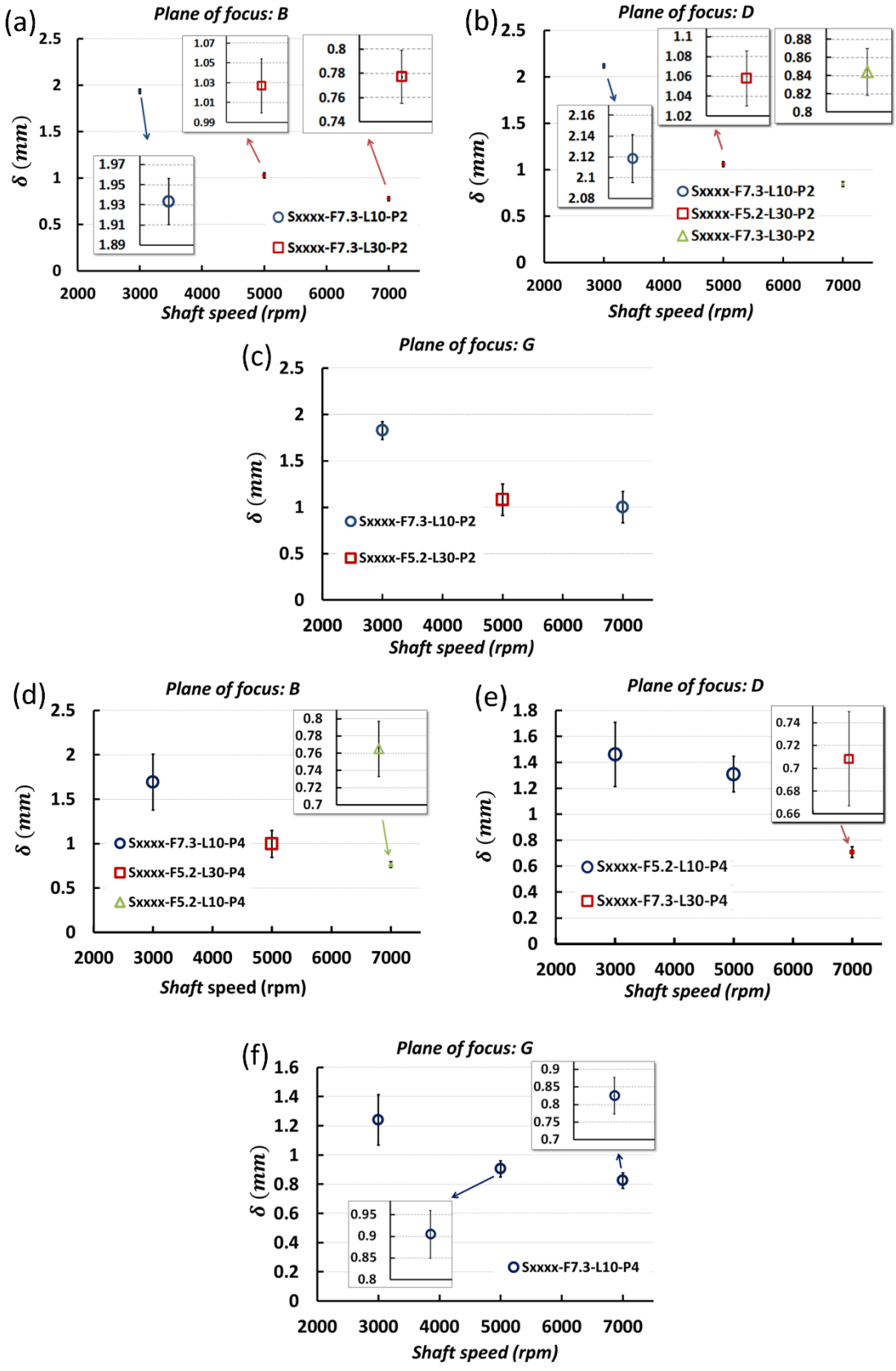


Figure 4.25: Detection of air-oil interface based on manual selection of 10 volunteers at different test point to determine the accuracy

4.2.7 Qualitative Analysis of Oil Film Thickness

Prior to presenting the quantitative results of oil film thickness, it is helpful to understand the flow features occurring in co-current (P2) and counter-current side (P4). The figures of oil film thickness based on different angular positions and shaft speeds are highlighted in Figure 4.26 and Figure 4.27 where the each images represent the following:

Figure 4.26a-c represent sample instantaneous HS images acquired at P2 depicting the air-oil interface at different shaft speeds, namely; 3000, 5000 and 7000 rpm. The corresponding median-stacked images are shown in Figure 4.26d-f. The instantaneous images of LDM-HS and its corresponding median-stacked images are shown in the adjacent bottom row in Figure 4.26g-i and Figure 4.26j-l respectively. The part of the HS image that is captured by LDM-HS imaging is highlighted by a dotted square in each HS image, note that the LDM-HS image produced is not a digital 'crop' view of the HS image but rather images taken at different instances. The horizontal dotted lines along each images taken are the radial location in which the film thickness measurements are made, additionally, solid-liquid interface was also highlighted in 'vertical dotted' line to avoid ambiguity. A similar classification was adopted for the counter-current side shown in Figure 4.27. Note that images for test cases of changing flow rate and axial load are not displayed here as there are insignificant differences made with the exception of plane G (36.8 mm) which seeing a rise in oil film thickness when load changes.

The mechanism of oil formation on the stationary circular wall (see Figure 4.26a) is as follows: The centrifugal action of the bearing cage breaks up the oil film at the cage-edge. The oil film broken down in the form of either drops, ligaments or sheets depending on the rotational speed of the cage. Subsequently, the oil imparted from the cage edge and impacts the stationary circular wall surrounding the bearing. Continuous addition of oil flow in this manner from the bearing cage accumulates to form a film on the surrounding wall. The oil film on this wall possess tangential momentum due to circumferential shear exerted by the rotating air flow between cage-edge and stationary wall.

Another concurrent phenomenon that influences the oil film profile is the outward axial displacement of oil from the gap between outer-race and the ball bearing cage. This is to satisfy the conservation of mass as the oil is continuously supplied to the bearing through under-race lubrication. The resultant combined mass of oil (due to oil breakup from the cage-edge and the axial displacement) collects at the front face and is subsequently displaced radially outward from the front face edge into the bearing chamber (see Figure 4.26a). Beyond the front face edge, oil film could stick to the surface or separates at the edge depending on magnitude of aerodynamic force and gravity.

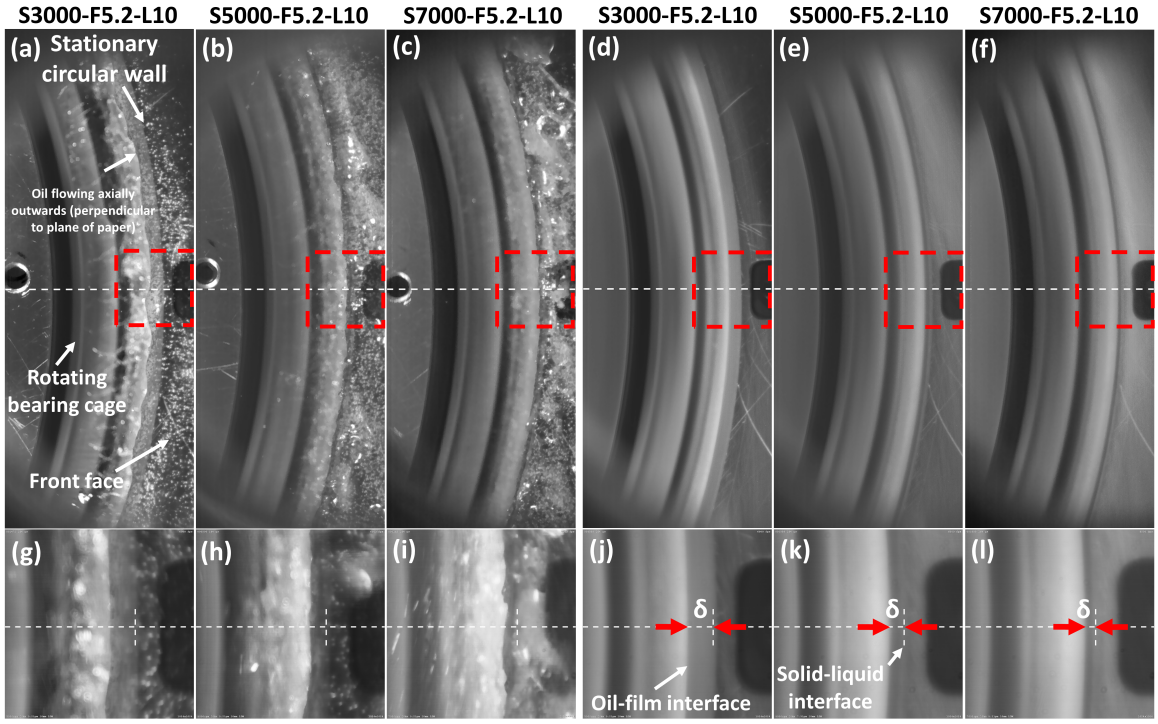


Figure 4.26: Sample HS images (top row) and LDM-HS (bottom row) at different shaft speeds at co-current side (P2), plane of focus D

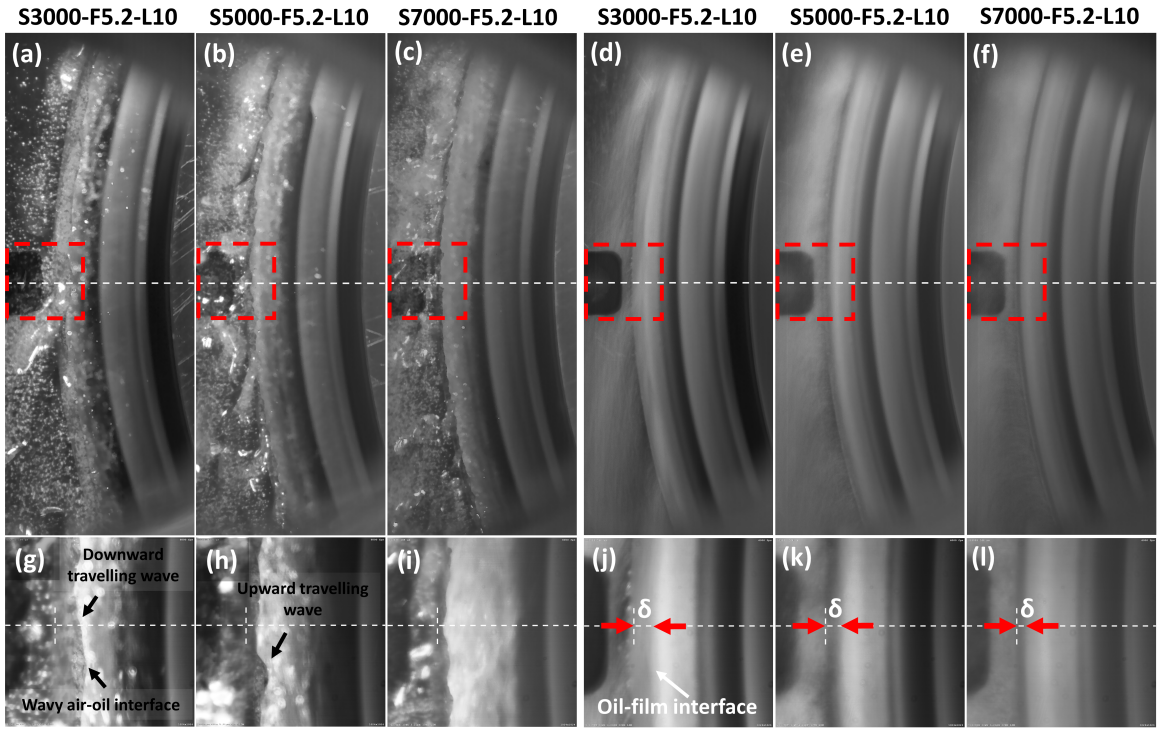


Figure 4.27: Sample HS images (top row) and LDM-HS (bottom row) at different shaft speeds at counter-current (P4), plane of focus D

It is observed that the air-oil interface at the co-current side is relatively less wavy (thus more uniform) as compared to counter-current side (HS and LDM-HS images are shown in Figure 4.27). This is also true for the higher oil flow rate (7.3 lpm) and higher axial bearing load cases although images for these cases are not shown here for brevity. This may be explained in the following manner: the counter-current regime is where the interface rotational shear is opposing the downward pull of the oil film due to gravity. This resulted in net reduced tangential drag on the oil film in counter-current regime as compared to co-current side. The relatively "lower" tangential velocity component in counter current side-oil-film is therefore influenced to great extent by the axially outward flowing oil mass from upstream as compared to co-current side. As a result, the oil film intermittently undulates which results in relatively non-uniform wavy film at the counter-current side. This can be clearly seen by comparing Figure 4.26j and Figure 4.27j. The oil film interface is hazier in Figure 4.27j as compared to Figure 4.26j.

The maximum undulation is witness when gravity is equal to the shear effect. At such situations, the flow field transits to 'shock' regime. This term is used in bearing chamber literature to indicate a transitional regime from the gravity-dominated pool flow to a shear dominated smooth flow mode. The important point here is that beyond a critical point when shear overcomes gravity, flow reversal is observed and the waves on the air-oil interface are observed to travel upwards (Figure 4.27h). In the present experiments, the critical speed at which flow reversal could be observed is estimated to be between 3000 and 5000 rpm in the counter-current regime.

The critical speed can be determined experimentally by observing the position at which the oil recirculation/hump (i.e. oil hump is a feature when there is a discontinuity in film profile [78]) that exist on the rising side of the chamber wall (e.g. angular position of 180 – 360°), this can be achieved by changing the shaft speed in a small and controllable step. A more precise method of identifying the critical speed is by measuring λ as detailed by Kay *et al*. [78]. λ is the of ratio of gravity to viscous force. The regime in which shock occurs has been theoretically defined to be between $3 \sim 5$. However, obtaining the λ is challenging as the viscous term involves measuring the velocity of the film profile which requires precise measurement of interfacial shear stress. Hence, the former is a faster method of identifying the critical speed and regime.

Beyond 5000 rpm, shear dominates to produce the shear-dominated smooth flow regime. The mechanisms of oil break-up and the dynamic effect of cage on film dynamics is discussed in Section 4.2.10 (contents from the section also being derived from publication of Santhosh *et al.* [109]) which describes qualitative and quantitative features of oil flow from the bearing cage edge when shaft rotational speed is systematically varied in steps.

4.2.8 Quantitative Analysis of Oil Film Thickness

This section reports measurements of film thickness obtained from optical technique based on the methodologies outlined in Section 4.2.1 to 4.2.5. The oil film thicknesses calculated at three different axial planes at viewing positions P2 (co-current regime) and P4 (counter-current regime) are shown in Figure 4.28a-c for 5.2 litres per minute cases and Figure 4.28d-f for 7.3 litres per minute cases. The speeds were varied from 3000 rpm to 5000 rpm and subsequently to 7000 rpm to access effect of shearing on film thickness. In all cases, the axial loads were also altered from 10 kN to 30 kN and are indicated by unfilling of marker colour (e.g., ■ to □), meanwhile changing position is indicated by changing shape (e.g. ● to ■). The uncertainty bands obtained from Section 4.2.6 have been incorporated in Figure 4.28. It is the standard deviation in the detection of oil film thickness.

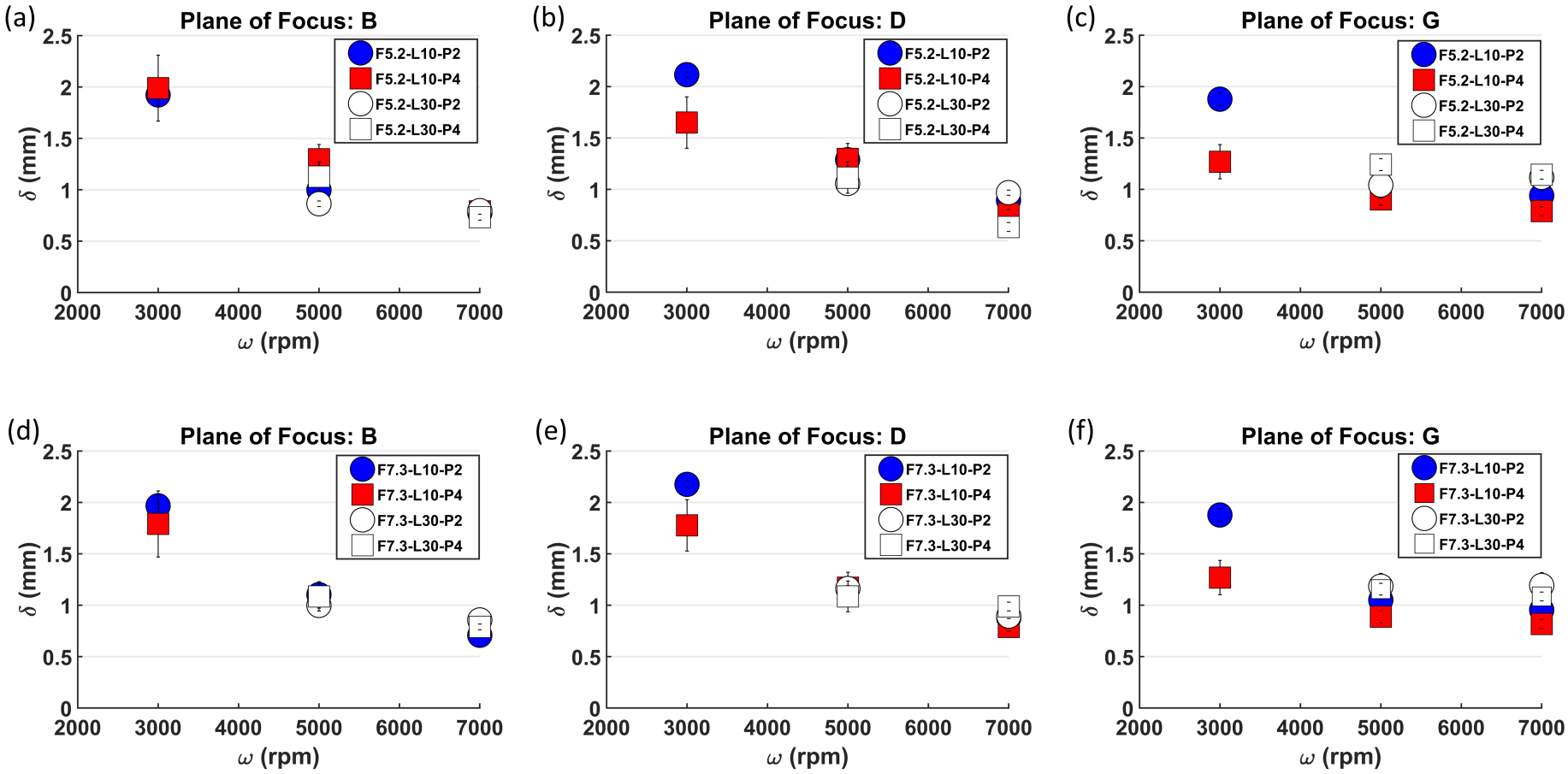


Figure 4.28: Variation of oil film thickness (δ) comparing co-current and counter-current regions (P2 and P4). Based on effect of shaft rotational speed, bearing axial load and oil flow rate. Planes B, D and G.

4.2.8.1 Effect of Speed, Gravity and Flow Rate

Based on the analysis, it is observed that the magnitude of oil film thickness lies between 0.7 mm and 2.2 mm for all flow conditions considered in present study at viewing position P2 and between 0.6 mm to 2 mm for all points at counter-current side. The most significant observation from these plots is that the oil film thickness decreases with increase in shaft rotational speed. In particular, for planes B and D, on the co-current side, δ at 5000 rpm is roughly half the value at 3000 rpm. There is a further decrease of 25 % at 7000 rpm as compared to 5000 rpm at planes B and D. The dependence of oil film thickness on shaft rotational speed can be explained in the following manner (following Glahn and Wittig [15]): increase in shaft rotational speed increases the circumferential air velocity in the core flow. As a result, the interfacial shear force increases. Consequently, the film velocity is increased. To satisfy continuity of mass, resultantly, the oil film thickness decreases.

It is observed that the percentage decrease in oil film thickness with increase in shaft rotational speed is less in the counter-current regime as compared to co-current regime. At planes B and D film thickness at 5000 rpm is roughly 60 % of the value at 3000 rpm. This can be understood as follows. In the counter-current regime the interfacial shear force at the air-oil interface has to overcome the opposing gravity effect. As a result, at same shaft rotational speed the resultant film velocity is lower in the counter-current regime as compared to co-current regime. Thus, the percentage reduction in oil film thickness in counter-current regime is lower.

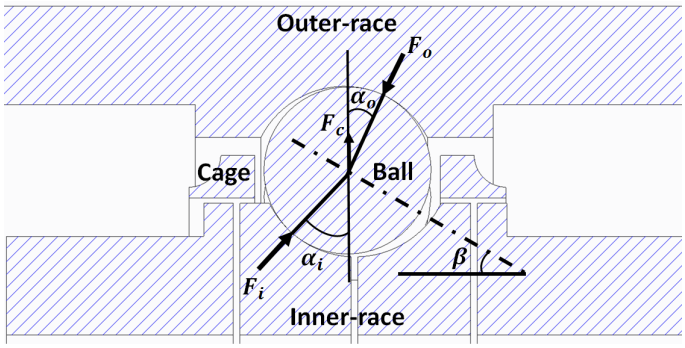
Film thicknesses at plane G, closer to the bearing tend to be slightly lower than at B and D. Also, at plane G it is observed that there is significant difference between the two viewing positions and in particular, the magnitude of oil film thickness is less at P4 as compared to P2 at a given shaft rotational speed. This is seen at plane B as well but the difference between co- and counter-current regimes' δ is less. At plane G the increase in shaft speed from 5000 rpm to 7000 rpm produces very little change in film thickness. This trend signifies axial variation of δ along the axial length from a region close to the ball to a region close to front face (i.e. from plane G to plane B). This underlines the importance of oil film thickness determination at various axial planes as δ is a local parameter which depends on both (a) azimuthal angle along the circumference and (b) axial distance in the bearing chamber.

Comparing Figure 4.28a-c with Figure 4.28d-f shows that increase in input volume flow rate did not produce significant variation in oil film thickness. There is some slight differences at both viewing positions (P2 and P4). However, the variations are not consistently up or down and are in any case essentially insignificant.

4.2.8.2 Effect of Axial Bearing Load

The variation of oil film thickness with change in axial bearing load is observed to be axial plane-specific. In particular, the variation in δ is insignificant with change in load at both co-current and counter-current sides at the outermost plane of visualisation (i.e. plane B). However at Plane G (Figure 4.28c and Figure 4.28f). The higher load cases (open symbols compared to filled) show slightly thicker films (around 30 % or so) at shaft speeds of 5000 rpm and 7000 rpm for both input oil flow rates.

This is interesting because Flouros in his 2004 study of an aero-engine ball bearing found very little change in split of oil front-to-rear across his test bearing as a function of load [94]. Preliminary analysis of scavenge data here also suggests very little change in front-rear split at high load compared to low load, this was based on the assessment of data-log file of the flow-meter. Foord [15] developed an analysis approach for high speed bearings. With reference to Figure 4.29, it is known that at higher axial load the point of contact of ball with outer-race travels clockwise as compared to its contact point at lower load moving further towards the lip and increasing the outer contact angle (α_0). The inclination angle of ball rolling axis (β) also increases at higher load. Consequently, the channel between the outer-race and ball opens up at higher load as compared to lower load. This may lead to a reduced pressure difference across the annular gap between cage and outer race leading to slower axial flowrate in the film and thus thicker film. The second source of oil mass into film, that disintegrated from cage-edge, is largely unaffected by load, perhaps not too surprising as α_i is not much affected by load. The difference in film thickness with respect to load is only really observed near the ball. At planes B and D no effect of load on film thickness was observed.



F_c = Inertial force acting at ball centre
F_i = normal force at inner contact
F_o = normal force at outer contact
α_i = inner contact angle
α_o = outer contact angle
β = inclination angle of ball rolling axis

Figure 4.29: Free body diagram depicting key forces and angles characterising ball-bearing statics [93]

4.2.9 Curve Fitting for Oil Film Thickness with Respect to Varying Operating Condition

The relation between oil film thickness with respect to changing operating condition such as shaft speed, oil flow-rate and bearing axial load can be expressed in a mathematical expression. This expression would be useful for users who are interested in using the film thickness data for bearing chamber design or CFD. In this section, empirical models for the oil film thickness as a dependent variable were presented as a function of independent variables – shaft speed, flow-rate and bearing axial load.

Three curve fitting functions available in MATLAB were tested, namely, Polynomial, Power Series and Nonlinear Regression Model. A high order polynomial function was tested and subsequently excluded since it fails to capture the trend and has predicted a negative film thickness at shaft speed of 9000 rpm.

In terms of second order Power Series, the film thickness variable can be expressed as $y = ax^n + b$, where a, b and n are the derived coefficients and x is the shaft speed. The determination factor (typically known as R square) was highly accurate with a value of 0.99 but this curve fitting function only permits a single independent variable (e.g. shaft speed) to be included in the model.

By taking the third approach, a general nonlinear regression model in the form of $\delta = a\,\omega^b\,f^c\,l^d$ was proposed for the curve fitting exercises. In the above expression, δ represents the film thickness, ω is the shaft speed, f is the oil input total flow rate and l is the bearing axial load. The coefficients calculated are a, b, c and d respectively.

The same data from Section 4.2.8 is used, the results are subdivided into co-current and counter-current side and are shown in Figure 4.30 subplot (a) to (f). Subsequently, the empirical models for film thickness as a function of operating condition are tabulated in Table 4.7. The models were derived based on having the unit for δ as millimetre, f as litre/min and l as kN.

In the Table 4.7, the weighted variable was given in the column - Main Factor, it is the main variable that affects the trend of the fitted curve, the plane of focus for the model and its angular position are listed as well. Note that for the same test condition at Plane of Focus G, an additional curve was fitted to obtain the trend that is affected by the parameter load. This was achieved by removing the data point at 3000 rpm.

Referring to Figure 4.30, the x-axis refers to shaft speed and y-axis refers to film thickness. The trend lines shown here are mainly for changing speed at fixed flow rate and load since their

effects were not significant with the exception of Plane G where the additional trend line for the effect of load was given.

An example of the trend line for the empirical model, $\delta = 11885\ \omega^{-1.1043}\ f^{0.13872} l^{-0.0622}$ at constant flow rate 5.2 lpm and axial load 10 kN is shown in Figure 4.30(a). The trend line enables the determination of the film thickness based on a specific operating speed. At operating shaft speed of 3000, 5000 and 7000 rpm respectively, the model yields film thickness of 1.872, 1.065 and 0.7345 mm respectively. For other models, the same calculation procedure applies based on the coefficient provided in the Table 4.7.

Table 4.7: List of coefficients derived for the empirical model using nonlinear regression model

No	Main Factor	Plane of Focus	Angular Position	a	b	c	d	R Square
1	Speed	B	P2	11885	-1.1043	0.13872	-0.062185	0.967
2		D		8638.1	-1.0216	0.0047	-0.0609	0.977
3		G		819.9	-0.8022	0.1005	0.0506	0.836
4	Load			0.5299	-0.0317	0.4375	0.0782	0.501
5	Speed	B	P4	9854.8	-0.9983	-0.2536	-0.0428	0.984
6		D		1201.4	-0.8432	0.1539	-0.0132	0.916
7		G		48.312	-0.5126	-0.0804	0.2522	0.923

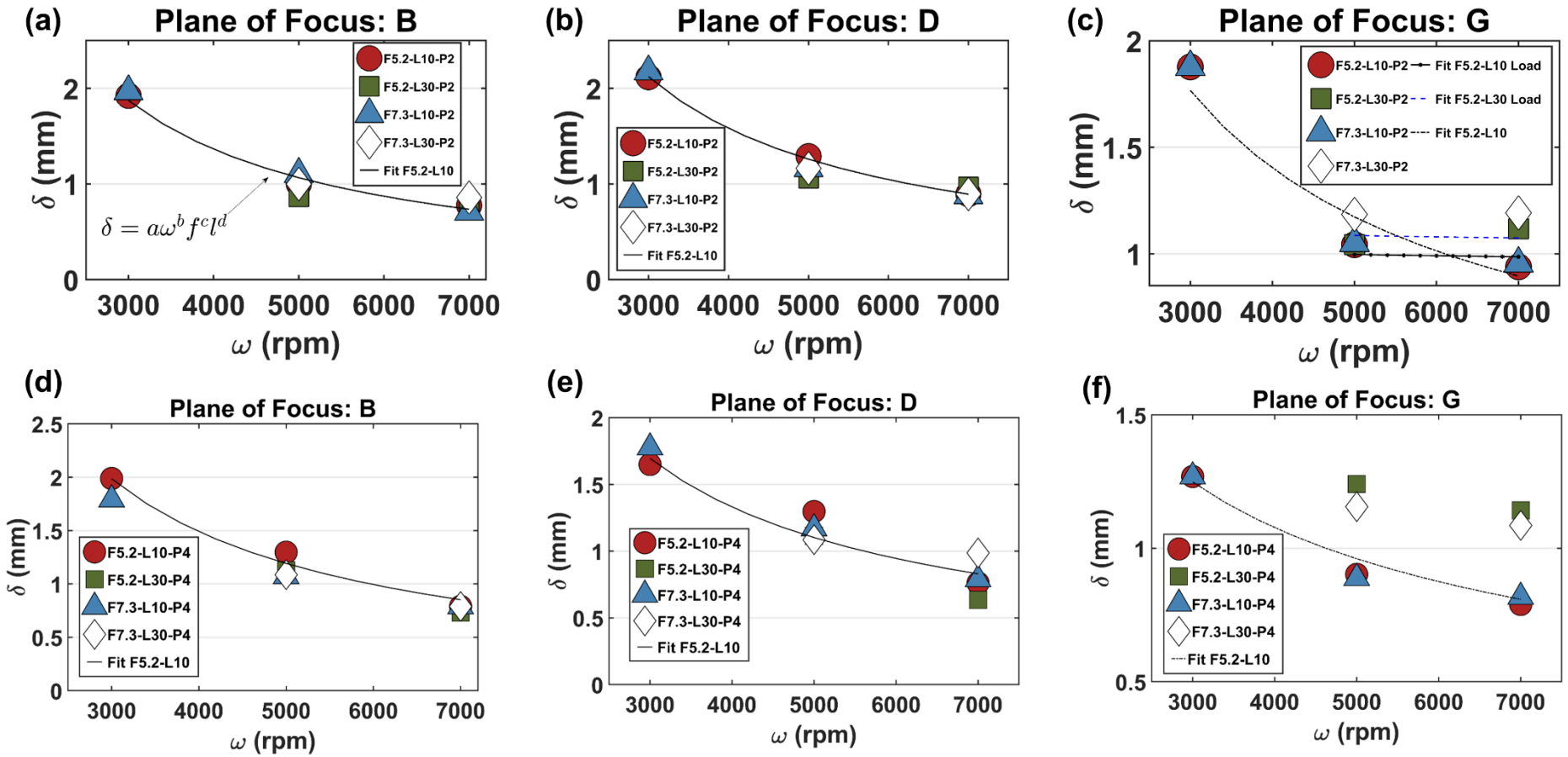


Figure 4.30: Curve fitted for oil film thickness versus changing shaft speed, oil flow rate and bearing axial load.
Subplot (a), (b) and (c) corresponded to curve fitted at co-current regime (P2).
Subplot (d), (e) and (f) corresponded to curve fitted at counter-current side (P4)

4.2.10 Error Propagation

In previous section, the correlation of film thickness with respect to various operating parameters (i.e. shaft speed, oil flowrate and bearing axial load) was derived. This section reports the error propagation on the response parameter film thickness caused by the accuracy of test instruments. To begin with, the total uncertainty of film thickness, $\Delta\delta$ derived from the generalized definition of Drosg [110] is provided in Equation (4.5) as follows:

$$\Delta\delta = \sqrt{(\Delta\delta_\omega)^2+\left(\Delta\delta_f\right)^2+(\Delta\delta_l)^2}$$
$$= \sqrt{\sum\left(\frac{\partial\delta}{\partial\omega}\right)^2.(\Delta\omega_{acc})^2+\left(\frac{\partial\delta}{\partial f}\right)^2.(\Delta f_{acc})^2+\left(\frac{\partial\delta}{\partial l}\right)^2.(\Delta l_{acc})^2} \quad (4.5)$$

Where $\Delta\delta_\omega$ is the derivative of film thickness correlation with respect to shaft speed, $\Delta\delta_f$ is the derivative of film thickness correlation with respect to oil flowrate, $\Delta\delta_l$ is the derivative of film thickness correlation with respect to bearing axial load.

Subsequently, $\Delta\omega_{acc}$, Δf_{acc} and Δl_{acc} are the accuracy of the test instrument in absolute value. An example of the error propagation or the total uncertainty of the film thickness for 3000 rpm at constant oil flowrate 5.2 lpm and bearing axial load 10 kN is provided as follows:

Firstly, the film thickness as a function of the shaft speed, oil flowrate and bearing axial load; $\delta = 11885\ \omega^{-1.1043}\ f^{0.13872} l^{-0.0622}$ is used. The derivatives of the film thickness with respect to shaft speed, oil flowrate and bearing axial load are given in Equation (4.6), (4.7) and (4.8) respectively.

The uncertainty component (derivative) of the film thickness with respect to shaft speed:

$$\frac{\partial\delta}{\partial\omega} = -13124.61\ \omega^{-2.1043} f^{0.13872} l^{-0.0622} \quad (4.6)$$

The uncertainty component (derivative) of the film thickness with respect to oil flowrate:

$$\frac{\partial\delta}{\partial f} = 2758.78\ \omega^{-2.1043} f^{-0.86128} l^{-0.0622} \quad (4.7)$$

The uncertainty component (derivative) of the film thickness with respect to bearing axial load:

$$\frac{\partial\delta}{\partial l} = -739.25\ \omega^{-1.1043} f^{0.13872} l^{-1.0622} \quad (4.8)$$

The accuracy of the shaft speed, $\Delta\omega_{acc}$ is 1 ± 0.271 rpm, Δf_{acc} is the accuracy of flow meter corresponding to 0.05 lpm and Δl_{acc} is the accuracy of the load cells which corresponds to 0.00269 kN. Therefore, the total uncertainty of the film thickness due to the accuracy of test instruments at 3000 rpm, 5.2 lpm and 10 kN is $\Delta\delta = 5.848 \times 10^{-5}\, mm$ and the relative uncertainty is calculated as 0.0031%. For shaft speed of 3000 rpm to 7000 rpm, the range of relative uncertainty for film thickness is 0.0031% to 0.000793%.

4.3 Mechanisms of Oil Breakup at Aero-engine Ball Bearing

This section describes experimental work conducted for the investigation of oil breakup from the edge of the orbiting cage based on observation as well as semi-empirical approach. Fundamental studies of liquid breakup from rotary disks and cups were systematically reviewed to find if geometrical and dynamical similarity exist, could it be scaled or be applied to that of bearing shedding. These include reviewing work of Fraser *et al.* [111], Dombrowski and Lloyd [112], Matsumoto *et al.* [26], and Frost [21]. Atomisation of droplets from rotating elements are fundamentally different to that of nozzle sprays. Droplets were produced either by Rayleigh-Taylor instabilities, Plateau-Rayleigh or Wave-Disintegration. The sizes of droplets produced are generally more uniform for ligament-type breakup as compared to jet-breakup from nozzle sprays. Lefebvre [32] suggested that the shape factor in droplet diameter distribution for rotary atomiser is as high as 7. Whereas, for spray they lie between 1.5 and 4. A higher value of shape factor produces uniform size droplets. The geometry of ball bearing cage could be seen as a hybrid of both cup and disk. With reference to Figure 4.31, the geometry could be explained as following:

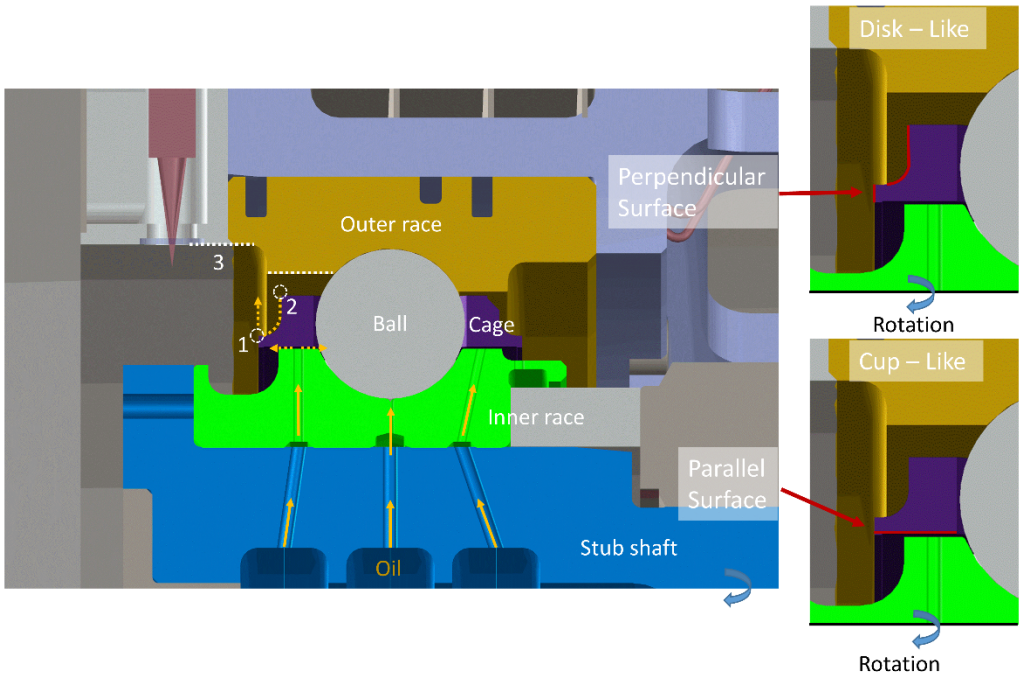


Figure 4.31: Cross-sectional view of *Trent* 1000 HP location bearing showing edges of bearing cage (marked as location '1' and '2') and static surfaces (marked as '3')

Oil is fed through front feed as centrifugal force is applied. The oil flows towards the cage landing and therefore splitting in both direction towards the ball and into the front chamber. The magnitude of centrifugal force is so significant that the oil sticks to the surface of the cage parallel to the shaft rotational speed, this could be seen in Figure 4.31 inset image labelled 'cup-like'. With continuous supply of oil, the oil exits axially towards the cage edge known as location '1' or flows along the cage surfaces towards '2' if the centrifugal force is low. The small perpendicular surface at '1' is only 2 mm which appears to be disk-like in shape. At low rotational speed, the oil could leave at location '2'. Extensive high-speed visualisations will be used to investigate these locations. Note that the axial plane of focus of cage edge is 30 mm or plane F.

To explain the definition of rotating disk or cup, following sketches were given in Figure 4.32. Based on Figure 4.32a, a common type of rotary disk is shown where oil is fed axially towards the perpendicular face of the disk which is rotated by a mechanical force. It produces droplets at the rim as the liquid gains speed via the rotating action. In various cases, it was reported that slippage of fluid and rotating surfaces occur which gives a much lower droplets velocity but to a minimum degree. Meanwhile for rotary cup in Figure 4.32b, oil is fed through a nozzle by direct impingement or in some cases, through a co-axis hole in the rotary cup. Oil flows along the parallel surfaces before leaving via the edge. It was reported that the angle and sharpness of the edge at the end of the rotary cup has profound impact on oil disintegration [112].

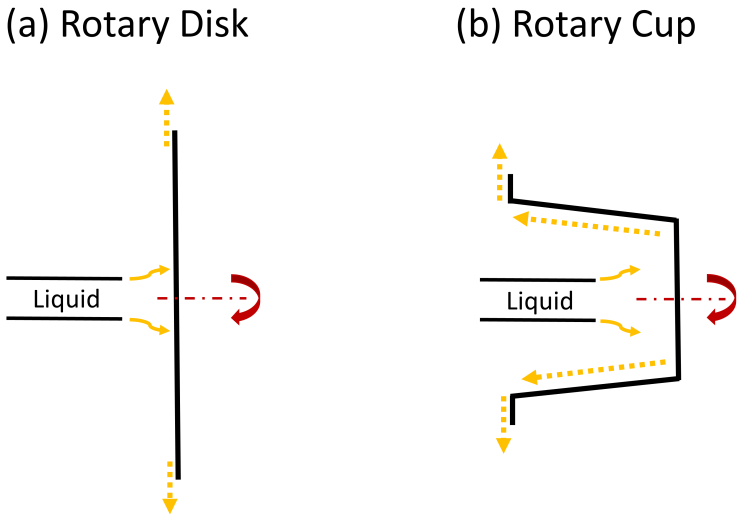


Figure 4.32: Direction of liquid flow for (a) Rotary disk and (b) Rotary cup

4.3.1 Experimental Test Cases for Characterisation of Oil-Breakup

Based on previously published literature of fundamental investigations of rotary systems, it was suggested that oil breakup mechanisms are dependent on rotational speed, liquid flow rate and fluid properties. For purpose of investigating the above features, HS images were taken at axial plane of focus F by parametrically changing the rotational speed to assess the oil-breakup regimes. It was rather unfortunate that the tests for changing oil flow rate, fluid properties and axial loads were deemed not possible due unexpected relocation of the test facility which impeded the schedule. Based on previously published observations on simple rotary devices, it was understood that three regimes existed which are known as direct-drop, ligament and oil sheet. The following experimental test cases were conducted to visualise these oil shedding mechanisms at cage edge and they are tabulated in Table 4.8:

Table 4.8: Experimental test cases considered for the investigations of oil breakup mechanisms based on changing: rotational speed, at constant flow rate and axial load

No	Rotational Speed (rpm)	Flow Rate (lpm)	Axial Load (kN)	Test Case Name
1	1000	5.2	10	S1000-F5.2-L10-P2
2	1100			S1100-F5.2-L10-P2
3	1200			S1200-F5.2-L10-P2
4	1300			S1300-F5.2-L10-P2
5	1500			S1500-F5.2-L10-P2
6	1700			S1700-F5.2-L10-P2
7	1800			S1800-F5.2-L10-P2
8	1900			S1900-F5.2-L10-P2
9	2000			S2000-F5.2-L10-P2
10	2200			S2200-F5.2-L10-P2
11	2400			S2400-F5.2-L10-P2
12	2600			S2600-F5.2-L10-P2
13	2800			S2800-F5.2-L10-P2
14	3000			S3000-F5.2-L10-P2
15	3200			S3200-F5.2-L10-P2
16	3400			S3400-F5.2-L10-P2
17	3600			S3600-F5.2-L10-P2
18	3800			S3800-F5.2-L10-P2
19	4000			S4000-F5.2-L10-P2

20	4300			S4300-F5.2-L10-P2
21	4500			S4500-F5.2-L10-P2
22	4700			S4700-F5.2-L10-P2
23	5000			S5000-F5.2-L10-P2
24	5300			S5300-F5.2-L10-P2
25	5500			S5500-F5.2-L10-P2
26	5700			S5700-F5.2-L10-P2
27	6000			S6000-F5.2-L10-P2
28	6300			S6300-F5.2-L10-P2
29	6500			S6500-F5.2-L10-P2
30	6700			S6700-F5.2-L10-P2
31	7000			S7000-F5.2-L10-P2

Table 4.8 above shows 31 test cases for speed of 1000 rpm to 7000 rpm which were carried out at fixed flow rate of 5.2 lpm and constant axial load of 10 kN to investigate the mechanisms of oil disintegrations. Note that the cage speed is 50% of rotational speed [93].

4.3.2 Qualitative Observations of Oil Shedding from Cage Edge

This section describes qualitative analysis of oil-breakup from the orbiting cage based on incremental increase in shaft speeds from 1000 rpm to 7000 rpm at constant oil input flow rate (5.2 lpm) and bearing axial load (10 kN). Corresponding to the trends in available literature, three commonly occurring disintegration modes were reported; direct-drop, ligament, sheet. The following quantitative analysis is aided with the reference of Figure 4.33 to Figure 4.44.

At initial shaft speed of 1000 rpm, the effect of surface tension and viscous forces were dominant and significant with respect to centrifugal force (i.e. inertia) which resulted in a fully wetted cage surface (see Figure 4.33a). The centrifugal force pushes the oil towards the outermost edge of the bearing cage (as labelled in Figure 4.33b). An oil torus was formed at the edge of location ‘2’ (classification of location ‘2’ can be referred in Figure 4.31 of Section 4.2.10), it is known as formation of ring by Fraser *et al.* [111]. These were the locations where the oil droplets are generated. Subsequently droplets of uniform sizes were released from the outermost edge due to centrifugal force (see Figure 4.33d,e). The observations were unique as they are atomisation by direct-drop formation occurred from the cage of an aero-engine ball bearing rotating at half the shaft speed. Although the understanding of droplet generation from the bearing cage at low shaft

speed may deemed unimportant for aero-engine application as engines do not operate at such speed. Nonetheless, it is useful from a CFD validation perspective and other fundamental study of fluid mechanics.

By increasing the speed to 1700 rpm, distinctive line of threads were formed along the edge of the bearing cage which is referred as location '1' in Figure 4.31. These threads were known as ligaments by earliest investigators and the phenomenon is termed as atomisation by ligament formation. To obtain ligaments, critical condition has to be met by either achieving critical flow rate (q) or speed (ω). At these conditions, the forces between centrifugal, viscous and surface tension are all in equilibrium such that waves were able to form on the surfaces creating the thread-shape ligaments when being amplified. (see Figure 4.34a). Due to the complexity of the geometry and lack of controllability of oil split, oil sheet is intermittently observed along with ligaments during one part of the cycle (see Figure 4.34b). This corresponded to the analysis made by Frost [21] that the eccentricity in oil feed is causing both regimes to occur in part of the cycles (see Figure 2.5). It is possible to deduce that the cycle where oil sheet existed is due to higher oil flow rate, whereas the ligament existing part is due to lower oil flow rate.

A unique feature of the oil sheet observed at such speed is the smoothness of the oil surface. They are undisturbed, pristine and extended radially outward as much as 6.85 mm from location '1'. This uniqueness was not seen for oil sheet of higher speed (i.e. ω > 4300 rpm) where they are ruffled throughout the radial and azimuthal direction (alternative meaning of ruffled is disordered). As such we referred them as 'laminar sheet' in this thesis and also through publication made by Santhosh *et al.* of G2TRC [109]. Example of laminar sheet is given in Figure 4.34c. At the periphery of the oil sheet; threads and droplets were produced (see Figure 4.34d,e). This type of disintegration mechanism was also known as 'rim disintegration' by Fraser *et al.* [111]. The effect of surface tension can be seen where they retracts or restore the sheet due to rupture. Surface tension pulls the sheet in the direction of opposing centrifugal force to achieve the smallest surface area where Fraser [111] described them in terms of contracting velocity of oil sheet (see Figure 4.34e for contraction). Correspondingly, the ligaments at low speed are known as 'primary ligament' due to their distinctive spacing and emission from a controlling surface (in location '1'). Another class of ligaments will be introduced in later part where they are different in many ways.

At 2000 rpm, sheet and ligament continue to exist. However, it is conceivable that more rupture occurs (see Figure 4.35a) and sheet continues to extend radially away from the edge. Moving into higher speed of 2400 rpm, the modes of disintegrations are still primary ligament with laminar sheet. At this speed, it is possible to deduce that ligaments grew in number along the same arc length (comparing Figure 4.36a of S2400-F5.2-L10-P2 with respected Figure 4.34a of S1700-

F5.2-L10-P2). Their diameters (visually) also reduced with respect to ligaments of lower speed (e.g., $\omega = 1700$ rpm). At subsequent speed of 3200 rpm, the frequency of primary ligament reduces, sheet no longer occupy the whole length of the arc instead they are shorter in both radial and azimuthal direction (see Figure 4.37b). In addition, the ligaments are also thinner and higher in number as indicated by Figure 4.37a,d. This corresponded with the small scale wave phenomenon at higher shearing rate (i.e. capillary waves which will be explained in Section 4.4), the wavelength decreases and hence allowing more ligaments to occupy the same surface.

In between speed of 3800 rpm and 4300 rpm, fully laminar sheet no longer existed. Oil sheet appears to be disordered and fundamentally different with that of laminar sheet (see Figure 4.40a-e). In particular, at higher speed the shearing effect of the gas surrounding the radially propagating oil sheet superimposed causing a more disturbed waves (i.e. sheet). These waves are the same as those observed by Fraser in spinning cup and can be either sinuous or dilatational or a combination of both. This type of liquid breakup mechanism is termed by Fraser as ‘wave disintegration’. The oil sheet disintegrates through half wavelength hence resulting in shorter oil sheet. The prominent feature of a wave-disintegrated sheet is its ruffled edges (see Figure 4.39a, Figure 4.40c, Figure 4.41b). The ligaments subsequently breaking from these ruffled sheets are termed ‘secondary ligaments’ in present study. A key difference between the primary ligaments and secondary ligaments is that in the latter mode, location 1 is no longer the controlling solid surface.

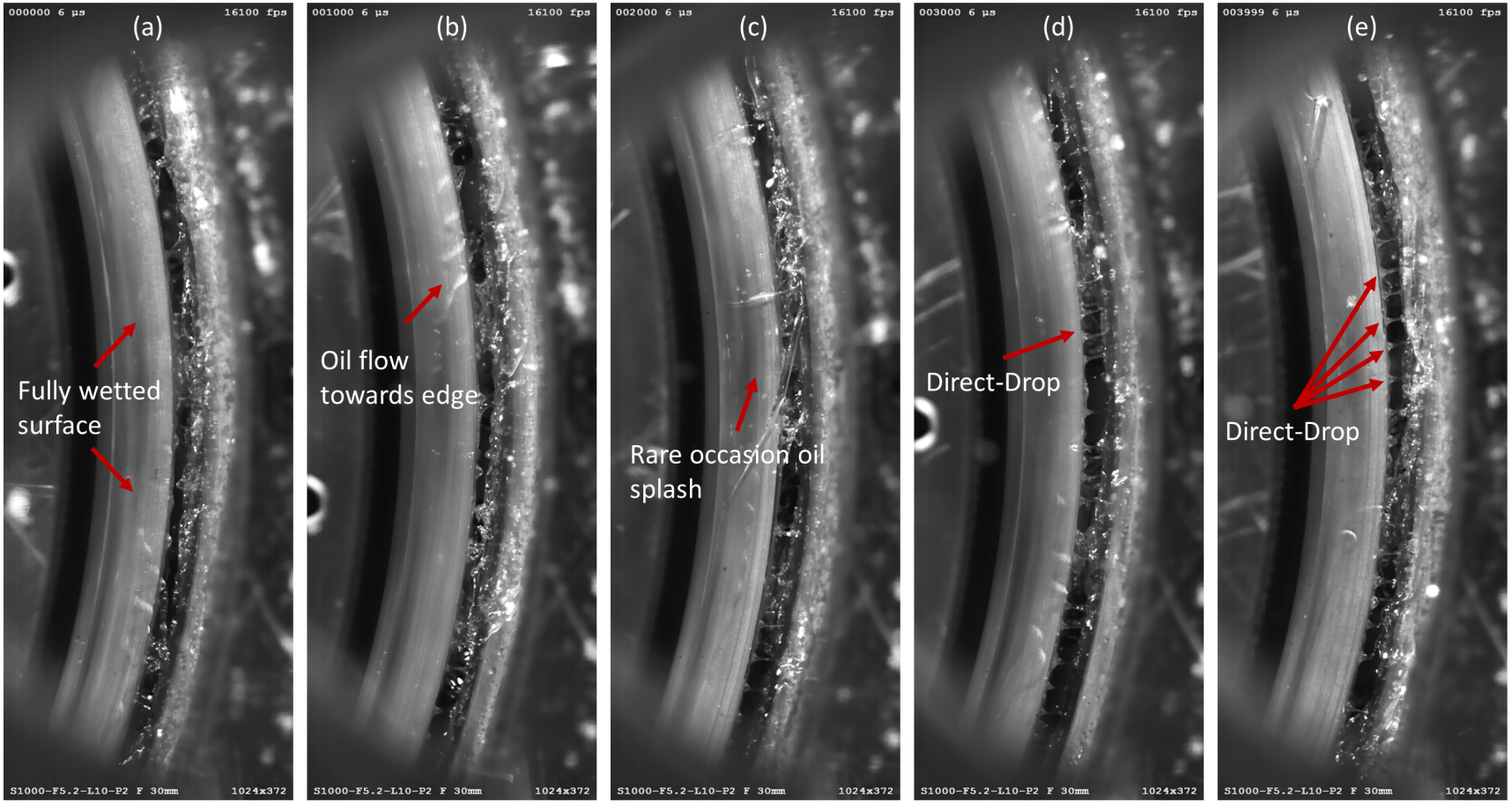


Figure 4.33: Oil-breakup mechanism (direct-drop) as seen from Plane F for S1000-F5.2-L10-P2
(a) $\boldsymbol{t = 0\ s}$ (b) $\boldsymbol{t = 0.062\ s}$ (c) $\boldsymbol{t = 0.124\ s}$ (d) $\boldsymbol{t = 0.186}$ s (e) $\boldsymbol{t = 0.2484}$ s

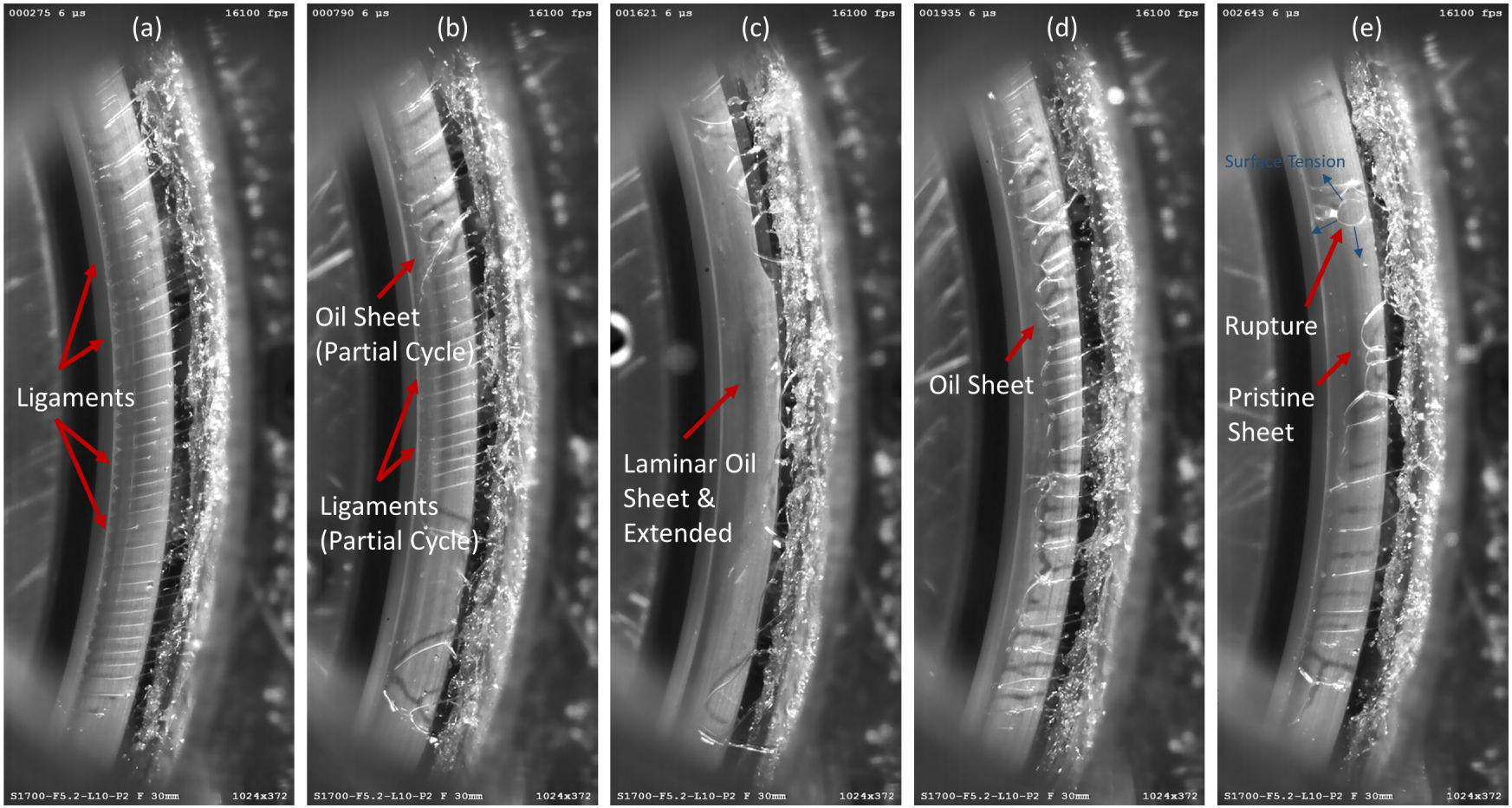


Figure 4.34: Oil-breakup mechanisms (ligament & sheet) as seen from Plane F for S1700-F5.2-L10-P2
(a) $\boldsymbol{t = 0.017}$ s (b) $\boldsymbol{t = 0.049}$ s (c) $\boldsymbol{0.1006}$ s (d) $\boldsymbol{t = 0.120}$ s (e) $\boldsymbol{t = 0.164}$ s

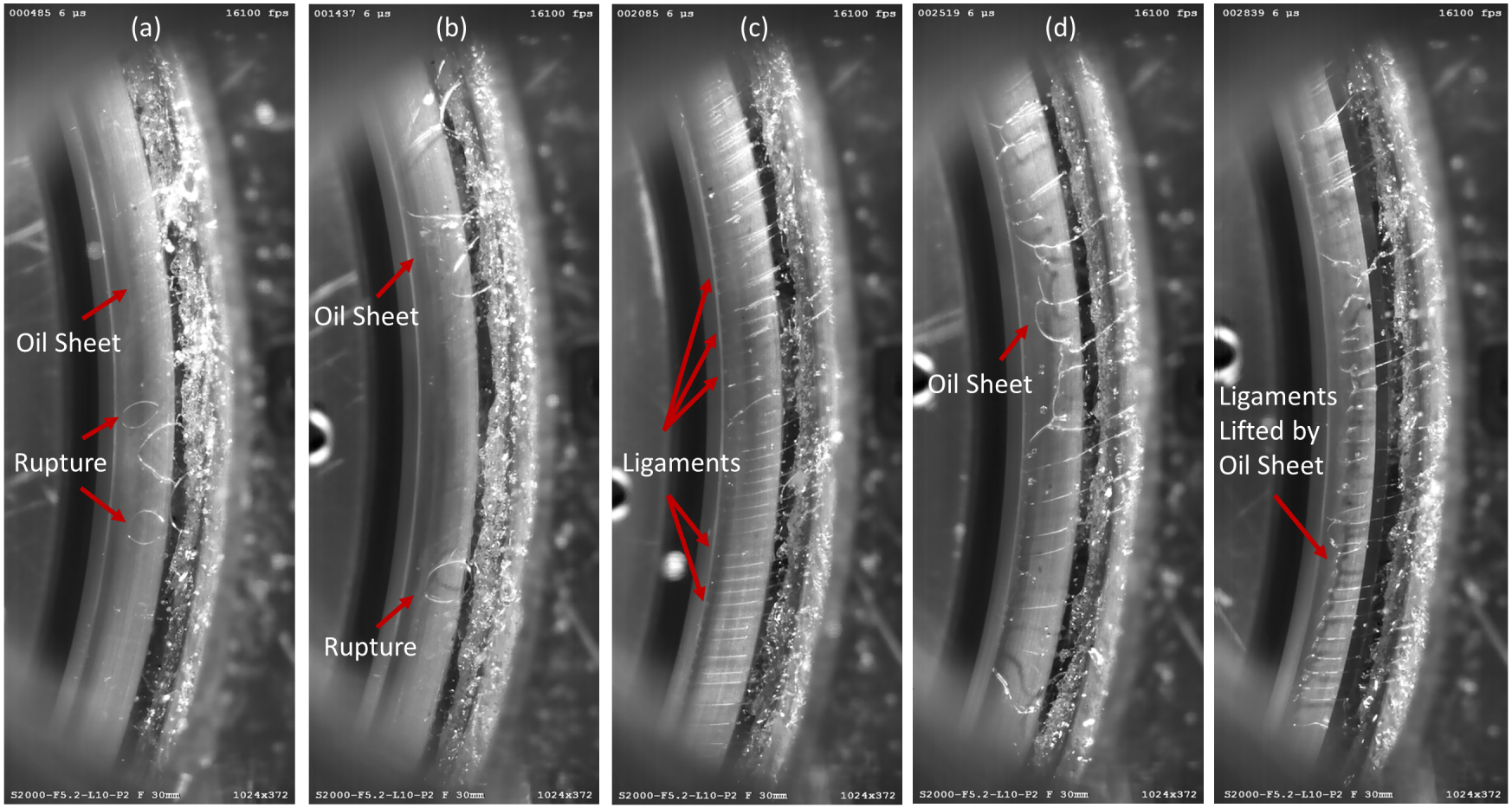


Figure 4.35: Oil-breakup mechanisms (sheet & ligament) as seen from Plane F for S2000-F5.2-L10-P2
(a) $\boldsymbol{t = 0.0301}$ s (b) $\boldsymbol{t = 0.0892}$ s (c) $\boldsymbol{t = 0.1295}$ s (d) $\boldsymbol{t = 0.1564\ s}$ (e) $\boldsymbol{t = 0.1763}$ s

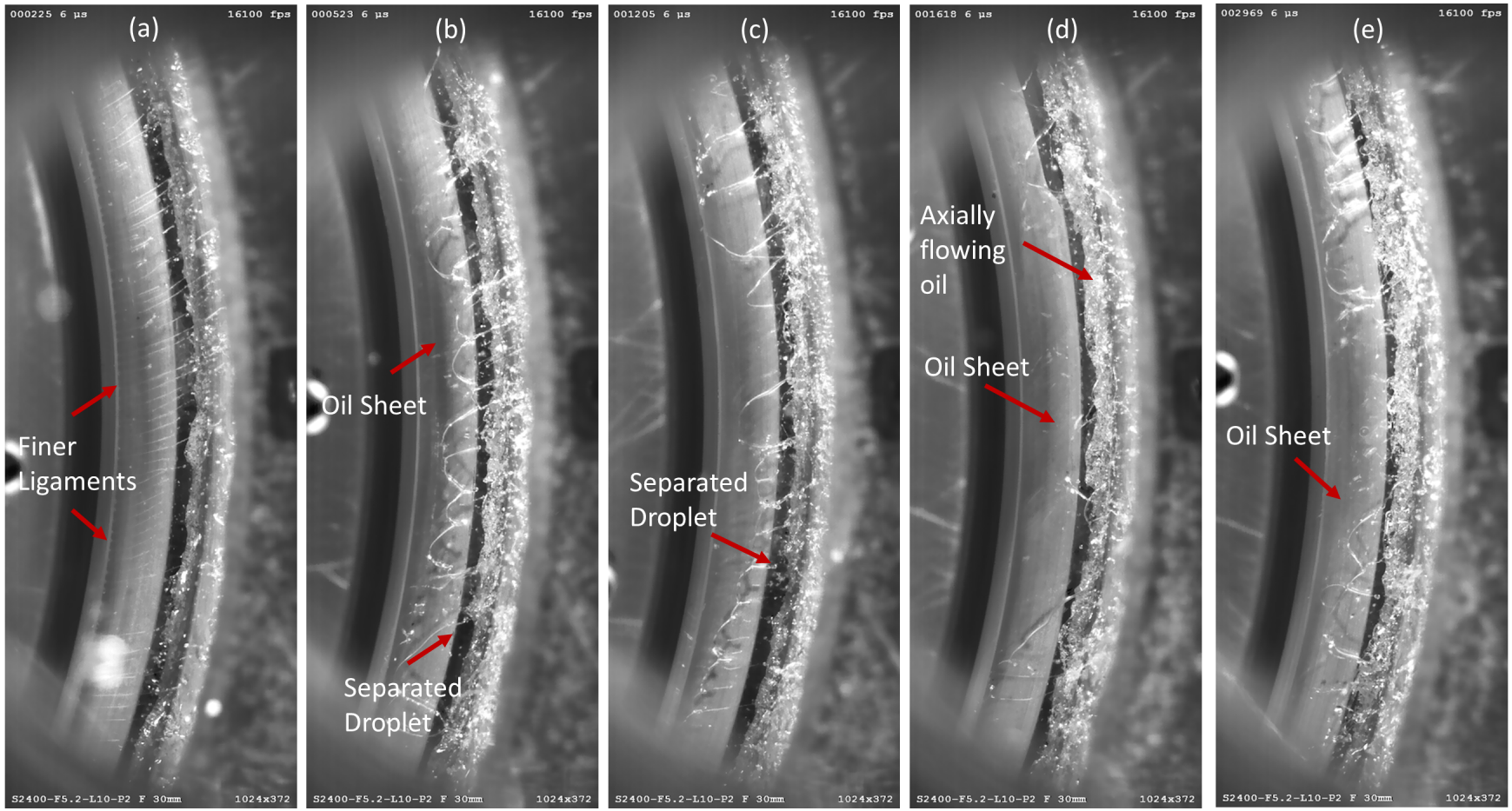


Figure 4.36: Oil-breakup mechanisms (fine ligament & sheet) as seen from Plane F for S2400-F5.2-L10-P2
(a) $\boldsymbol{t = 0.0139}$ s (b) $\boldsymbol{t = 0.0324}$ s (c) $\boldsymbol{t = 0.0748}$ s (d) $\boldsymbol{t = 0.1005\ s}$ (e) $\boldsymbol{t = 0.1844}$ s

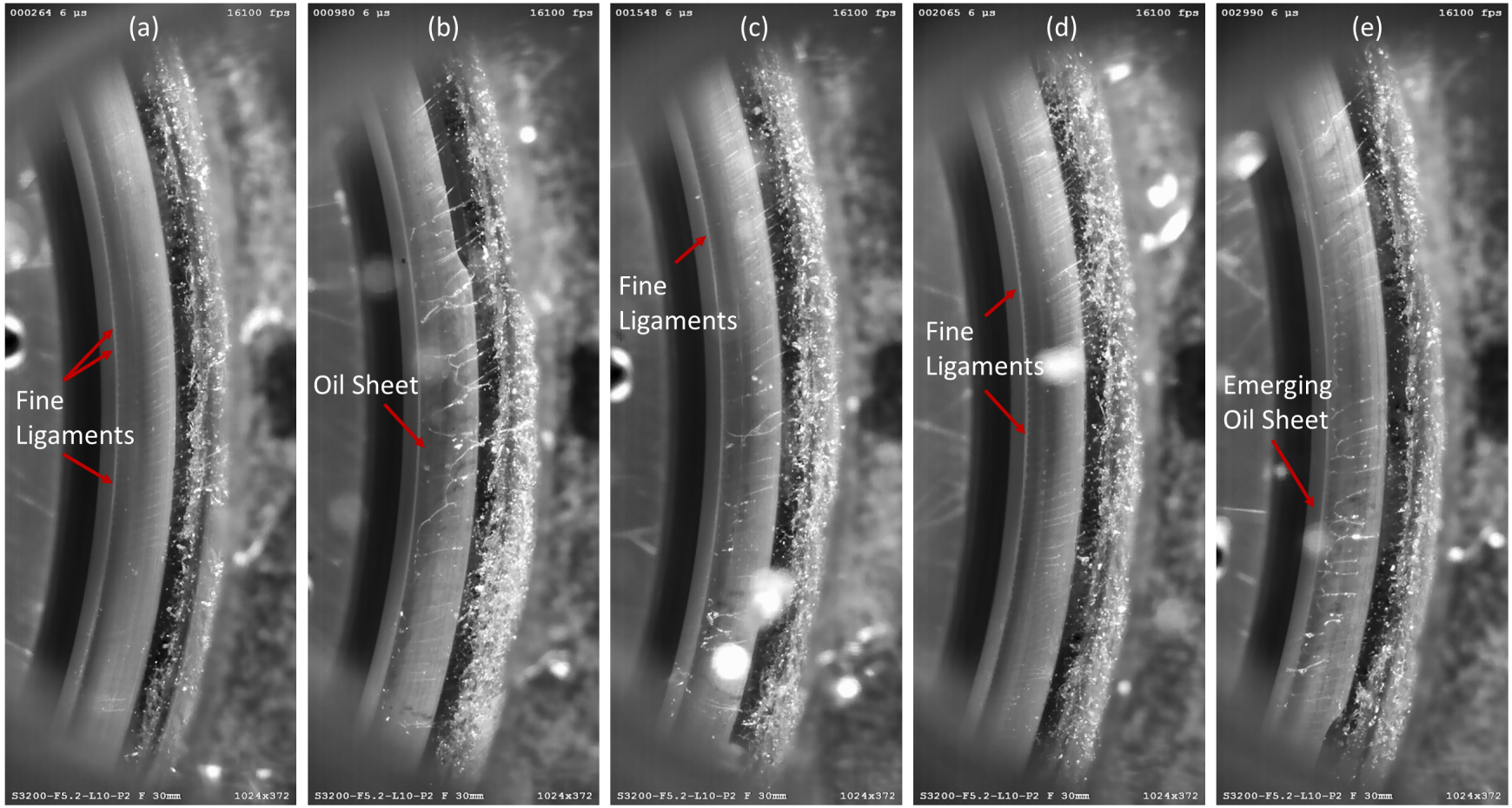


Figure 4.37: Oil breakup mechanisms (finer ligaments & sheet) as seen from Plane F for S3200-F5.2-L10-P2
(a) $\boldsymbol{t = 0.0164}$ s (b) $\boldsymbol{t = 0.0609}$ s (c) $\boldsymbol{t = 0.0961}$ s (d) $\boldsymbol{t = 0.1283}$ s (e) $\boldsymbol{t = 0.1857}$ s

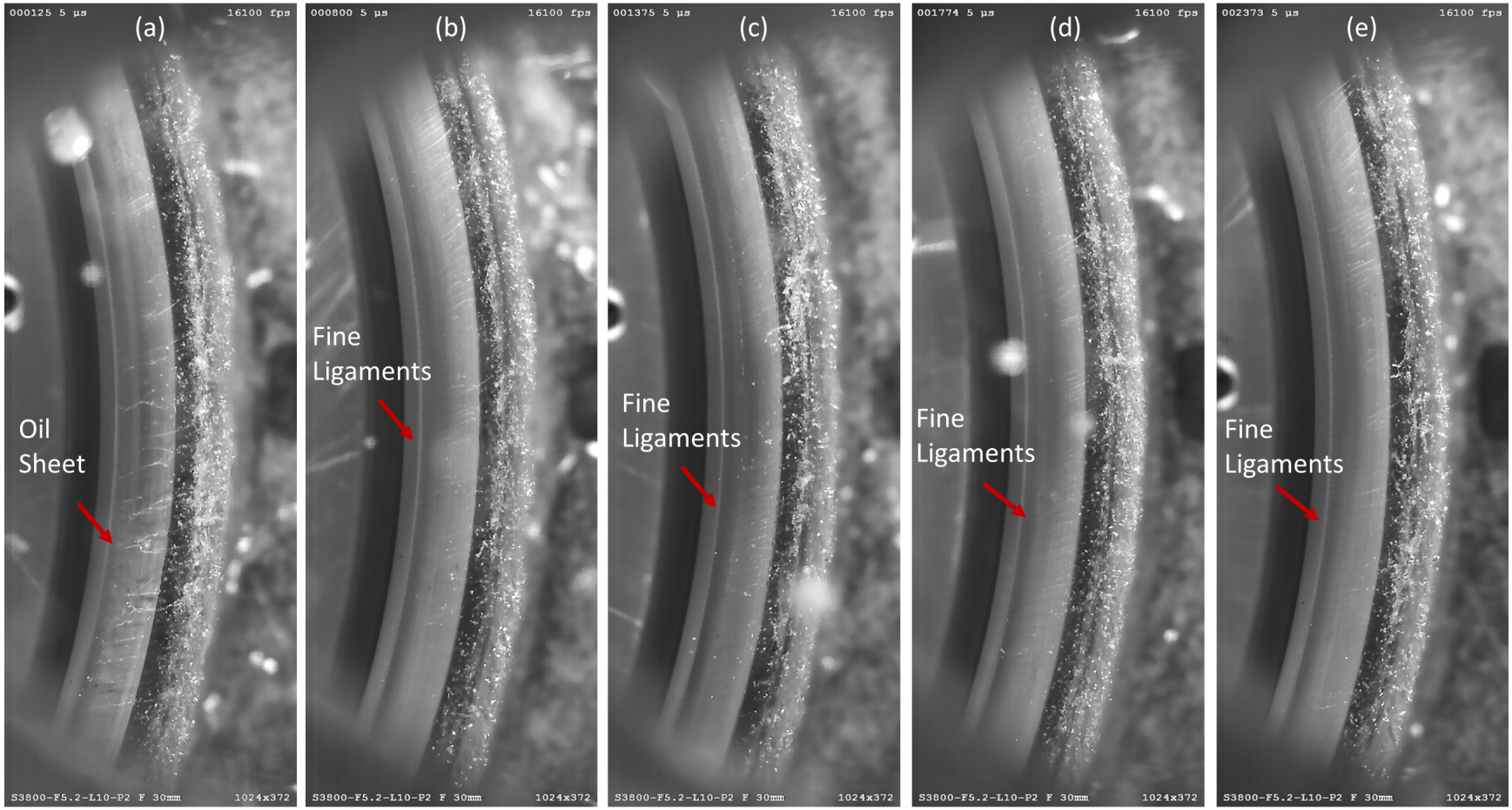


Figure 4.38: Oil-breakup mechanisms (sheet & extra-fine ligament) as seen from Plane F for S3800-F5.2-L10-P2
(a) $\boldsymbol{t = 0.0078}$ s (b) $\boldsymbol{t = 0.0497}$ s (c) $\boldsymbol{t = 0.0854}$ s (d) $\boldsymbol{t = 0.1102}$ s (e) $\boldsymbol{t = 0.1474}$ s

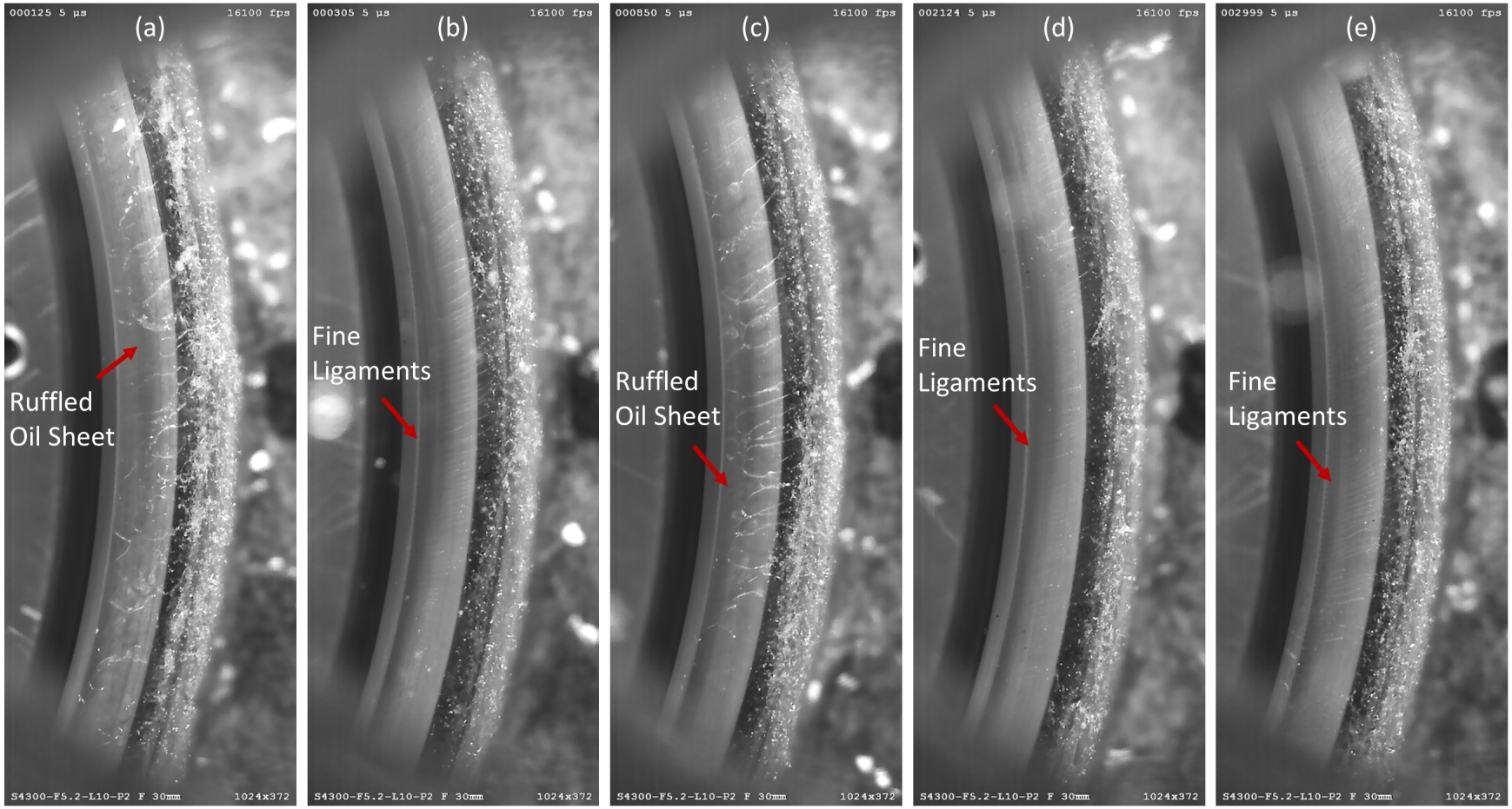


Figure 4.39: Oil-breakup mechanisms (ruffled sheet & finest ligament) as seen from Plane F for S4300-F5.2-L10-P2
(a) $\boldsymbol{t = 0.0078}$ s (b) $\boldsymbol{t = 0.0189}$ s (c) $\boldsymbol{t = 0.0528}$ s (d) $\boldsymbol{t = 0.1319}$ s (e) $\boldsymbol{t = 0.1863}$ s



Figure 4.40: Oil-breakup mechanisms (ruffled sheet) as seen from Plane F for S5000-F5.2-L10-P2
(a) $\boldsymbol{t = 0.0205}$ s (b) $\boldsymbol{t = 0.0450}$ s (c) $\boldsymbol{t = 0.0894}$ s (d) $\boldsymbol{t = 0.1366}$ s (e) $\boldsymbol{t = 0.1863}$ s

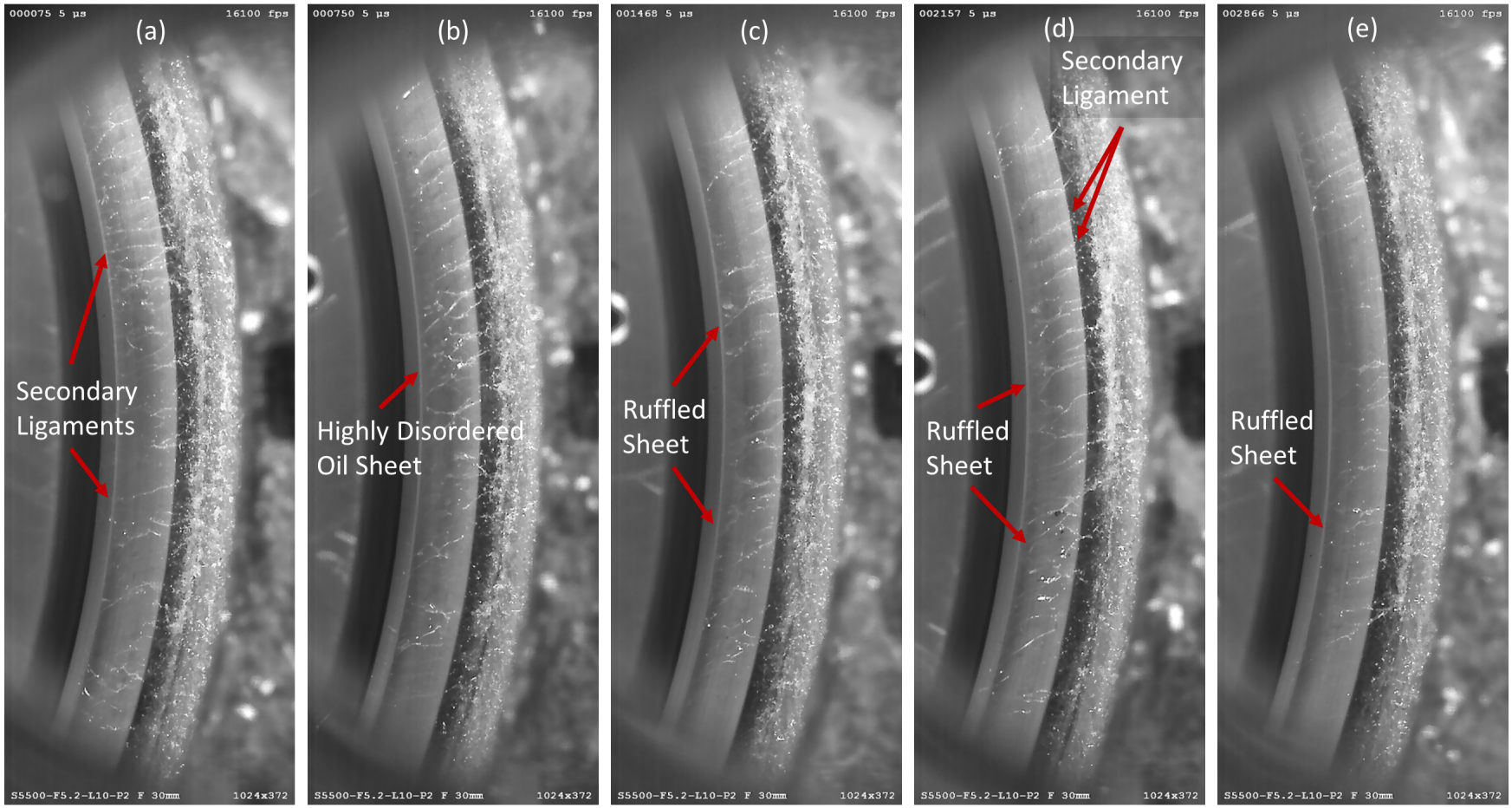


Figure 4.41: Oil breakup mechanisms (secondary ligaments & ruffled sheets) as seen from Plane F for S5500-F5.2-L10-P2
(a) $\boldsymbol{t = 0.0047}$ s (b) $\boldsymbol{t = 0.0466}$ s (c) $\boldsymbol{t = 0.0912}$ s (d) $\boldsymbol{t = 0.1340}$ s (e) $\boldsymbol{t = 0.1780}$ s

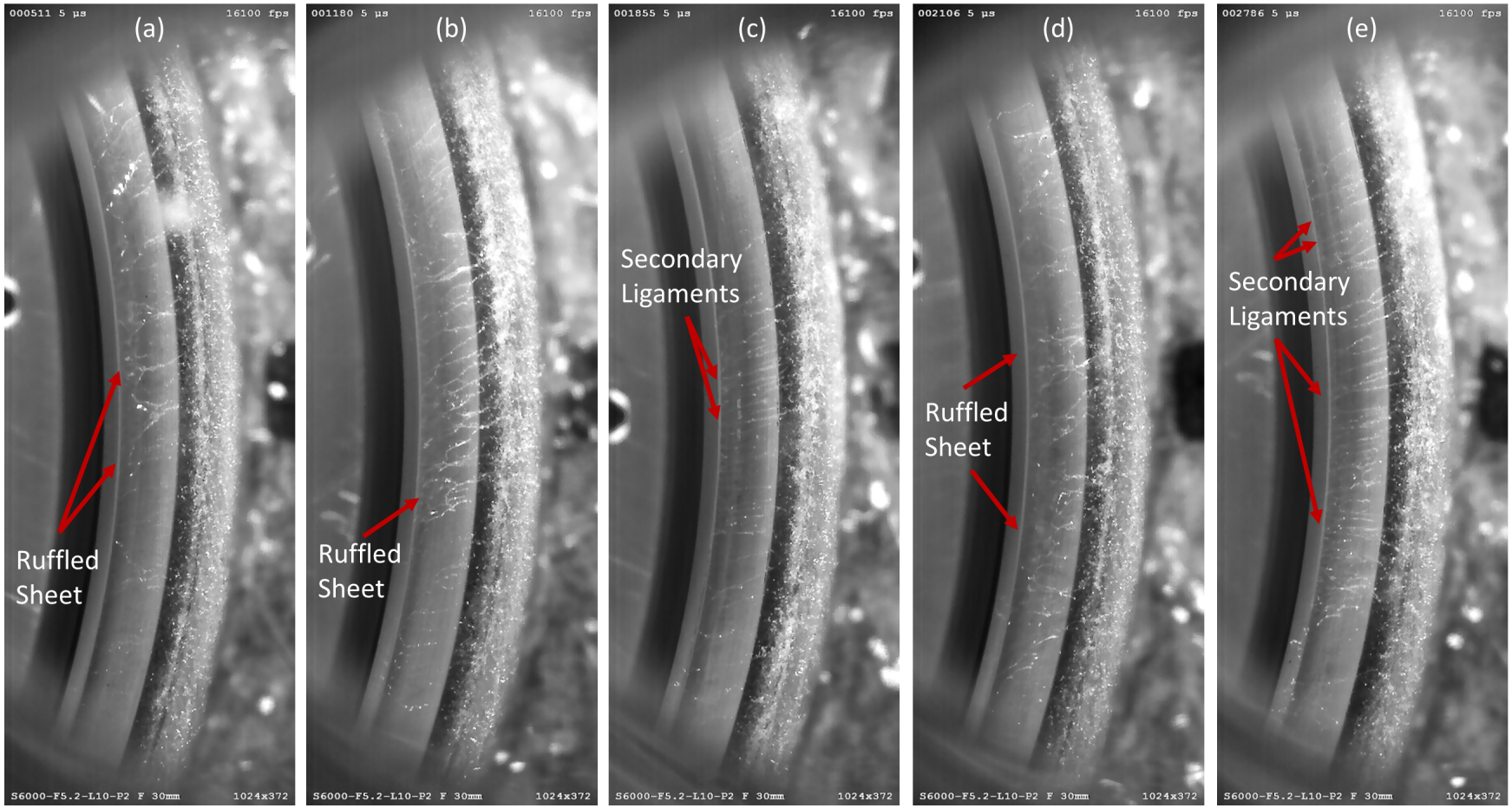


Figure 4.42: Oil breakup mechanisms (ruffled sheet & secondary ligaments) as seen from Plane F for S6000-F5.2-L10-P2
(a) $\boldsymbol{t = 0.0317}$ s (b) $\boldsymbol{t = 0.0733}$ s (c) $\boldsymbol{t = 0.1152}$ s (d) $\boldsymbol{t = 0.1308}$ s (e) $\boldsymbol{t = 0.1730}$ s

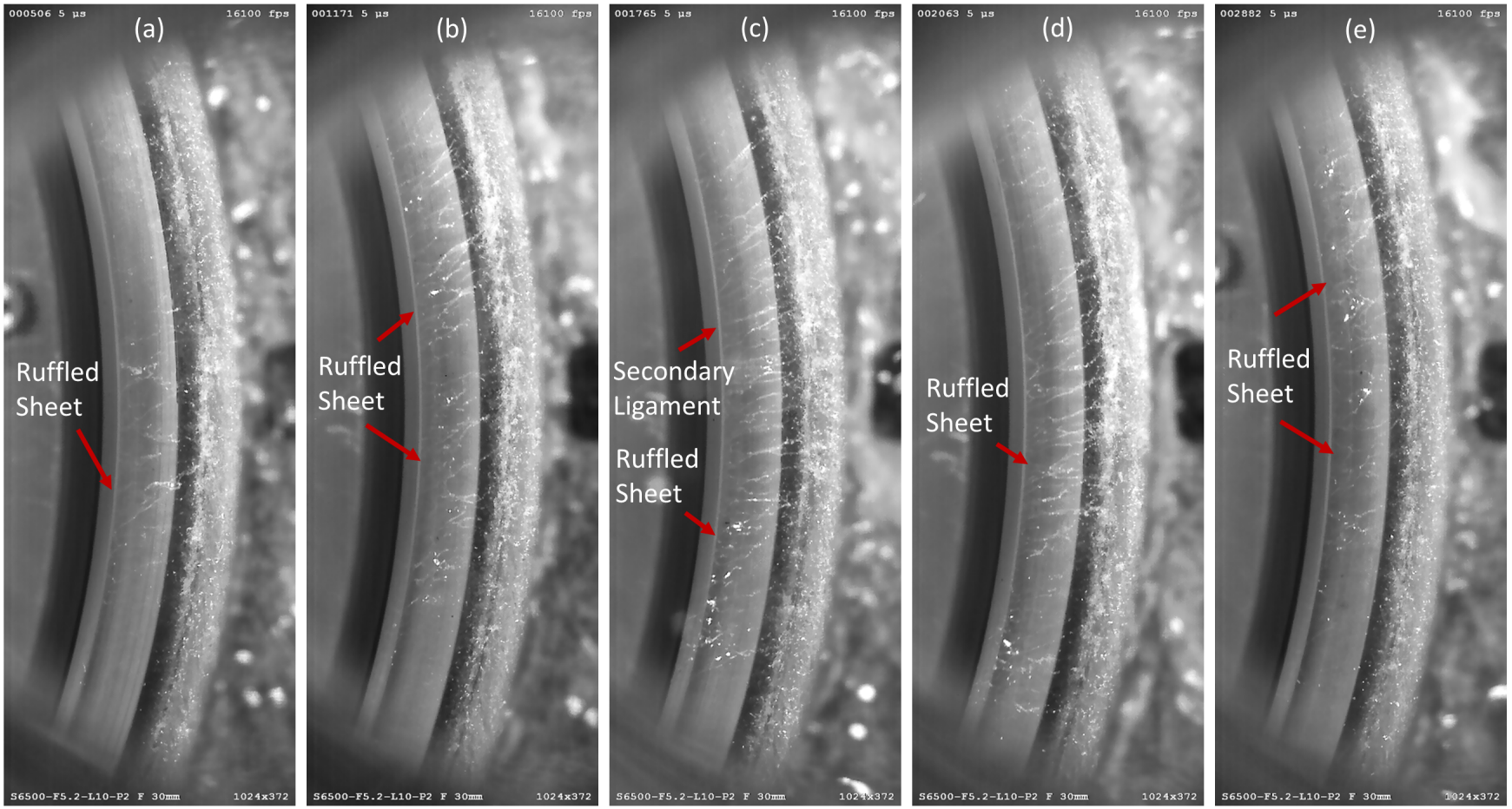


Figure 4.43: Oil breakup mechanisms (ruffled sheet & secondary ligaments) as seen from Plane F for S6500-F5.2-L10-P2
(a) $\boldsymbol{t = 0.0314}$ s (b) $\boldsymbol{t = 0.0727}$ s (c) $\boldsymbol{t = 0.1096}$ s (d) $\boldsymbol{t = 0.1281}$ s (e) $\boldsymbol{t = 0.1790}$ s

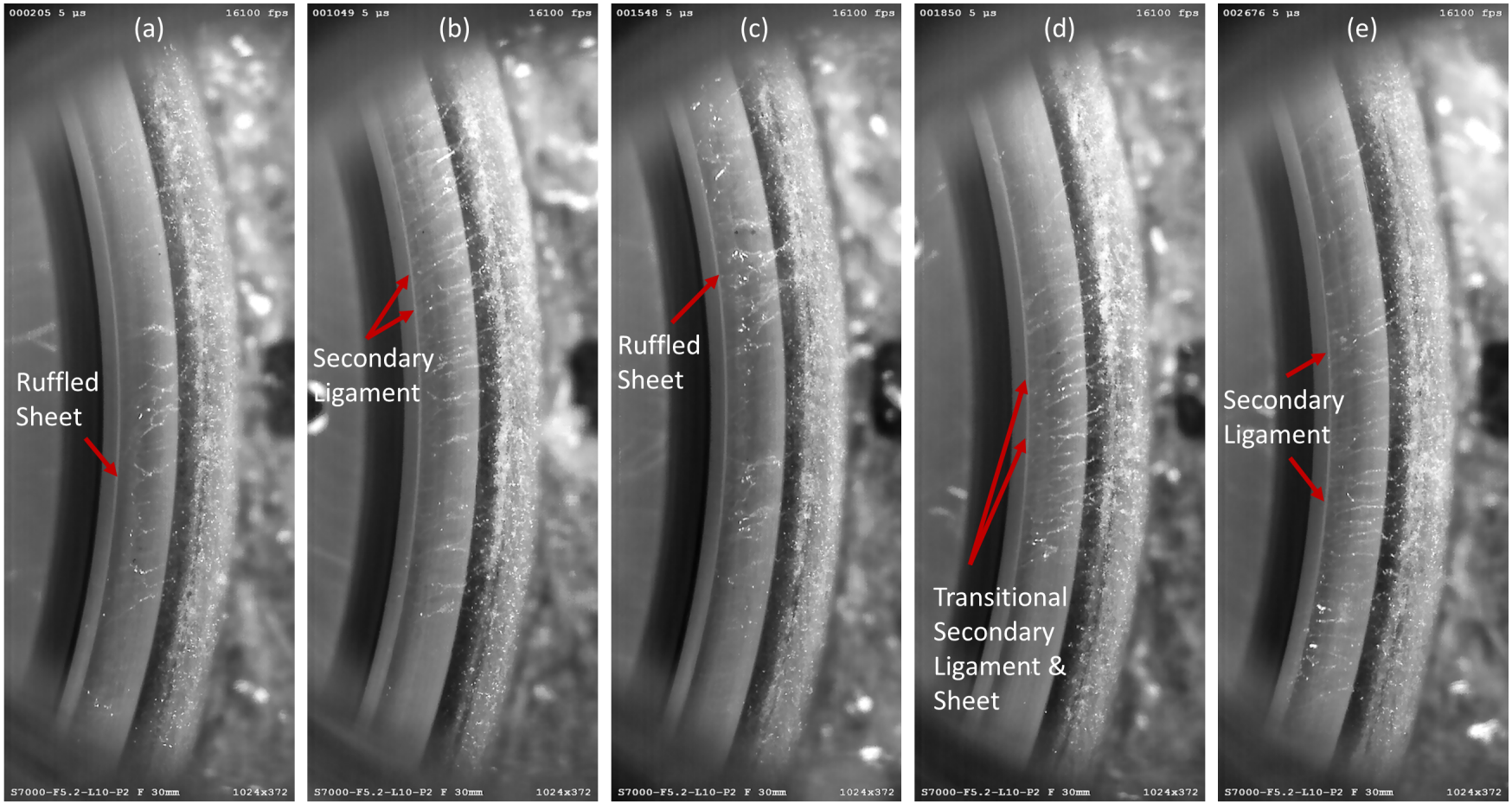


Figure 4.44: Oil breakup mechanisms (ruffled sheet & secondary ligaments) as seen from Plane F for S7000-F5.2-L10-P2
(a) $t = 0.0127$ s (b) $t = 0.0652$ s (c) $t = 0.0961$ s (d) $t = 0.1149$ s (e) $t = 0.1662$ s

These ligaments were emitted from the edge of the sheet. Example of secondary ligaments could be seen clearly in Figure 4.41a,d and Figure 4.42c,e. Another difference between primary and secondary ligament lies in the nature of secondary droplets that are produced from the tip of the thread. The satellite droplets produced from secondary ligaments represent a bimodal/multimodal type distribution where two or more distinctive ranges of droplet sizes were observed (see Figure 4.41a at S5500-F5.2-L10-P2). In contrast the satellite droplets produced from the primary ligament gives rise to a narrower size range. As a result, for primary ligament breakup mechanism, analytical expressions and empirical correlations were developed for droplet size, ligament number and ligament diameter by Kamiya and Wang *et al.* [23, 25]. However, the less repeatable nature of the secondary droplets produced from secondary ligaments poses problems in deriving such empirical correlations. In Section 4.3.4, the ligament number K is presented where a correlation could be developed using images from these test cases. A rig re-commissioning test was planned in 2018 to extend the study to beyond 7000 rpm allowing further characterisation of oil breakup mechanisms.

4.3.3 Summary of Oil Shedding & Preliminary Comparison

This section provides a summary of the oil-breakup mechanisms with reference to Figure 4.45 and subsequently validate previously published correlations. At speed below 1700 rpm, atomisation process occurred through direct-drop formation (see Figure 4.45a). Primary ligaments were formed when speed is increased from 1000 rpm to 1700 rpm (see Figure 4.45b). At this critical speed (i.e. 1700 rpm), the ligaments have distinctive spacing, constant size and quasi-periodic shedding frequency. Laminar sheets also existed together along the edge of the cage with the ligaments on part of the cycles from 1700 to 4300 rpm due to eccentricity that causes local variability in oil flow rates (see Figure 4.45c). As speed increases, the ligaments continue to exist with distinctive spacing but its characteristics diameter decreases and the ligament number rises (see Figure 4.45d). At speed beyond 4300 rpm, primary ligaments are no longer distinguishable and the structure of oil sheet fundamentally changed due to higher disturbances from air flow in the core. The pristine laminar sheet turned into a shorter oil sheet in both azimuthal and radial directions. These sheets were termed as ruffled sheet and the ligaments that released from the edge of these sheets (which is not the controlling surfaces) are known as secondary ligaments (see Figure 4.45e,f). A validation of the critical speeds based on previous correlations was made as shown in Figure 4.46 to assess its scalability.

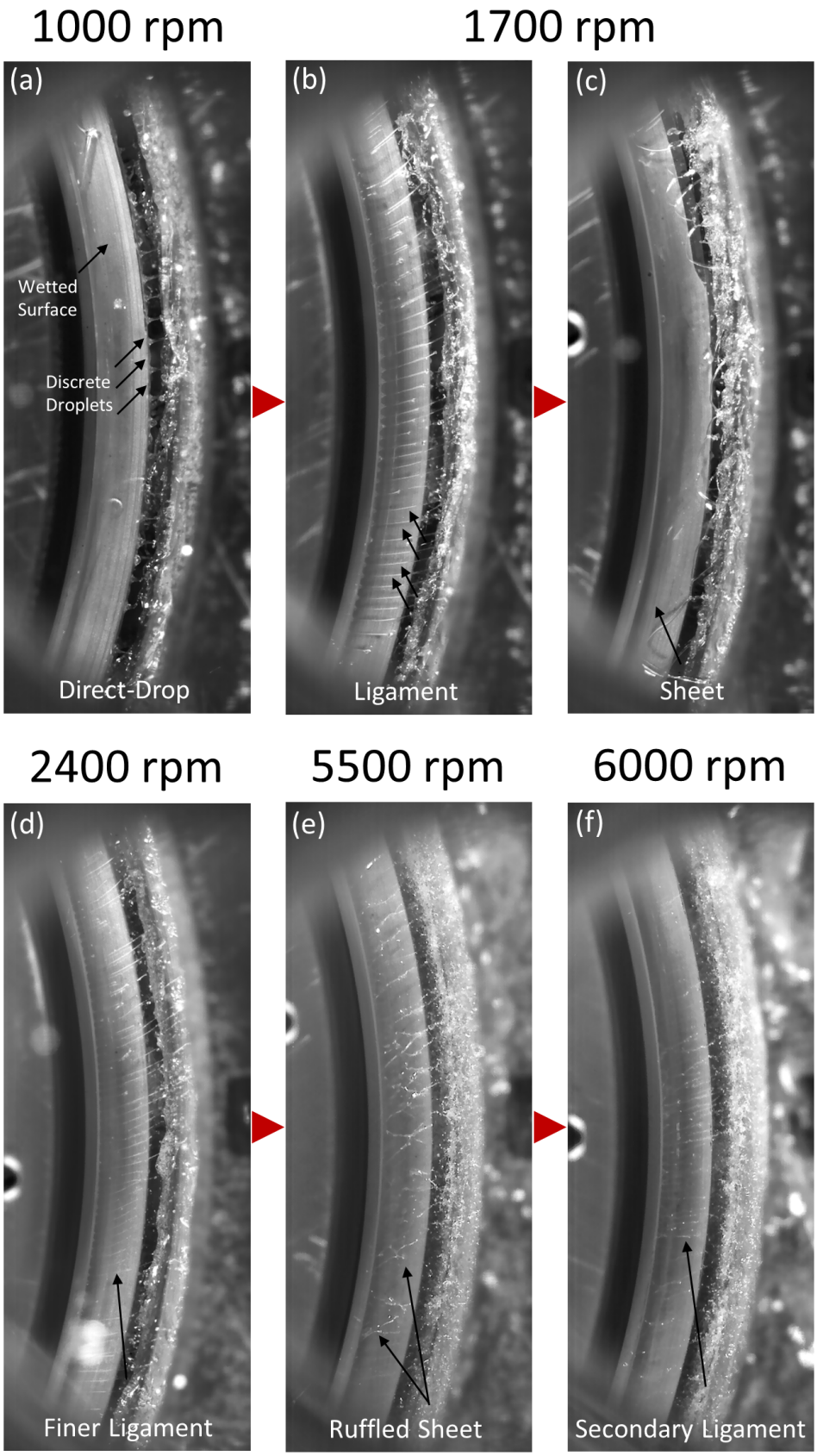


Figure 4.45: Oil shedding process beginning from direct-drop to ligament & sheet to ruffled sheet & secondary ligament operating based on changing shaft speed

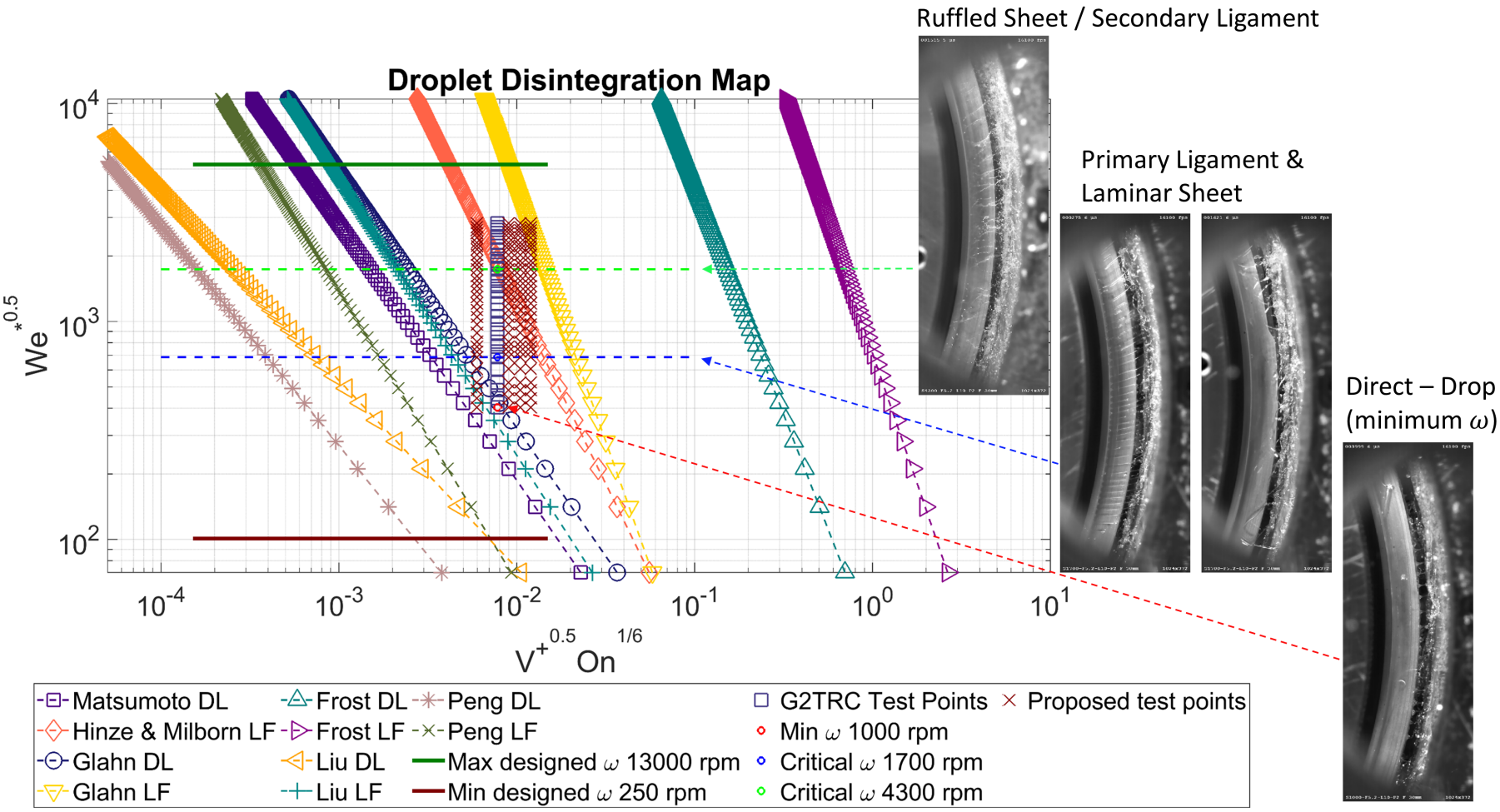


Figure 4.46: Validation of critical correlations based on observations

In the Figure 4.46, the droplet disintegration map was constructed based on previously available correlations. The regime map axes are based on that of Glahn *et al*. [28] which is suitable for operating range of aero-engine (see Figure 2.6). The x-axis represents the product of $V^{+0.5}On^{1/6}$ and y-axis represents $We^{*0.5}$ plotted on a logarithmic scale. The rotational speed ω is proportional to $We^{*0.5}$ and the flow rate q is proportional to $V^{+0.5}$. The correlations of various authors (e.g., Matsumoto *et al.* (from [28]), Hinze and Milborn [20], Glahn *et al.* [28], Frost, Liu *et al.* [27], and Peng *et al.* [33]) were explicitly stated in Table 2.1.

Note that in the legend, the maximum designed shaft speed of 13000 rpm and a minimum designed shaft speed of 250 rpm were drawn to dictate the bounded regions in which the test points could exist. Any operating speeds beyond these were not part of the assessments for aero-engine operating conditions. Also note that all the correlations were calculated on cage rotational speed which is half the shaft speed (i.e. $\omega = 50\%$). The available G2TRC test points (mentioned in Section 4.3.1) were shown as square marker ranging from 500 rpm to 3500 rpm (ω_{cage}) that corresponded to 1000 rpm and 7000 rpm for ω_{shaft}. In the legend, DL denotes direct-drop to ligament and LF denotes ligament to film or ligament to sheet (see Figure 4.46).

The non-dimensional parameters aimed at providing details as to whether scaling is possible from a simple geometry to a complex geometry and also to whether the correlations able to predict the transitions. From the above information, the correlations could be assessed systematically from the first to final legend. Here, major focuses will be made based on correlations close to the G2TRC test points. From the above figure, it is clear that many dimensionless correlations failed to capture the transitions except for Hinze and Milborn LF. First, Glahn *et al.* [28] modified their correlation of DL with respect to Matsumoto *et al.* and is closest one to critical speed of 1700 rpm where we observed the transition of direct drop to ligament. Glahn DL predicted the critical speed in which the transition occurs at 1081 rpm or We of 1.9048×10^5 at same flow rate. Liu *et al.* [27] and Peng *et al.* [33] DL were out-of-range as they overestimated the transition to occur at $We < 10^4$ or $\omega < 250$ rpm. This is due to the fact that Liu *et al*'s [27] correlation $Q^+ = 6.5\, We^{-1.161} St^{-0.0705}$ and $Q^+ = 5.13\, We^{-0.789} St^{0.036}$ are only applicable in a particular range of We which is $10^3 < We < 10^5$. Likewise, Peng *et al*'s [33] correlations were only applicable for $We = 0.815 \times 10^3 - 2.0 \times 10^5$. The scalability and usage of these database were poor as pointed by Glahn *et al* due to the differences in geometry and fluid properties [28]. Additionally, Frost's correlations are out of bound for most flow rates as they predicted that the transitions occur indefinitely even at the highest proposed flow rate. This is due to the criteria only satisfying a constant non-dimensional condition (i.e. $\sigma D\rho/\mu^2 = 0.0198$).

The analysis also shown that Hinze and Milborn LF predicted the critical speed at 4623 rpm or $We = 3.4842 \times 10^6$ which is close to what being observed by G2TRC at speed of 4300 rpm for ligament to ruffled sheet. However, Glahn LF correlation overestimated the phenomenon. The validity of Glahn *et al*'s [28] correlation was much closer as derivations were being done at We of 10^7 and the minimum and maximum G2TRC We is in the range of $10^5 - 10^6$. List of future test points (but not all) were marked in the regime map and also presented in Table 4.9. These enable non-linear regression analysis to be conducted which will enable the derivation of critical criterion.

Table 4.9: Visualisation test cases proposed for future study

No	Rotational Speed (rpm)	Oil Flow Rate (lpm)	Axial Load (kN)	Viewing Position
1	1000 – 7000 in step of 500	4	10	P2
2		4.5		
3		5.5		
4		6.0		
5		6.5		
6		7.0		
7		7.5		
8		8.0		

As the transition of droplet, ligament and sheet is less dependent on gravity, analysis at any angular position is suitable. However, note that different quality of imaging could be achieved depending on the clarity of that angular position. The generalised form for the criterion proposed by various authors and also summarised by Santhosh *et al.* [109] is given as follows:

$$V^+ = C\, We^a\, On^b \tag{4.9}$$

Where C, a and b are constant to be determined from the experiments. An example of non-linear regression analysis was performed in the determination of ligament number, K as shown in next Section.

4.3.4 Ligament Number – K

Ligaments could be observed when a critical flow rate or speed is achieved. Due to its stable structure, coherent spacing (λ) and distinctive structure (i.e. long thin thread); measuring the total number of ligament is highly possible with certain assumptions. The earliest analysis of ligament number, K were reported by Hinze and Milborn [20] as well as by Kamiya and Kayano [113]. Kamiya extended the analysis by providing an analytical expression for ligament number as well as comparing it with experimental model [23]. Subsequently, Frost, Liu *et al.* and Wang *et al.* reported similar type analysis under different operating conditions [21, 25, 27]. The following assumptions were made when calculating the ligament number, K in G2TRC's test cases:

1. Ligaments that are partially developed at transitional point of direct-drop to ligament are not considered (i.e. $\omega_{shaft} = 1600$ rpm).
2. Oil sheet could intermittently occupy one part of the cycle (out of the whole 360°), the ligaments are considered when a consistent λ and frequency of occurrence are achieved. This dictates that K is likely to be overestimated by some degree.
3. As only the parameter (speed) is investigated at this point in time, the correlation derived using nonlinear regression is true and only valid for constant stability number, St of 3.8875×10^{-5} (due to constant fluid properties and diameter).
4. Variation in oil flow rate is not tested and is kept constant at 5.2 lpm.

4.3.4.1 Operating Speeds where Ligaments Are Observed

Ligaments were observed from 1700 rpm to 4300 rpm. Below 1700 rpm, the centrifugal force and shearing were insufficient to grow the waves on the surface of the cage and therefore no ligaments were seen except direct-drops. At beyond 4300 rpm, no appreciable ligaments could be distinguished from the HS images both by naked eyes and enhanced images (i.e. increased contrast). The methodology of detection and nonlinear regression for K are reported in Section 4.3.4.2 and Section 4.3.4.3 respectively. The following speeds were used for calculation of Ligament number, K: 1700, 2000, 2400, 3200, 3800 and 4300 rpm respectively at constant flow rate 5.2 lpm, axial load 10 kN at angular position P2. The corresponded HS images for the above speeds are given in Figure 4.47 along with the λ labelled in inset "digitally zoomed" images.

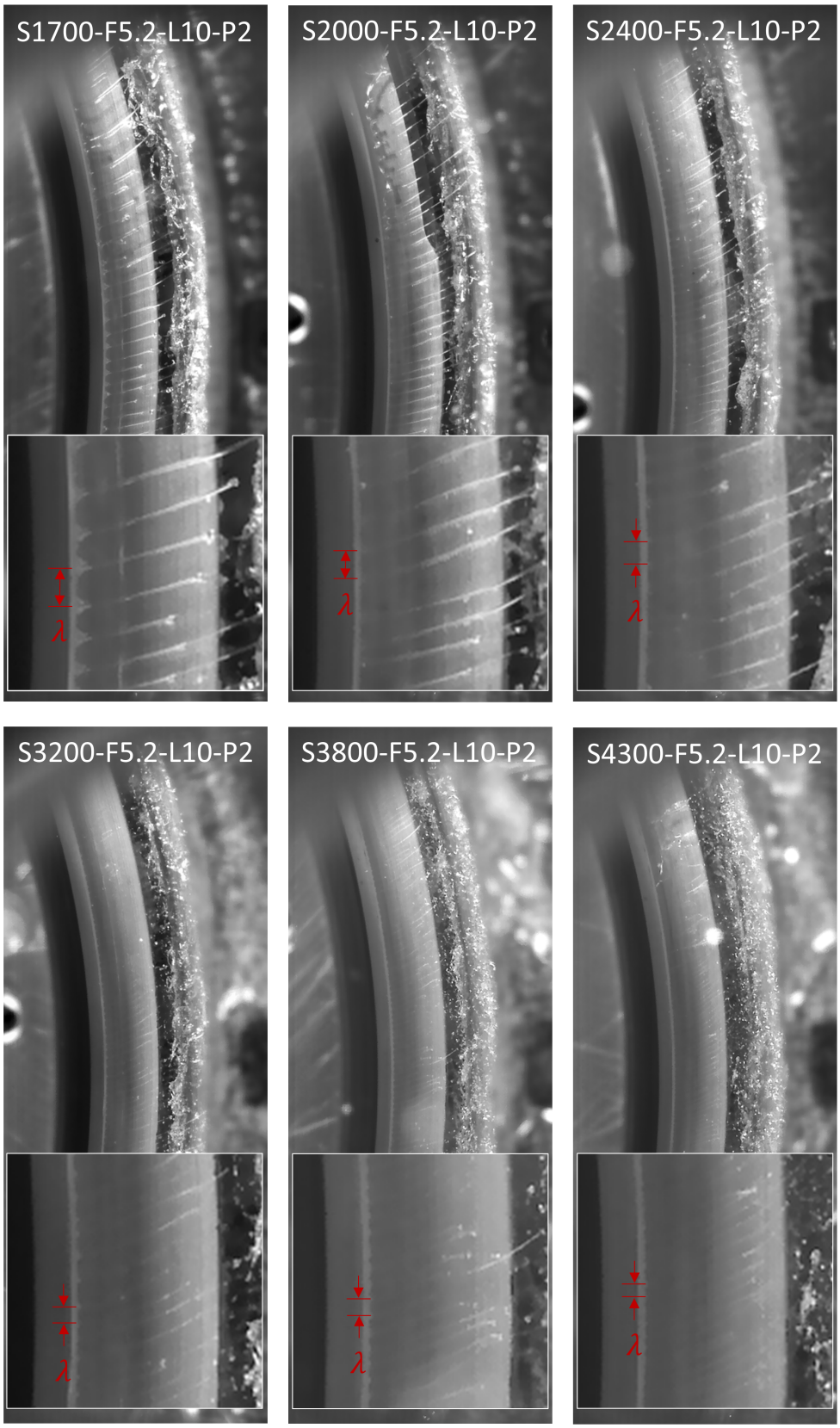


Figure 4.47: Observation of ligaments at different speeds ($\boldsymbol{\omega_{shaft}}$) and their corresponding spacing ($\boldsymbol{\lambda}$) shown in inset images

4.3.4.2 Methodology of Ligament Detection

Ligament number could be determined by dividing the total angle of the bearing (360°) with angular spacing (θ) in which two ligaments occupy. A MATLAB code is written which allows user to select the ligaments' location and subsequently outputting the angular spacing angle based on trigonometry. Figure 4.48 (left) shows the occurrence of ligaments at the edge of a rotating cage at flow condition S1700-F5.2-L10-P2. The image contrast and sharpness were first being enhanced using syntax *imadjust* and *imsharpen*. A built-in edge detection tool formulated by Canny is used to detect the edges of ligaments and the wave structures and finally converting them into binary (i.e. black & white) [114]. This post-processed image aids the user in identifying the location where ligaments left the cage. Prior to that, the centre coordinate was predetermined using linear algebra by solving three sets of equation for circle based on 3 known coordinates along an arc (or locus). The steps for determine the centre coordinates and marking the arc (see Figure 4.48, ─) are shown as following:

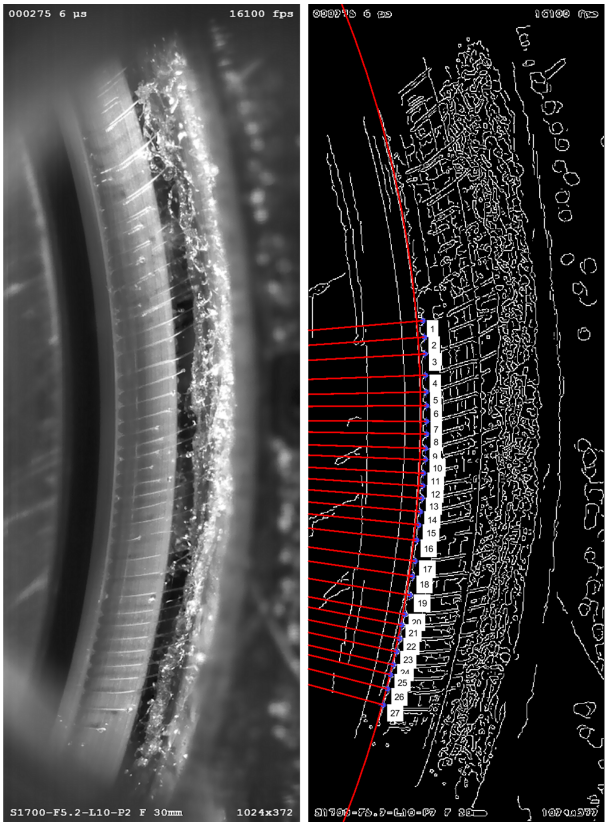


Figure 4.48: Instantaneous HS image and Canny's edge detection [114] showing ligaments locations from 1 to 27 pointing towards the central axis

1. First coordinate (x_1, y_1) of the arc is substituted into $(x_1 - h)^2 + (y_1 - k)^2 - (r^2)$
2. Second coordinate (x_2, y_2) of the arc is substituted into $(x_2 - h)^2 + (y_2 - k)^2 - (r^2)$
3. Third coordinate (x_3, y_3) of the arc is substituted into $(x_3 - h)^2 + (y_3 - k)^2 - (r^2)$

These systems of equations are solved algebraically using syntax *solve* which returns centre coordinates (h, k) and radius (r). The arc is then marked using equation of polar coordinate $x = r\cos(\theta)$, $y = rcos(\theta)$ based on calculated radius. Subsequently, *impoint* function returns all the coordinates of ligaments by user selection on the Canny's image and they are 'draggable' until a satisfied location is placed. With the obtained ligaments coordinates, Pythagoras's theorem is used to determine the chord length between two adjacent ligaments and Cosine's rule shown in Equation (4.10) is used to determine the angular spacing angle (θ). Note that not all images could be applied with edge detection filter. For images with higher speeds, the ligament locations are determined using same method but by identifying the thread. All the images used for ligament calculation could be referred in Appendix.

$$\theta = \cos^{-1}\left[\frac{r^2 + r^2 - chord^2}{2\,r^2}\right] \tag{4.10}$$

Based on the above methodologies, angular spacing angle (θ) and the calculated ligament number (K) are tabulated in Table 4.10.

Table 4.10: Operating conditions and their corresponding angular spacing angle and ligament number

Test Condition	**Plane of Focus**	**Angular Position**	**Angular Spacing Angle (θ)**	**Ligament Number (K)**
S1700-F5.2-L10	B	P2	0.7742°	465
S2000-F5.2-L10			0.7214°	499
S2400-F5.2-L10			0.5651°	637
S3200-F5.2-L10			0.4119°	874
S3800-F5.2-L10			0.3418°	1053
S4300-F5.2-L10			0.3020°	1192

4.3.4.3 Nonlinear Regression & Comparison of K with Published Data

Ligament number, K is defined as a function of speed, flow rate and fluid properties by previously mentioned authors. The dimensional analysis presented here will assess if there is any similarity between disintegration produced by a simple rotary atomizer and that of an aero-engine ball bearing based on comparison of K. A generalised form of equation for ligament number was proposed by Kamiya [23] as shown in Equation (4.11).

$$K = C\, We^{a} St^{b} \tag{4.11}$$

Where, K is ligament number, We is weber number, St is stability number. C, a and b represent first, second and third coefficient respectively. The following correlations are tabulated in Table 4.11 based on information from Kamiya, Frost, Liu *et al*. and Wang *et al.* [21, 23, 25, 27].

Table 4.11: Previously published correlations for ligament number

Author	Correlation	Range of Applicability
Kamiya [23]	$K_{opt} = 0.48\, We^{0.37}\, St^{-0.2}$ $K_{exp} = 0.574\, We^{5/12}\, St^{-1/6}$	$We = 10^{4} \sim 10^{5}$ $St = 10^{-3} \sim 10^{-2}$
Frost [21]	$K = 0.29 \left(\frac{\omega \rho D^2}{\mu}\right)^{0.93} \left(\frac{\sigma D \rho}{\mu^2}\right)^{-0.44}$	-
Liu *et al.* [27]	$K = 0.712\, We^{0.439}\, St^{-0.0705}$	$10^{3} < We < 10^{5}$ at $St = 2.0 \times 10^{-3}$ / 2.4×10^{-4}
Wang *et al.* [25]	$K = 0.576\, We^{0.458}\, St^{-0.0619}$	$We = 0.82 \times 10^{3} \sim 2.47 \times 10^{5}$ $St = 6.76 \times 10^{-6} \sim 1.43 \times 10^{-4}$
Hinze and Milborn [20]	$K = 0.574\, We^{1/4} \left(\frac{\rho \omega r^2}{\mu}\right)^{1/3}$	$We < 2.45 \times 10^{3}$ $St = 1.34^{-2} \sim 3.74 \times 10^{-2}$

Where, Weber number and Stability number is given as:

$$We = \frac{\rho \omega^2 r^3}{\sigma} \tag{4.12}$$

$$St = \frac{\mu^2}{\rho \sigma r} \tag{4.13}$$

By using the obtained experimental value K from Section 4.3.4.2, nonlinear regression analysis was performed to find the coefficient of C, a and b. This could be achieved by expressing the dependent variable K in a statistical model with respect to We and St. Although it was mentioned early that St is constant for all the test points conducted for calculation of K (i.e. assumption made). Note that ω here is cage speed (i.e. 50% of stubshaft speed according to [93]). Hence, the rotational speeds that were used for calculation of We is taken as half of shaft speeds (i.e. 850, 1000, 1200, 1600, 1900 and 2150 rpm respectively). Due to constant cage diameter and fluid properties, St is expressed as 3.8875×10^{-5}. Syntax *fitnlm* is used to solve the model function, *modelfun = @(b,x) b(1)*x(:,1).^(b(2)).*x(:,2).^(b(3))*; by supplying initial value for the coefficients $b(1)$, b(2) and b(3) as 0.567 0.458 -0.0619 (which is taken from Wang *et al.* [25]). With the initialisation, *MATLAB* iteratively solves the model function.

The nonlinear model obtained for Hee *et al.* [115] is given as:

$$K = 0.33811\, We^{0.53799} St^{-0.015162} \tag{4.14}$$

Where coefficients, C, a and b obtained are $0.33811, 0.53799$ and -0.015162 respectively. Based on nonlinear regression, the determination or R^2 is 0.997021. This correlation is well satisfied for We of 0.4617×10^6 to 2.9538×10^6 at constant St of 3.8875×10^{-5}. The estimation of K based on various authors and Hee *et al.* [115] is given in Figure 4.49.

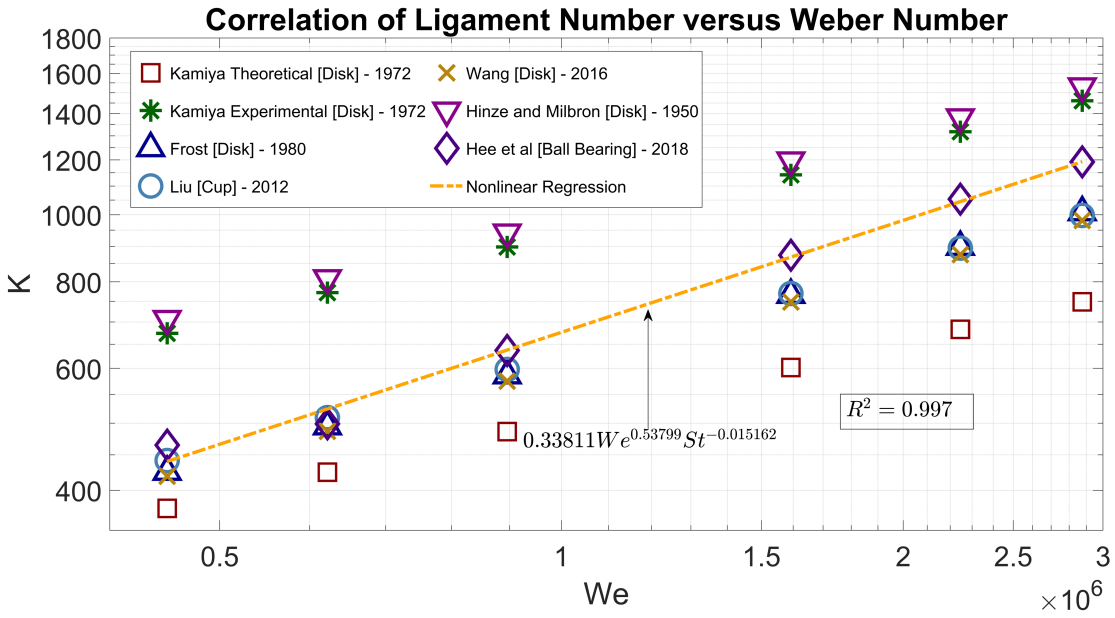


Figure 4.49: Plot of $\boldsymbol{K}$ versus $\boldsymbol{We}$ for comparison with published data

Analysis has shown that the ligament number produced in an aero-engine ball bearing cage agrees well with that of a simple of a simple rotary device such as disk or cup to a certain degree of extent. Calculation of mean absolute percentage error (MAPE) is made to compare the results for ligament number of various authors with that of our data. The difference between our K values and those of other authors (MAPE) is tabulated in Table 4.12.

Qualitative observation of images such as those in Figure 4.47 indicates that ligament spacing decreases as rotational speed increases. Thus ligament number on the cage rim increases with increasing speed. Correspondingly in Figure 4.49, the trend suggests that K is strongly dependent on We where it increases as shaft speed is increased. The correlation obtained for our test cases at Weber number of less than 8.59×10^5 overlaps with data points of Frost, Liu and Wang but poorly with Kamiya's theoretical and experimental correlations.

As We exceeds 8.59×10^5, data points for K begin to deviate further away from predicted values of published authors. This signifies the increasing 'transient' or intermittent phenomena of oil shedding in a more turbulent environment. The non-deterministic nature of turbulence could cause variability of local flow rate and therefore affect ligament number and formation.

The correlation closest to our data is Liu *et al.*'s [27] correlation with a mean average percentage error (MAPE) of 9.4%. The correlation outside the range of Liu *et al.* [27] in that their analysis is only applicable in the range of $10^3 < We < 10^5$ at $St = 2.0 \times 10^{-3}$ and $St = 2.4 \times 10^{-4}$. Whereas, G2TRC's test conditions are well above $We = 10^5$ and at lower St. Frost [21] on the other hand, expressed K in terms of Reynolds number and Ohnesorge number using diameter instead of radius. The correlation of Wang et al. [25] which was developed for the range of operating variables of $We = 0.82 \times 10^3$ to 2.47×10^5 is well below that of the rig's operating range despite having St of the same order as Hee *et al.* [115]. A MAPE of 11.8 % applies when comparing to Wang *et al.* [25].

The theoretical model of Kamiya *et al.* [23] which was developed on the basis of balancing the dissipation rate for kinetic energy, surface tension, viscous-deformation and centrifugal force was found to have a MAPE of 26.8%, significantly better than the experimentally derived correlation at 36.49%.

Table 4.12: Measurement of Mean Absolute Percentage Error (MAPE) measured relative to Hee *et al*'s [115] ligament number

Author	**MAPE**
Kamiya [23]	$M_{K_{opt}} = 26.83\ \%$ $M_{K_{exp}} = 36.49\ \%$
Frost [21]	$M_{K_{Frost}} = 9.98\ \%$
Liu *et al.* [27]	$M_{K_{Liu}} = 9.42\ \%$
Wang *et al.* [25]	$M_{K_{Wang}} = 11.83\ \%$
Hinze and Milborn [31]	$M_{K_{HM}} = 43.23\ \%$

4.4 Dynamics of Waves on Surfaces Close to an Aero-engine Ball Bearing

This section describes the characterisation of waves' structure of the thin film under the effect of shear. The phase interaction at the surface of the film was studied by assessing the frequency of wave, the wavelength and the type of wave spectrum. The effect of gravity at co-current and counter-current side on the dynamics of waves were also investigated. The operating conditions (e.g. shaft speed, flow rate and axial load) employed for the investigations are tabulated in Table 4.13 and Table 4.14. The choices for respective imaging technique at different test conditions are explained in Section 4.4.4.

Table 4.13: Experimental test cases considered for co-current regime

Test Condition	Shaft Speed (rpm)	Oil Flow Rate (lpm)	Axial Load (kN)	Type of Imaging
S3000-F5.2-L10-P2	3000	5.2	10	HS
S3000-F7.3-L10-P2	3000	7.3	10	HS
S5000-F5.2-L10-P2	5000	5.2	10	LDM-HS
S5000-F7.3-L10-P2	5000	7.3	10	LDM-HS
S5000-F5.2-L30-P2	5000	5.2	30	LDM-HS
S5000-F7.3-L30-P2	5000	7.3	30	LDM-HS
S7000-F5.2-L10-P2	7000	5.2	10	LDM-HS
S7000-F7.3-L10-P2	7000	7.3	10	LDM-HS
S7000-F5.2-L30-P2	7000	5.2	30	LDM-HS
S7000-F7.3-L30-P2	7000	7.3	30	LDM-HS

Table 4.14: Experimental test cases considered for counter-current regime

Test Condition	Shaft Speed (rpm)	Oil Flow Rate (lpm)	Axial Load (kN)	Type of Imaging
S3000-F5.2-L10-P4	3000	5.2	10	HS
S3000-F7.3-L10-P4	3000	7.3	10	HS
S5000-F5.2-L10-P4	5000	5.2	10	HS
S5000-F7.3-L10-P4	5000	7.3	10	HS
S5000-F5.2-L30-P4	5000	5.2	30	HS
S5000-F7.3-L30-P4	5000	7.3	30	HS

S7000-F5.2-L10-P4	7000	5.2	10	LDM-HS
S7000-F7.3-L10-P4	7000	7.3	10	LDM-HS
S7000-F5.2-L30-P4	7000	5.2	30	LDM-HS
S7000-F7.3-L30-P4	7000	7.3	30	LDM-HS

4.4.1 Surface Waves – Period & Frequency

Surface waves are classical mechanical waves that have been studied for over a century. They are universally observed in many areas opened to the atmosphere and in most cases, nonlinear [116]. Examples of mechanical waves are oceanic waves at the seas, ripples generated when pebble hits the surface of a pond and tidal waves generated by gravitational attraction between two celestial bodies (i.e. moon and earth). The understanding of wave is crucial, examples, waves frequently impact offshore wind turbines and eroding the coastal area. Here, we focus specifically on studying the wave structures on surfaces close to an aero-engine ball bearing driven by shear. A general wave spectrum of mechanical waves is given by Walter [117] in Figure 4.50 and classified in Table 4.15.

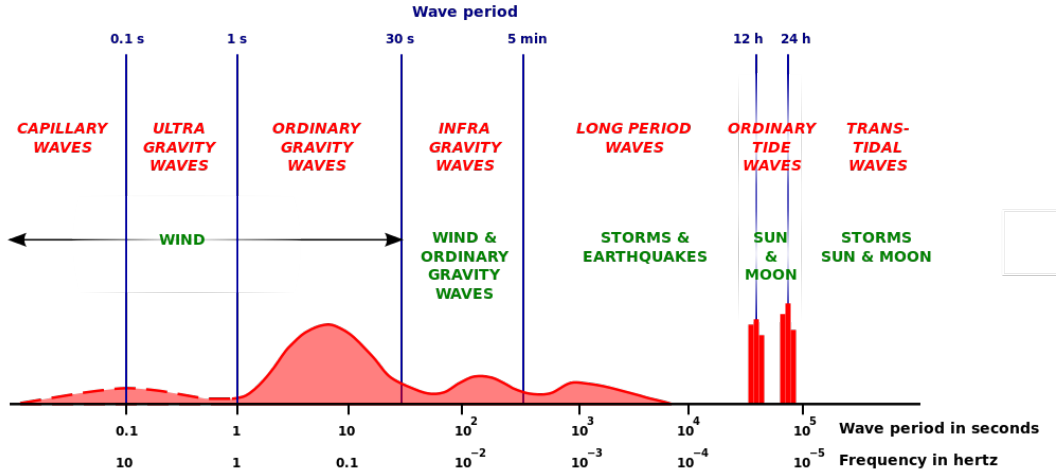


Figure 4.50: Classification of waves based on frequency spectrum [117]

Table 4.15: Classification of waves' spectrum [117]

Classification	Period, T	Frequency, f_{wave} (Hz)
Capillary waves	< 0.1 s	10
Ultra-gravity waves	0.1 ~ 1 s	1
Ordinary gravity waves	1 ~30 s	0.1
Infra-gravity waves	30 s ~ 5 min	10^{-2}
Long-period waves	5 min ~ 12 h	10^{-3} ~10^{-4}
Ordinary tides	12 h ~ 24 h	10^{-4} ~10^{-5}
Trans-tidal waves	≥ 24 h	10^{-5}

In this section, two types of wave that were observed are gravity-capillary wave and capillary wave. Gravity-capillary wave is generated when there is a disturbance caused by wind blowing parallel to its surface. Gravity-capillary wave is also known as wind-wave. The momentum is transferred from gas phase to liquid [118]. These waves transfer energy and mass when gravity force is activated to restore the surface back to equilibrium (i.e. fluid level). The overshooting of the restoration force on interface along with pressure fluctuations are what generated the wave structure. With gravity as the primary restoration force, it is termed as gravity-capillary wave. Based on Table 4.15, the frequency for gravity-capillary wave is in the order of 0.1 to 10 Hz.

With increasing shearing rate, the frequency increases which give rise to a second type of wave phenomenon known as capillary wave. Capillary wave contains much smaller wavelength and has higher frequency. The dominant restoring force is surface tension. The study of wave structures are important as the dynamics of thin film in bearing chamber affects the local heat transfer coefficient and droplet re-entrainment. Definitions for wave structure are fairly universal, reader could refer the peak, frequency and wavelength in Section 4.4.4.

4.4.2 Surface Waves – Instabilities

Various type of surface instabilities existed based on interaction between gas and liquid along the stationary chamber wall. There were very little published studies that deal with the interaction of oil film along stationary chamber wall and gas-phase due to limited optical access. However, a good body of works that deals with sheared liquid film flow along the channel and

pipe is available. For a non-moving viscous liquid in a duct sheared by air velocity of $U_a = 3.2\ m/s$ to $U_a = 7.8\ m/s$. Sclieren visualisation employed by Paquier *et al.* shows that wrinkles are produced at low wind speed due to pressure fluctuations in the turbulent boundary layer. Subsequently at high wind speed, waves of higher amplitudes are formed. These can be referred in Figure 4.51. And accordingly, the viscous damping is large that no 3D waves are seen.

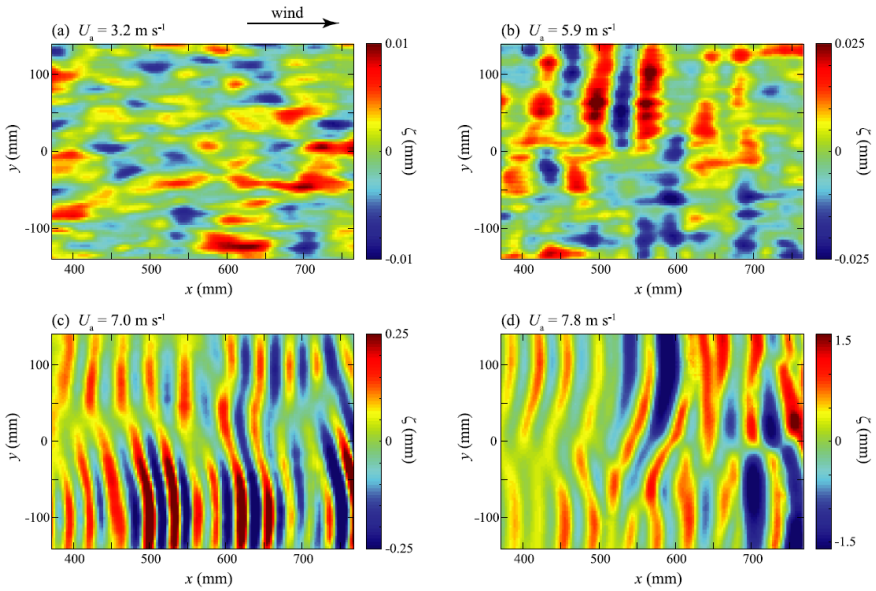


Figure 4.51: Instantaneous surface height measured using Synthetic Sclieren showing 'wrinkle' regime at (a) $\boldsymbol{U_a = 3.2}$ m/s and (b) $\boldsymbol{U_a = 5.9}$ m/s. Images at (c) and (d) are corresponding to 2D waves [118]

For a horizontal pipe in oil-gas application, Chen *et al.* [119] shows the regimes of stratified-wavy flow subject to increase in superficial gas velocity as following in Figure 4.52.

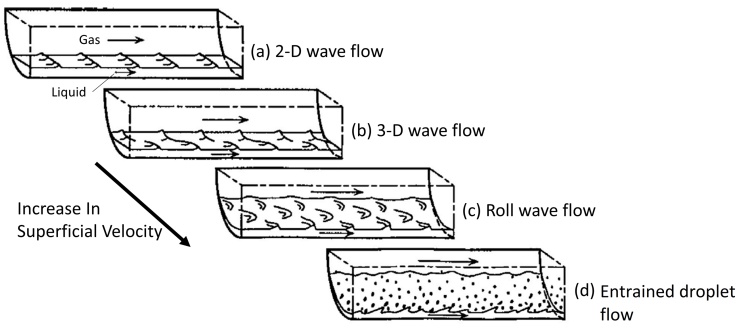


Figure 4.52: Regimes of horizontal stratified-wavy flow [119]

The waves were initialised from two-dimensional to three-dimensional (also known as squalls). At intermediate superficial gas velocity, roll waves (or Kelvin-Helmoltz) waves formed. When critical superficial gas velocity is reached, droplets are sheared from the tip of the waves and entrained into the gas. A regime map based on the gas velocity and Reynolds number of liquid are given by Hanratty for gas flowing co-currently with moving liquid. Hanratty proposed that at low air velocity and liquid Reynolds number, smooth and thick surface waves are seen. The wave-fronts are moving in same phase and are well-spaced between the crests. As air-velocity and liquid Reynolds number increases, the waves no longer maintain coherent structure. Instead, the wave-fronts appear to be out-of-phase. The increase in air velocity has transformed the wave into roll wave where the peak is moving faster than liquid below it causing the roll over. This instability mechanisms was first described by Kelvin-Helmoltz. With the increase in air velocity beyond 10 m/s, liquid atomisation from surface is observed. The features mentioned can be referred in Figure 4.53.

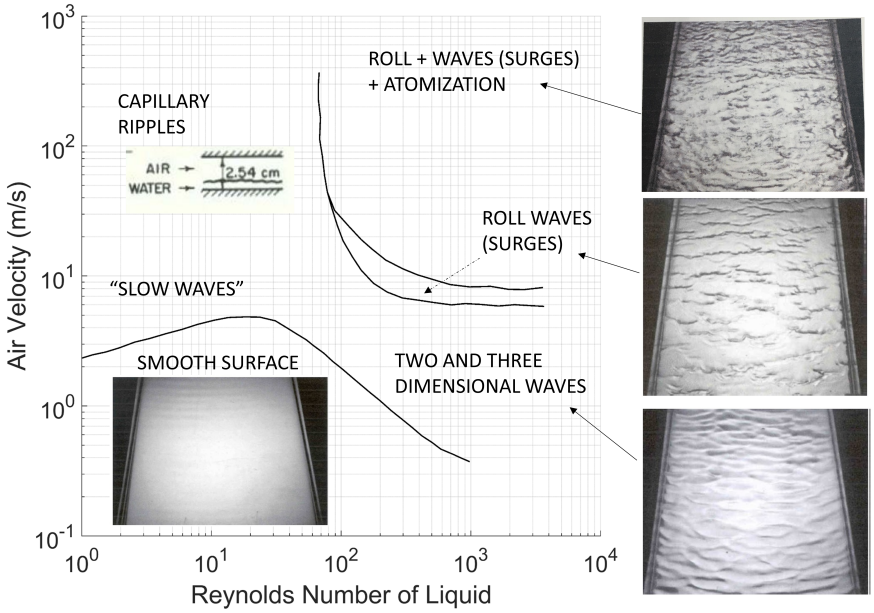


Figure 4.53: Wave patterns observed in gas-liquid flow. Regime map by Hanratty [120] and images from Lucie [121].

4.4.3 Critical Wavelength for Surface Waves

In present work, wavelength (λ) is calculated from either image of HS or LDM-HS as outlined in Table 4.13 and Table 4.14. To classify whether it is gravity-capillary wave or capillary wave, the measured wavelength is normalised by critical wavelength (λ_{crit}) proposed by Lamb [122]. The equation for determination of critical wavelength is given as following:

$$\lambda_{crit} = 2\pi \sqrt{\frac{\sigma}{(\rho_{liquid} - \rho_{gas})g}} \tag{4.15}$$

Where, σ is surface tension of the liquid, g is free fall acceleration, ρ_{liquid} is density of liquid phase and ρ_{gas} is density of gas. The surface wave is classified according to these conditions:

$$if \begin{cases} \lambda \ll \lambda_{crit}, & Capillary\ wave \\ \lambda \gg \lambda_{crit}, & Gravity - Capillary\ wave \end{cases} \tag{4.16}$$

The critical wavelength for this study is estimated as $\lambda_{crit} = 11.77$ mm. In the calculation, the value of oil surface tension of 0.0309 N/m is used based on property of Aeroshell 390 at temperature of 60℃ (based on thermocouples reading on bearing chamber wall). The oil density (ρ_{liquid}) is taken to be 897.4 kgm^{-3} and air density (ρ_{air}) is set as 1.067 kgm^{-3}.

4.4.4 Methods of Calculating – Wavelength & Frequency

In Section 4.4, it was highlighted that at which operating conditions LDM-HS images are preferred over HS images and vice versa. Figure 4.54 below justified the reason of using different imaging technique:

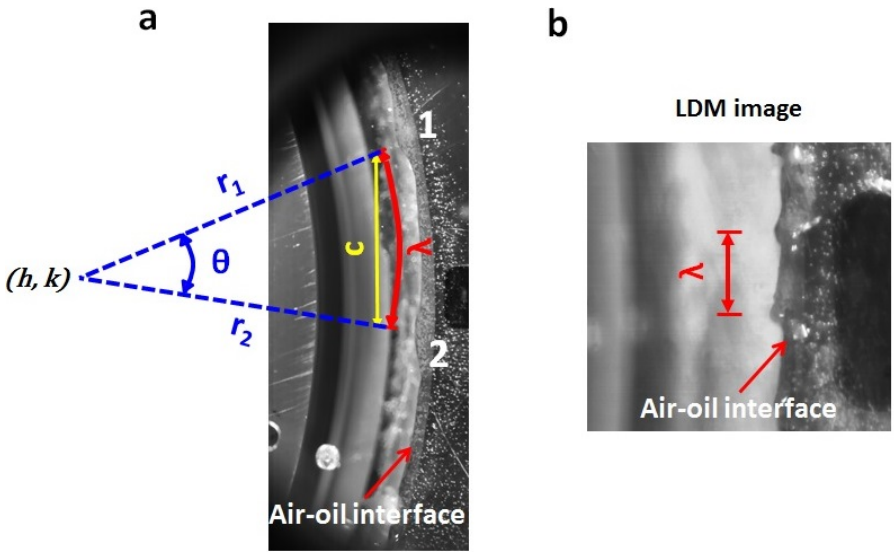


Figure 4.54: Determination of wavelength from (a) HS and (b) LDM-HS

At low speed of 3000 rpm, the wavelength could be identified based on two successive peaks that occupied the image resolution of 1024 × 384. The peaks are clearly labelled as '1' and '2' in Figure 4.54a. However, with increase in speed to 5000 rpm or even to 7000 rpm. The wavelength

decreases significantly and measuring the wavelength using HS will incur significant error due to low spatial resolution as outlined in Section 4.1.6. Hence, LDM-HS image is used to measure the wavelength. As wavelength is so much smaller than the radius of curvature of the chamber outer-race (i.e. $\lambda \ll r$), the wavelength for LDM-HS can be measured directly from successive peaks of the image resolution 1024 × 1024 since small-angle approximation stated that $\sin\theta \approx \theta$, $\tan\theta \approx \theta$. For HS, the wavelength is large and must not be approximated using small-angle approximation. Hence, trigonometry rules were applied to measure the arc length which is the wavelength. The details of the calculation of wavelength for HS is explained as following:

The wavelength of the surface wave for HS is calculated based on the formula of arc length:

$$r\theta = \lambda \tag{4.17}$$

Where, r is the radius from the centre of the polar coordinate system to crest of the surface wave, θ is the angle between the two crests measured from the centre. To reduce uncertainty, r is taken as the mean of r_1 and r_2 as shown in Figure 4.54, where r_1 and r_2 are the radii of the two crests of the surface waves. To determine θ, r_1 and r_2, the variables for chord length (c) and centre (h, k) are needed. *MATLAB* R2016b is used and similar to Section 4.3.4.2, three points along an arc are selected using syntax *impoint* (i.e. the static outer-race). This returns 6 variables (e.g. $x_i, x_{ii}, x_{iii}, y_i, y_{ii}, y_{iii}$) which allows three simultaneous equations for circle of the general form in Equation (4.18):

$$(x-h)^2 + (y-k)^2 - (r^2) \tag{4.18}$$

With the available coefficient h and k, r_1 and r_2 can be recomputed by using general form Pythogores theorem of the Equation (4.19):

$$r_1 = \sqrt{(x_1-h)^2 + (y_1-k)^2} \tag{4.19}$$

Where, x_1 and y_1 is the Cartesian coordinate of the first crest. Subsequently, the same step is repeated for r_2. The angle θ is worked out using cosine formula:

$$\cos\theta = \frac{chord^2 - (r_1^2 + r_2^2)}{(-2)r_1\, r_2} \tag{4.20}$$

And, the chord (c) is obtained by applying Pythogores Thorem on the vertical distance and horizontal distance of the two crests. With the computed angle (θ), the arc length in mm is determined by multiplying λ from Equation (4.17) with spatial calibration factor (mm/pixel). The following Table 4.16 and Table 4.17 summarise the wavelengths obtained.

Table 4.16: Experimental test cases for co-current regime (P2)

Test Condition	**Type of Imaging**	**Wavelength, λ (mm)**	**λ/λ_{crit} (-)**
S3000-F5.2-L10-P2	HS	29.80 ± 10.71	2.57 ± 0.92
S3000-F7.3-L10-P2		29.54 ± 11.19	2.55 ± 0.97
S5000-F5.2-L10-P2	LDM-HS	8.37 ± 2.60	0.72 ± 0.25
S5000-F7.3-L10-P2		7.03 ± 2.03	0.61 ± 0.18
S5000-F5.2-L30-P2		5.98 ± 1.35	$0.52 + 0.12$
S5000-F7.3-L30-P2		7.27 ± 1.49	$0.63 + 0.13$
S7000-F5.2-L10-P2		4.82 ± 0.98	$0.42 + 0.08$
S7000-F7.3-L10-P2		4.64 ± 0.76	$0.40 + 0.07$
S7000-F5.2-L30-P2		4.91 ± 1.21	$0.63 + 0.13$
S7000-F5.2-L30-P2		4.37 ± 1.23	$0.38 + 0.11$

Table 4.17: Experimental test cases for counter-current regime (P4)

Test Condition	**Type of Imaging**	**Wavelength, λ (mm)**	**λ/λ_{crit} (-)**
S3000-F5.2-L10-P4	HS	21.64 ± 5.84	1.87 ± 0.50
S3000-F7.3-L10-P4		21.40 ± 6.51	1.85 ± 0.56
S5000-F5.2-L10-P4		14.32 ± 4.70	1.24 ± 0.41
S5000-F7.3-L10-P4		9.42 ± 3.36	0.81 ± 0.29
S5000-F5.2-L30-P4		12.30 ± 4.72	1.06 ± 0.41
S5000-F7.3-L30-P4		12.27 ± 4.50	1.06 ± 0.39
S7000-F5.2-L10-P4	LDM-HS	4.44 ± 1.20	0.38 ± 0.10
S7000-F7.3-L10-P4		4.17 ± 1.25	0.36 ± 0.11
S7000-F5.2-L30-P4		5.23 ± 1.48	0.45 ± 0.13
S7000-F5.2-L30-P4		5.30 ± 1.00	0.46 ± 0.09

Note: $\lambda_{crit} = 11.84$ mm

In the study of surface waves, frequency (f) is also an important parameter. Frequency is measured using both HS and LDM-HS images when required. With reference to Figure 4.55, the frequency or the number of wave passing through a specific location is detailed as following:

A reference point such as a horizontal line is placed along the midpoint of the geometric feature. When a wave crest passes through the reference location, the frame number and frequency of camera are noted. By processing approximately 3000 images for each individual test cases, it is possible to obtain the frequency and their standard deviation (SD). It should be noted that the frequency for the wave is quasi-periodic (and irregular) as such the SD bar is included to inform about the level of unsteadiness within the surface waves. It is not possible in this stage to write an automated software that detect the peak accurately and returns the frequency passing through that reference location. However, a large number of images for each test cases is taken into consideration.

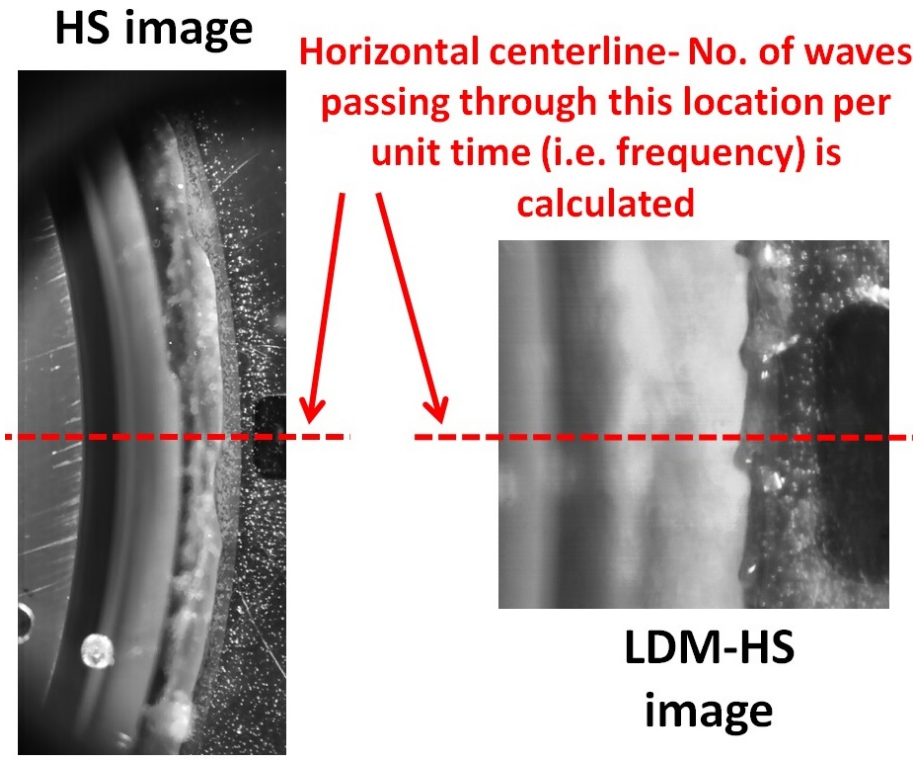


Figure 4.55: Reference location used for determination of surface wave frequency for HS and LDM-HS

The following Table 4.18 and Table 4.19 summarised the wavelengths obtained:

Table 4.18: Wave frequency for co-current side

Test Condition	Type of Imaging	Frequency, f_{wave} (Hz)
S3000-F5.2-L10-P2	HS	25 ± 11.2
S3000-F7.3-L10-P2		28 ± 12.0
S5000-F5.2-L10-P2	LDM-HS	134 ± 87
S5000-F7.3-L10-P2		173 ± 115
S5000-F5.2-L30-P2		141 ± 68
S5000-F7.3-L30-P2		137 ± 93
S7000-F5.2-L10-P2		161 ± 123
S7000-F7.3-L10-P2		178 ± 130
S7000-F5.2-L30-P2		229 ± 160
S7000-F5.2-L30-P2		257 ± 161

Table 4.19: Wave frequency for counter-current side

Test Condition	Type of Imaging	Frequency, f_{wave} (Hz)
S3000-F5.2-L10-P2	HS	20 ± 14
S3000-F7.3-L10-P2		13 ± 8
S5000-F5.2-L10-P2	LDM-HS	60 ± 31
S5000-F7.3-L10-P2		64 ± 43
S5000-F5.2-L30-P2		48 ± 27
S5000-F7.3-L30-P2		47 ± 25
S7000-F5.2-L10-P2		130 ± 125
S7000-F7.3-L10-P2		140 ± 81
S7000-F5.2-L30-P2		99 ± 66
S7000-F5.2-L30-P2		110 ± 72

4.4.5 Wavelength of Surface Waves – λ

For analysis of the wavelength of the surface waves, it is helpful to look at some of the qualitative observations along with quantitative results. The surface waves at co-current side (P2) and counter-current side (P4) are shown in Figure 4.56 and Figure 4.57 respectively. The ratio of wavelength (λ/λ_{crit}) is marked in each images indicating the type of regime and the respective mode observed. From left to right of the figure, rotational speed is in ascending order. The quantitative plots for ratio of wavelength are given after the figures.

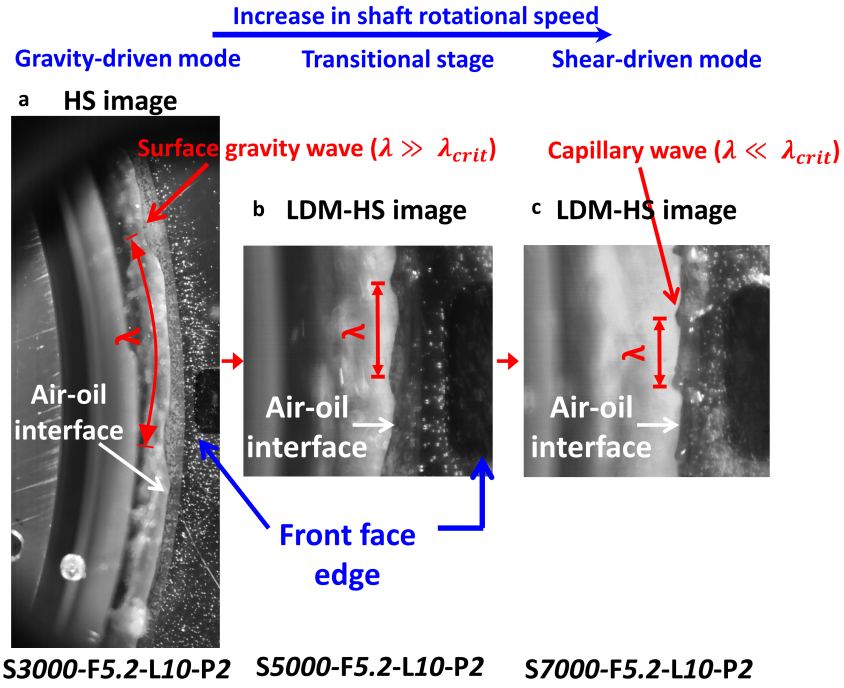


Figure 4.56: Instantaneous images depicting the transitioning of surface waves from gravity-capillary wave to capillary wave by increasing shaft rotational speed at co-current regime (P2)

Based on Figure 4.56, it is observed that the oil flow at low shaft speed of 3000 rpm is gravity-dominated at all flow rate and bearing loadings as $\lambda/\lambda_{crit} \gg 1$. The wavelength λ is measured to be around 29 mm (mean). In contrast at higher rotational speed of 7000 rpm, $\lambda/\lambda_{crit} \ll 1$ for all cases indicated that the dominant restoring force is surface tension. λ is measured to be around 5 mm. These waves were at complete different length scale where λ at high speed is at least 6 times smaller than that at low speed. The surface waves at intermediate shaft speed of 5000 rpm are observed to be transitional as $\lambda/\lambda_{crit} \sim 0.62$. The transition from gravity-capillary waves to capillary waves with increase in shaft speed is seen at both flow rates and there are also very little differences in the data obtained for the two flow rates (e.g. 5.2 lpm and 7.3 lpm).

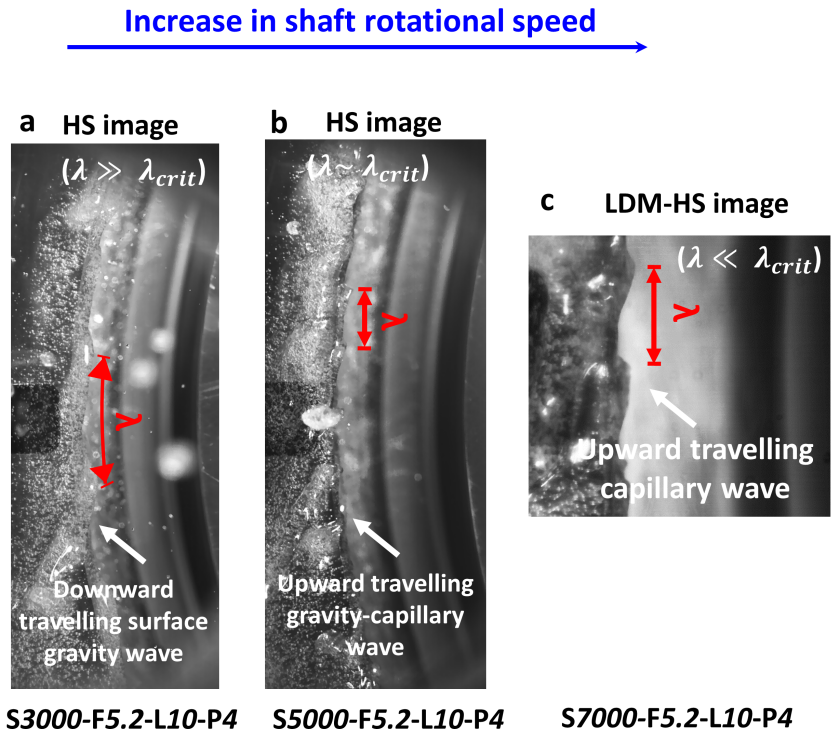


Figure 4.57: Instantaneous images depicting the transitioning of surface waves from gravity-capillary wave to capillary wave by increasing shaft rotational speed at counter-current regime (P4)

For counter-current side, the hydrodynamics of air-oil interface is different to that of co-current side due to forces of interaction between gravity and interfacial shear stress acting opposite to one another. First, the oil is highly three-dimensional where there is a stronger in-plane component. The wavelength at low speed of 3000 rpm is measured to be lower than co-current side but still within gravity-capillary range as $\lambda/\lambda_{crit} \gg 1$. Measuring the wavelength is harder due to the falling film and these films were formed only when a critical mass is attained from the in-plane axially exiting oil. It should be noted here that when 'shock regime' is reached (somewhere between 3000 to 5000 rpm), measuring the wavelength does not seem possible as standing wave will appears (a single large continuous rotating oil crest on the rising side). This also shows the reason why at 3000 rpm, the falling film appears to have shorter wavelength close to capillary regime. Whereas at 5000 rpm, they appeared to be have an 'opposite' effect.

Referring to Figure 4.56, the increase in rotational speed to 5000 rpm increases the gas velocity contributing to greater interfacial shear stress compared to gravity. Flow reversal occurs and it is known as 'beyond shock regime'. Note that the measurement of wavelength is made much easier since waves are travelling upwards with less undulation and appears to be much more planar. The size of the wavelength is intermediate at around 12.1 mm, hence HS images still need to be used.

At this speed, the waves transitioned to capillary waves later than co-current side as indicated by λ/λ_{crit} ~1.04 and they appeared to be 'delayed'. This is consistent with the criteria proposed by Lamb and the effect of gravity is seen here, to be most effective at counter-current side. At very high speed of 7000 rpm, all test cases collapsed on the same region where $\lambda/\lambda_{crit} \ll 1$ indicated a full transitioned to 'smooth-flow' or capillary wave regardless of angular position.

The analysis has shown the existence of small scale wave structure and large scale wave structure driven by both shear and gravity in the film close to surfaces of an aero-engine ball bearing for the first time. It also suggested that use of sector model and with no gravity is highly feasible which could cut-down cost for CFD simulation at speed beyond 7000 rpm.

Quantitative results for wavelength can be given in Figure 4.58 as following:

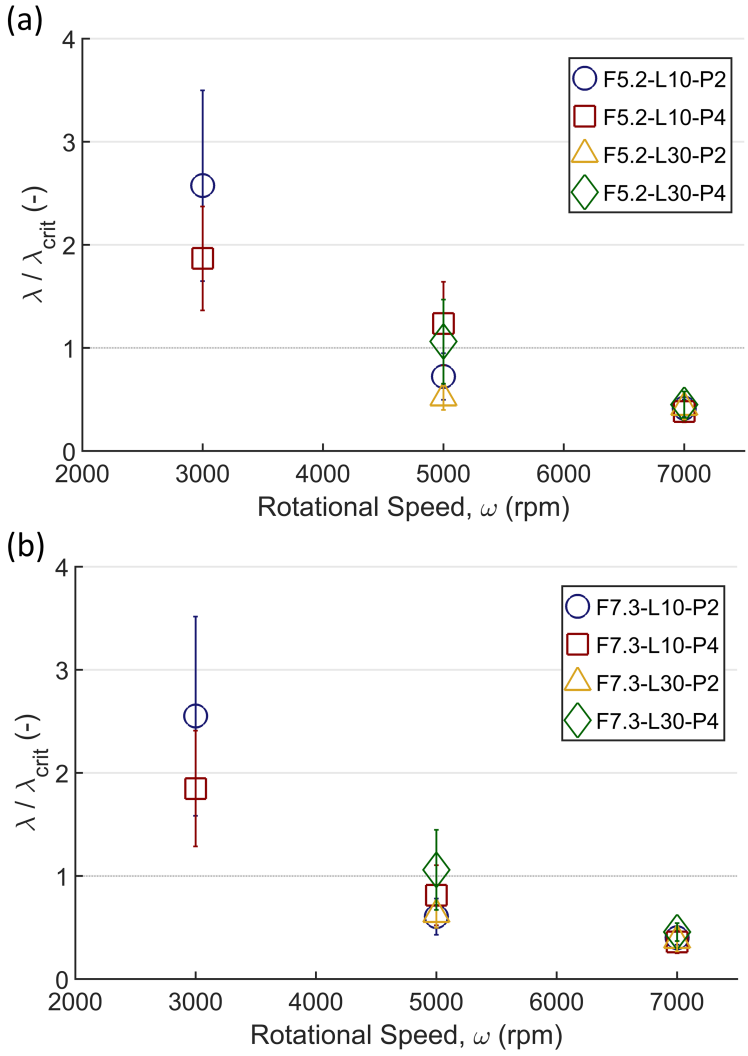


Figure 4.58: $\boldsymbol{\lambda/\lambda_{crit}}$ for con-current and counter-current regime for (a) flow rate 5.2 lpm (b) flow rate 7.3 lpm

4.4.6 Frequency of Surface Waves – f_{wave}

This subsection describes the frequency of surface waves measured using methodology outlined in Section 4.4.4. The graphs of wave frequency are given in Figure 4.59 for flow rate of (a) 5.2 lpm and (b) 7.3 lpm. The frequencies at both con-current and counter-current side are plotted on same graph for comparison.

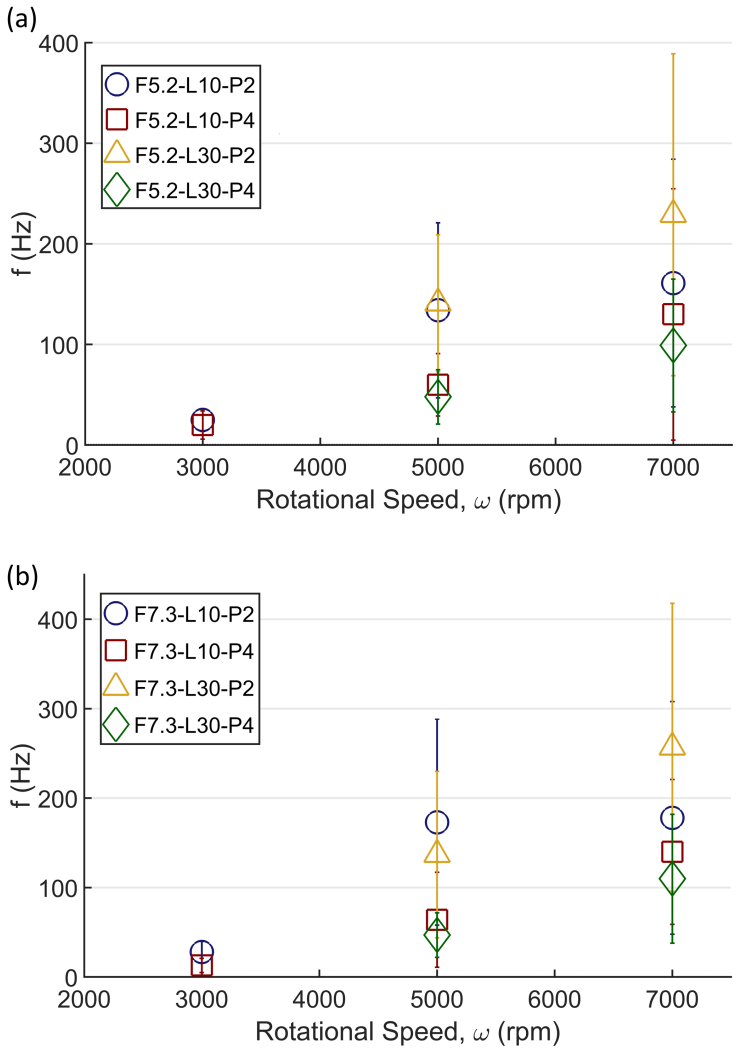


Figure 4.59: Wave frequency versus rotational speed for co-current and counter-current side at flow rate (a) 5.2 lpm (b) 7.3 lpm

Wave frequencies measured are corresponded to the physics of mechanical wave. The increased in interfacial shear stresses resulted in a smaller wavelength for surface waves when speed is increased, this effect must be compensated to conserve the standard wave's equation model (e.g

$v = f\lambda$). At low speed of 3000 rpm, the wave is gravity-capillary in nature and hence they took longer time to pass the reference point. The frequency for both co-current and counter-current were measured to be $13 \sim 25$ Hz (well within the wave spectrum for gravity-capillary wave of Figure 4.50 by Walter [117]). The small deviation in the frequency signified that the waves are 'more' periodic in nature. Meaning they are more regular in occurrence and therefore, gravity-capillary wave is more two-dimensional where wave-fronts tend to move with same phase.

By increasing the speed to 5000 rpm, interfacial shear stress increases resulting in a stronger shearing rate (and more turbulence). The frequency at co-current side increases by 451% from 3000 rpm to 5000 rpm. However, such increase is not seen for counter-current side. At both flow rates, the frequency only increase by 128% due to consistent result at both flow rates. It is further observed that the waves are no longer regular but highly three-dimensional. This three-dimensional waves contain irregular periodicity, contributing to larger deviations and with increased difficulty of measuring the waves' frequency, it is termed as 'quasi-periodic'.

At 7000 rpm, the quasi-periodic surface waves were less far apart. The mean frequencies were well above 100 Hz for all cases. However, at this speed, the difference in frequency for co-current side and counter-current side begins to reduce as the waves transitioned to 'smooth-flow' where influence of gravity is greatly reduced. The frequency for co-current side only increased by 41 % and 118 % for counter-current side. The trend is corresponded with the relation where frequency is proportional to the phase velocity, $v = f\lambda$. From the graph, it is also clear that the axial load from 10 kN to 30 kN is not affecting the frequency (see Figure 4.59a,b ○ ➞ △ and □ ➞ ◇ with exception of one test point F5.2-L30-P2 at 7000 rpm for both flow rates).

4.5 Summary of High Speed Imaging

The experimental investigations of oil disintegrations at the orbiting cage of an aero-engine ball bearing and the formation of thin film at the surfaces of the bearing containment are presented. Long distance microscope is reported to be able to spatially-resolve details 7.2 times higher compared to normal zoom lens. The need for different plane of imaging and angular positions are justified based on different flow features observed. At the axial plane that is very close to the ball, droplets, ligaments and oil sheets were observed to be released from the orbiting cage. Concurrently, at the annular gap between cage outer-landing and the bearing outer-race, oil was observed to be exiting axially and merged with the impinging flow. Moving further away, a dynamic layer of continuous oil film is seen to be occupying the surfaces of the bearing

containment. This film is also being driven by a strong azimuthal component of air velocity around the circumferential locations.

A new optical image-processing method was developed to measure the film thickness. By combining median-stacking formulation and gradient detection, the dynamically moving oil film can be decomposed into a steady-state solution and hence allowing the thickness to be measured by correlating the pixel-value with an object of known scale.

Based on the assessment of rotational speed at different angular positions referred to as co-current and counter-current side. The film thickness was seen to be exhibiting a strong relation with speed. First in co-current side, gravity accelerated the oil film and acts in the direction of interfacial shear stress. The film was seen to be fairly two-dimensional and laminar in nature. For rotational speed of 3000 rpm to 7000 rpm, film thickness decreases as a function of increasing interfacial shear stress. The increase in film velocity indicated that locally, the film thickness has to reduce in order to satisfy the momentum and mass conservation of the axial through flow. Uniquely at 3000 rpm, the film thickness was seen to be thinner at counter-current side compared to co-current side. These could be related to eccentricity and non-linear effect of the ball bearings.

The assessment of flow rates (i.e. 5.2 lpm and 7.3 lpm) at both locations indicated no significant differences on film thickness. For bearing axial load, it was found that at higher load (i.e. 30 kN) the film was observed to be thicker at axial location close to the ball bearing (i.e. plane F). This observation is consistent at both angular positions. It was postulated that the increase in axial load has changed the dynamics of the ball bearing and subsequently was affecting the thickness. According to quasi-static analysis of ball bearing by Foord [93], the increase in axial load increases the outer contact angle (α_0) and the ball rolling axis (β). This could potentially reduce the pressure differences at the gap across the annular area between cage and outer-race leading to slower axial flow and thus thicker film.

At counter-current side, the gravity acts against the interfacial shear stress. The observation at the location is unique and different with that of co-current side. At low shaft speed (i.e. 3000 rpm), film was seen to be falling off due to weaker momentum in azimuthal direction. It is highly three-dimensional similar to rimming flow studies that recirculation occurs at low interfacial shear stress. The film thickness was seen to be decreasing from 3000 rpm to 7000 rpm. Between 3000 rpm and 5000 rpm, the flow regime has transitioned from weak pooling flow to beyond shock regime. The flow has exceeded the critical speed and hence reversed in direction. At highest speed of 7000 rpm, the flow has transitioned to smooth flow where a uniformly coating layer of oil film is seen across the circumferential position. No appreciable differences for flow rate were observed. The measurement of film thickness at this angular position is more challenging as the gradient detection is poorer due to film undulations.

For qualitative analysis of oil disintegrations at the orbiting cage, three regimes of disintegrations were observed. At speed of 1000 to 1700 rpm, atomisation by direct-drop formation was seen where droplets of fairly uniform sizes were released from the outer-most radius of the bearing cage. At critical speed of 1700 rpm, the inertia is higher where ligaments of coherent interspacing were formed at the inner-radius of bearing cage. Concurrently, the variable in flow rate due to transient effect of the ball bearing has caused the existence of laminar sheet on part of the cycles. These phenomena were observed throughout the speed of 1700 rpm to 4300 rpm. At these range, the film is fairly laminar and undisturbed. The increase in speed at this range has also resulted in the increase in Ligament number. A correlation was developed for the ligament number as a function of Weber number and Stability number which can be given as $K = 0.33811\, We^{0.53799} St^{-0.015162}$. (N.B. it is valid for constant flow rate of 5.2 lpm and $St = 3.8875 \times 10^{-5}$).

Beyond 4300 rpm, primary ligament is no longer distinguishable by imaging and the structure of oil sheet has fundamentally changed. The sheet is shorter in both azimuthal and radial directions. Highly turbulent air disrupt the surfaces of oil sheet. Ligament-like structure was now seen to be releasing from the edge of the disordered sheet and is termed as secondary ligament. The droplets breakup from the surfaces and ligaments have larger size distributions. Dimensional analysis shows that many correlations were not valid for bearing shedding geometry and operating conditions. The closest one that predicts the occurrence of ruffled sheet is Hinze and Milborn's ligament to film correlation. Future test points were proposed to further characterise the regimes by varying the speed at different flow rates.

The characterisations of wave structures are also presented. Analysis shows that speed by far is the main factor that affects wave frequency and wavelength. At gravity-dominated speed of 3000 rpm of co-current side, ratio $\lambda/\lambda_{crit} \gg 1$ indicated that the surface wave is gravity-capillary in nature and the instabilities are dampened by gravity and viscous forces. In contrast, capillary wave was observed at higher speed of 7000 rpm where the ratio $\lambda/\lambda_{crit} \ll 1$ for all cases indicating that surface tension forces are more important. At intermediate speed of 5000 rpm, the surface wave was seen to be in the transitional regime (i.e. $\lambda/\lambda_{crit} \approx 1$). The wave frequency measured at 3000 rpm is $13 \sim 25$ Hz confirming the existence of gravity-capillary wave based on the wave's spectrum proposed by Walter [117]. The waves were seen to be more 'periodic' at low speed as opposed to 'quasi-periodic' at high speed which has higher deviations. In most cases, frequencies were measured to be lower at counter-current side compared to co-current side.

Chapter 5 Computational Fluid Dynamics

In this chapter, the computational modelling of jet-breakup and thin film formation in crossflow is described. The motivations behind the usage of Discrete Phase Model (DPM) and Eulerian Thin Film Model (ETFM) are explained in terms of cost benefits by comparing them with the conventional Volume-of-Fluid (VOF) method. The proposed modelling strategies for VOF-DPM-ETFM are made based on the knowledge gained from the experimental studies in Chapter 4. The developments of 2D thin film models by previous authors are highlighted to indicate the research gap and how these models could be implemented into bearing chamber modelling. A series of parametric studies based on changing the number of parcel injection streams, continuous-phase time-step, mesh densities, turbulent dispersion and film sub-models were systematically performed to assess the fidelity and numerical stability of coupling DPM-ETFM in the simulations. Prior to that, the theories underpinning computational fluid dynamics (CFD), model setup, choice for turbulence model and discretisation scheme are given.

5.1 Introduction

Computational Fluid Dynamics (CFD) is a numerical method of simulating fluid flow by means of solving the equations that govern fluid flow – Navier-Stokes equations. This method uses iterative solver and numerical algorithms to solve the nonlinear partial differential equations in order predict flows that are typically inaccessible to probes and instruments. It was foreseen that in future, experiments of a physical kind could be displaced by simulations [123]. CFD has been increasingly popular due to the increase in computational power and the reduction of hardware cost. The earliest usage of CFD is derived from aerospace where it was used to study aerodynamics of aerofoils [84]. It was envisaged that the benefits of simulation could lead to a 33% reduction in engine development cost and 36% in reduction in total number of developments engine [124]. It also allows a priori insight of complex flow structures in a system of interest, however, the models have to be 'exact' in the first hand using priori knowledge of the flow. This chapter focuses on providing the modelling strategies on the investigation of multiphase flow problems relevant to aero-engine application (e.g. bearing chamber simulation).

This chapter is structured in the sequence such that first, the motivation of CFD modelling is outlined along with previously published developmental works. Secondly, the theory underpinning CFD is described in terms of governing principles, turbulence modelling, numerical solver, multiphase solver and thin film models. Thirdly, the mesh generation and discretisation

are explained. In the studies, we investigated the fidelity of coupled Discrete-Phase Model and Eulerian Thin Film Model (also known as DPM-ETFM). Structural approach was taken in explaining the modelling steps, the success of the model and its issues. All simulations are conducted using commercial CFD code ANSYS Fluent Version 14.5 to Version 17.2.

5.2 Motivations of Computational Modelling

In Chapter 4, the experimental investigations of oil shedding from an aero-engine ball bearing and the formation of thin film close to the surfaces of the ball bearing were reported. These information are non-trivial in many ways. In *Lectures in Mathematical Models of Turbulence* [123], Launder and Spalding quoted "For a computer to provide realistic simulation of a flow process, it has to be supplied with a set of instructions (i.e. computer program) which embodies the implications of the conservation of laws of momentum, mass and energy, appropriate to a fluid in motion". First, the experimental data provides an insight into the flow structure of oil through an aero-engine ball bearing. Second, it provides the physical boundary conditions for a realistic flow simulation. And thirdly, the experimental data serves as a validation of the CFD models.

The understanding of multiphase flow is important in order to design a more efficient engine with optimised and lightweight oil system. General principles suggested that minimising heat-to-oil and maintaining a low chamber residence volume decreases the likelihood of oil decomposition [18, 125]. To support the design capability, many bearing chambers studies have been conducted both experimentally and computationally. Examples of computational work on bearing chamber with the research group could be referred to works of Adeniyi *et al*., Andrea *et al.*, Berthold *et al.* and etc [54, 65, 126]. Investigations of oil flow within micro-sized gaps of a dynamically rotating surfaces of engine representative geometry were made [6, 126]. However, many of these CFD simulations employed the use of conventional Volume-of-Fluid [60] or Euler-Euler approach which can be costly due to fine grid and time-step requirement as well as solving extra terms in the flow equations. The computational cost of VOF model was described by Bristot *et al.* [70] as impractical for engine optimisation studies. Bristot *et al.* [70] investigated a shear-driven flow in a simplified but representative model of a full 3D bearing chamber. It was demonstrated with an implicit time discretisation scheme coupled with Compressive Interface Reconstruction and solving the VOF multiphase model, a 2.2 seconds of flow time is needed to reach a 'stationary-state' equating to 12 days on 96 cores parallel cluster. Additionally, a flow time of 1.8 seconds was needed for sampling of the unsteady flow variables to obtain mean solution.

Application of the conventional VOF method for solving two-phase flow is inevitable in the vicinity of a three-dimensional flow structure. The experiment of Chandra *et al.* [125] revealed that the sump (i.e. scavange) region in a bearing chamber contains complex three-dimensional flow structure and recirculation, thus making VOF a suitable choice. At region further away from the sump, lubrication theory applied to rimming flow studies have indicated that smooth flow exists for high interfacial shear stress cases. This was confirmed in our experimental findings at speed beyond 5000 rpm where a thin film is formed at the outer-periphery of the chamber containment.

In smooth flow, interfacial shear stress is greater than gravity due to strong tangential component resulting in a uniformly coated film around the chamber wall. This flow is also very weak in radial component ($v_r \approx 0$). The two-dimensional nature of such thin film flow encouraged the development of so-called Eulerian Thin Film Model (ETFM) which has a much lower computational requirements than VOF as the grid requirements are relaxed. The model uses Eulerian formulation to solve the transport equations for mass, momentum and energy locally within the grids. An illustration of Eulerian approach in VOF and ETFM is shown in Figure 5.1 comparing the respective grid requirements.

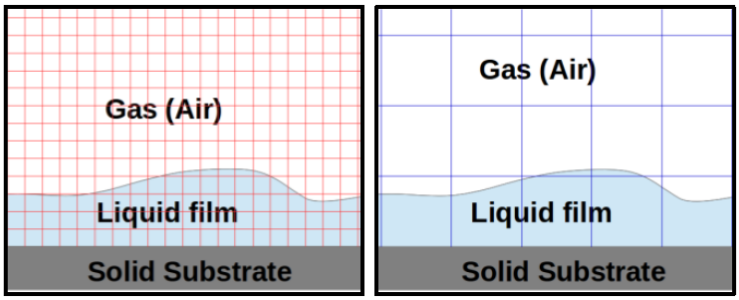


Figure 5.1: Illustration of film and interface resolution requirements for VOF (left) and ETFM (right) [81]

The proposed modelling approach for oil shedding and thin film is given in Figure 5.2. For the modelling of ligament and oil sheet breakup at the orbiting cage, a coupled VOF-DPM approach is proposed as experimental studies indicated that the shed droplets are of a size distribution that is significantly below the length scale of VOF cells. Meanwhile for the modelling of thin liquid film along with the impinging droplets, a coupled DPM-ETFM approach is proposed. To visualise the proposed modelling strategies, Figure 5.2 is given along with its cross-sectional diagram at A-A in Figure 5.3.

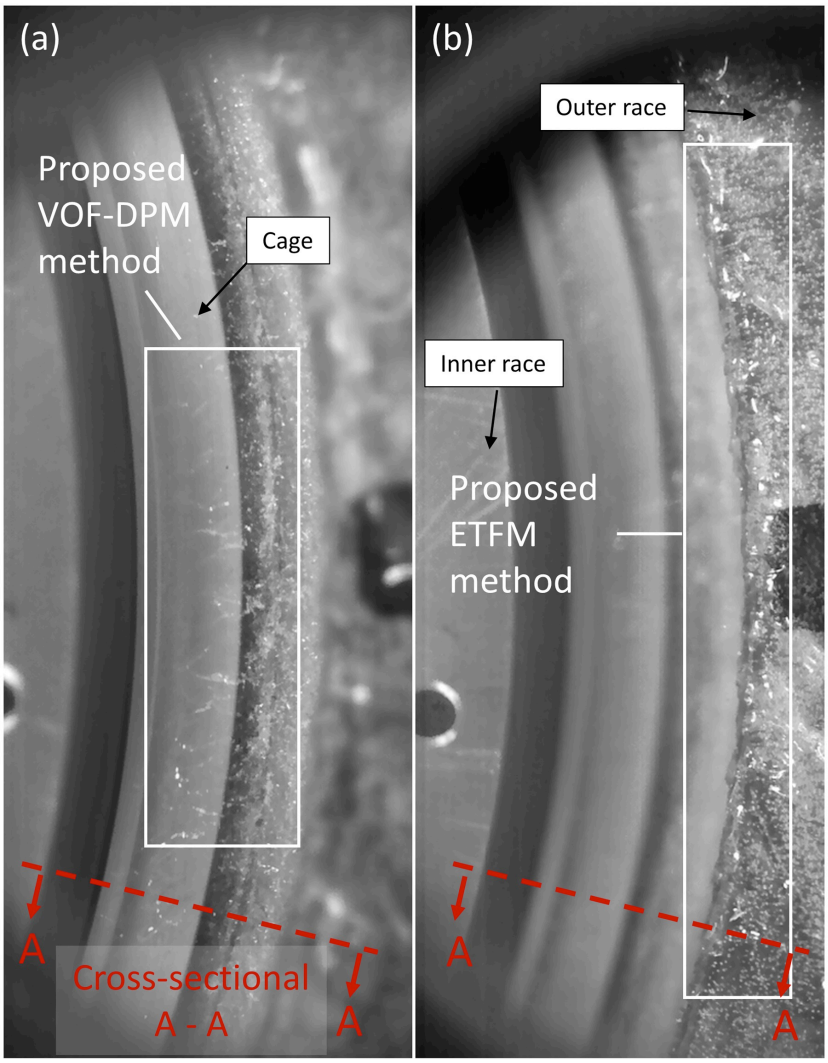


Figure 5.2: Proposed modelling approach for respective flow structures [127]

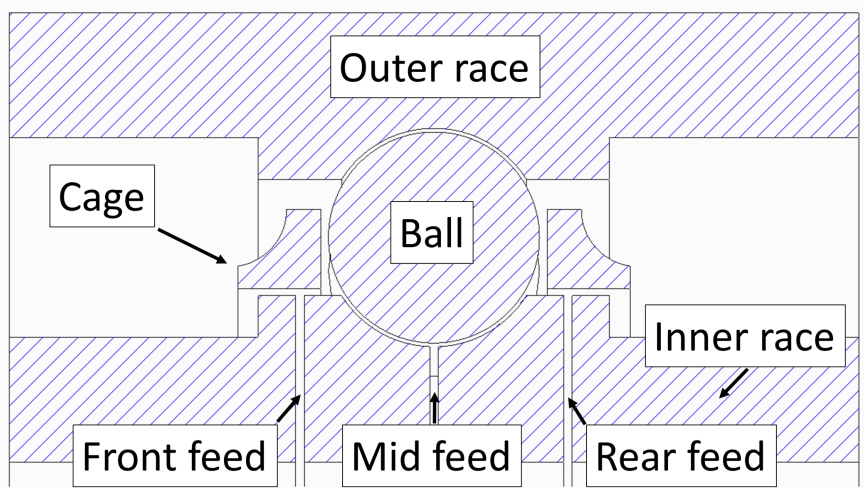


Figure 5.3: Cross-sectional view of aero-engine ball bearing corresponding to view A-A [127]

The motivation of the computational work here is to explore the feasibility of coupling VOF-DPM-ETFM. To do so, the model DPM-ETFM should work as intended. This is accomplished by validating the model with work of Shedd *et al.* [128] and Arienti *et al.* [13]. In this computational work, mineral spirits are injected into expansion duct normally via a plain orifice atomiser to the high velocity cross-flow. As liquid is injected, instabilities mechanisms caused the liquid to disintegrate and form droplets. The droplets impinge onto opposite surface and some travel with the flow depending on their mass and momentum. The formation of thin film on the surface is eventually transported by surface shear. The modelling approach will be made clear in subsequent sections.

5.3 The Developments of 2D Thin Film Model

Lubrication theory is the framework used in deriving two-dimensional thin film model by simplification of N-S equations. It contains several assumptions to be valid: The normal velocity component is insignificant compared to other components (e.g. axial and azimuthal of a rotating system), the fluid is treated as incompressible or weakly compressible and the film aspect ratio is very much less than 1 when measured relative to the length of the geometry. This equation could involves leading order term or several first order terms. Terms which have important contribution to the transport equation. 2D thin film model found many applications where such film existed such as analysis of pressure distribution, film thickness and load capacity of two contact surfaces. And often it has some resemblance to the Reynolds Equations. Typically a thin film by definition is a liquid resting or moving on a solid substrate where its thickness is very much smaller than the characteristics length of the geometry (i.e. $h \ll L$).

An early development of thin film model was made by Moffatt [129] where he applied lubrication theory in the analysis of rimming flow. This model assumed no surface tension and inertia contributions. And it was shown that the model only able to accommodate for low rotational speed such that $\partial h/\partial \theta$ is locally small and the initial film height for solution initialisation must also be sufficiently small (i.e. $Uh_o^2/va \ll 1$). Where h_o is the initial film height and a is radius of the cylinder. Other notations can be referred in Nomenclature.

Subsequently, Ashmore [130] developed and numerically tested the thin film model using approximation method with inclusion of surface tension term for solution stability. It was shown that the model is capable of simulating both smooth and pooling flow without inertia term. Numerical work of Pougatch and Frigaard [131] looked at solution stability of thin film flow inside a cylinder based on influences of gravity, inertia, viscous and surface tension forces.

Similarly their model lacks a 'proper' treatment of inertia as solution began to breakdown at $Re \gg 1$.

Kay *et al.* [78] indicated that in a typical aero-engine environment, the inertia term must be included due to shearing effect and addition of momentum flux arises from droplets impacting the film surface. In their model, a depth-averaged formulation similar to one used in the field of hydraulics and open-channel flow is integrated into the film model. The model demonstrated the ability to numerically simulate smooth, pool and shock flow with all terms retained. Subsequent improved model with inclusion of heat convection term for heat-transfer application is developed [132]. Elements of their model were implemented into commercial CFD code in ANSYS Fluent. In additional to work of Kay *et al.* [78], Kakimpa *et al*. [81] extended the work by developing an in-house implementation of the model for coupled VOF-ETFM bringing thin film modelling one step closer. The developed approach was applied to a bearing chamber representative model demonstrating the feasibility of such as approach and justifying the cost benefits. The study shows that the coupled VOF-ETFM model is able to predict thin film formation on grid densities well below the VOF volume fraction cut off point and this prevented artificial dry-out [79, 81]. Details of computational modelling are given in next sections.

5.4 Governing Equations

5.4.1 Continuity Equation

The continuity equation is a mathematical statement that matters are conserved in a flow. By treating the particles within the fluid as continuum rather than individual molecules and apply Taylor Series expansion to an infinitesimal fluid element. The equation of mass conservation in three-dimensional Cartesian coordinate in vector notation can be derived from the balance of mass flux in and out of the element:

$$\frac{\partial \rho}{\partial t} + div\,(\rho v) = 0 \tag{5.1}$$

The first term in Equation (5.1) denotes that the rate of change of density with time. The second term is the net mass flux out of the fluid element across its boundaries, known as convective term. It is unsteady, three-dimensional continuity equation for compressible flow. In the case of incompressible flow, the equation is simplified as $div(\rho v) = 0$ as the transient term $\partial\rho/\partial t \rightarrow 0$. All cases of the simulation are treated as incompressible flow since they are well below subsonic

regime (i.e. $Ma < 0.6$). It should be noted that the equation of the following form is used in computing:

$$\frac{\partial \rho}{\partial t} + div\,(\rho v) = S_M \tag{5.2}$$

Where, S_M is the mass source term which could include phase change from dispersed phase or secondary-phase.

5.4.2 Navier-Stokes Equation (N-S)

The unsteady Navier-Stokes equations are the governing equations for fluid flow. It can be derived by applying Newton's second law of motion and expressing viscous stresses as a function of strain rate on infinitesimal fluid element. The derivations of N-S equations are well described in many text books and step-by-step derivations will not be included here. The equations can be presented in vector form as [133]:

$$\overbrace{\rho\left(\underbrace{\frac{\partial \vec{v}}{\partial t}}_{\substack{time\\ dependent\\ acceleration}} + \underbrace{\vec{v}.\nabla\vec{v}}_{\substack{convective\\ acceleration}}\right)}^{Inertial\ terms} = \overbrace{\underbrace{-\nabla p}_{\substack{pressure\\ gradient}} + \underbrace{\nabla\mu[\nabla\vec{v} + (\nabla\vec{v})^T]}_{\substack{viscous\\ forces}}}^{surface\ forces} - \overbrace{F_s + \underbrace{\rho\vec{g}}_{gravity}}^{body\ forces} + \underbrace{\overrightarrow{S_m}}_{\substack{source\\ term}} \tag{5.3}$$

Referring to Equation (5.3), the terms on the left are inertial terms which represent the fluid's momentum. The external forces that acted onto the fluid element can be expressed in terms of surface forces, body forces and source term. The third term and fourth term in the right side are pressure gradient and viscous forces. The fifth term is surface tension and the sixth is gravitational force. Additional forces can be included in the sixth term (i.e. source term) such as momentum contribution from discrete phase as they coincide the respective grid.

5.5 Turbulence Modelling

5.5.1 Unsteady Reynolds-Averaged Navier-Stokes Equations (URANS)

In most engineering application, the flow is highly turbulent. Turbulent flow can be associated as random, chaotic, time-dependent motion and often non-deterministic [134]. Performing scale-resolving simulations like Direct Numerical Simulation (DNS) is impractical since it requires extremely fine grids and temporal-resolutions to resolve the large scale turbulence structure (L) down to the smallest scale eddies within viscous sublayer known as Kolmogorov length scale (η). And in most cases, these extremely small scale structures were not needed in engineering application although they are important in problems that involve skin-friction drag and heat transfer. Therefore, Reynolds decomposition is introduced into Equation (5.4) where the instantaneous velocity (exact) is expressed as the sum of mean and fluctuating part:

$$u(t) = \widetilde{U}(t) + u'(t) \tag{5.4}$$

Where, $u(t)$ is the instantaneous velocity in the full form N-S equations, $\widetilde{U}(t)$ is the mean velocity of the steady or unsteady flow. And $u'(t)$ is the fluctuating component. And by applying time-averaging process to the N-S equations, the process yields the Unsteady Reynolds-Averaged Navier-Stokes Equations (URANS).

The URANS for x-direction can be expressed as following [84]:

$$\begin{aligned} \frac{\partial \bar{\rho}\widetilde{U}}{\partial t} + div\left(\bar{\rho}\widetilde{U}\widetilde{U}\right) & \\ = -\frac{\partial \bar{P}}{\partial x} + div\left(\mu\, grad\, \widetilde{U}\right) & \\ + \left[-\frac{\partial(\overline{\bar{\rho}u'^2})}{\partial x} - \frac{\partial(\overline{\bar{\rho}u'v'})}{\partial y} - \frac{\partial(\overline{\bar{\rho}u'w'})}{\partial z}\right] + S_{Mx} & \end{aligned} \tag{5.5}$$

During Reynolds decomposition, extra stress terms were created yielding three normal stresses and three shear stresses. The normal stresses are expressed as $\tau_{xx} = -\rho\overline{u'^2}$, $\tau_{yy} = -\rho\overline{v'^2}$ and $\tau_{zz} = -\rho\overline{w'^2}$. Meanwhile, the shear stresses are expressed as $\tau_{xy} = \tau_{yx} = -\rho\overline{u'v'}$, $\tau_{xz} = \tau_{zx} = -\rho\overline{u'w'}$ and $\tau_{yz} = \tau_{zy} = -\rho\overline{v'w'}$. These terms are known as Reynolds stresses. In the equations, there are more unknown than equations. And for such closure problem, the flow must be 'modelled' to determine the artificial viscosity known as turbulent viscosity. Notably, the

earliest approach to modelling of turbulence is attributed to work of Boussinesq (refer [123]). The Reynolds stress is expressed as the product of mean velocity gradient and turbulent viscosity:

$$\tau_{ij} = -\rho\overline{u_i'u_j'} = \mu_t\left(\frac{\partial u_i}{\partial x_j} + \frac{\partial u_j}{\partial x_i}\right) - \frac{2}{3}\rho k\delta_{ij} \tag{5.6}$$

Since μ_t is not a property of fluid unlike molecular viscosity, the term must be expressed in term of calculable quantities. The turbulent eddy viscosity, μ_t can be obtained from a list of turbulence models such as one-equation model, two-equation model or second-moment closure model Reynolds Stress Model (RSM) which solves individual transport equations for stresses.

5.5.2 Choice of Turbulence Model – Menter $k-\omega$ SST Turbulence Model

The $k-\omega$ SST turbulence model by Menter [135] is highly suitable for industrial related flow (i.e. high Reynolds number and wall bounded). It overcomes some of the weaknesses of $k-\varepsilon$ model which failed to capture flow with strong separation and adverse pressure gradient. It also performs better in free shear flow compared to Spalart-Allmaras (SA) model. The model is robust, widely validated for its numerical stability and is accurate in predicting the shear stresses close to the wall. It is regarded as 'low' Reynolds number model where the first cell centroid should be within non-dimensional wall distance, y^+ of 1. Although y^+ insensitive formulation is included in the latest algorithm which will correct the equation depending on y^+ value. It is still recommended that the y^+ should be 1 for accurate predictions of wall values.

This model incorporates 'blending' function where in fully turbulent region (far away from the wall), a $k-\varepsilon$ based transport equation is used. And very near to the wall, the original $k-\omega$ model by Wilcox is used [86]. Comparing the model with RSM, RSM contains all terms for Reynolds Stresses which is inherently anisotropy as opposed to isotropy of $k-\omega$. Lee *et al.* [9]showed that it yields better results in Taylor-Couette turbulent flow in chamber-like geometry. However, RSM is several order of magnitude more expensive and often diverges easily without a high quality dense mesh. Latest formulation by Menter was shown to be able to accurately predict most general flows and was used by various authors in bearing chamber studies [6, 54, 126].

The turbulent viscosity, μ_t is obtained by solving two transport equations; turbulence kinetic energy (k) and specific dissipation rate (ω). For transport equation, k [136]:

$$\frac{\partial}{\partial t}(\rho k) + \frac{\partial}{\partial x_i}(\rho k u_i) = \frac{\partial}{\partial x_j}\left(\Gamma_k \frac{\partial k}{\partial x_j}\right) + G_k - Y_k + S_k \tag{5.7}$$

And for the transport equation, ω:

$$\frac{\partial}{\partial t}(\rho \omega) + \frac{\partial}{\partial x_i}(\rho \omega u_i) = \frac{\partial}{\partial x_j}\left(\Gamma_\omega \frac{\partial \omega}{\partial x_j}\right) + G_k - Y_k + S_k \tag{5.8}$$

In the above equations, G_k represents the generation of turbulence kinetic energy due to mean velocity gradients, G_ω represents the generation of ω. Γ_k and Γ_ω represent the effective diffusivity of k and ω, respectively. Y_k and Y_ω represent the dissipation of k and ω due to turbulence. A detail descriptions of all variables such as S_k and S_ω could be referred to original paper [135] or reference text book [84]. The turbulence model $k - \omega$ SST is used in all the simulations.

5.5.3 Near Wall Treatment

When a flow passes a surface, a boundary layer is formed. The concept of boundary layer was first conceived by Prandtl that the effect of frictions within the fluid (viscosity) present in a layer very close to the surface. The existence is important for wall-bounded flow. At very close to the surface, the velocity gradient is the largest contributing to very large local shear stresses. The viscous damping and near-wall features augment the turbulence in the outer-region through a process known as vortex stretching. This makes near wall modelling challenging since it affects the fidelity of numerical simulations. Turbulent boundary layer is universal, one could refers to comprehensive works of Osterlund on experimental studies of zero-pressure gradient turbulent boundary layer where the flow close to the wall is studied experimentally using hot-wire anemometry [137]. The velocity profile of a turbulent boundary layer for flow condition of $2530 < Re < 27300$ is presented in Figure 5.4.

In the y^+ of 0 to 5, the viscous effect is the strongest and the velocity profile is linearly varying with the wall distance. This layer is known as viscous sublayer. At y^+ of 5 to 30, the layer is known as the buffer layer. It is the bridging zone between the viscous sublayer and the turbulent outer-layer. In mesh generation, the first cell centroid should avoid being created in this region as it could incur error in modelling due to lacking relationship that clearly differentiating the regions. In region after $y^+ > 30$, viscous effect no longer dominant and the flow is said to be within the turbulent outer layer. Von Karman conceived the velocity profile as proportional to the logarithmic distance from the wall. This region is known as logarithmic sublayer or outer region where turbulence extract energy the greatest through gradient of mean flow.

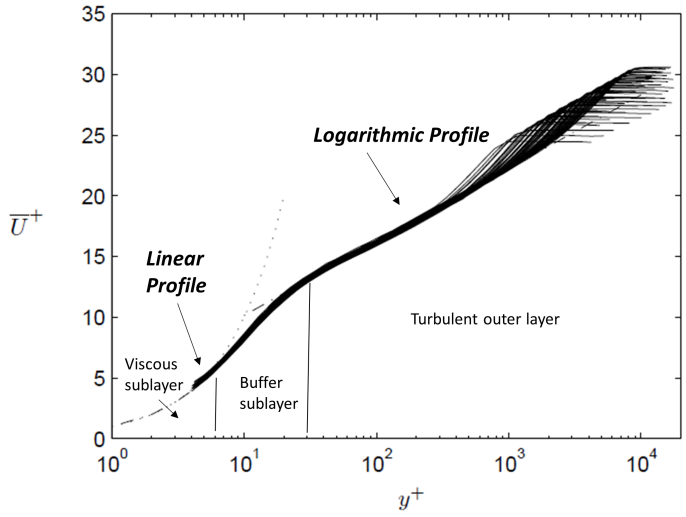


Figure 5.4: Mean velocity profile and subdivision of boundary layer. Flow condition at $2530 < Re < 27300$. Dash-dotted line ($\overline{U}^+ = (1/0.38)\ln y^+ + 4.1$) [137].

As the wall shear stress is important for transportation of liquid film. A near wall approach is preferred over the wall function approach. In wall function approach, the first cell centroid is placed somewhere within the outer region and a semi-empirical model is used to determine the profile within the sublayers. This method is only recommended for highly inviscid flow and if only the bulk feature is of interest (i.e. core). In contrast, the near wall approach involves resolving the flow all the way down to the viscous sublayer. For $k-\varepsilon$ model, a modification to the turbulence transport equation is made such that it is valid near the wall. For low-Re model like $k-\omega$ SST turbulence model, the model is valid to the wall by default. However, the first cell centroid should be within the viscous sublayer ($y^+ \approx 1$). The near wall modelling approach is used in this research. Mesh information is provided in Section 5.9.

5.6 Discretisation Scheme

5.6.1 Spatial Discretisation

A numerical discretisation scheme is needed to convert the nonlinear partial differential equations of N-S into a system of algebraic equations such that it can be solved numerically within the grids. In Fluent, the governing equations are discretised using Finite Volume Method (FVM) [84]. For simplicity, refer the variable of a scalar transport equation as ϕ over the control volume. The unsteady conservation equation for transport of a scalar quantity is given as following:

$$\int_V \frac{\partial \rho\phi}{\partial t}\, dV + \oint \rho\phi\vec{v}.\overrightarrow{dA} = \oint \Gamma_\phi \nabla\phi\,.\overrightarrow{dA} + \int_V S_\phi dV \tag{5.9}$$

Where, ρ is density, $\vec{v}$ is velocity vector (i.e. $u\hat{\imath} + v\hat{\jmath}$ in 2D), $\vec{A}$ is surface area vector, Γ_ϕ is diffusion coefficient for ϕ, $\nabla\phi$ is gradient of ϕ (i.e. $\frac{\partial\phi}{\partial x}\hat{\imath} + \frac{\partial\phi}{\partial y}\hat{\jmath}$ in 2D), S_ϕ = source of ϕ per unit volume. An example of discretisation of a cell or control volume is given as follows and with reference to [136] is as follows:

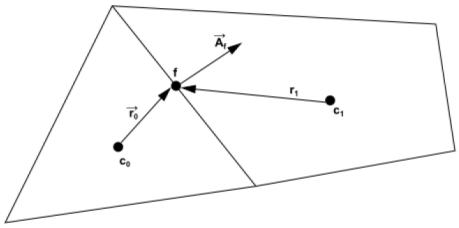


Figure 5.5: Discretisation of a 2D-triangular cell [136]

$$\frac{\partial \rho\phi}{\partial t}V + \sum_f^{N_{faces}} \rho_f \vec{v}_f \phi_f\,.\vec{A}_f = \sum_f^{N_{faces}} \Gamma_\phi\, \nabla_{\phi_f}.\vec{A}_f + S_\phi V \tag{5.10}$$

Where, N_{faces} is the number of faces enclosing the cell. ϕ_f is value of ϕ convected across the face f, $\rho_f\vec{A}_f\vec{v}_f$ is mass flux through the face, $\vec{A}_f$ is area of face f (i.e. $|A| = \left|A_x\hat{\imath} + A_y\hat{\jmath}\right|$ in 2D), $\nabla\phi = \left(\frac{\partial\phi}{\partial x}\right)\hat{\imath} + \left(\frac{\partial\phi}{\partial y}\right)\hat{\jmath}$, V is cell volume. For transient simulation, the time dependent first term in Equation (5.10) must be computed through temporal discretisation. There are several spatial discretisation scheme available such as centre differencing scheme, first-order upwind, second-order upwind and third-order MUSL [84].

5.6.2 Temporal Discretisation for Time-Marching

In an unsteady flow simulation, transient formulation is needed to temporally discretise the partial differential equation such that the time evolution of a variable ϕ of the next time advancement can be determined. This in contrast differs with steady-state simulation since the numerical solution is advanced by iteratively solving only the non-time-dependent terms. The mean variable is true, unchanged and is final regardless of any further iteration when converged. It should be noted that for transient formulation, the solution is true for each time-step at end of

the iterations but does not constitute to the final mean solution until a 'stationary-state' or time-average mean property is reached.

Temporal discretisation involves the integration of every term in the differential equations over a time-step denoted as Δt. There are several temporal discretisation scheme available. First, looking at the general expression for time evolution of variable, ϕ:

$$\frac{\partial \phi}{\partial t} = F(\phi) \tag{5.11}$$

Where, the function F is refers to any spatial discretisation. And for first-order discretisation the equation is given as following:

$$\frac{\phi^{n+1} - \phi^n}{\Delta t} = F(\phi) \tag{5.12}$$

And for second-order discretisation scheme:

$$\frac{3\phi^{n+1} - 4\phi^n + \phi^{n-1}}{2\Delta t} = F(\phi) \tag{5.13}$$

In the above Equation (5.11) and (5.12), ϕ is a scalar quantity, $n+1$ is the solution for the next time advancement $(t + \Delta t)$, n is the solution at current time (t) and $n-1$ is the solution of previous time. We computed the first-order accurate implicit time discretisation. To ensure solution stability during time-marching, the time-step size (Δt) is chosen such that it 'approximately' satisfies the Courant-Friedrichs-Lewy (CFL) number of 1. The Δt can be determined by using CFL expression given in Equation (5.14):

$$CFL = \frac{|\vec{u}|}{\left(\frac{\Delta x}{\Delta t}\right)} \tag{5.14}$$

And by rearranging Equation (5.14), Δt can be express as:

$$\Delta t \leq \frac{\Delta x}{|\vec{u}|} \tag{5.15}$$

The Δt should be smaller than the ratio of characteristics length (Δx) of the computational cell to the flow velocity $(|\vec{u}|)$. Implicit formulation is unconditionally stable for choices of time-step. Hence, a range of time-steps was tested by systematically varying the courant number from small, intermediate to large (see Section 5.12.2). This enables the assessment of the sensitivity of the solution with respect to changes in time-dependent variables and help decide the most cost effective time-step without sacrificing on solution accuracy.

5.6.3 Pressure-Velocity Coupling (P-V)

In the modelling of compression and incompressible flow, the velocity field can be derived from the momentum equation. And for density-based solver which is suited for compressible flow, the equation of state for gases is used to determine the pressure field. However, in a weakly compressible flow such as pressure-based solver there is not link between the momentum equation and pressure. A pressure-correction equation is used instead for extraction of pressure field. There are two numerical algorithms for pressure-based solver: (1) Segregated and (2) Coupled [84].

In Segregated P-V solver, the variables are solved sequentially by calculating one variable at a time. Subsequently, the variables are updated sequentially until a mass flux is balanced and the solution is converged. This method is less memory-intensive since not all variables need to be stored at one time. However it takes a longer time to reach a converged solution. For the coupled solver, a system of equations consisting the momentum and pressure-correction terms are solved simultaneously. This method improves convergence stability but requires $1.5 \sim 2$ times more memory per unit time-step. Although each time-step takes longer to iterate the convergence time is reduced. In the simulations of this chapter, Coupled P-V scheme is used to obtain the pressure-field.

5.7 Discrete-Phase Model

This section describes theory underpinning Euler-Lagrangian particle tracking method, it was mentioned in Section 5.2 that the modelling of droplet is carried out by DPM since the interface tracking of a collective number of particles are prohibitive using VOF. The sub-models for interaction between DPM with continuous phase and ETFM in the simulations are given in subsequent sections.

5.7.1 Particle Force Balance Equation

The particles are tracked in the Lagrangian frame of reference by integrating the particle force balance equation [136]:

$$\frac{d\overrightarrow{u_p}}{dt} = \frac{\vec{u} - \vec{u}_p}{\tau_r} + \frac{\vec{g}(\rho_p - \rho)}{\rho_p} + \vec{F} \tag{5.16}$$

In the above differential equation, the particle's acceleration is expressed as sum of all forces acting on it. The first term on the right is drag force per unit particle mass computed through the relative velocity of particle and fluid phase. It is the dominant force that determines the trajectory of the particle. The second term represents the relative density between phases. The third term is the external forces acting on the particle. External forces such as secondary breakup are included in the $\vec{F}$ term which caused significant changes to the momentum source. The coefficient of drag, C_d for particle is computed through particle relaxation time, τ_r:

$$\tau_r = \frac{\rho_p d_p^2}{18\mu} \frac{24}{C_d Re} \tag{5.17}$$

Where, C_d is computed from a list of Drag Laws in Fluent. And for the spray modelling simulation, the coefficient is taken from the Dynamic Drag Model Theory developed by Liu *et al.* [138] which is corresponded with the choice of Arienti *et al.* [13].

5.7.1.1 Dynamic Drag Model

At relatively high velocity environment, droplets could deform and their shapes could change dynamically. Liu *et al.* discovered that the standard drag coefficient in their KIVA-2 model does not accurately representing the actual trajectories of the spray. They proposed a drag model that accounts for the droplet distortion, oscillation and relative motion between the gas-phase and dispersed phase [138]. The drag coefficient of a sphere is related to the Reynolds number as:

$$C_{d,sphere} \begin{cases} 0.424 & Re > 1000 \\ \frac{24}{Re}\left(1 + \frac{1}{6}Re^{2/3}\right) & Re \leq 1000 \end{cases} \tag{5.18}$$

Where, Re is the relative Reynolds number computed based on:

$$Re = \frac{\rho_g d_p \left|\vec{u}_p - \vec{u}\right|}{\mu_l} \tag{5.19}$$

In the Equation (5.19), ρ_g is the density of gas-phase, d_p is droplet diameter, μ_l is viscosity of the liquid and $\left|\vec{u}_p - \vec{u}\right|$ is relative velocity between gas and particle. In addition to the flow condition, the droplet distortion is also taken into account based on:

$$C_d = C_{d,sphere}(1 + 2.632y) \tag{5.20}$$

Here, y is the droplet distortion and is determined from similar formulation taken from Taylor Analogy Break Model (TAB):

$$\frac{d^2y}{dt^2} = \frac{C_F}{C_b}\frac{\rho_g}{\rho_l}\frac{u^2}{r^2} - \frac{C_k\sigma}{\rho_l r^3}y - \frac{C_d\mu_l}{\rho_l r^3}\frac{dy}{dt} \tag{5.21}$$

For initial distortion y is set as 0, hence the drag coefficient of a sphere is obtained.

5.7.1.2 Interphase Momentum Exchange

As particle passes a grid, the contribution of mass and momentum from particles could be large enough to sufficiently affecting the flow field. The effect is known as two-way turbulence coupling and by default one-way coupling is activated. This can be included through interphase momentum exchange as following:

$$F = \sum\left(\frac{18\mu C_D Re}{\rho_p d_p^2 24}\left(u_p - u\right) + F_{other}\right)\dot{m}_p \Delta t \tag{5.22}$$

Where, μ is viscosity of fluid, ρ_p is density of particle, d_p is particle diameter, Re is relative Reynolds number, u_p is velocity of particle, u is velocity of fluid, C_D is drag coefficient, $\dot{m}_p$ is mass flow rate of the particles, Δt is time step and F_{other} is additional interaction forces. In this model, the interphase momentum exchange is transferred iteratively until no changes occur (e.g. mass, momentum and energy). Here, the particle is treated as inert with no interaction with energy equation and only momentum exchange. With the computed F, it is included as momentum source in the continuous phase momentum equation.

5.7.2 Primary Atomisation of Plain Orifice Model

When liquid exits the constriction of an atomiser (i.e. plain orifice), the liquid jet accelerates due to the constriction of the nozzle. Instabilities are developed on the gas-liquid interface leading to the breakup of ligaments. The instabilities are associated with RT instabilities and KH instabilities. There are several atomisation models available in Fluent and these models are based on semi-empirical model of some kind. In order to match the behaviour of the experimental nozzle, the plain-orifice atomiser sub-model available in Fluent is used [136].

5.7.2.1 Nozzle State

The internal nozzle state of a plain-orifice atomiser is important to obtain the initial droplet size, velocity and dispersion angle. Three states are defined as (1) single-phase nozzle flow (2) cavitating nozzle flow (3) flipped nozzle flow by Soteriou *et al.* [139]. In single-phase nozzle flow, the liquid fully filled the orifice. Whereas for cavitating nozzle vapour pockets are formed just immediate to the inlet corners. Whereas, for flipped nozzle flow the downstream gas surrounds the liquid jet inside the nozzle. These regimes lead to different discharge properties. The parameters that determine the nozzle state are Reynolds number based on hydraulic head (Re_h):

$$Re_h = \frac{d\rho_l}{\mu}\sqrt{\frac{2(p_1 - p_2)}{\rho_l}} \tag{5.23}$$

And Cavitation number (K):

$$K = \frac{p_1 - p_v}{p_1 - p_2} \tag{5.24}$$

Where, d is the nozzle diameter, p_1 is the upstream pressure set by user (default value of 10000 Pa is used), p_2 is downstream pressure based on value of the cell where injection point is, μ is viscosity, ρ_l is liquid density. The K value for the inception of cavitation is give as:

$$K_{incep} = 1.9\left(1 - \frac{r}{d}\right)^2 - \frac{1000}{Re_h} \tag{5.25}$$

Where in Equation (5.25), r is radius of curvature of the inlet (such as chamfering angle of inlet). If the chamber angle is 0 (i.e., sharp-edge nozzle), the $K_{incep} \approx 1.9$. And for flip nozzle state, the expression of K is given as:

$$K_{crit} = 1 + \frac{1}{\left(1 + \frac{L}{4d}\right)\left(1 + \frac{2000}{Re_h}\right)e^{70(\frac{r}{d})}} \quad (5.26)$$

The computed K is compared to K_{incep} and K_{crit} to determine the state. In all cases of simulation. The nozzle state was found to be single-phase where the following criteria is met $K > K_{incep}$ and $K \geq K_{crit}$. Hence, the coefficient of discharge for single-phase is determined by:

$$C_d = \frac{1}{\frac{1}{C_{du}} + 20\frac{(1 + \frac{2.25L}{d})}{Re_h}} \quad (5.27)$$

And C_{du} is the ultimate discharge coefficient, and is taken from:

$$C_{du} = 0.827 - 0.0085\frac{L}{d} \quad (5.28)$$

Where L is the length of the orifice and d is the diameter of orifice. Based on nozzle parameters defined by Shedd *et al.* [128] and Arienti *et al*. [13], $L = 1\ mm$ and $d = 0.5\ mm$. And the density of liquid for mineral spirits, ρ_l is given as $780\ kg/m^3$.

5.7.2.2 Exit Velocity

The exit velocity is the speed at which the droplet is exiting the nozzle outlet. It is taken directly from the equation for conservation of mass, this is only true for single-phase nozzle as:

$$u = \frac{\dot{m}_{eff}}{\rho_l A} \quad (5.29)$$

If other nozzle state is obtained, different formulations must be considered and it can be referred from Fluent Theory Guide [136]. For the simulations, u of 12.7 m/s is obtained and $\dot{m}_{eff}$ of 0.001945 kg/s should be prescribed in Fluent based on A and ρ_l of Arienti *et al.* [13].

5.7.2.3 Spray Angle, θ

Spray angle (or dispersion cone angle) is an important parameter in physics of primary atomisation. In most orifice atomiser, the angle is narrow as mentioned by Lefebvre [32], the angle is determined from work of Ranz *et al*. [140] as following:

$$\frac{\theta}{2} = \begin{cases} \tan^{-1}\left[\frac{4\pi}{C_A}\sqrt{\frac{\rho_g}{\rho_l}}\frac{\sqrt{3}}{6}\right] & singlephase, cavitating \\ 0.01 & flipped \end{cases} \tag{5.30}$$

And in Equation (5.30), the parameter C_A is determined from work of Reitz *et al.* [141]:

$$C_A = 3 + \frac{L}{3.6d} \tag{5.31}$$

For the simulation, C_A was analytically calculated based on Equation (5.31) and specified as 3.556. Note that for a realistic spray simulation, the droplets are randomly distributed spatially based on the dispersion angle at initial injection such that they are evenly spread for smoother momentum calculation.

5.7.2.4 Droplet Diameter Distribution

The spray characteristics that create particles of a size distribution have been experimentally known to follow the Rosin-Rammler distribution [32]. The generalised mathematical model for the relation of mass fraction to Rosin-Rammler distribution can be given as:

$$m(D; D_{RR}, n)\begin{cases} \frac{n}{D_{RR}}\left(\frac{D}{D_{RR}}\right)^{n-1} e^{-\left(\frac{D}{D_{RR}}\right)^n} & D \geq 0 \\ 0 & D < 0 \end{cases} \tag{5.32}$$

Where, n is the shape factor which is ~3.5 for single-phase internal nozzle state. D_{RR} is Rosin-Rammler diameter determined from Wu *et al.* [142] and Lefebvre' correlations [32]. The Sauter mean diameter, d_{32} is determined based on Weber number and radial integral length:

$$d_{32} = 133.0\lambda We^{-0.74} \tag{5.33}$$

Where, $\lambda = d/8$, λ is the radial length scale at jet exit by taking d as the nozzle diameter. And for Weber number, We:

$$We = \frac{\rho_l u^2 \lambda}{\sigma} \tag{5.34}$$

Where, ρ_l is liquid density, u is fluid exit velocity, λ is radial length scale defined earlier. σ is surface tension of the liquid. The Rosin-Rammler distribution most probably diameter, d_o based on Lefebvre [32] is:

$$d_o = 1.2726\, d_{32} \left(1 - \frac{1}{s}\right)^{1/s} \tag{5.35}$$

And s is the spread parameter or shape factor. At this stage, all the parameters required for initialisation of the Rosin-Rammler distribution model has been prescribed. Fluent [136] enables user to prescribe the number of parcel stream that representative of the distribution. This is known as standard parcel release method and can be given as:

$$NP = \dot{m}_s \frac{\Delta t}{m_p} \tag{5.36}$$

Where, NP is the number of particles per parcel per injection stream, $\dot{m}$ is the mass flow rate of the parcel stream, Δt is the time-step size and m_p is the mass of particle obtained from the product of volume of sphere with density of the injection at that particular diameter. For 500 injection streams, the NP of a particle diameter of 91.5 μm is 0.62. And for 50 injection streams, NP of the same particle diameter 91.5 μm is increased to 6.22. The more parcel streams are injected, the closer are the particles to the distribution. Note that overly low NP could be costly although improves accuracy and convergence stability.

The following Table 5.1 is created to describe the shape function (spread) and Rosin-Rammler diameter at one injection time-step 5×10^{-5} s. The particle histogram for parcel number 50, 500, 1000 and 2000 are shown in Figure 5.6 to inform on how close is the size distribution to the function. And the cumulative mass fractions of the Rosin-Rammler distribution are also given in Figure 5.7.

Table 5.1: Rosin-Rammler parameters for size distributions per injection time-step ($\Delta t = 5 \times 10^{-5}$ s)

Parcel Number	**50**	**500**	**1000**	**2000**
Spread, n	4.0557	3.6376	3.5748	3.5323
Rosin-Rammler, D_{RR} (μm)	125.75	143.97	142.29	144.34
Parcel Mass (kg)	1.945×10^{-9}	1.945×10^{-10}	9.725×10^{-11}	4.8625×10^{-11}
Total Mass (kg)	9.725×10^{-8}			

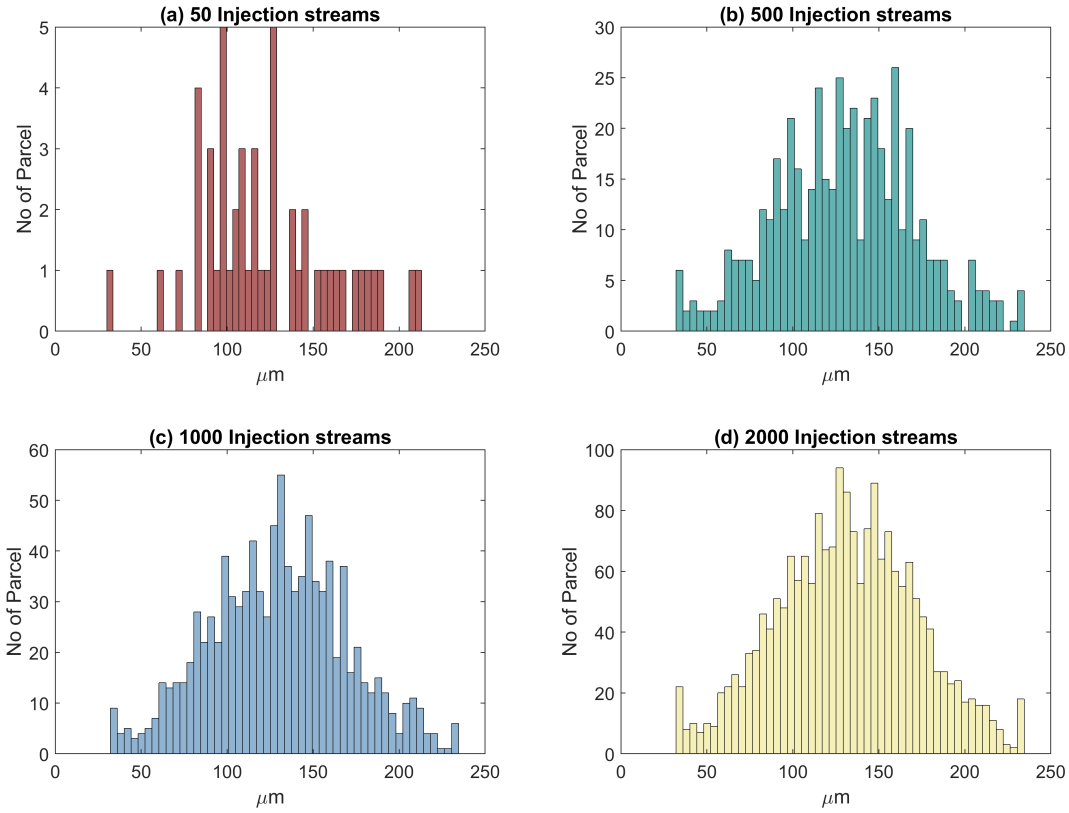


Figure 5.6: Particle size distribution based on different injection streams

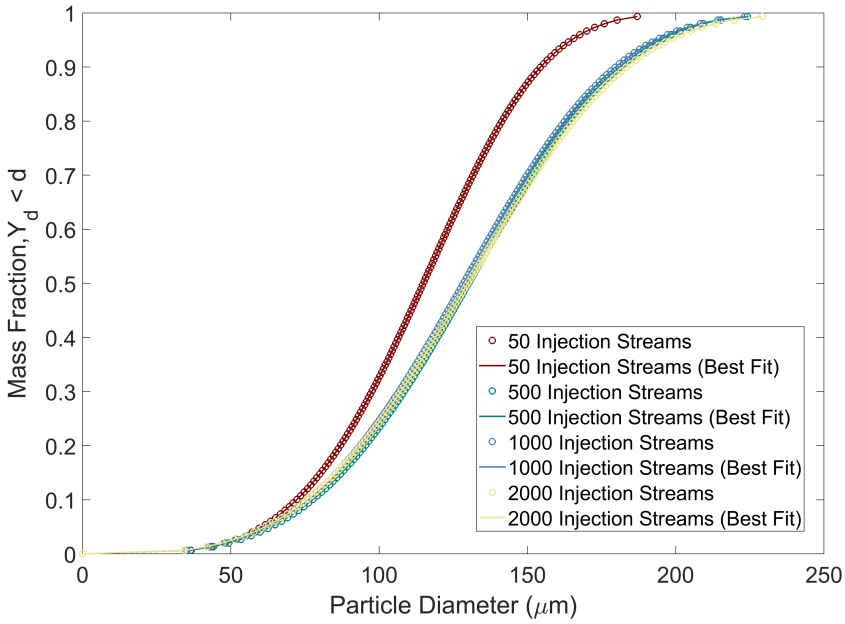


Figure 5.7: Cumulative mass fraction for Rosin-Rammler distributions

5.7.3 Secondary Atomisation of Droplets

Droplets when subjected to high aerodynamics force, could undergo instabilities leading to breakup. Several breakup models were proposed for such phenomena, namely, Taylor Analogy Breakup (TAB), Wave model, KHRT model and Stochastic Secondary Droplet (SSD) model. To match the model used by Arienti *et al.* [13], the Taylor Analogy Breakup model is selected. TAB model is based on the notion that the dynamics properties of a droplet can be modelled as spring and mass system. A well-known equation for spring-mass system is given as:

$$F - kx - d\frac{dx}{dt} = m\frac{d^2x}{dt^2} \tag{5.37}$$

In TAB, O'Rouke and Amsden described the droplet distortion analogy based on the following expressions [143]:

$$\frac{F}{m} = C_F\frac{\rho_g u^2}{\rho_l r} \tag{5.38}$$

$$\frac{k}{m} = C_k\frac{\sigma}{\rho_l r^3} \tag{5.39}$$

$$\frac{d}{m} = C_d\frac{\mu_l}{\rho_l r^2} \tag{5.40}$$

They relate the external force (F) in terms of relative velocity of the droplet, the commonly known spring constant (k) in terms of restoring spring surface tension and finally the viscous damping of a spring system (d) is expressed in terms of droplet viscosity. Note that in each expression, there are additional coefficients such as C_F, C_k and C_d. They are given as 1/3, 8 and 5 respectively. By substituting $x = yC_b r$, expressing C_d as 0.5 and integrate them. The final form equation is obtained:

$$\begin{aligned} y(t) = We_c + e^{-(t/t_d)}\Big[&(y_0 - We_c)\cos(\omega t) \\ &+ \frac{1}{\omega}\left(\frac{dy_0}{dt} + \frac{y_0 - We_c}{t_d}\right)\sin(\omega t)\Big] \end{aligned} \tag{5.41}$$

For full description of the constituents' equation in Equation (5.41), refer to paper of O'Rouke and Amsden [143]. The final form Equation (5.41) is solved at each DPM time-step, and when $y > 1$ or when x is greater than half the radius; breakup occurs. Subsequently, the physics for child droplets produced during the breakup must be described.

Fluent uses energy equation to equate that of parental droplet to child droplets. In the simulation, one parental parcel is expressed as a split of ten child parcels. This number is kept constant for all simulations for consistency. The velocity of the child droplets is described as following:

$$v_{normal} = C_b r \frac{dy}{dt} \tag{5.42}$$

The above explanations of TAB can be better visualised using the diagram of spring-mass system as shown in Figure 5.8.

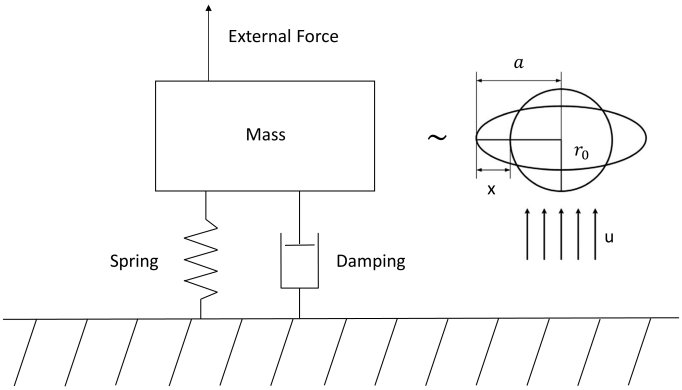


Figure 5.8: Taylor Analogy Breakup based on spring-mass system [136]

5.7.4 Turbulent Dispersion of Particles

The standard particle trajectories use fluid-phase mean velocity, $\widetilde{U}(t)$ to determine the motion of the particle in integration of force balance Equation (5.16). The effect of turbulent flow on particle motion can be included. The velocity fluctuation is added to the instantaneous velocity based on $\widetilde{U}(t) + u'(t)$. The approach is known as stochastic tracking. To include the random effect of turbulence on the particle, stochastic tracking uses discrete random walk (DRW) to compute the fluctuating velocity components based on the lifetime of a turbulent eddy. The velocity fluctuation is computed by assuming that the lifetime of an eddy follows the Gaussian probability distribution, ζ. The fluctuating component is given as:

$$u' = \zeta \sqrt{\overline{u'^2}} \tag{5.43}$$

Where $\sqrt{\overline{u'^2}}$ is the root-mean square of the fluctuating velocity component computed from the turbulent kinetic energy (assuming isotropy for all two-equation turbulence models):

$$\sqrt{\overline{u'^2}} = \sqrt{\overline{v'^2}} = \sqrt{\overline{w'^2}} = \sqrt{2k/3} \tag{5.44}$$

5.8 Eulerian Thin Film Model

5.8.1 Continuity Equation for ETFM

To reduce the computational cost of tracking the liquid interface the Eulerian Thin Film Model (ETFM) is solved on the boundary of the bottom surface. The ETFM solves the continuity and moment equations for 2D thin film based on the following formulations. For mass conservation of the film:

$$\frac{\partial \rho_l h}{\partial t} + \nabla_s.\left(\rho_l h \overrightarrow{V_l}\right) = \dot{m}_s \tag{5.45}$$

Where, ρ_l is the liquid density, h is the film height at respective grid, ∇_s is the surface gradient operator (i.e. $\nabla_s \overrightarrow{V_l} = \frac{\partial U}{\partial x} + \frac{\partial V}{\partial y}$). And $\dot{m}_s$ is the mass source per unit grid area due to droplet impingement, removal or phase change.

5.8.2 Momentum Equation for ETFM

For momentum conservation of 2D thin film, the following Equation is given [136]:

$$\begin{aligned} &\frac{\partial \rho_l h \overrightarrow{V_l}}{\partial t} + \nabla_s\left(\rho_l h \overrightarrow{V_l}\overrightarrow{V_l} + \overline{\overline{D_V}}\right) \\ &= -h\nabla_s P_L + \rho_L h \overrightarrow{g_\tau} + \frac{3}{2}\overrightarrow{\tau_{fs}} - \frac{3\mu_l}{h}\overrightarrow{V_l} + \dot{q} \end{aligned} \tag{5.46}$$

Where,

$$P_L = P_{gas} + P_h + P_\sigma \tag{5.47}$$

$$P_h = -\rho h(\vec{n}.\vec{g}) \tag{5.48}$$

$$P_\sigma = -\sigma \nabla_s.(\nabla_s h) \tag{5.49}$$

The terms on the left hand side of the Equation (5.46) describe the transient and convective effect of the film. On the right hand side of the equation, the effect of gas-flow pressure on the film is described in the first term (P_{gas}) and the effect of gravity normal to the film surface is described by second term (P_h), this term is known as the spreading term. The effect of surface tension is given in third term (P_σ). The effect of gravity parallel to film that accelerates the film is given by second term on the right side of Equation (5.46). The third term represents the net viscous shear force at the gas-film interface, while the fourth term is the viscous force at the film-wall interface.

The final term is associated with droplet collection or film separation. Note that in arriving at the shear and viscous terms on the right hand side, a parabolic film velocity profile is assumed.

5.8.3 DPM Collection

When a discrete phase particle impinges onto the film, the mass from the DPM is added into the film mass source term via the following equation:

$$\dot{m}_s = \dot{m}_p \tag{5.50}$$

Where, $\dot{m}_p$ is the particle stream mass flow rate impinging on the surface. Meanwhile for momentum transfer, the following source term is used:

$$\dot{\vec{q}}_s = \dot{m}_p(\overrightarrow{V_p} - \overrightarrow{V_l}) \tag{5.51}$$

Here, $\overrightarrow{V_p}$ is particle stream velocity and $\overrightarrow{V_l}$ is film velocity.

5.8.4 Splashing

During interaction with the wall film, particles could splash and produce smaller particles. The formulation of splashing criteria in ETFM is similar to that of Lagrangian Wall Film. The threshold for splashing event is based on impingement energy developed by Stanton and O'Rouke [59]:

$$E^2 = \frac{\rho V_r^2 d_p}{\sigma}\left(\frac{1}{\min\left(\frac{h_0}{d_p}, 1\right) + \delta_{bl}/d_p}\right) \tag{5.52}$$

Where, V_r is relative velocity of the particle in the reference to the impinged wall (i.e. $V_r^2 = \left(V_p - V_w\right)^2$) and has lower value if the wall is moving in same direction as the impinging particle. The rest of the notations can be referred at Nomenclature and the equation for δ_{bl} can be referred in the Fluent Theory Guide [136]. The critical impinging energy, E_{cr} is defined as 57.7. With the defined criteria, the diameter distribution sampling is obtained from correlation of Mundo *et al.* [49]. Although splashing was not included in present work, it was proposed for future study.

5.8.5 Edge Separation

At the edge of the expansion, film could separate when the inertia force overcomes gravity and surface tension. Fluent activates this sub-model when two criteria are met: (1) the critical angle and (2) the Weber number. Three models are available for the calculation of mass flux of droplets leaving the surface and also for the diameter, namely, Foucart, O'Rouke [144] and Friedrich [145]. For determination of the film Weber number, the following equation is used:

$$We_f = \frac{\rho_f u_f^2 h_f}{\sigma} \tag{5.53}$$

Where, ρ_f is the density of film, u_f is film velocity, h_f is film height and σ is surface tension. Friedrich's separation model is used in this simulation to determine shed particle size and flux as their expression includes angle, gravity and surface tension in the force balance calculation. In comparison, O'Rouke and Amsden's separation criteria lack the treatment of inertial and surface tension terms. Furthermore, it was only numerically tested for film less than 100 μm. The separation model was not validated with any experimental result unlike Friedrich's criteria. Friedrich's model is based on the notion of force balance between film inertia to overcome surface tension and gravity at the corner of an expansion. The non-dimensional equation for critical force ratio is given as:

$$Force\ Ratio = \left\{ \frac{We_f}{1 + \frac{1}{\sin\theta} + Fr_{hf} We_f \left(\frac{L_b}{h_f}\right)\left(\frac{1}{\tan\theta}\right)} \right\} \tag{5.54}$$

Where, We_f is film Weber number defined from Equation (5.53), $r_{hf} = g h_f / u_f^2$ and L_b is the characteristics length of the film after the corner taken from experimental correlations of Arai and Hashimoto [146]:

$$L_b = 0.0388 + h_f^{0.5} Re_f^{0.6} We_{rel}^{-0.5} \tag{5.55}$$

For full descriptions of We_{rel} and Re_f, refer to [145]. Since our gas velocity, U_g of 82 m/s has well exceeded the gas velocity of Friedrich *et al.* [145]. The film Weber number is determined by extrapolating the graph of We_f versus Re_f at U_g of 82 m/s in the data provided by them using power curve fitting in MATLAB. Based on rough wall model (not Fluent), it is possible to predict that a film Reynolds number of 123 is needed to maintain approximately 100 μm of film at the point of separation for 82 m/s [145]. Therefore, a critical Weber number of 2.9 is obtained. The

extrapolation is shown in Figure 5.9. The critical angle and film Weber number are set as 90° and 2.5 respectively.

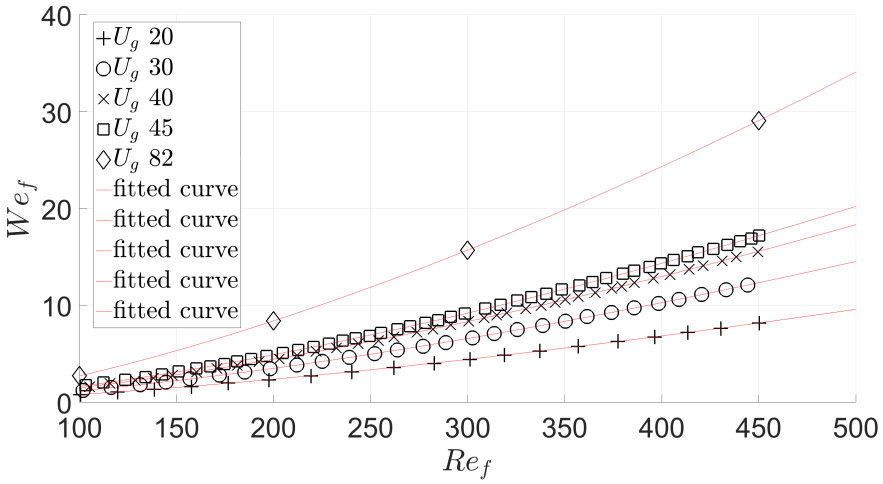


Figure 5.9: We_f vs Re_f at gas velocity of 82 m/s using power curve fitting [145]

With the determined Force Ratio, the mass flux of fluid separation was taken from the experimental data of Friedrich *et al.* [145]. Fluent defined the mass flux by curve fitting onto Friedrich model as:

$$\gamma = 1 - \exp\left(0.411544\left(\frac{1 - Force\ Ratio^2}{Force\ Ratio}\right)\right) \tag{5.56}$$

And for separated droplet diameter, it is taken as a function of height. The separation models were found to be unstable during implementation in Fluent and will be discussed in further details in Section 5.13.

5.8.6 Shear Stripping

At high relative velocity, Kelvin-Helmholtz (K-H) instability occur on the interface of liquid and gas. It was also observed experimentally by Shedd *et al.* [128] from original study of jet-breakup in cross flow and the formation of thin film that droplets were atomised from the surface of the waves via this type of instability. The mechanisms is based on the imposed perturbations (e.g. shear stress) exceeding that of damping mechanisms such as gravity, viscosity and surface tension [147]. The growth of perturbations with time give rise to the shedding of droplets.

The implementations of K-H instability in Fluent for atomisation of liquid from the crest of the wave are based on work of Lopez *et al.* [148] and Mayer [149]. In order for the perturbation to grow, a minimum wavelength has to be reached. Mayer proposed the minimum wavelength, λ_{min} in Equation (5.57) as:

$$\lambda_{min} = \left(\frac{\nu}{f}\right)^{\frac{2}{3}} = 2\pi\sqrt[3]{16}\left(\frac{\mu_l\sqrt{\frac{\sigma}{\rho_l}}}{\beta\rho_g V_g^2}\right)^{2/3} \tag{5.57}$$

Note that the sheltering parameter, β in Equation (5.57) is defined as 0.3 by Jeffreys [149]. And ν is not standard kinematic viscosity but having the form of Equation [149].

$$\nu = \frac{8\pi^2\mu_l}{\rho_l} \tag{5.58}$$

The description for the frequency of wave formation (capillary wave) is based on Taylor's analytical solution and given in Lopez *et al*'s [148] paper as:

$$R(\alpha) = 0.384\, k_o u_g \sqrt{\frac{\rho_g}{\rho_f}} = 0.384\left(\frac{\rho_g u_g^2}{\sigma}\right)\sqrt{\frac{\rho_g}{\rho_f}} \tag{5.59}$$

Where, k_o is defined as the wave number of 'dangerous' wave and for the above Equation (5.59) the coefficient 0.384 is only valid for water and other low viscosity liquids. For other conditions, readers could refer to paper of Lopez *et al.* [148]. The parameters for growth of waves are described. Mayer gave the expression of average droplet size, D from the atomisation as:

$$D = F\bar{\lambda} \tag{5.60}$$

The average effective wavelength, $\bar{\lambda}$ is given as 4.5 λ_{min} by Mayer. And F is dimensionless configurable factor (default and by Jeffreys as 0.14) which is known as diameter coefficient in Fluent. The final parameter is the mass flux of droplets stripping and Fluent gave the expression as:

$$\dot{m} = C\frac{9}{2}\rho_l R(\alpha)\lambda_{min} \tag{5.61}$$

The mass coefficient, C is by default 0.5 and is user definable. And the rest of the notations can be referred in Nomenclature. For the mass to be removed, the critical number has to be defined. Fluent defined the criteria for stripping in terms of critical shear rate, τ_{crit} (Pa). However, this

could leads to severe convergence instabilities as there are not related to the state of the fluid (i.e. film velocity and thickness). The critical stripping criterion in terms of critical Weber number must be activated from the Text User Interface (TUI) and the code is given in Section 5.12.7.

The empirical basis of the critical stripping Weber number is not straight forward, Fluent suggests 0.06 as a good parameter in tutorial guide without justification. A good review of the criteria for onset of shear stripping can be referred to the works of Lopez *et al.,* Dallman *et al.*, Kataoka and Ishii, Owen and Azzopardi [148, 150]. The above co-authors studied the entrainment of liquid in small vertical annular flow. Notably, Dallman *et al.* derived the coefficient of entrainment as:

$$\varepsilon = k_A \left(\frac{W_{LF} - W_{LFC}}{P}\right) u_g^2 \rho_g^{1/2} \rho_f^{1/2} \tag{5.62}$$

The entrainment rate, ε lacks the surface tension term which dampens the K-H instabilities. Kataoka and Ishii proposed an improvement to that by including surface tension term in We_g and verified it experimentally. This is given in Equation (5.63):

$$\frac{\varepsilon D}{\mu_f} = k \left[We_g \left(\frac{\Delta\rho}{\rho_g}\right)^{\frac{1}{2}} \left(Re_{lf} - Re_{lfc}\right)\right]^{0.925} \left(\frac{\mu_g}{\mu_f}\right)^{0.26} \tag{5.63}$$

The Equation (5.63) also included additional terms such as liquid flow rate (Re_{lf}) and the critical Reynolds number for entrainment to occur know as Re_{lfc}. Owen reported that the critical Reynolds numbers are unreliable with some reported as high as 170 and 400. Owen and Azzopardi defined the Re_{lfc} as 82 and 78 respectively in their annular flow studies [150]. However these numbers were very difficult to be expressed in terms of critical Weber number defined by ANSYS Fluent. First, Fluent defined the shear Weber number using the Equation (5.64):

$$We_s = \frac{V_S^2 H_f \rho_f}{\sigma} \tag{5.64}$$

Where, velocity of shear V_S is defined based on $(\tau_w H_f)/(2\mu_f)$. Note that Weber number of film, We_f is different with We_s in Fluent. For We_f, mean velocity of the film is used in the computation.

Very few authors studied the shear stripping based on dimensional analysis of critical Weber number, these could be credited to work of Kim and Peterson [151] and also work of Andreussi [152]. Kim and Peterson [151] studied the critical Weber number for onset of liquid entrainment in capillary driven heat pipes. They categorised previous entrainment models as shear-induced

model and wave-induced model. In general cases, shear-induced models were found to have critical weber number less than that of wave-induced model. The critical Weber numbers were proposed to be within 0.1 to 20.

Subsequently, the onset of droplet entrainment studied by Andreussi [152] pointed that the critical gas velocity for the entrainment was lower than expected and similar to observation of Azzopardi, at a certain liquid Reynolds number no entrainment occurs even the gas velocity is high. The critical Weber number was experimentally determined in an annular downward flow studies to be different with that of Kim and Peterson as it does not involve heat transfer across the wall and no vapour in gas-phase. The We_{crit} was found to be 5.5×10^{-3}. From literature surveys, it was found that combination of Kim and Peterson [151] expression, shear velocity obtained from Fluent exported wall shear stress value and critical wavelength from Shedd *et al.* [128]can be used to estimate the Critical Weber number.

Kim and Peterson defined the critical Weber number, We_{vc}:

$$We_{vc} = \frac{\rho_v U_{vc}^2 \lambda_c}{\sigma} \tag{5.65}$$

Where, subscript (v) denotes vapor, U_{vc} is critical vapor velocity, λ_c is critical wavelength and σ is surface tension. By modifying the Equation (5.65) in terms of liquid film. The following Equation is obtained:

$$We_{crit} = \frac{\rho_l V_s^2 \lambda_c}{\sigma} \tag{5.66}$$

Where, the density and surface tension are expressed in terms of film material and V_s is taken as shear velocity defined earlier. Shedd *et al.* hypothesised the disappearance of ripple has gave off the fine droplets. Using the expressing Kelvin-Helmholtz instability theory from Ghiaasiaan [153] in Equation (5.67), Shedd *et al.* obtained the critical wavelength (λ_c) as $21\ \mu m$. And note that the fluid properties used are mineral spirits and standard gas density. For relative velocity (U_r) Shedd *et al.* used $80\ m/s$ [128].

$$\lambda_c = \frac{2\pi\sigma(\rho_l + \rho_g)}{\rho_l \rho_g U_r^2} \tag{5.67}$$

By substituting the value of λ_c of $21\ \mu m$ and the value of V_s (which was calculated using exported wall shear stress of a non-stripping case (i.e. case 7 in Section 5.10) along with the film height,

H_f)) into Equation (5.66), the We_{crit} is obtained and plotted in Figure 5.10. The We_s is also plotted in Figure 5.10 to give an idea that they both carry different definitions.

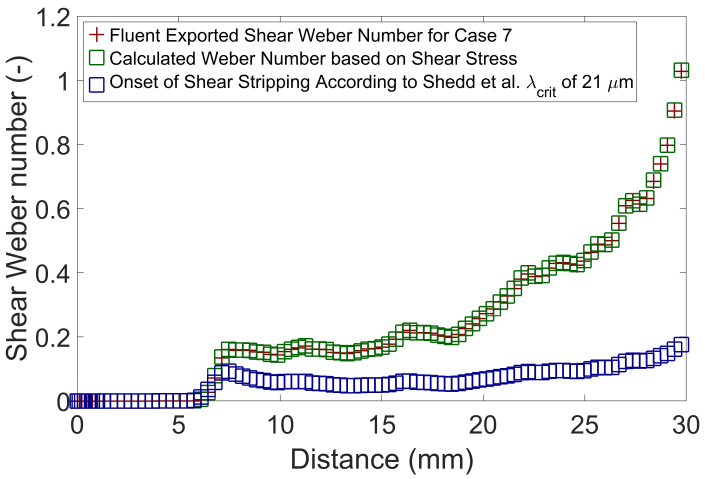


Figure 5.10: critical Weber number for onset of shear stripping

From the above Figure 5.10, it is clear that the average critical shear Weber number obtained using critical wavelength of 21 μm is 0.1063. Hence, a critical Weber number of 0.1 is used. This dictates that the film will be stripped until the Weber number that based on shear stresses approaches 0.1.

5.9 Mesh and Grid Generation

The domain in which the flow is simulated follows that of Arienti *et al.* [13] and Shedd *et al.* [128] except with minor modifications which will be explained later. To save computational cost, a straight duct is first generated and ran with several test cases as it was estimated that the shear force is so great that the effect of expansion has minor influence on film solution. Subsequently the highest 'fidelity' model was ran with expansion to assess the effect of film separation. The uniformity and linear structure of the expansion meant that structure hexahedral cell is best suited for the application. ICEM meshing software is used to generate grid based on global coordinate system and inertial frame of reference.

For the expansion, the length (l), height (h) and width (w) are set as 75 mm, 25 mm and 30 mm respectively. The first section has a length of 50 mm from inlet to the edge of expansion and the second section has a length of 25 mm from the edge of expansion to the outlet. The most important section of the geometry is the 10 mm gap between the top plate and bottom surface where film is formed as a correct velocity profile needs to be representative of the experimental model. For the

width, an initial test run was conducted and was found out that the width of the duct of 30 mm was sufficient to cover the film without affecting its solution. Illustration of the grid (expansion) can be shown in Figure 5.11.

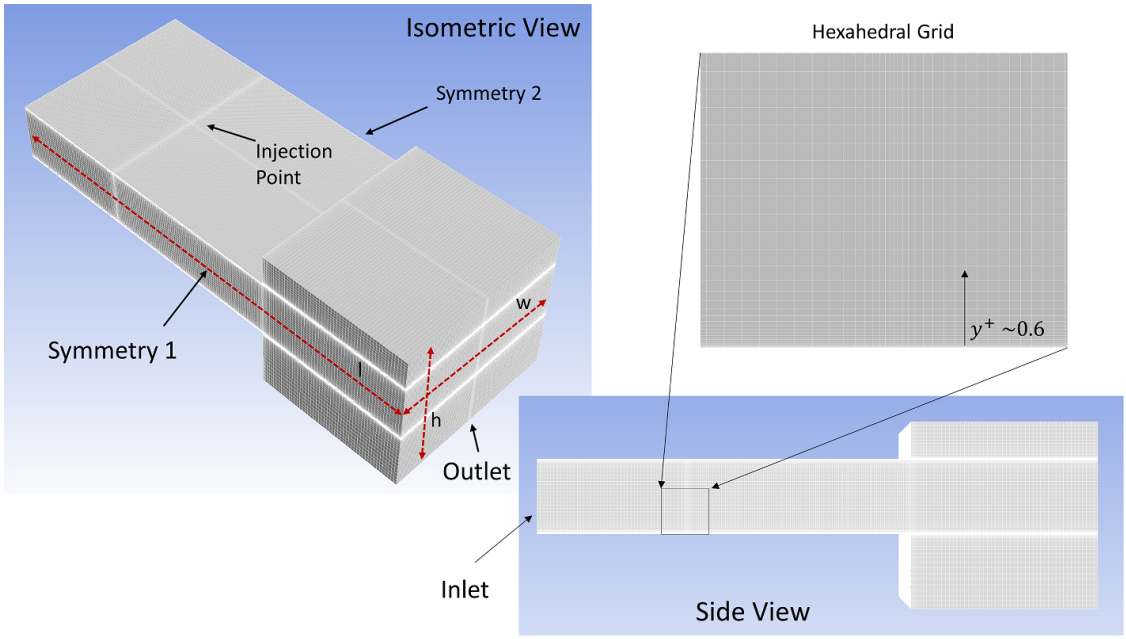


Figure 5.11: Hexahedral grid generation based on structured mesh

A wall y^+ of 0.6 was created as shown in Figure 5.11 to ensure that the low-Re turbulence model is valid down to the viscous sublayer without resolving to wall function. It was created by using grow ratio of 1.1 and at least 10 – 20 cells are within the boundary layer. At the injection point, the cell is also grown smoothly along the streamwise and spanwise direction to ensure that the solution gradient does not experience a large jump during the coupling between DPM and continuous-phase. A table is used to summarise the geometry and its corresponding grid density.

Table 5.2: Hexahedral grid density and corresponding geometry

Classification	**Geometry Type**	**Grid Density (Cells)***
M1	Straight	0.380M
M2		0.920M
M3		2.200M
M4	Expansion	3.100M

Based on Table 5.2, 4 grid were generated M1, M2, M3 and M4. From M1 to M3, the mesh is designated as straight duct and could easily be visualised as being a straight rectangular duct with no edges like one shown in Figure 5.11. There are few implications of using a straight duct. First, the film could continue to build up after the location where edge supposed to exist and this film could provide some form of 'resistance'. Secondly, the pressure field at the edge of expansion might be different to that of straight duct and could affect the solution. Mesh M4 is effectively similar to that of M3 but with the expansion section.

5.10 Numerical Settings

The spatial discretisation for pressure, momentum and turbulence are solved using the second-order upwind scheme. By industry practice, the second-order provide higher accuracy compared to first-order. Since the solution is computed using incompressible solver, the Pressure-Velocity Coupled scheme is used to obtain the pressure field. It reduces the convergence time but uses more memory and takes longer iteration per unit time-step. A number of test cases were conducted to investigate the effects of changing the number of particle injection streams, continuous phase time-step, mesh density, effect of turbulent dispersion (DRW) model and film sub-models. These are summarised in Table 5.3 and the areas of applicability are:

a) Cases 1, 2 and 3 are compared to assess the optimum number of particles needed to statistically representing the jet-breakup. An over-large number of injections will induce high computational cost with no benefit in accuracy. Conversely, too few improves simulation speed at the expense of accuracy.
b) The second series of parametric tests uses cases 1, 4 and 5 to inform the optimum airflow timestep needed to obtain accurate particle trajectories with reasonable cost. An excessively large timestep increases convergence speed at the expense of accuracy whereas an excessively small timestep introduces unnecessary cost with no gain in accuracy.
c) Parametric testing was conducted using cases 7, 8 and 9 to find the optimum mesh density for both accuracy and cost.
d) Cases 6 and 7 are used to assess the need for turbulent dispersion on particle trajectory nothing that this also influences the film solution.
e) Case 10 is used to examine the effect of gas pressure on film solution (e.g., gas static pressure and hydrostatic pressure of film).

f) The parametric test using cases 7 and 11 is used to examine the effect of the shear stripping model (Kelvin-Helmholtz instability) on film solution.

Table 5.3: Airflow time-step, injection number, particle time-step, cell count and sub-models

Case No	Continuous phase time-step, Δt (s)	No of injection streams	Particle time-step, Δt_p (s)	Cell count (k) & Sub-model
1	5×10^{-6}	500	5×10^{-5}	380
2	5×10^{-6}	1000		380
3	5×10^{-6}	2000		380
4	1×10^{-5}	500		380
5	1×10^{-4}	500		380
6	1×10^{-5}	2000		2200
7	1×10^{-5}	2000		2200 DRW
8	1×10^{-5}	2000		920 DRW
9	1×10^{-5}	2000		380 DRW
10	1×10^{-5}	2000		3000 DRW P_{gas}, P_h
11	1×10^{-5}	2000		2200 DRW STP

For all cases, a standardised particle breakup number of 10, step length factor (λ in Fluent) of 10, gravity and the standard parcel releasing method are used. From case 7 onwards, the effect of turbulent dispersion is included. To save computational cost, case 1 to 9 and 11 are ran on a straight duct (non-expansion) without including the separation and splashing terms unless stated otherwise.

Case 10 is ran with surface tension and is switched off soon after instability kicks in and only qualitative result for surface tension case is provided in discussion part. The separation criteria along with gas-to-film momentum (two-way) coupling are also switched off due to instability.

Convergence stability was found to be poor for the steady-state air-flow simulation case due to large change in local momentum source term when particle breakup occurred. Despite increasing the relaxation factor, it was still not possible to maintain a converged solution for the physics involved. The reasoning for using 5×10^{-5} s for Δt_p is given in particle time-step sensitivity studies in Section 5.10.3.

5.10.1 Physics of Jet Breakup and Thin Film Formation in Crossflow

The DPM-ETFM computational work presented here is modelled on geometry investigated experimentally by Arienti *et al.* [13] and Shedd *et al.* [128]. The experimental configuration is represented schematically in Figure 5.12.

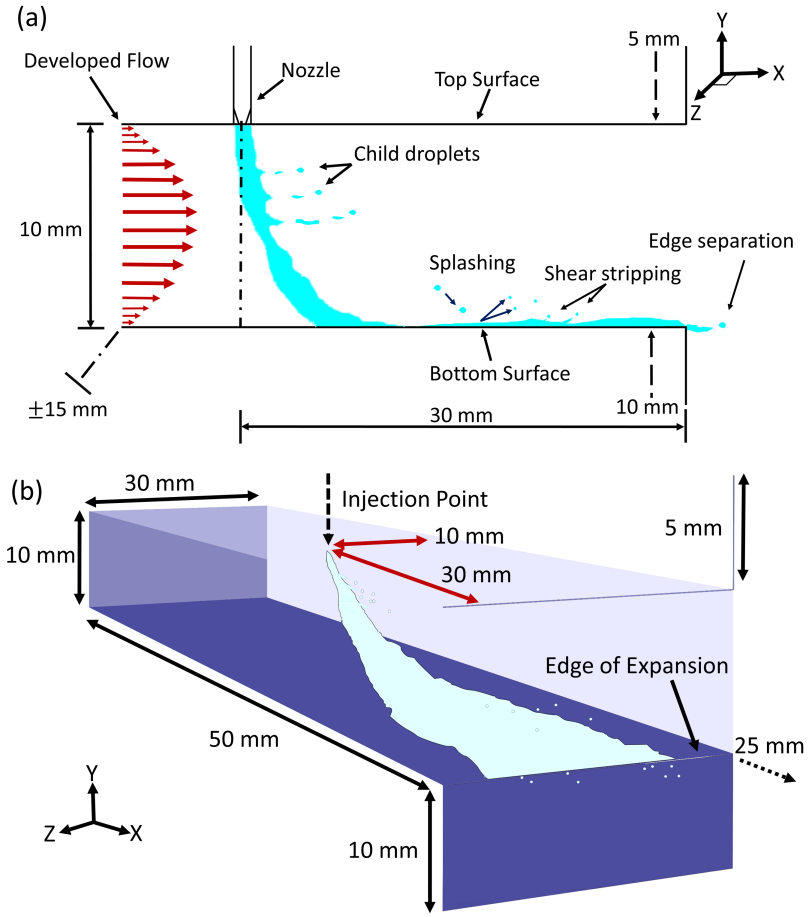


Figure 5.12: (a) 2D Schematic of the domain for jet-breakup in cross-flow and phenomena governing the flow (b) 3D Schematic of jet-breakup in cross-flow

In the experiments mineral spirits are injected into the expansion duct via a plain orifice nozzle normal to the crossflow. As liquid is injected, instability mechanisms cause the liquid to breakup and form droplets. The heavy droplets deflect and impinge onto the bottom surface forming a thin film. Meanwhile, lighter droplets exit the domain.

5.10.2 Flow Development

To confirm that the flow across the duct is indeed turbulent, the standard equation for Reynolds number from fluid mechanics text book is used [154]. The characteristic length used is 10 mm which is the channel height, air density of 1.2 kg/m^3 and dynamic viscosity of air at 1.837×10^{-5} Pa.s are used. The Reynolds number obtained for the duct is 53,565 indicating turbulent regime as it is greater than the Reynolds number of turbulent flow in a pipe of the value 4,000 [154]. Prior to running the jet-breakup simulation, a fully developed flow is prescribed at the inlet section by supplying the velocity components (V_x, V_y, V_z) and the relevant turbulence quantities (k, ϵ, ω). Each inlet flow was recycled 4 times using a separate rectangular duct of the same area (and most important the normal length) and first cell wall distance (y^+). The duct length is 100 times the inlet characteristic length and is developed by supplying a constant velocity of 82 m/s [13]. Wall y^+, wall shear stress (τ_w) and velocity-profile in the mid-plane are checked to confirm fully developed flow. Mesh independence studies were performed on selected y^+ to ensure the mesh density in all three directions was acceptable. A mesh with y^+ of less than 0.6 (cell height of 0.00255 mm) was made for use with the low-Re $k\omega - SST$ turbulence model as mentioned in Section 5.9. Figure 5.13 shows the developed quantities for inlet.

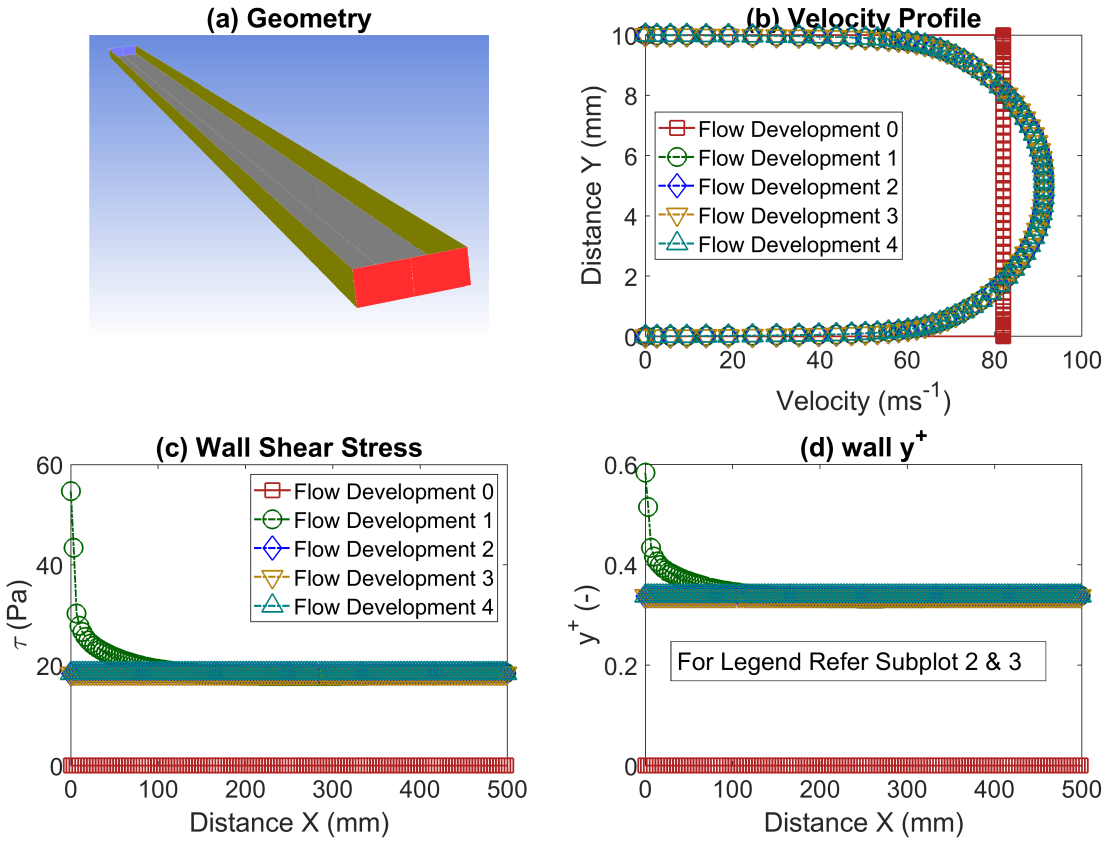


Figure 5.13: Flow development for turbulence quantities at the inlet

5.10.3 Sensitivity Study for Particle Time-Step Size

The spray physics in the jet-simulation involves transient formulation as mentioned. Particle time-step size is required in the computation of drag force that decides its trajectory. The purpose of this section is to define an appropriate time-step size required for the integration of particle force balance equation. A low particle time-step size resulted in poorly captured drag force, hence different impingement locations and physics. An overly prescribed particle time-step size (in other word: small Δt_p) slows the simulation speed as particle is advanced at a sufficiently small step incurring significant cost. Since it is not possible to know the resultant velocity component for droplet trajectories before the simulation. Particle time-step sensitivity studies were performed based on parameters shown in Table 5.4 and the resulting particle trajectories are displayed in Figure 5.14.

Table 5.4: Parameters of sensitivity studies for particle time-step size

Case No	**1**	**2**	**3**	**4**
Particle time-step, Δt_p (s)	5×10^{-3}	5×10^{-4}	5×10^{-5}	1×10^{-5}
Continuous phase time-step, Δt (s)	1×10^{-5}			
Ratio of time-step	$\Delta t_p = 500\,\Delta t$	$\Delta t_p = 50\,\Delta t$	$\Delta t_p = 5\,\Delta t$	$\Delta t_p = \Delta t$
Inject at	Fluid flow time-step		Particle time-step	Same
Accuracy	Under-predicted drag force		Good coupling	
Cost	-		Cheaper than 4	Expensive

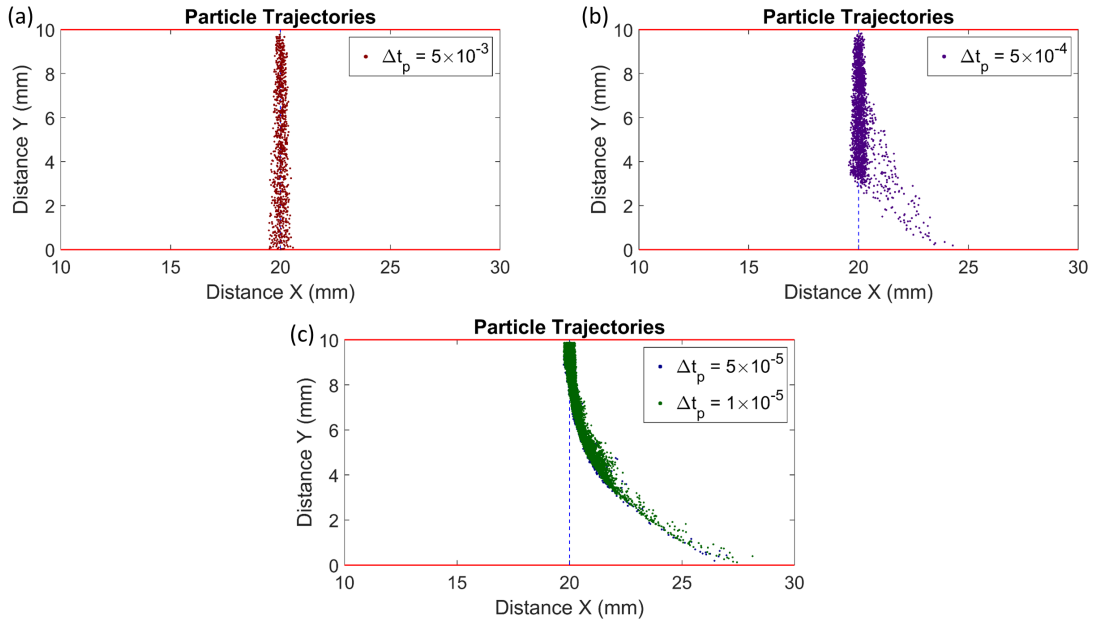


Figure 5.14: Computed trajectories at flow time $\boldsymbol{t = 9 \times 10^{-4}}$ s

Referring to Figure 5.14, 4 test cases were conducted with decreasing time-step size for the particle tracking (from 5×10^{-3} s to 1×10^{-5} s). All test cases were injected with 500 parcel injection streams for consistency and keeping the airflow time-step same. Test case 1 has the largest particle time-step followed by test case 2 and 3. For test case 4, particle time-step and airflow time-step are basically the same. Hence injecting them at either time-step makes no difference to the total particle count. Test case 3, however, is being injected at every 5 airflow time-step. It enables the cost and accuracy to be evaluated by comparison with test case 4.

Note that test case 1 and 2 were not being injected at particle time-step as doing so will resulted in discontinuous jet and by physics itself not representing the 'true' flow (see Figure 5.14(a),(b)). The purpose of running test case 1 and 2 is to enable the analysis of an appropriate 'physical' time-step size by comparing them with that of test case 3 and 4. The above trajectories only display particles with diameter greater than 121 μm by filtering them in MATLAB since smaller particles from breakup model impede the analysis.

First by looking at Δt_p of 5×10^{-3} s, it is clear that the particles lack the drag component and are not being affected by the crossflow. This is unphysical as the particles behaved 'stiffly'. By reducing Δt_p to 5×10^{-4} s, the particles still travelled too much in space and only began to be affected at the tip of the jet.

The most physical Δt_p were found to be 5×10^{-5} s and 1×10^{-5} s based on comparing these trajectories with Arienti *et al.*'s [13] particle trajectories. Both the trajectories showed particles' deflection and it is shown that test case 3 overlapped with test case 4. Despite higher injection frequency (not to be confused with flow-rate), no gain in accuracy is seen by smoother momentum and mass distributions in each grid. Hence, the cheaper test case 3 of $\Delta t_p = 5 \times 10^{-5}$ s was selected as the optimum step-size to be used across all future studies. And depending on the physics involved, the cost-saving and accuracy can be adjusted by injecting at particle time-step as shown above. Hence, it should not be taken as the axiom/standard for all type of simulations.

5.10.4 Mass Convergence

The convergence criteria were set as 1×10^{-6} for all residuals. The selected monitoring variable used to judge convergence was the sum of mass at the bottom surface. The results are analysed when the mass variable stop changing with respect to time. An example of mass convergence is shown in Figure 5.15.

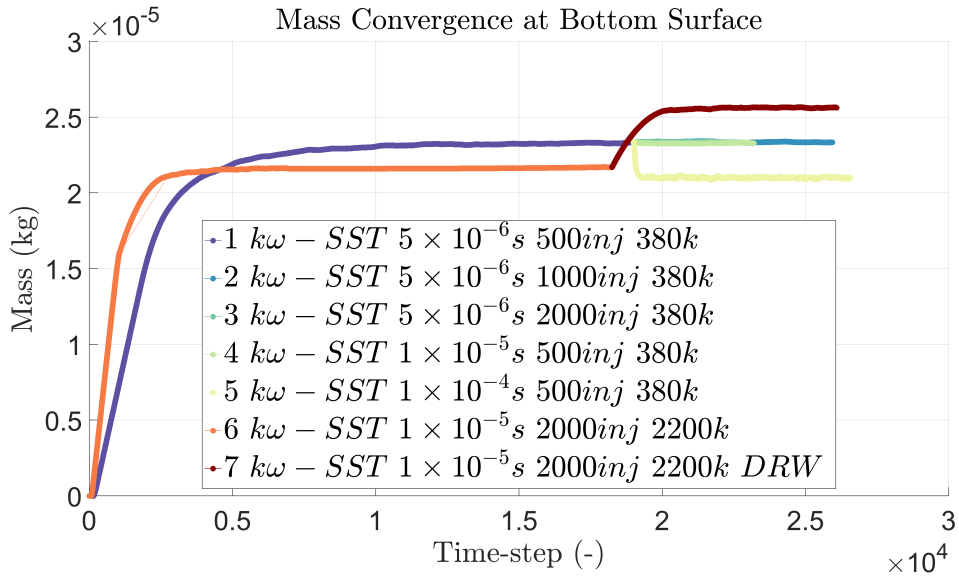


Figure 5.15: Mass convergence at bottom surface (legend shows turbulence model, timestep, number of injections, mesh size and activity of discrete random walk)

Mass convergence monitoring shows that simulations took an average of 5000 time-steps to reach a non-time-dependent solution. The mass collected in most cases was in the order of $2 \sim 2.5 \times 10^{-5}$ kg for straight duct cases. It should be noted that a different sum of mass would be obtained if a larger area is made after the separation point (i.e. longer distance towards the outlet). A step-by-step approach of running the simulation saves computational cost as well as ensuring numerical stability, this is shown by case 7 where turbulent dispersion is switched from end of case 6. Temporal averaging was carried out to get the mean solutions for the transient results (e.g. film thickness, velocity) using MATLAB™ and the instantaneous maximum and minimum of the sampling are obtained using standard deviation.

5.11 Field Variables

5.11.1 Particle Field

It is useful to first examine how particles behaves after being injected into the domain from the top surface via the orifice atomiser model. The Figure 5.16 shows the computed parcel and hence the particles trajectories as they are subjected to high shearing crossflow. The colormap shown on the scale depicts the size of the particles (in millimetres) within the domain. It can be seen that the particles are injected into the domain at the top surface; the location is 30 mm away from the expansion. As these particles enter the domain, the momentum from the shearing cross-flow causes instabilities in the droplets. As the instabilities exceed surface tension and viscous damping droplet breakup occurs. A range of smaller particles are produced in the process as defined by Taylor Analogy Break (TAB) [143]. This process occurs some distance away from the wall where the flow is relatively inviscid and high in velocity compared to close to the wall. The small particles gain momentum from the air and travel downstream towards the pressure-boundary or outlet. Meanwhile, the aerodynamic blockage of the large particles creates a region of low pressure behind the jet (shown in Figure 5.17b). These large particles deflect minimally due to larger mass and diameter and hit the surface to form film (detailed analysis of particles' impingement is given in Section 5.11.2).

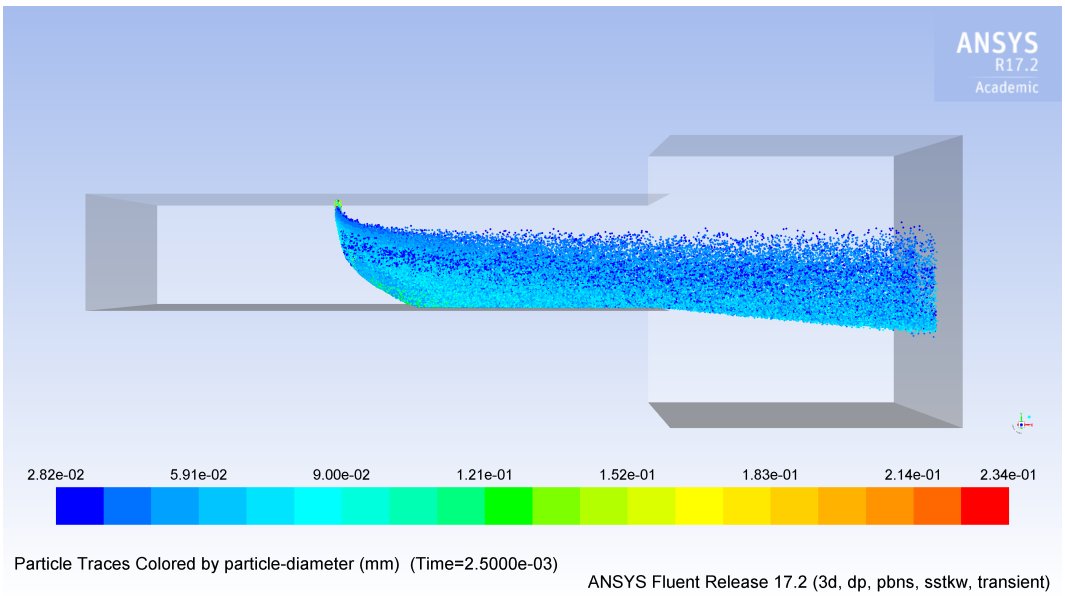


Figure 5.16: Particle trajectories in high shearing crossflow

5.11.2 Particle Diameter and Pressure Field

To better classify the flow features, the particle diameter and corresponding pressure field at a flow time of 2.5 ms are shown in Figure 5.17. The diameter colormap of Figure 5.17a ranges from 2.82 μm to 234 μm taken from a test case with primary and secondary atomisation activated (no splashing, edge separation and stripping on the ETFM). In the main image of Figure 5.17a, diameters smaller than 121 μm are hidden for clarity. A particle diameter analysis indicates that the maximum local particle impingement size is 121 μm, which means that the majority of particles greater than 121 μm underwent TAB. A clear indication of such phenomenon is shown by the first inset image on the right of Figure 5.17a where 'large' particles generated by the nozzle deflect and breakup before hitting the opposite surface (refer to label: 0.13 ~ 0.234 mm). The purpose of showing from 130 μm instead of 121 μm is to prove that much larger particles did not made it to the surface. Meanwhile, particles that are smaller than 121 μm that originate from orifice primary atomization or from Taylor Analogy Breakup deflect and are transported by the cross-flow. This can be seen in the second inset image of Figure 5.17a (refer to label: 0 ~ 0.121 mm).

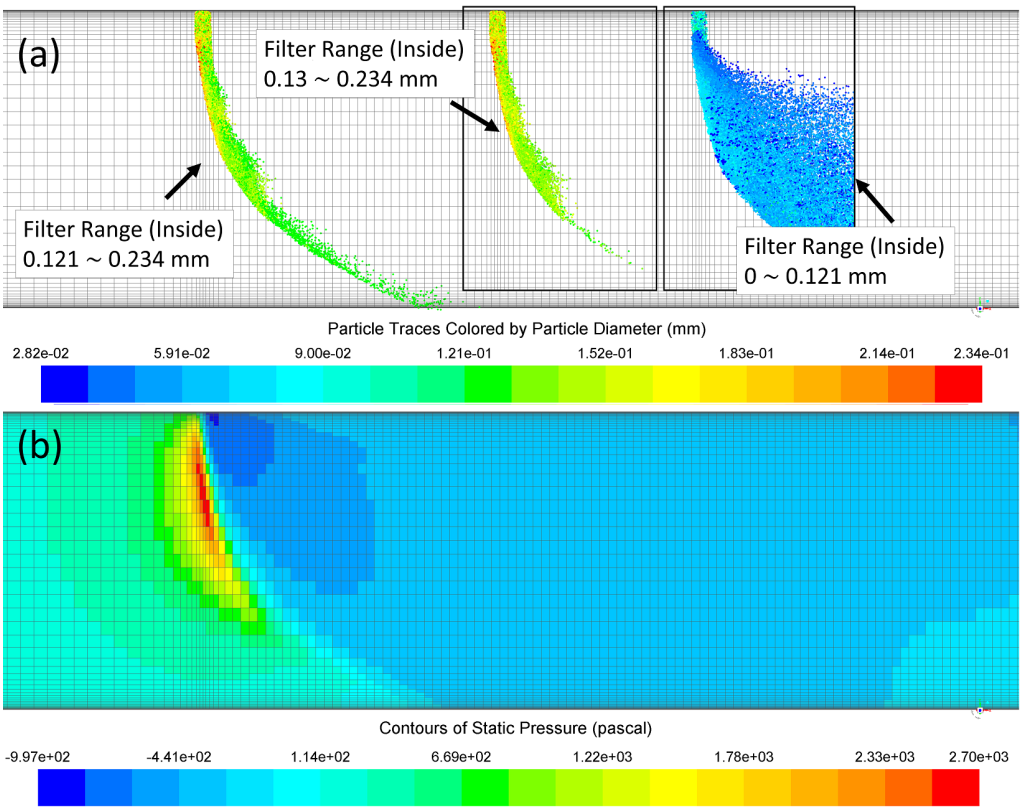


Figure 5.17: (a) Particle diameter and corresponding (b) Pressure field

5.11.3 Velocity Field

In terms of velocity field, the mid-plane velocity contours are given in Figure 5.18. The subplot 1 above the velocity contours of Figure 5.18 shows the velocity magnitude normalised using the velocity inlet (i.e. 82 ms^{-1}) and being scaled with a factor of 300 on each vertical location labelled along the X-direction. Each plot is progressed on a 5 mm increment. Where the inlet is $X = 0$ mm and outlet is $X = 75$ mm. The contour in the inlet region shows the velocity field of the fully developed flow. It corresponds to the normalised plot showing an undisturbed parabolic velocity profile for distance, $X = 0, 5, 10$ and 15 mm (see Figure 5.18, marker 'Without Jet'). Upon hitting the jet/particles at distance $X = 20$ mm, the interphase momentum exchange resulted in a lower velocity at the rear of the jet due to breakup and particle deflection. This can be seen clearly on Figure 5.18 marker 'With Jet' for 20 mm to 75 mm. The shear flow has a distorted and weakened velocity immediately after the particle path.

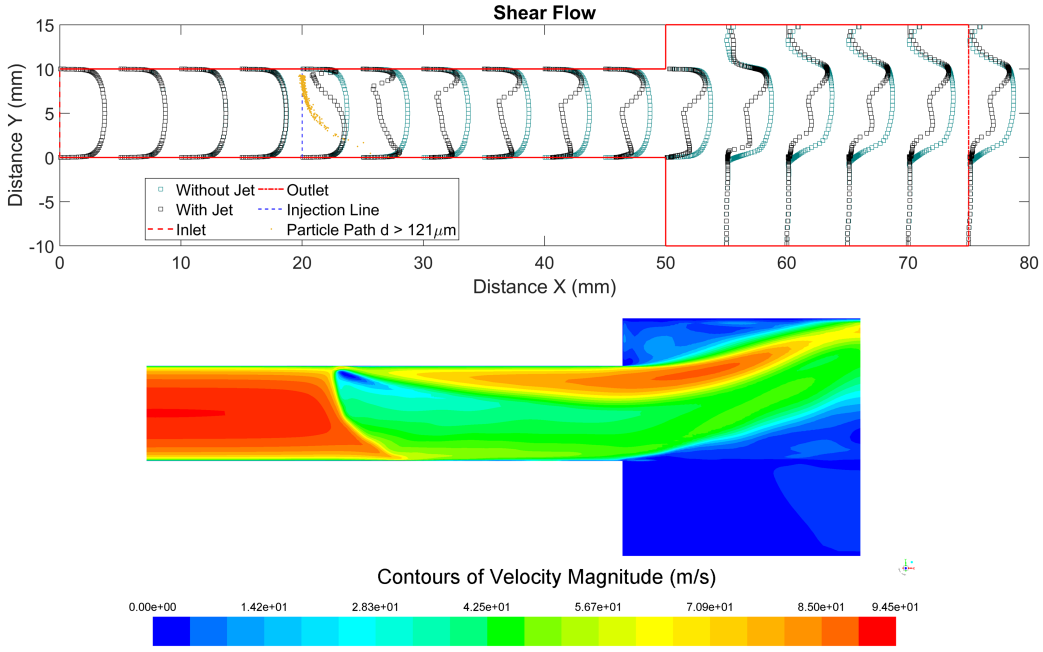


Figure 5.18: Normalised velocity and velocity contours taken at mid-plane of the expansion

5.12 Solution Variables

In this section, the computed film thickness is compared with published data by systematically assessing the following parameters:

(a) Number of particle injection streams
(b) Airflow time-step, Δt_{air}
(c) Mesh densities
(d) Turbulent dispersion
(e) Pressure gradient and spreading term
(f) Stripping criteria

The results are presented via the series of plots in Figure 5.20 and Figure 5.21. For all the subplots, film thickness values at the mid-line of the film surfaces are compared with published results from Arienti *et al.* [13]. The chosen case has jet velocity, $v_{jet} = 12.7\ ms^{-1}$ ($J = 15$ and $We_G = 193$). Published quantitative observation from Shedd *et al.* [128] is also used to inform discussion. The computational results of Ingle *et al.* [155] are also included for comparison. In the legend, the statement of "1 $k\omega - SST$ $5 \times 10^{-6}s$ $500inj$ $380k$" denotes test case no. 1, choice of turbulence model $k\omega - SST$, airflow time-step (Δt_{air}) of $5 \times 10^{-6}s$, 500 parcels injected for mesh density of 380k. All results are shown with mean and standard deviation values unless stated otherwise. For clarity, the plots are stacked in accordance to the assessments mentioned above. The location of the mid-line mentioned for film thickness measurement and wall shear stress measurements are given in Figure 5.19. Wall shear stress is measured from the 0 to 50 mm line when necessary and in all cases film thickness is presented from 20 to 50 mm line (Note that for film thickness results, 20 mm is offset to 0 mm for clarity).

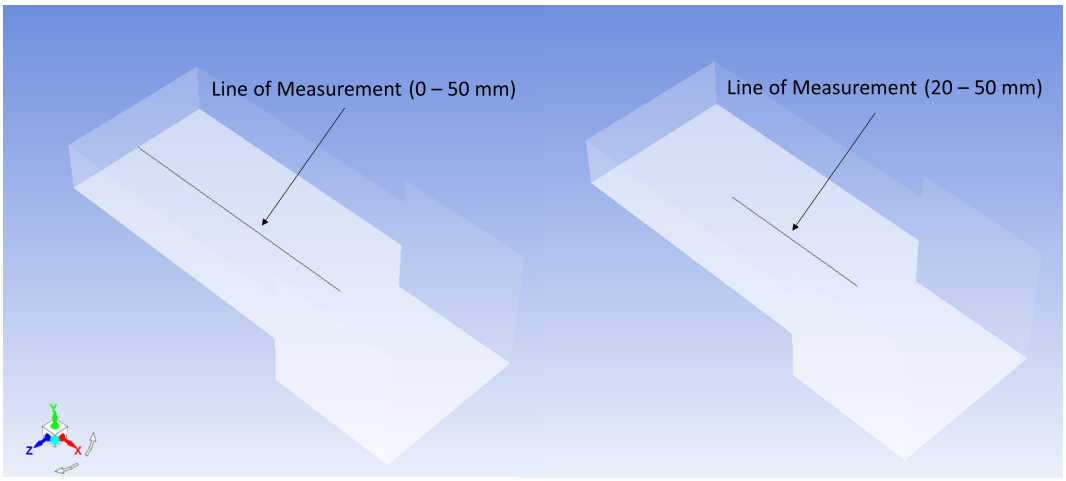


Figure 5.19: Line of measurement for relevant variables and film thickness

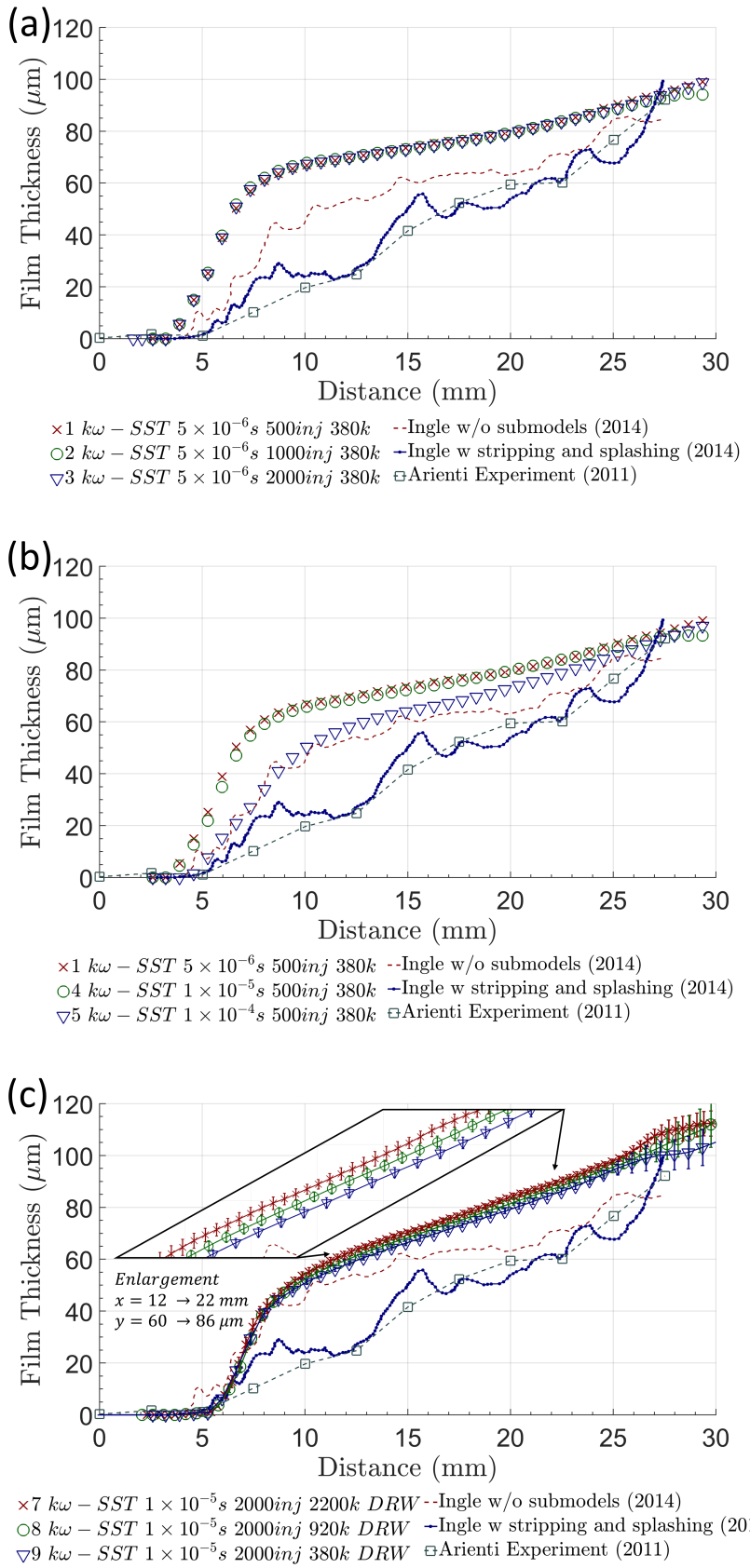


Figure 5.20: Film thickness measurement along mid-line based on effect of (a) Number of particle injection streams (b) Airflow time-step, Δt_{air} (c) Mesh densities

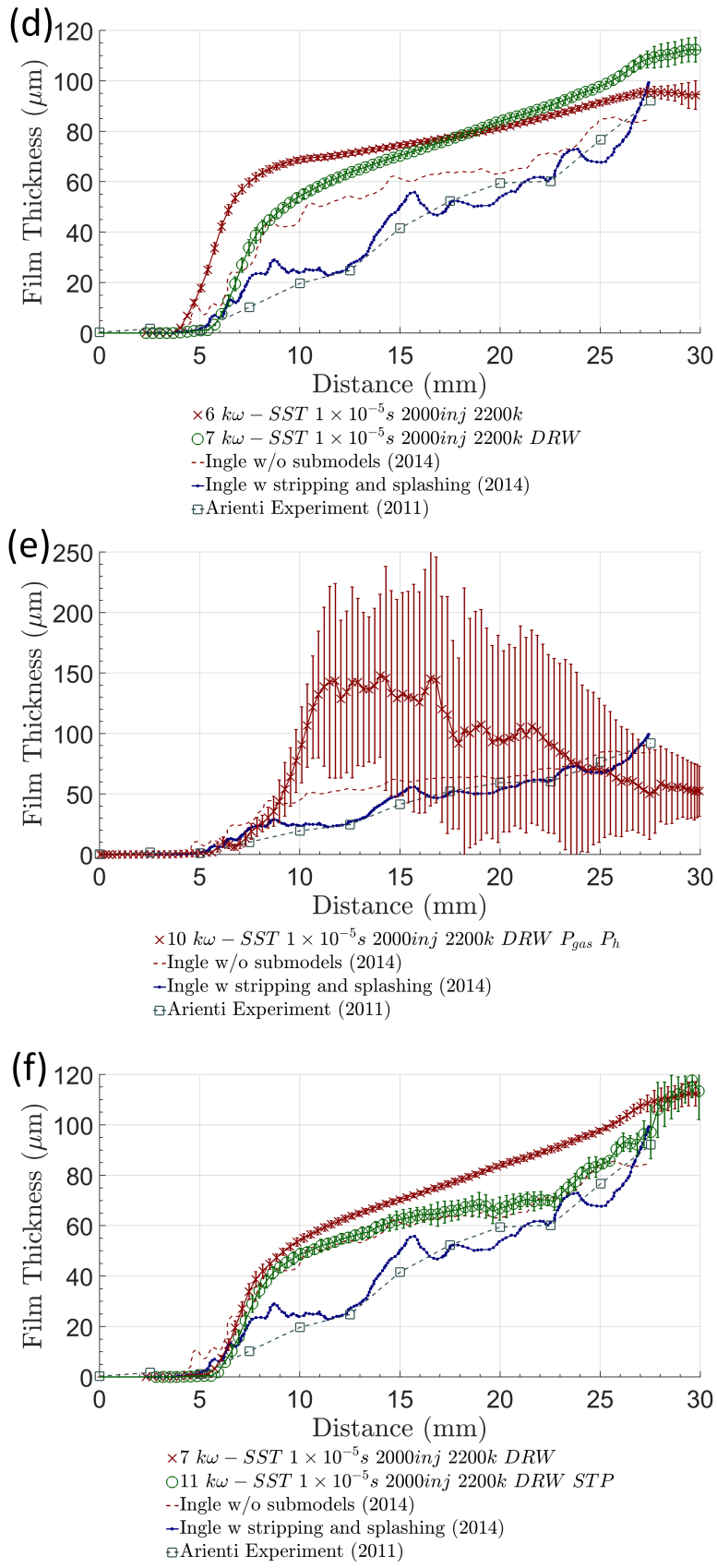


Figure 5.21: Film thickness measurement along mid-line based on effect of
(d) Turbulent dispersion (b) Pressure gradient with spreading term (d) Stripping criteria

5.12.1 Number of Injection Stream

Looking first at Figure 5.20a, it is apparent that increase in the number of parcel injection streams has an insignificant effect on computed film thickness. All three cases (500, 1000 and 2000 injections) overlap each other showing no variation. On this graph no standard deviation (SD) bars were included for purpose of clarify as all lines collapse in the same region. This figure suggests that a minimum of 500 injections are needed for capturing the breakup features for adequate interphase coupling. It was shown that the film grows at approximately 3.5 mm away from the injection point with very little waviness as compared to the computational model of Ingle *et al.* [155]. In these models, only momentum and gravity terms are activated. The film thickness increases as droplets are transported towards the rear. By referring to Figure 5.6, the histogram of particle size distribution shows that the statistical representation of the jet based on parcels number of 50 is insufficient (which is not ran in these test cases) where many particle sizes were not present to fit the curve (e.g., missing parcel of 50 μm). When the disintegration process and impingement process stabilises, the particle size distribution changes where the distribution is skewed to the left with more child parcels occupying particle sizes from $\sim 25\ \mu m$ to $75\ \mu m$ (see Figure 5.22b), this information was extracted based on examining the particle history file of all residence particles in the domain at a particular time-step (e.g. $t = 2.5 \times 10^{-3}$ s).

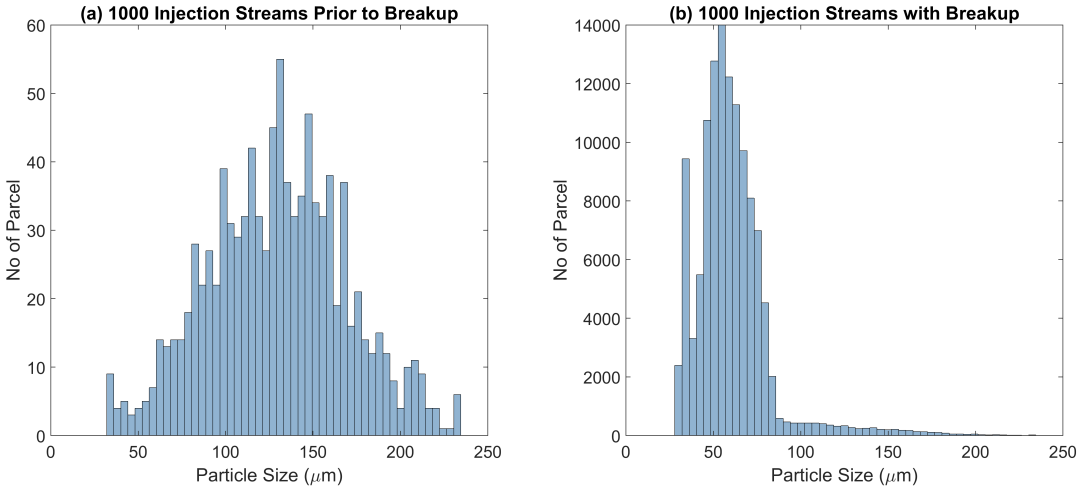


Figure 5.22: Particle distribution (a) before and (b) after breakup for 1000 injection streams where (a) is taken at $t = 5 \times 10^{-5}$ s and (b) is taken at $t = 2.5 \times 10^{-3}$ s

5.12.2 Airflow Time-Step

In the data presented in Figure 5.20b the airflow time-step (Δt_{air}) is varied to assess the effect of different cell convective Courant numbers (CFL) on the film solution while keeping other parameters constant. The corresponding maximum convective CFL in the smallest cells for $5 \times 10^{-6} s$, $1 \times 10^{-5} s$ and $1 \times 10^{-4} s$ are 4.49, 8.98 and 89.8 respectively. The smallest and intermediate time-step studies show that the film thickness result did not differ significantly. However for the largest time-step ($1 \times 10^{-4} s$), the interphase momentum coupling greatly reduces due to tenfold increase in Courant number. Although the computed film thickness is closer to the published result the drag term in the particle trajectory calculation differs significantly due to inaccurate coupling. The same argument applies with regard to air-film momentum coupling. In this case, the airflow time-step should be optimally be $1 \times 10^{-5}\ s$ or CFL 8.98 to remain accurate and cost effective for the chosen cell size. By looking more in-depth into the continuous-phase velocity and wall shear stresses. Figure 5.23 shows that the wall shear stresses for $\Delta t_{air} = 1 \times 10^{-4} s$ at $X > 25$ mm are larger than the rest. These corresponded to the velocity quantities at $X = 30$ and 35 mm, the component very close to the wall is higher and hence resulted in thinner film.

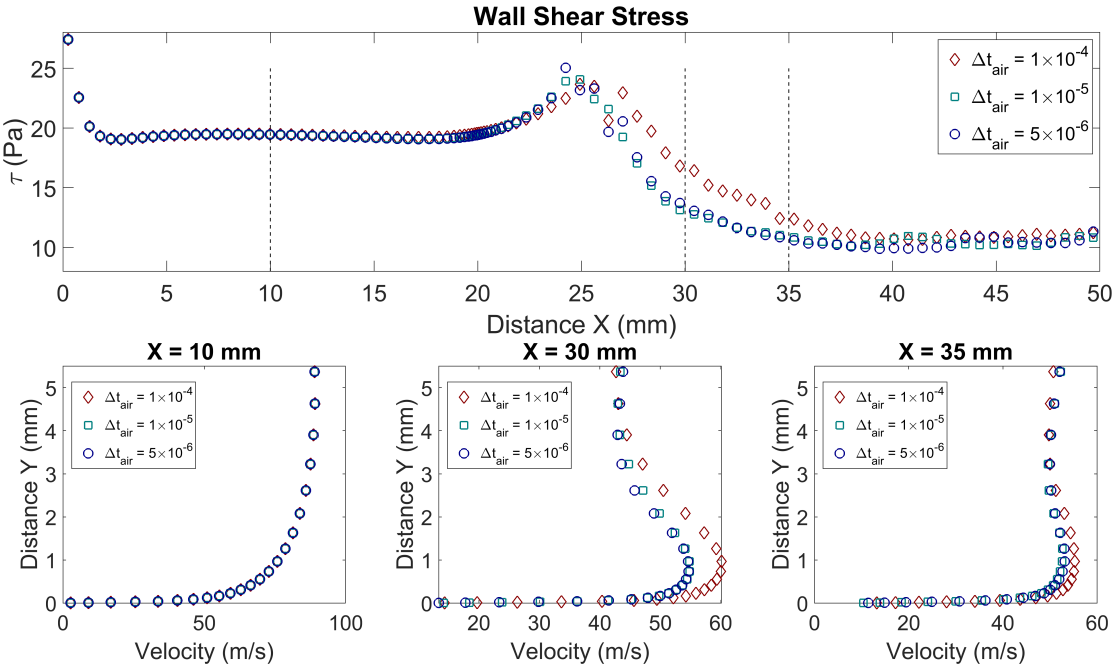


Figure 5.23: The component of wall shear stress with its corresponding velocity magnitude

5.12.3 Mesh Dependency Test

A mesh dependency test was carried out to check the sensitivity of the solution to changes in grid density. In multiphase flow, grid sensitivity is complicated and has multiple parameters affecting it. Three meshes (e.g., 380k, 920k and 2200k) were used with the highest number of injection streams and optimum air flow time step (as defined in Section 5.12.2) to assess the effect of grid density on film solution. The results are shown plotted in Figure 5.20c. The grids were refined in all three directions while keeping the same y^+ (less than 1). Measuring film thickness is a good variable as multiple effects are taken into account. The effect of mesh is primarily on core flow which affects momentum coupling, breakup model, particle spreading and momentum transport of film. The grid sensitivity studies show that film thickness for the 380k cell mesh differs by approximately 6% to 2200k cells. The grid refinement shows systematic increase in film thickness value. The standard deviation bars are plotted to take into account the effect of film waviness. The bars show that solution change is not affected by waviness of film and the 2200k cell mesh is used for subsequent studies.

5.12.4 Turbulent Dispersion

Looking at turbulent flow quantities it was noted that the velocity fluctuations could vary significantly between 1 – 10 % (turbulent intensity measured based on mean velocity of 82 ms^{-1}). These fluctuations could significantly impact particle trajectory and interphase coupling. The effect of velocity fluctuations are therefore included in trajectory calculation for more realistic particle distribution in the domain. Figure 5.20d shows data facilitating direct comparison of computed film thickness with and without the discrete random walk model. Results show that turbulent dispersion caused significant changes to the computed film thickness. The film thickness in the region 5 mm to 15 mm from the injection point is closer to the experiment values of Arienti *et al.* [13] with the turbulent dispersion model active.

Significant changes to the film thickness could be due to factors such as particle spreading on the surface and interphase momentum coupling. Figure 5.24 compares the film DPM-mass source with and without DRW. Film spread on the surface for the non-turbulent case (Non-DRW is narrower as compared to the turbulent dispersion case (DRW). In the DRW case the highest mass source region extends further upstream.

The corresponding mid-plane velocity fields shown in Figure 5.25 show that velocity fluctuations result in a noticeably different flow field. The DRW case has a much lower velocity at the injection pooint as shown by the blue segment (0 to 3.09 m/s).

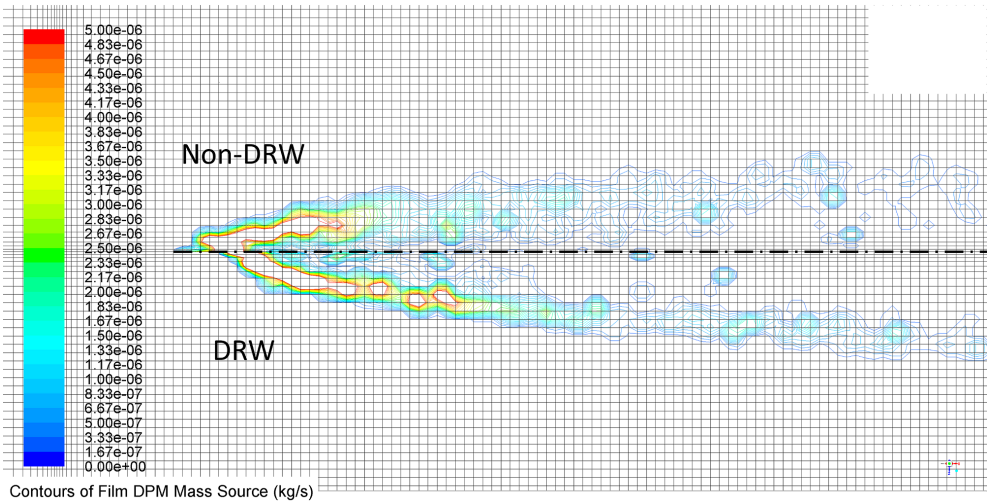


Figure 5.24: DPM mass source on bottom surface due to turbulent dispersion

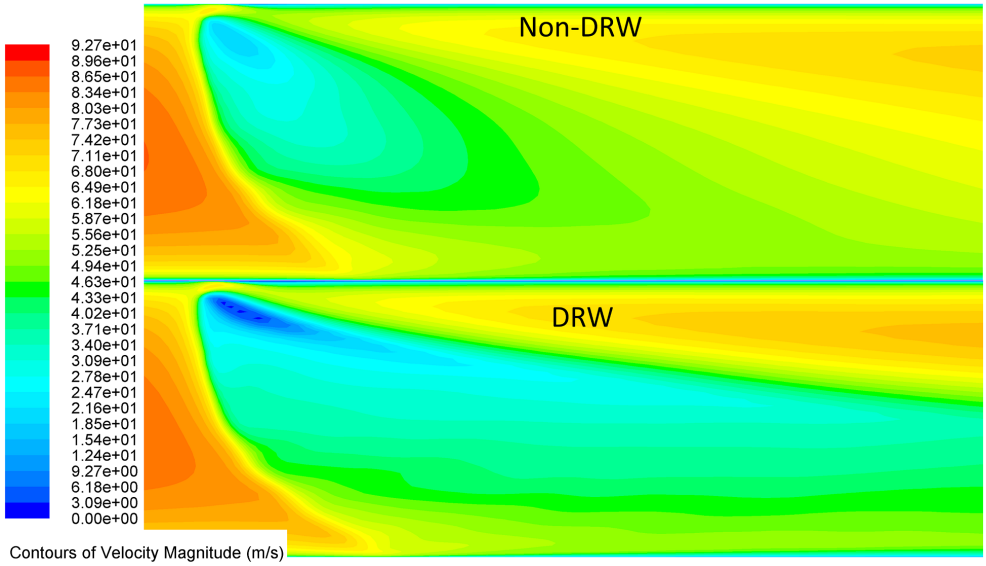


Figure 5.25: Velocity field on mid-plane due to turbulent dispersion

5.12.5 Pressure Gradient and Spreading

The effect of gas pressure is significant on the film dynamics. Based on Figure 5.20e, inclusion of the pressure gradient term causes significant waviness to the film due to streamwise and spanwise translation of the film as pressure gradient force is taken into account in momentum transportation. The film tends to flatten and lump up periodically. The effect of film transportation in the spanwise direction is also shown in Figure 5.26a, where it is seen that the pressure gradient force compresses the film and spreads it into multiple peaks. The cut-section view of film thickness Figure 5.26 is taken at x = 20 mm from the injection point. The film distribution due to pressure gradient could also be related to the velocity of the film in z-direction. Referring to in Figure 5.26b it is seen that at z equal to approximately $\pm$ 1.5 mm, the velocity components are at maxima (based on mean plus deviation). This pushes the film laterally contributing to higher thickness at three locations (z = -4, 0 and 4 mm). Bi-directional spanwise translation occurs most prominently at 0 mm as indicated by oscillation of the z-velocity (see deviation bar).

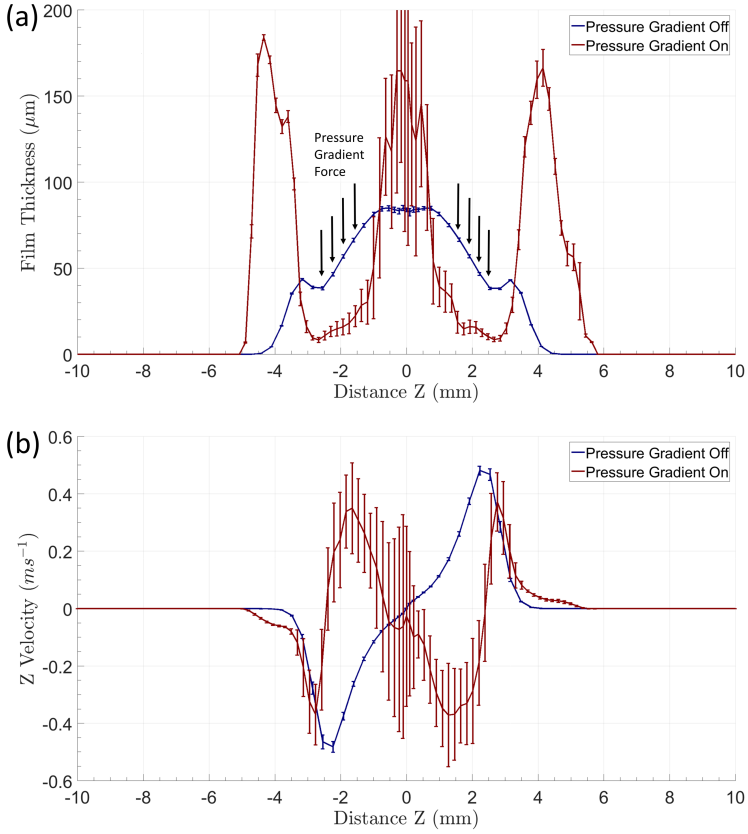


Figure 5.26: Pressure gradient effect on (a) Time-averaged spanwise film thickness and (b) Time-averaged spanwise z-velocity

Conversely, the non-pressure gradient film lacks all the features of pressure gradient film. The former has an 'out-of-phase' velocity profile centred at 0 mm (refer to Figure 5.26b). It reflects a 'symmetrical' centre 2D film thickness profile. The planar views of the film thickness are illustrated in Figure 5.27 for both non pressure gradient and pressure gradient.

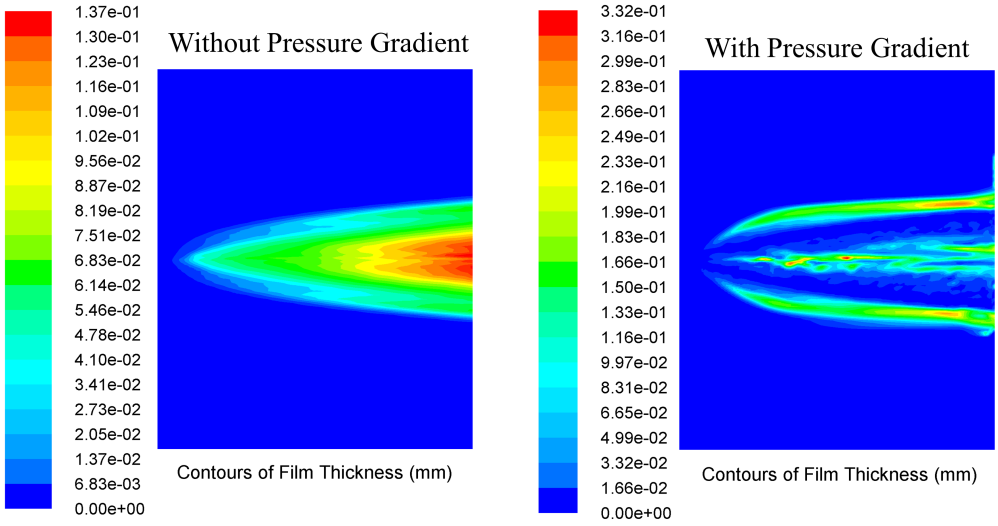


Figure 5.27: Contour of film thickness for non-pressure gradient term (static pressure and hydrostatic pressure) and with pressure-gradient term

5.12.6 Instabilities of Surface Tension

The pressure gradient force is further evaluated with inclusion of surface tension. Convergence difficulty was faced when the surface tension term was switched on together with gas-film two way coupling and separation at edge (tested on expansion duct). To arrive to the state shown in Figure 5.28 the solver was relaxed by maintaining a maximum film CFL of less than 0.01 with 1000 explicit film temporal sub-iterations (to capture the capillary waves [82]) while separation and film-gas two-way momentum coupling at interface are switched off. The surface tension term tends to dampen the film such that it reverses in the direction of the gas path. Based on the outcome of these cases, the stripping case was conducted without the pressure gradient force and surface tension restoring force.

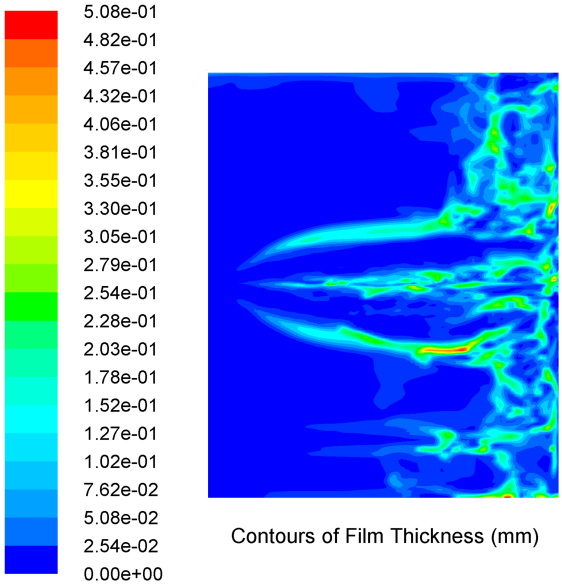


Figure 5.28: Contour of film thickness for full pressure gradient term (including surface tension)

5.12.7 Stripping Criteria

At high relative velocities between gas and film, Kelvin Helmoltz waves were seen by Shedd *et al.* [128] with regard to their experiment at the same flow condition. These waves grow and eventually strip off particles from the surface of the film. To enable mass to be removed from the film surface in the computational model, a critical stripping Weber number is needed. The typical stripping criterion documented by ANSYS-Fluent is based on critical shear (Pa) which lead to severe convergence instabilities as this quantity has no direct link to state of the film. To express stripping criterion in terms of film state and shearing velocity a Weber number stripping criteria is preferable and this is implemented via a command line in the text user interface (*enable-film-weber-stripping-criterion #t*).

By conducting rigorous analysis of the empirical basis for critical Weber number which is given in Section 5.8.6. The critical Weber number in Equation (5.66) can be expressed as $\rho_l V_s^2 \lambda_c / \sigma$ and the λ_c is based on K-H instability theory taken from Ghiaasiaan [153]. The critical Weber number calculated is close to value suggested by ANSYS (i.e. $We_{crit} = 0.06$). Applying this condition allows liquid to strip from the film bringing it to a thickness value closer to experiment as shown in Figure 5.20f. However, note that Andreussi [152] defined an even lower number of 5.5×10^{-3}. And these numbers should be test for future cases to assess their effects on film solution.

5.12.8 Error Calculation

The percentage difference between experiment and CFD for the grid point along the measurement line could calculated based on the formula of root mean square error (RMSE) given in Equation (5.68):

$$RMSE = \sqrt{\frac{\sum_{i=1}^{n}\left(h_{cfd} - h_{exp}\right)^2}{n}} \tag{5.68}$$

By interpolating the grid point with equal spacing with the film thickness values for CFD and compared with the published data the normalized root mean square error (NRMSE) for cases 7, 10 and 11 is obtained as 49.05%, 83.33% and 28.9% respectively. Based on all the cases, the set-up with the stripping model has the best accuracy. By doing comparison with Ingle cases, it was found that Ingle's Fluent case file contains many counter-intuitive settings [155]. These include only performing one-way turbulence coupling where the continuous phase impacting particle trajectories and having the airflow time-step of 1×10^{-4} s. One way turbulence coupling resulted in significantly different jet trajectories and the time-step of 1×10^{-4} s is known to cause changes in film solution although it is closer to experiment as shown in the results of air flow time-step studies. Further analysis is being conducted to examine numerical stability when separation and film-gas two-way momentum coupling are switched on.

5.13 Summary of CFD

The computational studies of jet-breakup and the formation of thin film in crossflow for application relevant to bearing chamber are described. Motivations behind the usage of Discrete Phase Model (DPM) and Eulerian Thin Film Model (ETFM) are to reduce the high cost associated with conventional CFD method like Volume-of-Fluid (VOF), furthermore Bristot *et al.* [54] reported the difficulty of capture the interface of waves associated with turbulence damping of $k-\omega$ SST Turbulence model.

Based on the observations in the vicinity of aero-engine ball bearing, droplets and ligaments were seen to be released from the rotating cage and at very high speed and a thin layer of continuous film was formed on the surfaces close to the ball bearing. The thin film and droplets were found to be well below the cut-off point of VOF. Using DPM and ETFM as a modelling strategy at the vicinity of the bearing chamber is a reasonable approach. ETFM employed a depth-averaged

approach that simplifies the three-dimensional N-S equations into two-dimensional thin film equation. The ability to couple VOF-DPM-ETFM could potentially realise the design-capability of engines and allowing optimisation studies. Kay *et al.* [78] formulated the thin film model by inclusion of inertia and heat convection terms. Subsequently Kakimpa *et al.* [81] successfully demonstrated the ability of coupling VOF-ETFM.

The CFD modelling of jet-breakup in crossflow and thin film formation were simulated using Fluent's Euler-Lagrangian and Eulerian Thin Film Models as a necessary first step towards establishing a satisfactory coupling between DPM and ETFM models.

- The results for the injection study show 500 injections are adequate to ensure a statistical representation of the particle range in the domain. The computed film thickness is insensitive to increase in injection number.
- In terms of air-flow timestep, a minimum time-step of $1 \times 10^{-5} s$ is needed to ensure sufficient interphase momentum coupling. This corresponds to a Courant number of 8.98 for the smallest streamwise cell size (0.1 mm).
- Systematic mesh refinement indicates that film thickness changes slightly with increase in mesh density and a 2200k cell mesh was used for subsequent study.
- In terms of particle trajectory calculation, instantaneous velocity that includes velocity fluctuation yields film thickness values closer to experiment with a NRMSD of 49.05%. Including turbulent dispersion modifies the particle field, velocity field and particle spreading on surface.
- Inclusion of the pressure gradient force in the film momentum equation results in a more wavy film due to spanwise and streamwise translation of the film. A NRMSD of 83.33% is obtained for this case.
- The most accurate modelling with DPM-ETFM was achieved by including film stripping, accounting for Kelvin Helmholtz instabilities. The computed film thickness has a difference of 28.9% compared to experimental data.
- Convergence stability issues were faced when gas-film momentum coupling, separation and surface tension were switched on. Severe numerical instability was also faced for the stripping case when the stripping criterion was expressed in terms flow variables (e.g. in pascal) instead of film state (e.g. in We_s). For case where gas-film momentum coupling and separation are on, a high film velocity of approximately Mach number 1 is observed in the simulation and is causing divergence. Momentum exchange at the interface needs to be study carefully.

Although the CFD work here could be seen to be different in terms of the geometry with respect to the experimental work conducted, it is inevitably important that the stability and fidelity of the coupled models are fully assessed before implementing in a more complex geometry such as the bearing chamber. Extending the work of previous authors, the CFD models used in this thesis is more efficient, for example, two-equation turbulence model was used and thin film was simulated using ETFM, in comparison to Arienti *et al*'s [13] model, LES was used to resolve the continuous phase and VOF was used to resolve the thin liquid film which is significantly more expensive.

In relation to the work of Ingle *et al.* [155] where the authors used the same CFD models and submodels as what was presented in this thesis. The above computational work has shown that gas-film momentum two-way coupling at the interface is unstable and lead to divergence. This thesis also reported on the stability of using the surface tension and pressure gradient term in the film which was previously not mentioned by previous authors. Further looking at the actual CFD file of Ingle *et al.* [66] that was available in the ANSYS customer portal, the time-step size used was $1 \times 10^{-4} s$ which falls within the category of inaccurate time-step size as shown by the work of this thesis. Subsequently, the publication of Ingle *et al.* [66] did not mention about the time-step size used, neither do the authors perform any time-step study. As such the value from this thesis was presented as above where the CFD investigations have established criteria that will enable future modelling of film flow in an aero-engine bearing chamber. The work represents an advance in bearing chamber modelling capability although clearly future work is required.

Chapter 6 Conclusion

Very few prior studies have investigated the two-phase flow from an aero-engine ball bearing. This presented research describes the investigations of oil shedding from an aero-engine ball bearing conducted by employing experimental and computational methods. The aim of the research is to improve heat and oil management of an aero-engine through comprehensive understanding of the flow from an aero-engine ball bearing. It offers a potential improvement in optimisation of oil system by providing high quality experimental data and an improved modelling methodology. This chapter summarises the main findings from the research and clarifies the contribution to knowledge. Recommendations for future work are made.

6.1 Summary of Main Findings

Investigations were conducted in two parts, experimental and computational. Experimental investigations were conducted to obtain physical insights and to provide validation data for future computational modelling. Computational studies were conducted to develop a framework for multiphase modelling and to provide modelling strategies for solving problems related to multiphase flow in an aero-engine ball bearing. These are challenging as complex two-phase flow exist in the region of interest from the mixing process between sealing gas and the lubricating oil. A bespoke oil shedding test rig was utilised, it operates in an ambient environment with the absence of sealing airflow and pressure differential across chambers, thus somewhat simplifying the conditions.

In the experimental investigations, high-speed imaging was employed to investigate the dynamics of films on the surfaces close to a *Trent* 1000 aero-engine ball bearing. Investigations were also made to study the modes of droplet disintegration from the orbiting cage. A new optical technique was developed in G2TRC jointly between this project and a linked project to measure the thickness of the thin film on the bearing containment utilising ‘median-stacking’, gradient detection and spatial calibration. This approach differs greatly to those found in the literature where most authors use ultrasonic, conductance or capacitance methods to directly measure the film thickness. Such approaches are susceptible to problems arising from bubbles within the fluid. The optical technique, however, relies heavily on image quality and chamber environment. This method at the moment is point-wise in nature. An extension to the image processing could be made to enable researchers to azimuthally resolve the film thicknesses. Another limitation is that

the optical approach requires clear images currently only possible to be realised at very low speed (e.g. ω < 3000 rpm).

The high-speed imaging revealed that interfacial shear stress and gravity were the primary components that drove the phenomena observed on the thin film on the chamber wall. Tangential velocity drove the film circumferentially around the chamber wall, and the airflow derived its momentum from the rotating stub-shaft and inner-race. Gravity is the major component that pulls the film towards the scavenge region, noted in particular at the low speed of 3000 rpm where the film was seen to be detaching on the counter-current side.

Conversely at a higher rotational speed of 7000 rpm, the film is largely being affected by surface forces (interfacial shear stress) and less by the body force (gravity). A relationship was established showing that the increase in shaft rotational speed decreases the film thickness in order to conserve the mass and momentum of the film. The measurements indicated that these film thicknesses were in the order of $2.1 \sim 0.7$ mm for speeds of 3000 rpm to 7000 rpm. No substantial effect of flow rate on the film thickness was reported.

Uniquely in the bearing oil shedding test rig, the effect of axial load was found to be axial-plane specific. Increasing axial load resulted in an increase of film thickness at the gap between the cage and outer-race, whereas no such effect was seen further away from the bearing. These results were attributed to be coming from the effect of changing ball bearing dynamics as indicated by Foord's model [93] where the outer contact angle (α_0) and the ball rolling axis (β) modified the clearance close to the balls.

Qualitative analysis of the modes of oil disintegration were made for the orbiting cage of the *Trent* 1000 aero-engine ball bearing. Three regimes of oil disintegration similar to those of simple rotary atomisers were noted, namely, direct-drop, ligament and sheet. The studies were extended with classification of secondary ligament and ruffled sheet being observed for the aero-engine bearing geometry and operating conditions. The transitions between regimes were confirmed to be a function of Weber number similar to those observed in classical studies. Assessments of flow rate and fluid properties on regime change were not conducted and as part of this study. At shaft speed less than 1700 rpm, direct-drop was observed followed by the concurrent occurrence of primary ligament and laminar sheet after achieving critical speed 1700 rpm. The simultaneous occurrence was associated with variability of the local flow rate at the surfaces due to the complex geometry and the non-deterministic nature of the turbulent environment. It was noted that such behaviour was originally postulated by Frost [21] who stated that the eccentricity of oil feed in the rotating system could cause such features to occur.

The characterisation of ligament number (K) (of primary ligaments) in terms of Weber number and Stability number was made for the first time for aero-engine components. The correlation can be provided as:

$$K = 0.33811\, We^{0.53799} St^{-0.015162}$$

This is valid based on constant fluid properties for the rig fluid (Aeroshell 390) at constant flow rate (5.2 lpm) and radius.

In the final part of the experimental studies, wave analysis was performed. A multiscale wave structure was observed on the surfaces of the thin film. At low speed, the waves were seen to be within the gravity-capillary wave regime that is associated with low frequency and phase-speed. They are two-dimensional and fairly laminar in nature on the co-current side. However on the counter-current side, waves appeared to be three-dimensional and structurally wavier (undulating) at different circumferential locations due to gravity. These observations were consistent with theoretical studies of rimming flow where three regimes exist, namely, pool, shock and smooth. At 3000 rpm, the observation of pooling flow was seen as oil flows from both co-current and counter-current sides were directed towards the bottom. At 5000 rpm, 'beyond' shock regime was attained where oil on the rising side reverses and is driven in the same direction as the rotating shaft. The shock regime is estimated to be between 3000 to 5000 rpm, and further experimental test is needed to confirm the critical value. Nonetheless, smooth flow was seen at 7000 rpm. This information will be useful for computational modelling of the shock regime with imposed axial through flow further validating the fidelity of the multiphase model.

Relations for wave frequency and wavelength with respect to shaft speed were established. Wave frequency is found to be proportional to the shaft rotational speed and inversely for the wavelength. The high frequency wave exhibits highly irregular periodicity as the phases were not moving in-plane. These small scale wave structures were classified as capillary waves, whereas, the larger wavelength surface waves are known as gravity-capillary waves. The analysis also showed that the effect of gravity delays the transition from gravity-capillary waves to capillary waves. These represent, for the first time analysis of multiscale wave structures for an aero-engine ball bearing. A list of future research opportunities is proposed in Section 6.3, employing the use of Planar Laser Induced Fluorescence (LIF) / Brightness Based Laser Induced Fluorescence (BBLIF) to further characterise the structure of the film and thicknesses in detail using an approach similar to that used by Alekseenko *et al.* [156, 157].

For the computational investigations, reviews of the development of thin film modelling capability and the cost benefits were conducted. These indicated that the coupling between DPM-ETFM should be evaluated before moving onto a higher level coupling such as VOF-DPM-

ETFM. The stability and fidelity of the model is explored based on simulating and comparing results with the case of Arienti *et al.* [13] and Shedd *et al.* [128]. Modelling strategies for two-phase flow simulation of bearings and bearing chambers are developed.

The study of jet-breakup and thin film formation in a cross-flow was performed. These computational studies indicated that the model was capable of modelling the discrete phase and thin film to a certain level of accuracy but instability remains when certain terms were activated. Systematic studies indicated that an optimum particle injection time-step, airflow time-step, injection number and mesh density is needed to balance the cost and accuracy. Inclusion of velocity fluctuation in the instantaneous velocity led to significant difference to the film solution including pressure gradient force and film stripping model also significantly affected the computed solution. By far, inclusion of the film stripping model yields results closest to the experiment. Convergence instability issues were faced when gas and film share the same velocity at the cell centre and this was also the case with activation of film separation. These instabilities where indicated by a non-physical high mean film velocity close to Mach number of 1. Including a surface tension term is also found to lead to instability and further evaluations need to be conducted.

6.2 Contribution to Knowledge

This research represents for the first time close visualisation of multiphase flow through an actual HP location bearing (Trent 1000) operating at moderate speeds. The characterisation of oil film was extended beyond only measuring the film thickness as performed by early investigators to understanding the dynamics of waves and modes of oil disintegration. Dimensional analysis of oil disintegration was performed on the aero-engine ball bearing and indicated that most correlations derived from simple rotary devices were not transferable based on the operating conditions and complex geometry of interest. A correlation for ligament number was developed for aero-engine operating conditions and geometry for the first time. With the established understanding of the flow structure in the vicinity of an aero-engine ball bearing, future validation was made possible to assess the fidelity of the computational models. Additionally, modelling strategies were also developed as part of the research to efficiently couple DPM-ETFM for application to an aero-engine bearing chamber. The stability and accuracy of the model were assessed using the test case of jet-breakup and thin film formation in cross-flow and results indicated that such an approach is feasible. This research paves the way for a future more advanced framework such as coupled VOF-DPM-ETFM for full chamber simulation.

6.3 Recommendations for Future Work

With the rig due to be recommissioned soon, a potential list of future work is presented both experimentally and computationally as following:

6.3.1 Experimental Investigations

1. Detailed visualisation and analysis of oil separation at the edge of the chamber wall (axial plane: 0 mm) of angular position P1. This involves characterising the modes of ligament breakup (such as Plateau-Rayleigh breakup, shear breakup and etc) along with secondary droplet production. This information will be useful for modelling multiphase flow at the edge and to inform design process. The visualisation of liquid impingement as a function of changing parameters is also highly interesting as it affects the secondary droplet productions or re-entrainment into the core of an actual aero-engine bearing chamber. This could be achieved by pure imaging from angular position P4 looking at towards P3 at an oblique angle.
2. The measurements of film velocity is important for both computational modelling as well as from an engine design perspective. A dye could be injected through a pulsation mode into the lubricating oil via the probe insertion hole. This enables the high-speed camera to spatially and temporally resolve the mean film velocity by tracking the dye. Alternatively, seeding particles of low Stokes number could also be introduced into the oil. The light sheet needs to be inserted potentially on a new casing with larger transparent section allowing the tracer particles to be illuminated. Cross-correlation could be performed revealing the velocity profile of the film, this method is similar to Particle Image Velocimetry (PIV). Brightness-based laser induced fluorescence (BBLIF) is the third possible application that can be used for the imaging of wave structures and film thicknesses. Illustration of the proposed techniques for dye tracking and BBLIF are given in Figure 6.1.
3. Investigation of the droplet size produced from the ligaments and oil sheet at the orbiting cage could be challenging as Phase Doppler Particle Analyser (PDPA) require the laser to be incident at angle that is difficult to achieve. It is possible to explore the use of strobe flashing combined with the Long Distance Microscope. As the strobe flash is approximately twice the lumens of continuous mode (e.g. 22000 lumens vs 12700 lumens), the particles could be captured with lower exposure time leading to sharper interface hence allowing the size to be determined using a pre-defined spatial resolution.

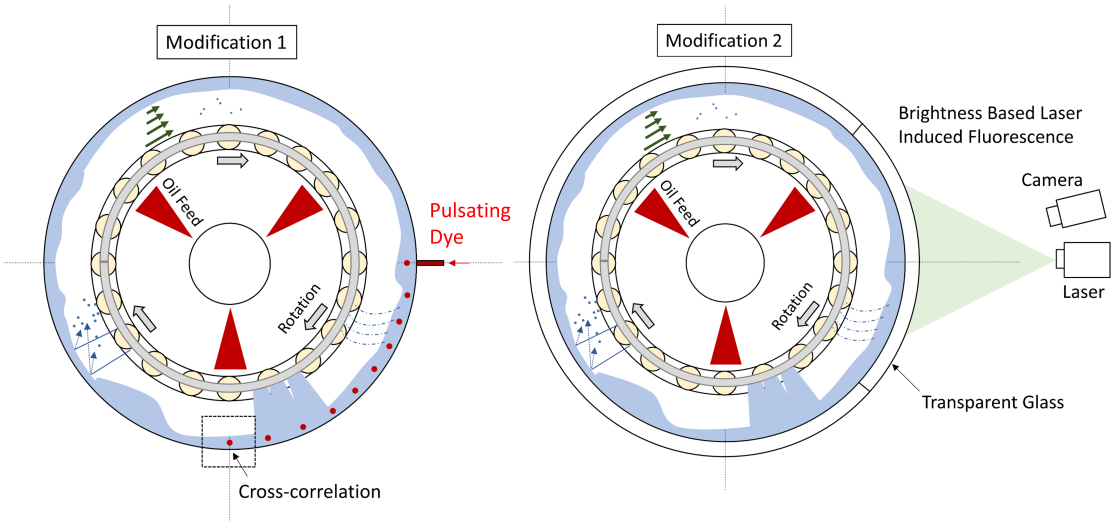


Figure 6.1: Proposed dye tracking for film velocity measurement and BBLIF for details waves and film thickness analysis

4. It is proposed to extend the analysis of the regime map by parametrically changing the rotational speed at different flow rates and axial loads. The correlation for ligament number should also be assessed with changing flow rate and fluid properties such that it can be applicable for most operating conditions.
5. The time-series film thickness data can reveals a lot of information, in particular on how interfacial shear stress is affecting the film waviness. Fast-fourier transform (FFT) could be performed based on having a more advance algorithim that can accurately detect the film thickness at each frame-rate. To achieve this, the images taken by the high-speed camera should be clear such that the image processing and image gradient thresholding method can be applied effectively to obtain a clear air-oil interface. Based on the way the film thickness data was extracted using optical technique, performing FFT analysis will not be possible. It has been proposed that this can be a part of the future work.

6.3.2 Computational Investigations

1. The coupling between VOF-DPM-ETFM is highly attractive for full chamber simulation. The ligaments and sheets could be resolved with VOF, the breakup into droplets could be transitioned to DPM based on their sphericity. The DPM can then be tracked using the Euler-Lagrangian approach until they are absorbed into the thin film which is being modelled using ETFM. As this is a significant piece of computational work, it is not

possible to implement this case study in the time available in this PhD. However, strong recommendation of this numerical study has been proposed for future work.

2. The fidelity of gas-liquid interface capture in a highly-sheared environment is not only the interest of experimentalists but also challenging to model. Potential application opportunities are wide ranging, from annular flow in oil and gas production to engine applications. As described by Chew, Peduto *et al.* and Bristot *et al.* [54, 55, 63], early thin film models, existing turbulence models and interface capturing methods are still unable to accurately predict the momentum exchange. Droplet impingements further complicate the problem. The experimental data could serve as a validation tool for the study of momentum exchange of a computational model.
3. In the experimental study, the oil film was seen to transition from pooling flow to smooth flow. It is possible to estimate that the shock regime could potentially be somewhere between 3000 rpm to 5000 rpm. The recirculation of oil film at the rising side of the shock regime could be determined experimentally and multiphase CFD could be used to validate the fidelity of the models. This is more challenging to model compared to classical rimming flow due to strong axial component from oil flow.

References

[1] ACARE, "Beyond Vision 2020 (Towards 2050)," 2010, [Online]. Available: http://www.gppq.fct.pt/h2020/_docs/brochuras/transportes/a%20background%20document%20from%20acare.pdf.

[2] ACARE, "European Aeronautics: A vision For 2020," 2001, [Online]. Available: https://www.acare4europe.org/sites/acare4europe.org/files/document/Vision%202020_0.pdf.

[3] Rolls Royce, *The jet engine*. John Wiley & Sons, 2015.

[4] Rolls Royce, "Rolls-Royce Holdings plc Annual Report," 2017.

[5] T. Piazera de Carvalho, "Two-phase flow in open-cell metal foams with application to aero-engine separators," PhD, Mechanical Engineering The University of Nottingham, 2016.

[6] A. A. Adeniyi, H. Morvan, and K. Simmons, "A Computational Fluid Dynamics Simulation of Oil–Air Flow Between the Cage and Inner Race of an Aero-engine Bearing," *Journal of Engineering for Gas Turbines and Power,* vol. 139, no. 1, pp. 012506-012506-8, 2016.

[7] A. J. Mitchell, K. Simmons, and D. Hann, "Experimental Investigation Into Droplet Impingement Upon Moving Films Using High Speed Video and Thermal Imaging," *ASME Proceedings,* no. 57342, p. V001T01A038, 2015.

[8] T. Okawa, T. Shiraishi, and T. Mori, "Effect of impingement angle on the outcome of single water drop impact onto a plane water surface," *Experiments in Fluids,* journal article vol. 44, no. 2, pp. 331-339, February 01 2008.

[9] C. W. Lee, P. C. Palma, K. Simmons, and S. J. Pickering, "Comparison of Computational Fluid Dynamics and Particle Image Velocimetry Data for the Airflow in an Aeroengine Bearing Chamber," *Journal of Engineering for Gas Turbines and Power,* vol. 127, no. 4, pp. 697-703, 2004.

[10] P. F. Brown, "Bearings and dampers for advanced jet engines," *SAE Transactions,* pp. 998-1009, 1970.

[11] P. Gloeckner, M. Martin, and M. Flouros, "Comparison of Power Losses and Temperatures between an All-Steel and a Direct Outer Ring–Cooled, Hybrid 133-mm-Bore Ball Bearing at Very High Speeds," *Tribology Transactions,* vol. 60, no. 6, pp. 1148-1158, 2017/11/02 2017.

[12] R. J. Parker, "Present technology of rolling-element bearings," 1983.

[13] M. Arienti *et al.*, "Modeling Wall Film Formation and Breakup Using an Integrated Interface-Tracking/Discrete-Phase Approach," *Journal of Engineering for Gas Turbines and Power,* vol. 133, no. 3, pp. 031501-031501-7, 2010.

[14] S. Wittig, A. Glahn, and J. Himmelsbach, "Influence of High Rotational Speeds on Heat Transfer and Oil Film Thickness in Aero-Engine Bearing Chambers," *Journal of Engineering for Gas Turbines and Power,* vol. 116, no. 2, pp. 395-401, 1994.

[15] A. Glahn and S. Wittig, "Two-Phase Air/Oil Flow in Aero Engine Bearing Chambers: Characterization of Oil Film Flows," *Journal of Engineering for Gas Turbines and Power,* vol. 118, no. 3, pp. 578-583, 1996.

[16] A. Glahn, M. Kurreck, M. Willmann, and S. Wittig, "Feasibility Study on Oil Droplet Flow Investigations Inside Aero Engine Bearing Chambers—PDPA Techniques in Combination With Numerical Approaches," *Journal of Engineering for Gas Turbines and Power,* vol. 118, no. 4, pp. 749-755, 1996.

[17] P. Gorse, K. Willenborg, S. Busam, J. Ebner, K. Dullenkopf, and S. Wittig, "3D-LDA Measurements in an Aero-Engine Bearing Chamber," *ASME Proceedings,* no. 36886, pp. 257-265, 2003.

[18] P. Gorse, S. Busam, and K. Dullenkopf, "Influence of Operating Condition and Geometry on the Oil Film Thickness in Aeroengine Bearing Chambers," *Journal of Engineering for Gas Turbines and Power,* vol. 128, no. 1, pp. 103-110, 2004.

[19] W. Kurz, K. Dullenkopf, and H.-J. Bauer, "Influences on the Oil Split Between the Offtakes of an Aero-Engine Bearing Chamber," *ASME Proceedings,* no. 44700, pp. 2251-2259, 2012.

[20] J. O. Hinze and H. Milborn, "Atomization of Liquids by Means of a Rotating Cup," *Journal of Applied Mechanics,* pp. 145 - 153, 1950.

[21] A. R. Frost, "Rotary atomization in the ligament formation mode," *Journal of Agricultural Engineering Research,* vol. 26, no. 1, pp. 63-78, 1981/01/01/ 1981.

[22] H. Peng, X. Shan, J. Kang, X. Ling, and D. Wang, "Influence of rotary disk configurations on droplets characteristics in molten slag granulation for waste heat recovery," *Applied Thermal Engineering,* vol. 135, pp. 269-279, 2018/05/05/ 2018.

[23] T. Kamiya, "An analysis of the ligament-type disintegration of thin liquid film at the edge of a rotating disk," *Journal of Chemical Engineering of Japan,* vol. 5, no. 4, pp. 391-396, 1972.

[24] D. Wang, X. Ling, and H. Peng, "Simulation of ligament mode breakup of molten slag by spinning disk in the dry granulation process," *Applied Thermal Engineering,* vol. 84, pp. 437-447, 2015/06/05/ 2015.

[25] D. Wang, X. Ling, H. Peng, Z. Cui, and X. Yang, "Experimental Investigation of Ligament Formation Dynamics of Thin Viscous Liquid Film at Spinning Disk Edge," *Industrial & Engineering Chemistry Research,* vol. 55, no. 34, pp. 9267-9275, 2016/08/31 2016.

[26] S. Matsumoto, K. Saito, and Y. Takashima, "Phenomenal transition of liquid atomisation from disk," *Journal of Chemical Engineering of Japan,* vol. 7, no. 1, pp. 13-19, 1974.

[27] J. Liu, Q. Yu, and Q. Guo, "Experimental investigation of liquid disintegration by rotary cups," *Chemical Engineering Science,* vol. 73, pp. 44-50, 2012/05/07/ 2012.

[28] A. Glahn, S. Busam, M. F. Blair, K. L. Allard, and S. Wittig, "Droplet Generation by Disintegration of Oil Films at the Rim of a Rotating Disk," *Journal of Engineering for Gas Turbines and Power,* vol. 124, no. 1, pp. 117-124, 2000.

[29] A. Glahn, M. F. Blair, K. L. Allard, S. Busam, O. Schäfer, and S. Wittig, "Disintegration of Oil Jets Emerging From Axial Passages at the Face of a Rotating Cylinder," *Journal of Engineering for Gas Turbines and Power,* vol. 125, no. 4, pp. 1003-1010, 2003.

[30] A. Glahn, M. F. Blair, K. L. Allard, S. Busam, O. Schäfer, and S. Wittig, "Disintegration of Oil Films Emerging From Radial Holes in a Rotating Cylinder," *Journal of Engineering for Gas Turbines and Power,* vol. 125, no. 4, pp. 1011-1020, 2003.

[31] S. Matsumoto, D. Belcher, and E. Crosby, "Rotary atomizers-Performance understanding and prediction," in *IN: ICLASS-85; Proceedings of the Third International Conference on Liquid Atomisation and Spray Systems, London, England, July 8-10, 1985. Volume 1 (A87-13826 03-34). London, Institute of Energy, 1986, p. IA/1/1-IA/1/21.*, 1986, vol. 1.

[32] A. H. M. Lefebvre, V. G., *Atomization and Sprays*. 2017.

[33] H. Peng, N. Wang, D. Wang, and X. Ling, "Experimental Study on the Critical Characteristics of Liquid Atomization by a Spinning Disk," *Industrial & Engineering Chemistry Research,* vol. 55, no. 21, pp. 6175-6185, 2016/06/01 2016.

[34] P. Gorse, K. Dullenkopf, H. J. Bauer, and S. Wittig, "An Experimental Study on Droplet Generation in Bearing Chambers Caused by Roller Bearings," *ASME Proceedings,* no. 43147, pp. 1681-1692, 2008.

[35] M. Flouros, "Reduction of Power Losses in Bearing Chambers Using Porous Screens Surrounding a Ball Bearing," *Journal of Engineering for Gas Turbines and Power,* vol. 128, no. 1, pp. 178-182, 2005.

[36] M. B. Krug, D. Peduto, W. Kurz, and H.-J. Bauer, "Experimental Investigation Into the Efficiency of an Aero-engine Oil Jet Supply System," *Journal of Engineering for Gas Turbines and Power,* vol. 137, no. 1, pp. 011505-011505-7, 2014.

[37] P. R. Childs, *Rotating flow*. Elsevier, 2010.

[38] G. Taylor, "Stability of a Viscous Liquid Contained between Two Rotating Cylinders Phil. Trans. R. Soc. Lond. A January," 1923.

[39] D. Coles, "Transition in circular Couette flow," *Journal of Fluid Mechanics,* vol. 21, no. 3, pp. 385-425, 1965.

[40] J. A. Cole, "Taylor-vortex instability and annulus-length effects," *Journal of Fluid Mechanics,* vol. 75, no. 1, pp. 1-15, 1976.

[41] E. L. Koschmieder, "Turbulent Taylor vortex flow," *Journal of Fluid Mechanics,* vol. 93, no. 3, pp. 515-527, 1979.

[42] J. Kaye and E. C. Elgar, *Modes of adiabatic and diabatic fluid flow in an annulus with an inner rotating cylinder*. Cambridge, Mass.: M.I.T. Research Laboratory of Heat Transfer in Electronics, 1957.

[43] K. M. Becker and J. Kaye, "Measurements of Diabatic Flow in an Annulus With an Inner Rotating Cylinder," *Journal of Heat Transfer,* vol. 84, no. 2, pp. 97-104, 1962.

[44] A. A. Hashmi, K. Dullenkopf, H.-J. r. Bauer, and M. Klingsporn, "Experimental Investigation of Lubrication Oil Film Dynamics in a Typical Aero-Engine Bearing Chamber Environment," *ASME Proceedings,* no. 54655, pp. 797-807, 2011.

[45] W. Kurz and H.-J. Bauer, "An Approach for Predicting the Flow Regime in an Aero Engine Bearing Chamber," in *ASME Turbo Expo 2014: Turbine Technical Conference and Exposition*, 2014, vol. Volume 5C: Heat Transfer, V05CT16A037.

[46] S. Wittig, J. Himmelsbach, B. Noll, H. J. Feld, and W. Samenfink, "Motion and Evaporation of Shear-Driven Liquid Films in Turbulent Gases," *Journal of Engineering for Gas Turbines and Power,* vol. 114, no. 2, pp. 395-400, 1992.

[47] S. K. Alghoul, C. N. Eastwick, and D. B. Hann, "Normal droplet impact on horizontal moving films: an investigation of impact behaviour and regimes," *Experiments in Fluids,* journal article vol. 50, no. 5, pp. 1305-1316, May 01 2011.

[48] A. Bisighini, G. E. Cossali, C. Tropea, and I. V. Roisman, "Crater evolution after the impact of a drop onto a semi-infinite liquid target," *Physical Review E,* vol. 82, no. 3, p. 036319, 09/24/ 2010.

[49] C. Mundo, M. Sommerfeld, and C. Tropea, "Droplet-wall collisions: Experimental studies of the deformation and breakup process," *International Journal of Multiphase Flow,* vol. 21, no. 2, pp. 151-173, 1995/04/01/ 1995.

[50] F. T. Johnson, E. N. Tinoco, and N. J. Yu, "Thirty years of development and application of CFD at Boeing Commercial Airplanes, Seattle," *Computers & Fluids,* vol. 34, no. 10, pp. 1115-1151, 2005/12/01/ 2005.

[51] H. Xiao and P. Cinnella, "Quantification of model uncertainty in RANS simulations: A review," *Progress in Aerospace Sciences,* 2019.

[52] B. G. Vinod Kumar, J. W. Chew, and N. J. Hills, "Rotating Flow and Heat Transfer in Cylindrical Cavities With Radial Inflow," *Journal of Engineering for Gas Turbines and Power,* vol. 135, no. 3, pp. 032502-032502-12, 2013.

[53] S. Dong, "Direct numerical simulation of turbulent Taylor–Couette flow," *Journal of Fluid Mechanics,* vol. 587, pp. 373-393, 2007.

[54] A. Bristot, H. P. Morvan, K. Simmons, and M. Klingsporn, "Effect of Turbulence Damping in VOF Simulation of an Aero-Engine Bearing Chamber," *ASME Conference Proceedings,* no. 50794, p. V02BT41A013, 2017.

[55] J. W. Chew, "Analysis of the Oil Film on the Inside Surface of an Aero-Engine Bearing Chamber Housing," *ASME Proceedings,* no. 78729, p. V001T01A082, 1996.

[56] M. Farrall, K. Simmons, S. Hibberd, and P. Gorse, "A Numerical Model for Oil Film Flow in an Aeroengine Bearing Chamber and Comparison to Experimental Data," *Journal of Engineering for Gas Turbines and Power,* vol. 128, no. 1, pp. 111-117, 2004.

[57] S. Jiro, M. Kobayashi, S. Iwashita, and H. Fujimoto, "Modeling of Diesel Spray Impingement on a Flat Wall," SAE Transactions, 1994. [Online]. Available: https://doi.org/10.4271/941894.

[58] C. Bai and A. D. Gosman, "Development of Methodology for Spray Impingement Simulation," SAE Transactions, 1995. [Online]. Available: https://doi.org/10.4271/950283.

[59] D. W. Stanton and C. J. Rutland, "Modeling Fuel Film Formation and Wall Interaction in Diesel Engines," SAE Transactions, 1996. [Online]. Available: https://doi.org/10.4271/960628.

[60] C. W. Hirt and B. D. Nichols, "Volume of fluid (VOF) method for the dynamics of free boundaries," *Journal of computational physics,* vol. 39, no. 1, pp. 201-225, 1981.

[61] C. Young and J. W. Chew, "Evaluation of the Volume of Fluid Modelling Approach for Simulation of Oil/Air System Flows," *ASME Proceedings,* no. 47268, pp. 1249-1257, 2005.

[62] A. A. Hashmi, K. Dullenkopf, R. Koch, and H.-J. r. Bauer, "CFD Methods for Shear Driven Liquid Wall Films," *ASME Proceedings,* no. 43994, pp. 1283-1291, 2010.

[63] D. Peduto, A. A. Hashmi, K. Dullenkopf, H.-J. r. Bauer, and H. Morvan, "Modelling of an Aero-Engine Bearing Chamber Using Enhanced CFD Technique," *ASME Proceedings,* no. 54655, pp. 809-819, 2011.

[64] A. Crouchez-Pillot and H. P. Morvan, "CFD Simulation of an Aeroengine Bearing Chamber Using an Enhanced Volume of Fluid (VOF) Method: An Evaluation Using Adaptive Meshing," *ASME Proceedings,* no. 45738, p. V05CT16A033, 2014.

[65] A. A. Adeniyi, H. P. Morvan, and K. A. Simmons, "A Transient CFD Simulation of the Flow in a Test Rig of an Aeroengine Bearing Chamber," *ASME Conference Proceedings,* no. 45738, p. V05CT16A030, 2014.

[66] G. E. Cossali, A. Coghe, and M. Marengo, "The impact of a single drop on a wetted solid surface," *Experiments in Fluids,* journal article vol. 22, no. 6, pp. 463-472, April 01 1997.

[67] A. L. Yarin, "Droplet Impact Dynamics: Splashing, Spreading, Receding, Bouncing…," *Annual Review of Fluid Mechanics,* vol. 38, no. 1, pp. 159-192, 2006.

[68] D. Peduto, "Oil droplet impact dynamics in aero-engine bearing chambers: correlations derived from direct numerical simulations," PhD, The University of Nottingham & KIT, 2015.

[69] M. B. Krug, W. Kurz, C. Höfler, and H.-J. Bauer, "Evaluation of the Volume-of-Fluid Method for the Numerical Modelling of an Aero Engine Bearing Chamber," in *The 22nd International Symposium on Air Breathing Engines (ISABE 2015), Phoenix, AZ, USA, October 25-30, 2015*, 2015, pp. 1-10.

[70] A. Bristot, H. P. Morvan, and K. A. Simmons, "Evaluation of a Volume of Fluid CFD Methodology for the Oil Film Thickness Estimation in an Aero-Engine Bearing Chamber," *ASME Proceedings,* no. 49712, p. V02CT39A007, 2016.

[71] Y. Egorov, M. Bouchker, A. Martin, S. Pigny, M. Scheuerer, and S. Willemsen, "Validation of CFD codes with PTS-relevant test cases," in "5th Euratom Framework Programme ECORA project," 2004.

[72] P. Tkaczyk, "CFD simulation of annular flows through bends," The University of Nottingham, 2011.

[73] R. E. H. White, T.W. , "Effect of fluid properties on condensate behaviour," *TAPPI,* vol. 41, no. 2, pp. 71 - 76, 1958.

[74] J. Williams, "Thin film rimming flow subject to droplet impact at the surface," PhD, The University of Nottingham, 2009.

[75] C. Wang, H. P. Morvan, S. Hibberd, and K. A. Cliffe, "Thin Film Modelling for Aero-Engine Bearing Chambers," *ASME Proceedings,* no. 54617, pp. 277-286, 2011.

[76] C. Wang, H. P. Morvan, S. Hibberd, K. A. Cliffe, A. Anderson, and A. Jacobs, "Specifying and Benchmarking a Thin Film Model for Oil Systems Applications in ANSYS Fluent," *ASME Proceedings,* no. 44670, pp. 229-234, 2012.

[77] H. Foucart, C. Habchi, J. F. Le Coz, and T. Baritaud, "Development of a Three Dimensional Model of Wall Fuel Liquid Film for Internal Combustion Engines," SAE Transactions, 1998. [Online]. Available: https://doi.org/10.4271/980133.

[78] E. D. Kay, S. Hibberd, and H. Power, "Inertial effects at moderate Reynolds number in thin-film rimming flows driven by surface shear," *Physics of Fluids,* vol. 25, no. 10, p. 102108, 2013/10/01 2013.

[79] B. Kakimpa, H. P. Morvan, and S. Hibberd, "Thin-Film Flow Over a Rotating Plate: An Assessment of the Suitability of VOF and Eulerian Thin-Film Methods for the Numerical Simulation of Isothermal Thin-Film Flows," *ASME Proceedings,* no. 56734, p. V05CT15A027, 2015.

[80] J. Rice, A. Faghri, and B. Cetegen, "Analysis of a free surface film from a controlled liquid impinging jet over a rotating disk including conjugate effects, with and without evaporation," *International Journal of Heat and Mass Transfer,* vol. 48, no. 25, pp. 5192-5204, 2005/12/01/ 2005.

[81] B. Kakimpa, H. P. Morvan, and S. Hibberd, "The Numerical Simulation of Multi-Scale Oil Films Using Coupled VOF and Eulerian Thin-Film Models," *ASME Proceedings,* no. 49682, p. V001T01A020, 2016.

[82] B. Kakimpa, H. Morvan, and S. Hibberd, "The Depth-Averaged Numerical Simulation of Laminar Thin-Film Flows With Capillary Waves," *Journal of Engineering for Gas Turbines and Power,* vol. 138, no. 11, pp. 112501-112501-10, 2016.

[83] J. Liu and J. P. Gollub, "Solitary wave dynamics of film flows," *Physics of Fluids,* vol. 6, no. 5, pp. 1702-1712, 1994/05/01 1994.

[84] H. K. Versteeg and W. Malalasekera, *An introduction to computational fluid dynamics: the finite volume method*. Pearson Education, 2007.

[85] B. E. Launder and D. B. Spalding, "The numerical computation of turbulent flows," *Computer Methods in Applied Mechanics and Engineering,* vol. 3, no. 2, pp. 269-289, 1974/03/01/ 1974.

[86] D. C. Wilcox, "Reassessment of the scale-determining equation for advanced turbulence models," *AIAA journal,* vol. 26, no. 11, pp. 1299-1310, 1988.

[87] Y. Zhiyin, "Large-eddy simulation: Past, present and the future," *Chinese journal of Aeronautics,* vol. 28, no. 1, pp. 11-24, 2015.

[88] J. SMAGORINSKY, "GENERAL CIRCULATION EXPERIMENTS WITH THE PRIMITIVE EQUATIONS," *Monthly Weather Review,* vol. 91, no. 3, pp. 99-164, 1963.

[89] F. Roelofs, *Thermal Hydraulics Aspects of Liquid Metal Cooled Nuclear Reactors*. Woodhead Publishing, 2018.

[90] A. A. Adeniyi, H. Morvan, and K. Simmons, "A Multiphase CFD Approach for Modelling of the Aeroengine Bearing Sector - SILOET II (T5.4.3) PART I," 30/05/2015 2015.

[91] J. Tu, G. H. Yeoh, and C. Liu, *Computational fluid dynamics: a practical approach*. Butterworth-Heinemann, 2018.

[92] A. I. o. Aeronautics and Astronautics, *AIAA guide for the verification and validation of computational fluid dynamics simulations*. American Institute of aeronautics and astronautics, 1998.

[93] C. A. Foord, "High-speed ball bearing analysis," *Proceedings of the Institution of Mechanical Engineers, Part G: Journal of Aerospace Engineering,* vol. 220, no. 5, pp. 537-544, 2006.

[94] M. Flouros, "Oil Pumping in High Speed and High Loaded Ball Bearings," no. 41693, pp. 359-363, 2004.

[95] M. Flouros, "Correlations for heat generation and outer ring temperature of high speed and highly loaded ball bearings in an aero-engine," *Aerospace Science and Technology,* vol. 10, no. 7, pp. 611-617, 2006/10/01/ 2006.

[96] M. Flouros, M. Hirschmann, F. Cottier, P. Gloeckner, and K. Dullenkopf, "Active Outer Ring Cooling of High-Loaded and High-Speed Ball Bearings," *Journal of Engineering for Gas Turbines and Power,* vol. 135, no. 8, 2013.

[97] R. Santhosh, J. L. Hee, K. Simmons, and G. Johnson, "Experimental Investigation Into Oil Shedding And Film Flow Near A Trent 1000 HP Bearing At Shaft Speeds Up To 7000 RPM," 10th Oct 2016 2016.

[98] R. Stables, K. Simmons, and G. Johnson, "Statement of Requirement (SOR) for SILOET2, Work Package 5.4 Test Rig," 2013.

[99] Nikon. *Understanding Focal Length* [Online]. Available: https://www.nikonusa.com/en/learn-and-explore/a/tips-and-techniques/understanding-focal-length.html.

[100] Nikon. *DSLR Camera Basics - Setting Exposure: Shutter Speed and Aperture* [Online]. Available: https://imaging.nikon.com/lineup/dslr/basics/04/02.html

[101] Nikon. *DSLR Camera Basics - Aperture* [Online]. Available: https://imaging.nikon.com/lineup/dslr/basics/04/04.html.

[102] David. (2013). *Exposure Guide* [Online]. Available: https://epress.earlham.edu/dxknox12/2013/11/.

[103] Andy. *Aperture* [Online]. Available: http://www.andyc.photography/blog/.

[104] T. E. Ltd. *OG3 Oval Gear Flowmeter* [Online]. Available: https://www.flowmeters.co.uk/og3-oval-gear-pd-positive-displacement-swept-volume-flow-meters/.

[105] Fluke. (2004). *Fluke 80PK-26* [Online]. Available: https://www.fluke.com/en-gb/product/accessories/probes/fluke-80pk-26.

[106] Siemens. *Siemens Load Cell* [Online]. Available: https://new.siemens.com/global/en/products/automation/process-instrumentation/weight-measurement/load-cells/siwarex-wl280-rn-s-sa.html.

[107] M. Petrou and C. Petrou, *Image processing: the fundamentals*. John Wiley & Sons, 2010.

[108] L. R. White, J. D. Helfand, H. R. Becker, E. Glikman, and W. d. Vries, "Signals from the Noise: Image Stacking for Quasars in the FIRST Survey," *The Astrophysical Journal,* vol. 654, no. 1, p. 99, 2007.

[109] R. Santhosh, J. L. Hee, K. Simmons, G. Johnson, D. Hann, and M. Walsh, "Experimental Investigation of Oil Shedding From an Aero-Engine Ball Bearing at Moderate Speeds," *ASME Proceedings,* no. 50923, p. V07AT34A018, 2017.

[110] M. Drosg, *Dealing with uncertainties*. Springer, 2007.

[111] R. P. Fraser, N. Dombrowski, and J. H. Routley, "The filming of liquids by spinning cups," *Chemical Engineering Science,* vol. 18, no. 6, pp. 323-337, 1963/06/01/ 1963.

[112] R. P. Fraser, N. Dombrowski, and J. H. Routley, "The production of uniform liquid sheets from spinning cups," *Chemical Engineering Science,* vol. 18, no. 6, pp. 315-321, 1963/06/01/ 1963.

[113] T. Kamiya and A. Kayano, "On the Ligament-Type Disintegration by the Rotating Disk. Applicability of the ligament type disintegration on the disk to that at the edge of the disk," *Chemical engineering,* vol. 35, no. 5, pp. 541-546,a1, 1971.

[114] J. Canny, "A Computational Approach to Edge Detection," *IEEE Transactions on Pattern Analysis and Machine Intelligence,* vol. PAMI-8, no. 6, pp. 679-698, 1986.

[115] J. L. Hee, K. Simmons, D. Hann, and M. Walsh, "Characterisation of Waves and Ligaments in Films Close to an Aeroengine Ball Bearing," in *ASME Turbo Expo 2019: Turbomachinery Technical Conference and Exposition*, 2019: American Society of Mechanical Engineers Digital Collection.

[116] R. G. Dean and R. A. Dalrymple, *Water wave mechanics for engineers and scientists*. World Scientific Publishing Company, 1991.

[117] W. H. Munk, "Origin and generation of waves," Scripps Institute of Oceanography La Jolla California 1951.

[118] T. B. Aydin, C. F. Torres, H. Karami, E. Pereyra, and C. Sarica, "On the characteristics of the roll waves in gas–liquid stratified-wavy flow: A two-dimensional perspective," *Experimental Thermal and Fluid Science,* vol. 65, pp. 90-102, 2015/07/01/ 2015.

[119] X. T. Chen, X. D. Cal, and J. P. Brill, "Gas-Liquid Stratified-Wavy Flow in Horizontal Pipelines," *Journal of Energy Resources Technology,* vol. 119, no. 4, pp. 209-216, 1997.

[120] T. J. Hanratty, "Interfacial instabilities caused by air flow over a thin liquid layer," in *Waves on Fluid Interfaces*, R. E. Meyer, Ed.: Academic Press, 1983, pp. 221-259.

[121] L. Bertin, "Air - Liquid Flows Around an Obstacle," Internal Report. 2005.

[122] H. Lamb, *Hydrodynamics*. Cambridge university press, 1993.

[123] B. E. Launder and D. B. Spalding, *Lectures in mathematical models of turbulence*. Academic Press, 1979.

[124] J. W. Chew and N. J. Hills, "Computational fluid dynamics for turbomachinery internal air systems," *Philosophical Transactions of the Royal Society A: Mathematical, Physical and Engineering Sciences,* vol. 365, no. 1859, pp. 2587-2611, 2007.

[125] B. Chandra, K. Simmons, S. Pickering, S. H. Collicott, and N. Wiedemann, "Study of Gas/Liquid Behavior Within an Aeroengine Bearing Chamber," *Journal of Engineering for Gas Turbines and Power,* vol. 135, no. 5, pp. 051201-051201-11, 2013.

[126] M. Berthold, H. Morvan, C. Young, and R. Jefferson-Loveday, "Towards Investigation of External Oil Flow From a Journal Bearing in an Epicyclic Gearbox," *ASME Conference Proceedings,* no. 50923, p. V07AT34A010, 2017.

[127] J. L. Hee, K. Simmons, B. Kakimpa, and D. Hann, "Computationally Efficient Modelling of Oil Jet-Breakup and Film Formation for Bearing Chamber Applications," *ASME Proceedings,* no. 51012, p. V02CT42A031, 2018.

[128] T. Shedd, M. Corn, J. Cohen, M. Arienti, and M. Soteriou, "Liquid Film Formation by an Impinging Jet in a High-Velocity Air Stream," in *47th AIAA Aerospace Sciences Meeting including The New Horizons Forum and Aerospace Exposition* (Aerospace Sciences Meetings: American Institute of Aeronautics and Astronautics, 2009.

[129] H. Moffatt, "Behaviour of a viscous film on the outer surface of a rotating cylinder," *Journal de mécanique,* vol. 16, pp. 651-673, 1977.

[130] J. Ashmore, A. E. Hosoi, and H. A. Stone, "The effect of surface tension on rimming flows in a partially filled rotating cylinder," *Journal of Fluid Mechanics,* vol. 479, pp. 65-98, 2003.

[131] K. Pougatch and I. Frigaard, "Thin film flow on the inside surface of a horizontally rotating cylinder: Steady state solutions and their stability," *Physics of Fluids,* vol. 23, no. 2, p. 022102, 2011.

[132] E. D. Kay, S. Hibberd, and H. Power, "A depth-averaged model for non-isothermal thin-film rimming flow," *International Journal of Heat and Mass Transfer,* vol. 70, pp. 1003-1015, 2014/03/01/ 2014.

[133] A. A. Adeniyi, "A coupled Lagrangian Eulerian framework to model droplet to film interaction with heat transfer," PhD, Mechanical Engineering, University of Nottingham, 2015.

[134] Y. S. Kachanov, "Hypothesis on deterministic turbulence," *European Journal of Mechanics - B/Fluids,* vol. 40, pp. 30-33, 2013/07/01/ 2013.

[135] F. R. Menter, "Two-equation eddy-viscosity turbulence models for engineering applications," *AIAA Journal,* vol. 32, no. 8, pp. 1598-1605, 1994/08/01 1994.

[136] ANSYS Inc, "ANSYS Fluent Theory Guide Release 17.1 ", 2016.

[137] J. M. Osterlund, "Experimental studies of zero pressure-gradient turbulent boundary layer flow " PhD, Royal Institute of Technology, Kungl Tekniska Hogskolan Stockholm, Sweden, 1999.

[138] A. B. Liu, D. Mather, and R. D. Reitz, "Modeling the Effects of Drop Drag and Breakup on Fuel Sprays," SAE Transactions, 1993. [Online]. Available: https://doi.org/10.4271/930072.

[139] C. Soteriou, R. Andrews, and M. Smith, "Direct Injection Diesel Sprays and the Effect of Cavitation and Hydraulic Flip on Atomization," SAE Transactions, 1995. [Online]. Available: https://doi.org/10.4271/950080.

[140] W. E. Ranz, "Some experiments on orifice sprays," *The Canadian Journal of Chemical Engineering,* vol. 36, no. 4, pp. 175-181, 1958.

[141] R. D. Reitz and F. V. Bracco, "Mechanism of atomization of a liquid jet," *The Physics of Fluids,* vol. 25, no. 10, pp. 1730-1742, 1982/10/01 1982.

[142] P.-K. Wu, L.-K. Tseng, and G. Faeth, "Primary breakup in gas/liquid mixing layers for turbulent liquids," *Atomization and Sprays,* vol. 2, no. 3, 1992.

[143] P. J. O'Rourke and A. A. Amsden, "The Tab Method for Numerical Calculation of Spray Droplet Breakup," SAE Transactions, 1987. [Online]. Available: https://doi.org/10.4271/872089.

[144] P. J. O'Rourke and A. A. Amsden, "A Particle Numerical Model for Wall Film Dynamics in Port-Injected Engines," SAE Transactions, 1996. [Online]. Available: https://doi.org/10.4271/961961.

[145] M. A. Friedrich, H. Lan, J. L. Wegener, J. A. Drallmeier, and B. F. Armaly, "A Separation Criterion With Experimental Validation for Shear-Driven Films in Separated Flows," *Journal of Fluids Engineering,* vol. 130, no. 5, pp. 051301-051301-9, 2008.

[146] T. Arai and H. Hashimoto, "Disintegration of Thin Liquid Sheet in Cocurrent Gas Stream : Wave Motion of Thin Liquid Sheet and Breakup Patterns," *Transactions of the Japan Society of Mechanical Engineers Series B,* vol. 51, no. 470, pp. 3336-3343, 1985.

[147] T. C. L. Yue, "Numerical simulation of multiphase jet fragmentation using Smoothed Particle Hydrodynamics," PhD, The University of Nottingham, 2015.

[148] M. A. Lopez de Bertodano, C.-S. Jan, and S. G. Beus, "Annular flow entrainment rate experiment in a small vertical pipe," *Nuclear Engineering and Design,* vol. 178, no. 1, pp. 61-70, 1997/12/02/ 1997.

[149] M. Ernest, "Theory of Liquid Atomisation in High Velocity Gas Streams," *ARS Journal,* vol. 31, no. 12, pp. 1783 - 1785, 1961.

[150] D. G. Owen, "An experimental and theoretical analysis of equilibrium annular flows," PhD, University of Birmingham, British Library, 1986.

[151] B. H. Kim and G. P. Peterson, "Analysis of the critical Weber number at the onset of liquid entrainment in capillary-driven heat pipes," *International Journal of Heat and Mass Transfer,* vol. 38, no. 8, pp. 1427-1442, 1995/05/01/ 1995.

[152] P. Andreussi, "The onset of droplet entrainment in annular downward flows," *The Canadian Journal of Chemical Engineering,* vol. 58, no. 2, pp. 267-270, 1980.

[153] S. M. Ghiaasiaan, *Two-Phase Flow, Boiling, and Condensation: In Conventional and Miniature Systems*. Cambridge: Cambridge University Press, 2007.

[154] F. M. White, "Fluid mechanics," 2015.

[155] R. Ingle, R. Yadav, H. Punekar, and J. Cao, "Modeling of Particle Wall Interaction and Film Transport Using Eulerian Wall Film Model," *ASME Proceedings,* no. 49644, p. V001T03A006, 2014.

[156] S. V. Alekseenko, V. A. Antipin, A. V. Cherdantsev, S. M. Kharlamov, and D. M. Markovich, "Investigation of Waves Interaction in Annular Gas–Liquid Flow Using High-Speed Fluorescent Visualization Technique," *Microgravity Science and Technology,* journal article vol. 20, no. 3, pp. 271-275, September 01 2008.

[157] I. Zadrazil, J. S. An, A. Cherdantsev, and C. Markides, "Development of LIF techniques applied to gas-liquid annular flows."

Appendix

[See Next Page]

Images for calculation of Ligament number

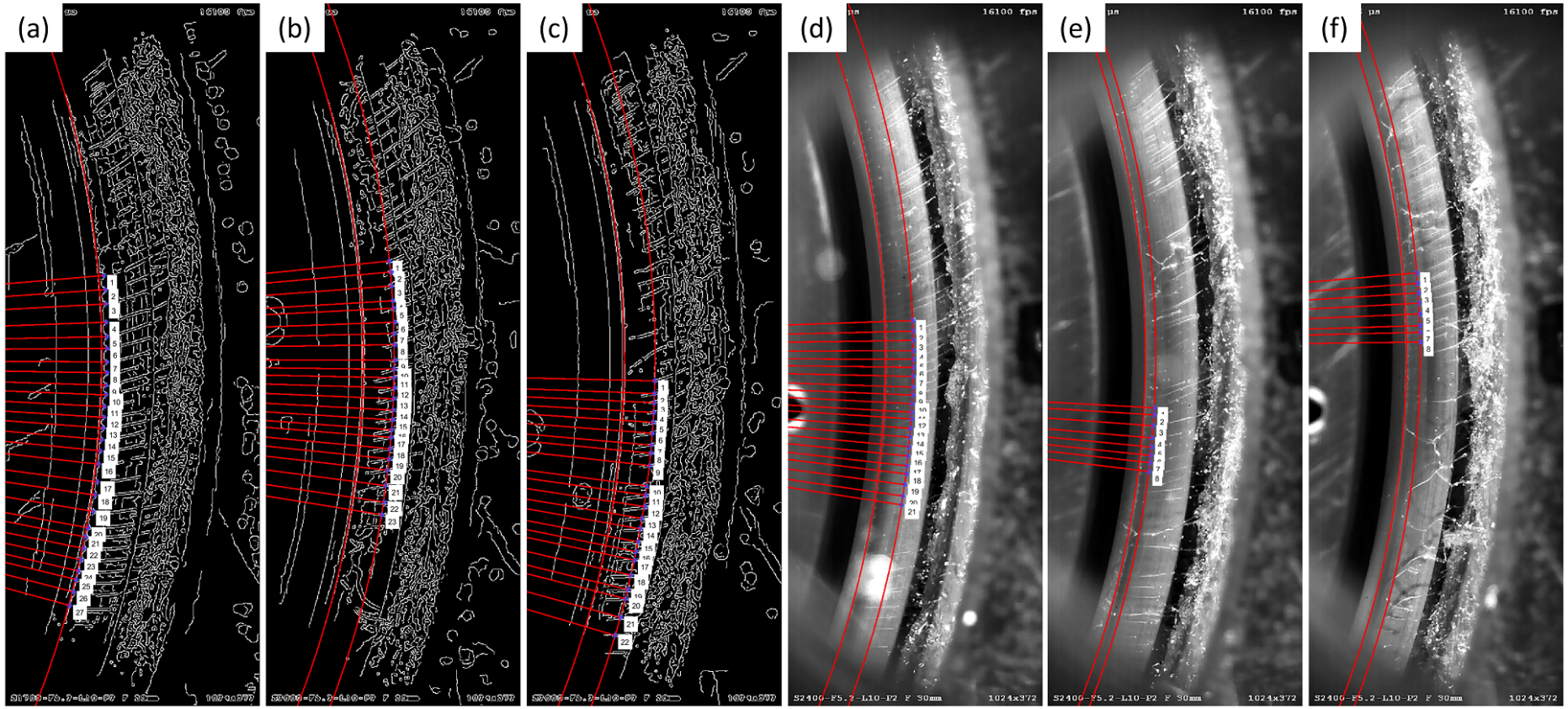


Figure A 1: Images of ligament at (a) S1700-F5.2-L10-P2 (b) (c) S2000-F5.2-L10-P2 (d) (e) (f) S2400-F5.2-L10-P2

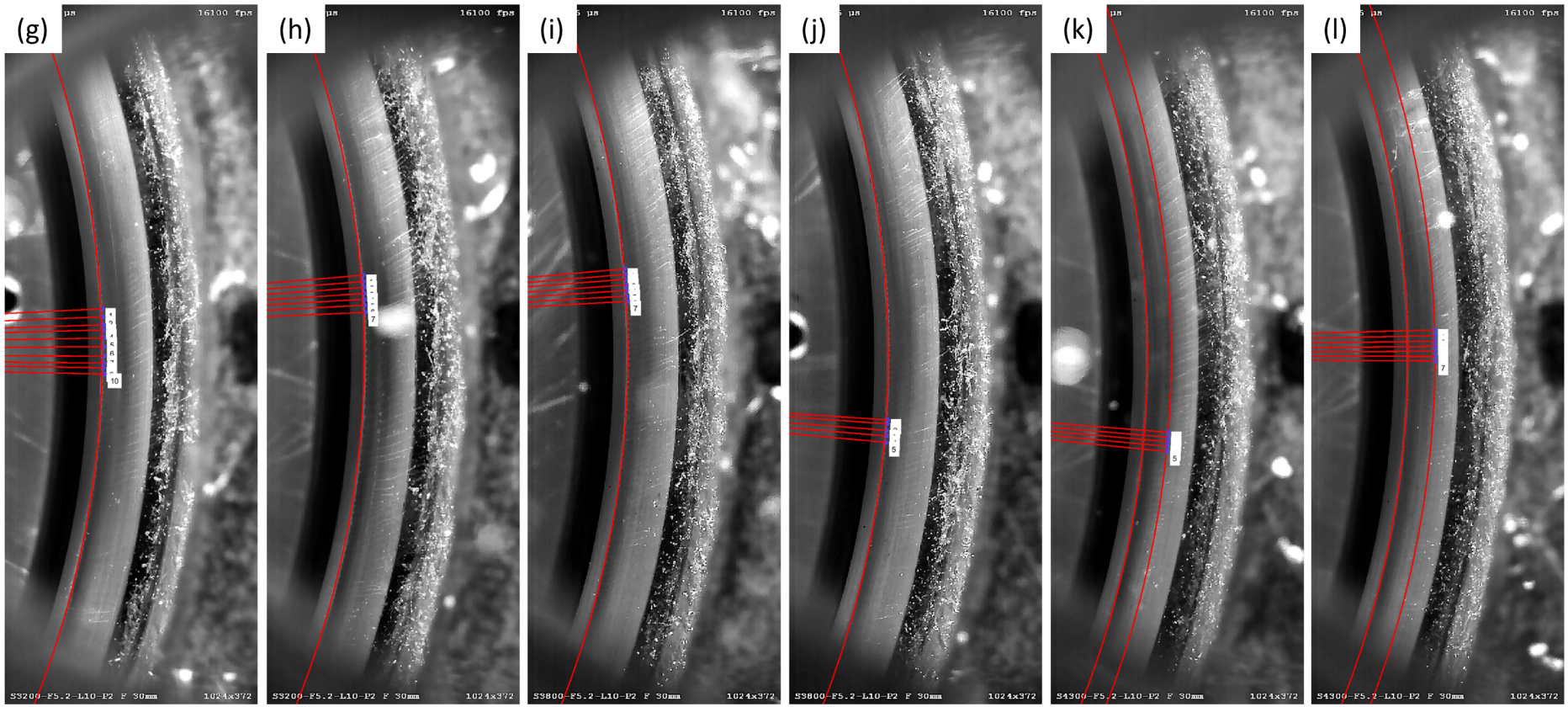


Figure A 2: Images of ligament at (g) (h) S3200-F5.2-L10-P2 (i) (j) S3800-F5.2-L10-P2 (k) (l) S4300-F5.2-L10-P2

Parallel Code for Median-Stacking

```
%% Code for Median and Mean Image processing using
clear       %clear workspace & free-up memory from MATLAB workspace
clc         %clear command window
%myFolder - location where all the tiff images are stored after being
%exported from MOTION STUDIO

%MAKE SURE CURRENT FOLDER on the left IS THE FOLDER THAT THIS CODE WISH TO WORK ON.
%REASON BECAUSE imread split the calculation into 4 parts. And it is not
%importdata
%WINDOW 7 Setting

myFolder = 'H:\MATLAB Code\Example demonstration'      %Specify the folder address that contains
the images to be postprocessed
cd (myFolder)                                          %change current folder
filePattern = fullfile(myFolder,'*.tif');              %read tif extension at the folder specified
tiffFiles = dir(filePattern);                          %List the contents of a folder in strut
format

%IF the imwrite has been executed. Additional tiff images will be detected
%by matlab hence ensure that only raw images are there.
j = 1                                                  %Indexing
user = input('Please set the step (1 = total no images/1, 2 = total no images/2)')
%The number of images to be processed. (1 means all images contain in the folder, 2 means half of
it)
test = 1:user:length(tiffFiles);                       %Display total number of images
being processed
D_Array = zeros(256,372,length(tiffFiles)/user,'single');      %Create a 3D array to increase
efficiency in calculation, 3D_Array is not used as not allowed, single precision is chosen as it
permits for 8GB RAM
t = [256 512 768 1024];                                %Due to limited RAM, median
calculation is break into 4 parts

tic %Begin the counter to measure postprocessing time
for index = 1:4                                        %subdivide the postprocessing into
4 segments to save computational resources
    baseFileName = tiffFiles(j).name;                  %the first tiffFiles(1).name
    fullFileName = fullfile(myFolder, baseFileName);   %Select from the folder
    Image_A=imread(fullFileName,'PixelRegion',{[t(index)-256+1,t(index)],[1,372]}); %Subdivide it
into 4 segments and read the image of the segment specified by pixel region
    Image_A_single = im2single(Image_A);                %Convert the image uint8 into
single precision
    D_Array(1:256,1:372,1) = Image_A_single;            %Fill up the array created
earlier with first image, basically this for loop is to stack the images into 3D

    index_2 = 1;                                        %Perform same method for the rest
of the images by stacking into 3D array
    for j = 2:user:length(tiffFiles)
        C = tiffFiles(j).name;
        D_Array(1:256,1:372,index_2) = imread(C,'PixelRegion',{[t(index)-
256+1,t(index)],[1,372]}); %Read image of the segment with size specified by pixel region
        index_2 = index_2 + 1;
    end

D_Array_median(t(index)-256+1:t(index),1:372) = median(D_Array,3);  %Calculate the median from the
3D array
D_Array_avg(t(index)-256+1:t(index),1:372) = mean(D_Array,3) ;      %Calculate the mean from the
3D array

end
toc %Tic Toc tells the time of processing (eg 355 seconds)

% Display Median image and write it into the folder
image = uint8(D_Array_median);                         %convert the D_Array_median into unassigned
interger 8 as this is 8 bit format
[r,c] = size(image);                                   %Check the size of the image
figure(1)                                              %Open window 1
Array_new_display = im2uint8(image);                   %double convert into uint8 for assurance
using matlab im2uint8 function before display the image using figure
imshow(image);
set(gca,'Units','normalized','Position',[0 0 1 1]);    %normalized the image for 1 to 1 (0 0 1 2)
will shift the only display one half of the image
set(gcf,'Units','pixels','Position',[896 1 c r]);      %PC monitor(Full HD has 1920 x 1080), the
image will be display at pixel column 896 and row 1
hold on;
file_store_name=sprintf('Median_of__%d_Images.tif',j);  %The name that will be saved with j
indicated the total number of images processed
file_store_dir=fullfile(myFolder, file_store_name);     %Save it in myFolder, with the string
defined earlier
f = getframe(gcf)                                       %Getframe function is to output the exact
image from the figure displayed
imwrite(f.cdata,file_store_dir)                         %imwrite is to save the tiff image into
the folder (Median-stacked image)

% Display Mean image and write it
```

```
image_avg = uint8(D_Array_avg);                          %convert the D_Array_avg into unassigned
interger 8 as this is 8 bit formats
[r1,c1] = size(image_avg)                                %check the size of the image_avg
figure(2)                                                %Open window 2
Array_new_display_avg = im2uint8(image_avg);             %double convert into uint8 for assurance
using matlab im2uint8 function before display the image using figure
imshow(Array_new_display_avg);
set(gca,'Units','normalized','Position',[0 0 1 1]);      %normalized the image for 1 to 1 (0 0 1 2)
will shift the only display one half of the image
set(gcf,'Units','pixels','Position',[896 1 c r]);        %PC monitor(Full HD has 1920 x 1080), the
image will be display at pixel column 896 and row 1
hold on;
file_store_name=sprintf('Mean_of__%d_Images.tif',j);     %The name that will be saved with j
indicated the total number of images processed
file_store_dir=fullfile(myFolder, file_store_name);      %Save it in myFolder, with the string
defined earlier
f = getframe(gcf)                                        %Getframe function is to output the exact
image from the figure displayed
imwrite(f.cdata,file_store_dir)                          %imwrite is to save the tiff image into
the folder (Time averaging mean image)
```